Tampere University

LATIFEH AZIZI

Structure-function of Talin1

An integrin adaptor protein involved in health and disease

Tampere University Dissertations 832

Tampere University Dissertations 832

LATIFEH AZIZI

Structure-function of Talin1

An integrin adaptor protein involved in health and disease

ACADEMIC DISSERTATION
To be presented, with the permission of
the Faculty of Medicine and Health technology
of Tampere University,
for public discussion in the auditorium F114
of the Arvo building, Arvo Ylpön katu 34, Tampere,
on 18th of August, at 12 o'clock.

ACADEMIC DISSERTATION
Tampere University, Faculty of Medicine and Health Technology
Finland

Responsible supervisor and Custos	Professor Vesa Hytönen Tampere University Finland	
Supervisor	PhD Paula Turkki Tampere University Finland	
Pre-examiners	Professor Susanna Fagerholm University of Helsinki Finland	Associate Professor Guillaume Jacquemet University of Turku Finland
Opponent	Professor Aki Manninen University of Oulu Finland	

Cover design: Roihu Inc.

ISBN 978-952-03-2983-9 (print)
ISBN 978-952-03-2984-6 (pdf)
ISSN 2489-9860 (print)
ISSN 2490-0028 (pdf)
http://urn.fi/URN:ISBN:978-952-03-2984-6

Carbon dioxide emissions from printing Tampere University dissertations have been compensated.

PunaMusta Oy – Yliopistopaino
Joensuu 2023

To my parents

ACKNOWLEDGEMENTS

This thesis was carried out at Tampere University, Faculty of Medicine and Health Technology in the Protein Dynamics research group. It would not have been possible to come to this point if I did not have the support of many smart people working along with me, to which I would like to express my sincere gratitude.

First, I want to thank to my supervisor Professor Vesa Hytönen, to whom I am forever grateful for giving me the great opportunity to be a member of his group; he encouraged me to learn and conduct research in an inspiring environment. This thesis would not be possible without his continuous support, insights, ideas, and encouragement toward the completion of my PhD studies. Thank you for guidance, patience and making this possible. I've learned a lot and have grown as scientist.

I am eternally grateful to my co-supervisor PhD Paula Turkki for her extremely valuable contribution to the work, for her enthusiasm, and for giving me the confidence to go on through the obstacles I have encountered. I am thankful for all the work she has done to teach me and help me with my experiments and manuscripts, for her patience and for her friendship.

I want to thank Professor Ben Goult and his lab members for the amazing collaboration times, for all his support and help during a challenging time to finalize the manuscripts for submission.

I would like to express my sincere gratitude to Professor Aki Manninen, University of Oulu, for accepting to be my opponent during the public defence. I am also grateful to the pre-examiners of my dissertation, Professor Susanna Fagerholm, University of Helsinki, and Associate Professor (tenure track) Jacquemet Guillaume, University of Turku, for their excellent suggestions to improve my work.

I also wish to thank Professor Bernhard Wehrle-Haller (University of Geneva), Professor R. Holland Cheng (The University of California, Davis) and senior research fellow Teemu Ihalainen (Tampere University) for being members of my thesis committee, for their expert advice, support, and encouragement to finish my thesis. I would like to thank Professor Bernhard Wehrle-Haller for our collaboration, his excellent tips and for the amazing time during my visit to his lab in Geneva.

I would like also to thank Professor Emeritus Markku Kulomaa, 'Kuku', for providing me an opportunity to enter his group when I was looking for opportunities as a newly graduated master student. Thanks to him, I got introduced to the biotechnology field in a friendly and positive environment as well as to Vesa´s group, and could start my life journey in science, where I am now for more than 10 years.

Of course, I want to thank all my former and present colleagues for the highly motivating work atmosphere, for their contributions and friendship, which fills my heart both with warmth and sadness, knowing that I have to leave my science family. My special thanks goes to PhD Vasyl Mykuliak and PhD Sampo Kukkurainen for their amazing contribution into the bioinformatic works and all the help, guidance and support I got from both of them throughout the projects. Vasyl has been closely contributing into my last papers, I would say I could not finish my papers without his amazing contribution, support and patience. Thank you so much for your significant and important participation to the papers. I would like to thank Juha, Jenni, Rolle, Soili, Magda, Anssi, Elina, Barbara, Sanna, Niila, Minna, Vili, and many others I got to know and sometimes become friends with, in our dining areas and in the corridors, for their accompany and nice discussion. I would like to thank Ulla Kiiskinen and Niklas Kähkönen for their amazing help and sharing their extensive knowledge on the technical know-how throughout the years.

I am grateful for the financial support for my research and this dissertation work, including the Doctoral Programme at Tampere University, Anu Kirra´s Foundation, the Finnish Cultural Foundation, Alfred Kordelin Foundation, Fimlab laboratories, the City of Tampere, Academy of Finland and Sigrid Juselius Foundation.

Finally, I would like to thank my family and friends for their contribution outside the lab. I would like to thank Julia B. and Mervi for being my friends and for all the support I needed in my good and bad times, we shared many moments together. I am extremely thankful to have you in my life.

In particular, I am deeply grateful to my parents, my mom and dad (Maman and Baba) for their sacrifices, love, and support. I wish I could share my accomplishments with my dad and big brother Ismail, but they are no longer here. As much as I feel lost without their support, I have been keep going through their memories and advice, although from time-to-time it has not been easy. My mom has been the rock to keep our spirit up and family together. I am thankful for the rest of my family members, my brothers and sisters and their lovely children to be in my life. My special thanks to my beautiful niece Sofia for bringing a smile to my face on her school trip in the mornings. You are such a beautiful girl and we all love you to the moon and back.

"Alone we can do so little; together we can do so much." - Helen Keller

Latifeh Azizi
Tampere
01.07.2023

ABSTRACT

A cell is the smallest structural and functional unit of an organism. Cells dynamically interact with their surrounding environment. The substance filling the space between cells is a network of proteins and polysaccharides and is called extracellular matrix the (ECM). Cell surface receptors play a vital role in mediating cell-ECM and other interactions. Integrins are cell surface receptors participating in a wide range of biological processes including cell adhesion, homeostasis, immune responses, and cancer. One of the most important aspects of integrins is the bidirectional signalling across the plasma membrane. Coordinated interaction between ECM, receptors and cytoskeleton is essential in the cell adhesion process. Talin is a cytoplasmic protein that binds directly to integrin β-subunits, regulating integrin signalling and connecting them with the actin cytoskeleton. In healthy cells, when talin undergoes force-induced mechanical unfolding, new recognition sites are exposed for binding to cytoskeletal proteins that are involved in mechanotransduction. Dysregulation of talin or its activators may lead to diseased state, deviating integrin activation and mechanotransduction. Furthermore, such disorder may cause changes in cell migration, spreading and overall survival. In publications I and II, we have focused on the structure and function of the talin head domain using molecular dynamic simulations, cell biology and biochemical analyses. We found that a flexible loop in the talin head subdomain F1 is important for β3-integrin clustering. In addition, we found that the C-terminal poly-lysine motif in the talin head mediates FERM interdomain contacts, assuring the FERM-folded configuration of the talin head. In publications III and IV, disease-associated talin point mutations were investigated. We found that even small changes in talin can lead to dramatic effects on cell function. In publication III, we developed a bioinformatic pipeline and scoring system to analyse talin1 point mutations that were found to be associated with cancer in previous studies. An I392N point mutation in the F3 domain increased cell migration and invasion but decreased integrin β1 activation. An L2509P point mutation in the dimerization domain led to a non-polarised cellular phenotype and disruption of adhesion maturation due to a lack of dimerisation and actin binding of the talin´s mutant. Publication IV discusses the identification of a *de novo* heterozygous variant P229S found from a patient with complex phenotype. This mutation led to local alterations of the F2-F3 domain interface compromising integrin activation, adhesion composition and cell migration. Furthermore, point mutations found from spontaneous coronary artery dissection (SCAD) patients were investigated (unpublished data), adding considerable supportive data demonstrating the impact of talin point mutations on cell function. Our findings suggest that disease associated point mutations in talin1 can affect cell behaviour and may contribute to the progression of different diseases. In addition, the importance of proper connections between integrins and the actin cytoskeleton through talin1 is a critical factor for cell´s health.

TIIVISTELMÄ

Solu on organismin pienin rakenteellinen ja toiminnallinen yksikkö. Solut ovat dynaamisesti vuorovaikutuksessa ympäröivän ympäristönsä kanssa. Solujen välisen tilan täyttävää ainetta, joka on proteiinien ja polysakkaridien verkosto, kutsutaan soluväliaineeksi (engl. extracellular matrix, lyh. ECM). Solun pintareseptoreilla on tärkeä rooli solu-ECM:n ja muiden vuorovaikutusten välittämisessä. Integriinit ovat solun pinnan reseptoreita, jotka osallistuvat monenlaisiin biologisiin prosesseihin, mukaan lukien soluadheesio, homeostaasi, immuunivaste ja syöpä. Yksi integriinien tärkeimmistä tehtävistä on kaksisuuntainen signalointi solukalvon läpi. Koordinoitu vuorovaikutus ECM:n, reseptorien ja solutukirangan välillä on olennaista solujen kiinnittymisessä. Taliini on solun sisällä ilmentyvä proteiini, joka sitoutuu integriinin β-alayksikköihin, säädellen integriinien signalointia ja yhdistäen ne solutukirangan kanssa. Julkaisuissa I ja II keskityimme taliinin pää-domeenin rakenteeseen ja toimintaan molekyylidynamiikkasimulaatioiden, solubiologian ja biokemiallisten analyysien avulla. Havaitsimme, että joustava silmukka taliiinin F1 aladomeenissa on tärkeä β3-integriinien klusteroitumisessa. Lisäksi havaitsimme, että taliinin pää-domeenissa oleva C-terminaalinen poly-lysiini-motiivi välittää taliinin pään aladomeenien välisiä kontakteja varmistaen taliinin pää-domeenin laskostumisen FERM-muotoon. Julkaisuissa III ja IV tutkittiin sairauteen liittyviä taliinin pistemutaatioita. Huomasimme, että pienetkin muutokset taliinissa voivat johtaa merkittäviin muutoksiin solujen toiminnassa. Julkaisussa III kehitimme laskennallisen menetelmän ja pisteytysjärjestelmän analysoimaan talini1-pistemutaatioita, joiden on aiemmissa tutkimuksissa havaittu liittyvän syöpään. I392N:n pistemutaatio F3-domeenissa lisäsi solujen migraatiota ja invaasiota, mutta vähensi integriini-β1-aktivaatiota. L2509P pistemutaatio taliinin dimerisaatiodomeenissa johti solujen polarisoitumisen katoamiseen ja häiritsi adheesion kypsymistä. Tämä johtuu taliinin dimerisoitumisen häiriintymisestä ja aktiinin sitoutumisen heikentymisestä. Julkaisu IV käsittelee *de novo* heterotsygoottisen variantin P229S analysoimista. Mutaatio löydettiin potilaalta, jolla on monimutkainen fenotyyppi. Tämä mutaatio johti paikallisiin muutoksiin taliinin F2-F3-domeenirajapinnassa, aiheuttaen muutoksia integriinin aktivoitumisessa, solujen adheesioiden rakenteessa ja solujen liikkumisessa. Lisäksi tutkittiin taliinin pistemutaatioita, joita löydettiin spontaania sepelvaltimoiden dissektiota (SCAD) sairastavilta potilailta (julkaisematon data). Havaitsimme yhteyden taliinin pistemutaatioiden ja solujen toiminnan välillä. Tuloksemme korostavat integriinin ja solutukirangan välisen yhteyden tärkeyttä solujen ja kudosten toiminnassa.

TABLE OF CONTENTS

List of Figures

List of Tables

ABBREVIATIONS

2D	Two-dimensional
3D	Three-dimensional
aa	Amino acid
ABS	Actin binding site
AKT	Ak strain transforming, a serine/threonine kinase, also called protein kinase B or PKB
CAD	Coronary artery disease
Cas	Cas family scaffolding protein
CDK-1	Cyclin-dependent kinase-1
CRC	Colorectal cancer
DCM	Dilated cardiomyopathy
DD	Dimerization domain
DH	Dimerization helix
DLC1	Deleted in liver cancer 1
DOPC	1,2-dioleoyl-sn-glycero-3-phosphocholine
DSC	Differential Scanning Calorimetry
EC	Endothelial cell
ECM	Extra Cellular Matrix
EDC	1-Ethyl-3-(3-dimethylaminopropyl
EGF	Epidermal growth factor
ERK	Extracellular signal-regulated kinase
FA	Focal adhesion
FAK	Focal adhesion kinase
FERM	4.1 protein, ezrin, radixin, moesin
Fn	Fibronectin
FRET	Förster resonance energy transfer
GBM	Glioblastoma multiforme
GSK-3	Glycogen synthase kinase-3
GT	Glanzmann thrombasthenia
GWAS	Genome-wide association study

HCC	Hepatocellular carcinoma
HDs	Hemidesmosomes
HUVEC	Human umbilical vein endothelial cells
IBS	Integrin binding site
ICAM	Intercellular adhesion molecules
ILK	Integrin-linked kinase
IN segment	Inhibitory segment
KANK	Kidney ankyrin repeat -containing protein
LOX	Lysyl oxidase
MD	Molecular dynamic
MDS	Myelodysplastic syndrome
MEF	Mouse embryonic fibroblasts
MKF	Mouse kidney fibroblast
MOP	Membrane orientation patch
MS	Multiple Sclerosis
MW	Molecular weight
NBT II	Nara bladder tumour II
NHS	N-Hydroxysuccinimide
NPC	Nasopharyngeal carcinoma
NPxY	Conserved PTB-domain-binding motif: asparagine-proline variable-tyrosine
NxxY	Conserved PTB-domain-binding motif: asparagine-variable-variable-tyrosine
OSC	Ovarian serous carcinoma
PDB	Protein data bank
PDGF	Platelet derived growth factor
PEE	Postencephalitic epilepsy
PFA	Paraformaldehyde
PH	Pleckstrin homology
PI3K	Phosphatidylinositol 3 kinase
PINCH	Particularly interesting new cysteine and histidine-rich protein
PIP2	Phosphatidylinositol-4,5-bisphosphase
PIPKIγ	Phosphatidylinositol 4-phosphate 5-kinase type-1 gamma
PKB	Protein kinase B
PTB	Phosphotyrosine binding
PVDF	Polyvinylidene fluoride

RALS	Right angle light scattering
siRNA	Small interfering RNA
RGD	Arginine-Glycine-Aspartic acid
RIAM	Rap1-GTP interacting adapter molecule
RT	Room temperature
SAXS	Small-angle X-ray scattering
SCAD	Spontaneous coronary artery dissection
SCC	Squamous cell carcinoma
SEC	Size exclusion chromatography
SLS	Static light scattering
Src	Pronounced "sarc", as it is short for sarcoma, proto-oncogene tyrosine-protein kinase Src, a non-receptor tyrosine kinase protein
TIP3P	Transferable intermolecular potential with 3 points
TEM	Transmission electron microscopy
TNBC	Triple-negative breast cancer
VASP	Vasodilator-stimulated phosphoprotein
VBS	Vinculin binding site
Vn	Vitronectin
VSMC	Vascular smooth muscle cells
WT	Wild type

One-letter codes for amino acids

A	alanine
C	cysteine
D	aspartic acid, aspartate
E	glutamic acid, glutamate
F	phenylalanine
G	glycine
H	histidine
I	isoleucine
K	lysine
L	leucine
M	methionine
N	asparagine
P	proline
Q	glutamine
R	arginine
S	serine
T	threonine
V	valine
W	tryptophan
Y	tyrosine

LIST OF ORIGINAL PUBLICATIONS

This thesis is based on the following original publications, which in the texts have been referred with Roman numerals I to IV. The original publications have been reproduced with the permission of the copyright holders.

I Kukkurainen, S., **Azizi, L.***, Zhang, P.*, Jacquier, M. C.*, Baikoghli, M., von Essen, M., Tuukkanen, A., Laitaoja, M., Liu, X., Rahikainen, R., Orłowski, A, Jänis, J., Määttä, J.A.E., Varjosalo, M., Vattulainen, I., Róg, T., Svergun, D., Cheng, R.H., Wu, J., Hytönen, V.P.**, Wehrle-Haller, B.** (2021). The F1 loop of the talin head domain acts as a gatekeeper in integrin activation and clustering. J. Cell Sci. 133, jcs239202.

II Zhang, P., **Azizi, L.**, Kukkurainen, S.*, Gao, T.*, Baikoghli, M.*, Jacquier, M. C.*, Sun, Y., Määttä, J. A. E., Cheng, R. H., Wehrle-Haller, B., Hytönen, V.P., Wu, J. (2020). Crystal structure of the FERM-folded talin head reveals the determinants for integrin binding. Proc. Natl. Acad. Sci. U. S. A. 117, 32402–32412.

III **Azizi, L.**, Cowell, A. R., Mykuliak, V. V., Goult, B. T., Turkki, P. and Hytönen, V. P. (2021). Cancer-associated talin point mutations disorganise cell adhesion and migration. Sci. Rep. 11, 347.

IV **Azizi, L.***, Varela, L.*, Turkki, P.*, Mykuliak, V. V., Korpela, S., Ihalainen, T. O., Church, J., Hytönen, V. P. and Goult, B. T. (2022). Talin variant P229S compromises integrin activation and associates with multifaceted clinical symptoms. Hum. Mol. Genet. 31, 4159-4172.

*, ** Equal contributions

AUTHOR´S CONTRIBUTION

Publication I, II	Produced talin/integrin plasmids, performed recombinant protein expression, purification, and analysis of different talin and integrin constructs. Performed liquid chromatography methods including analytical light scattering. Performed differential scanning calorimetry, biosensor analysis of talin–integrin interactions and participated in small-angle X-ray scattering analysis of the proteins. Participated in manuscript writing and revision.
Publication III, IV	Designed and produced expression plasmids. Performed cell analysis experiments (migration and invasion assays, immunostaining, confocal imaging, and western blotting). Performed screening of talin mutants using bioinformatics methods. Wrote the first draft of the manuscript, revised, and accepted the final version.

1 INTRODUCTION

Living cells continuously receive mechanical cues from their environments, translating these signals to biochemical information (mechanotransduction). This is a fundamental cellular process taking place, for example, at cell-ECM contacts, also known as focal adhesions. At focal adhesions sites, cells are physically connected to the ECM through integrin receptors associated *via* their cytoplasmic domains to the actin cytoskeleton.

Talin is an important integrin-associated protein that plays an essential role in cell adhesion (Haining et al., 2016a; Sun et al., 2016b). In vertebrates, talin1 is expressed in nearly all tissues and regulates integrin and focal adhesion signalling. The major findings of talin function were from studies demonstrating that the talin1 head binds the cytoplasmic tails of β-integrin subunits, leading to "inside-out" integrin activation (Calderwood et al., 1999; Tadokoro et al., 2003). The rod domain of talin has the ability to sense mechanical forces and regulate the assembly and maturation of focal complexes (Dedden et al., 2019). The rod domain (residues ~482-2541, C-terminal) binds to actin filaments and other adaptor proteins and is also involved in talin dimerization.

Dysregulation and/or changes in the structure and expression level of talin are connected to different disease states affecting cell adhesion, spreading and migration (Wei et al., 2017; Tang et al., 2021; Vafaei et al., 2020; Xu et al., 2015). For example, in the metastatic tissues of human prostate specimens, significantly higher talin expression level has been observed as compared with the primary prostate tumour (Sakamoto et al., 2010). Talin is also upregulated in other cancerous diseases such as hepatocellular carcinoma (Kanamori et al., 2011), oral squamous cell carcinoma (Lai et al., 2011), ovarian serous carcinoma (Tang et al., 2013) and brain tumour glioblastoma (Sen et al., 2012). Since talin has long list of binding partners, there is also long list of other potential pathologies in which it could be involve to, such as hematologic disorder (Moura et al., 2022) and heart diseases (Aoyama et al., 2020; Turley et al., 2019).

Our studies brings up further the important role of talin1 in the cell and the disease states caused by talin1 misfunction. Understanding diseases associated with cell adhesion at a molecular level will help to untangle the adhesion mechanism in the disease condition and may help to the development of preventive and personalized therapies.

2 REVIEW OF THE LITERATURE

2.1 The extracellular matrix has a dynamic structure and composition

The interactions of cells with their extracellular matrix (ECM) define the development of an organism (Mecham, 2001). The ECM has multiple functions, and it is a major component of the cellular microenvironment. It has a highly dynamic structure that influences cellular function, modulating fundamental aspects of the cell biology. In addition to its structural role, it influences many diverse functions from basic cell behaviour to cell proliferation, adhesion, migration, differentiation, and cell death (Hynes, 2009; Lu et al., 2011). The ECM comprises of approximately 300 proteins including major components such as collagens, proteoglycans, elastin, glycoproteins, fibronectin, vitronectin, laminin and matricellular proteins (Mecham, 2001). Each component has different physical and biochemical properties making the ECM highly dynamic and variable. Mechanical, biophysical and biochemical changes in the ECM composition result in changes in the cell behaviour (Lu et al., 2011; Mecham, 2001). The physical properties of the ECM include rigidity, density, porosity, insolubility, topography, and other characteristics important in supporting tissue structure and contribute to cell migration and anchoring (Lu et al., 2011; Yue, 2014).

The ability of cells to sense, respond and transduce mechanical messages into intracellular biochemical messages is termed as mechanotransduction, and it is important for organ development and tissue homeostasis. Various mechanosensors in a cell, from ion channels in the plasma membrane to cytoplasmic proteins and the nucleus itself, encounter conformational changes in response to force. While many studies have focused on the mechanotransduction by integrins (Ross et al., 2013), there is now a growing number of studies showing the contribution of the ECM, different focal adhesion proteins, and ligand interactions in this process (Uray and Uray, 2021). Modification in the composition and regulation of the ECM have been linked to onset and progression of many diseases such as cancer, osteoarthritis, and fibrosis (Bonnans et al., 2014). The mechanical signals sensed by the cell through

adhesion molecules and changes in the mechanical characteristics of the ECM play an important role in both physiological and pathological functions (Uray and Uray, 2021).
The cell and the ECM have a two-way give-and-take relationship. Cells produce, secrete and remodel ECM for mediating ECM composition and topography. The ECM in return transmit signals through its receptors to affect cell´s activity and characteristics. This reaction mechanism is vital for a prompt response of cells to changes in the surrounding environment. The biology of ECM has extensive implications in different areas such as wound healing, cancer invasion and metastasis and biomedical engineering (Yue, 2014).

2.1.1 Cell migration strategies in the ECM

Cells sense their physical environment through mechanotransduction, which applies to all cellular processes where cells detect, translate, and respond to mechanical stimuli, converting them into biochemical signals (Jaalouk and Lammerding, 2009).

Different types of movement has been identified by cells in the ECM, which generally has been classified as individual (single-cell) and collective movement. In individual cell movement, cell migrate as a single element and exert only transient contacts with other migratory cells (Friedl, 2004). Although the classification of cell migration modes are much more complicated in different environment, in general, single-cell migration has been divided into two modes of mesenchymal and amoeboid movements. Fibroblasts, different stem cells and some cancer cells usually have mesenchymal migration mode with strong adhesion to the ECM, actin-based protrusions and elongated morphology in 3D environment (Bear and Haugh, 2014). The amoeboid migration mode is used for example in germ cells and immune cells such as leukocytes. In this migration mode, cells have more rounded morphology, experiencing rapid shape changes through extension and retraction membrane protrusions with weak adhesions, leading to higher migration speed of the cell (Lämmermann and Sixt, 2009).

Collective cell migration occurs as a cluster or monolayer of cells with strong adhesive contacts (Friedl, 2004). Epithelial and mesenchymal cells both have collective migration mode, which is important for wound healing, tissue remodelling and cancer cell invasion. Through mechanotransduction at cell-cell junctions, cell-ECM interfaces and intracellular signalling cascades, signals are transmitted to the entire mass of the cell (Mayor and Etienne-Manneville, 2016; Haeger et al., 2015; SenGupta et al., 2021).

In directed cell migration, cells migrate toward a chemical or physical cue. Random cell migration refers to the intrinsic ability of cells to migrate. However, in contrast to Brownian particles, randomly migrating cells have a directional persistence, meaning that even if the direction of movement is chosen randomly in an isotropic environment, cells continue to move in the direction they have previously taken (Dang and Gautreau, 2018).

Cell migration is essential, for example, during embryonic development, immune response, and wound healing. When cell migration is misregulated, it can cause severe damage to the organism, leading to chronic inflammation, cancer formation and metastasis, and vascular diseases (Carmona-Fontaine et al., 2008; Case and Waterman, 2015). A cell´s spontaneous polarization and adaptation to a changing environment (chemical, electrical, mechanical, or other physical stimuli) is a fundamental process both at single cell and multicellular level (Rappel and Edelstein-Keshet, 2017).

Cell migration on 2D substrates has been studied extensively because of the simplicity of the visualization of cellular processes. On a 2D substrate, cells adhere and spread, which gives them a flat shape. Through actin polymerization, cells migrate by membrane extension in structures called lamellipodia, followed by adhesion to the substrate at focal adhesion sites (Ladoux and Nicolas, 2012). In 3D substrates, cell migration modes range from bleb-based to protrusion-based. Blebs are the consequence of the intracellular pressures without actin polymerization and enable membrane expulsions. Cells use blebs to squeeze through existing pores in the ECM. This amoeboid migration is quite fast and characterized by weak cell-ECM adhesion and low ECM degradation (Mierke, 2015; Paluch and Raz, 2013). In the protrusion-based migration, actin-rich protrusions are formed by actin polymerization.

Similar to the 2D lamellipodia-driven migration, the actomyosin contraction in 3D cultures causes the cell body to move in the direction of protrusions (Martins and Kolega, 2006). In combination with strong cell-ECM adhesion and ECM degradation, the formation and contraction of protrusions results in a mesenchymal migration mode (invasion) (Caswell and Zech, 2018).

2.2 Cell-ECM adhesion dynamics

Cells can sense the mechanical stimuli through a diverse group of membrane-anchored receptors such as ion channels, cell membrane-spanning G-protein-coupled receptors, integrins and cadherins. The integrin- and cadherin-based adhesion complexes are found at cell-ECM and cell-cell contact sites, respectively (Paluch et al., 2015). There are different types of adhesion complexes. Focal adhesions, invadopodia/podosomes, and adherent junctions are actin cytoskeleton-associated adhesion complexes. Hemidesmosomes and desmosomes are intermediate filament-associated adhesion complexes (Zuidema et al., 2020).

The morphology, size, shape, and subcellular distribution of cell-matrix adhesions depends on multiple factors, including matrix properties and the cellular components involved. Despite the heterogeneity of cell-ECM adhesion structures, many of them share two common features: 1) they are mediated by integrins and 2) they interact with the actin cytoskeleton (Geiger et al., 2001; Wu, 2007). As mentioned previously, fibronectin, vitronectin and various collagens are the extracellular ligands anchoring these adhesions. Generally, the assembly of cell-ECM adhesion is initiated by interaction of cell surface integrins with an ECM protein (such as fibronectin), leading to integrin clustering and the formation of cell-ECM adhesion structures. Furthermore, as the number of cellular components bound to the cytoplasmic tail of integrin increase, the adhesion sites evolve from small size to large structures (Wu, 2007). Based on their size (~0.1 - ~10 µm) and localization, cell-ECM adhesion can be classified into nascent adhesions, focal complexes, focal adhesions and fibrillar adhesions.

2.2.1 Nascent adhesions

Nascent adhesions are small (<0.25 µm in diameter) and found at the leading edge of the cell, the lamellipodium (Figure 1). These adhesions are unstable and disappear after approximately one minute. Nascent adhesions typically consist of several tens of integrins organized into a cluster serving as a platform for recruiting other proteins such as talin and paxillin. This small assembly can initiate the maturation into more stable focal complex and focal adhesion structures (Henning Stumpf et al., 2020; Sun et al., 2014; Tabarin et al., 2014). A recent study using ChoK1 epithelial cells and in 2D environment, suggested that nascent adhesion maturation is initiated by the exposure of a vinculin binding site (VBS) in the R8 of talin by force-independent interaction with vinculin (Han et al., 2021b).

The adhesion types showed in Figure 1 are a broad overview of the classical adhesion complexes in 2D cell culture environment. There are other adhesion types such as reticular adhesions (Lock et al., 2018)and hemidesmosomes (HDs) (Pora et al., 2019). Reticular adhesions are formed during interphase and mediated by integrin αvβ5. They are enriched in phosphatidylinositol-4,5-bisphosphate (PtdIns(4,5)P2)-binding proteins and can form without talin and F-actin (Lock et al., 2018). HDs are multiprotein complexes connecting the ECM to the keratin cytoskeleton of the epithelial cells. For example in the skin, HDs provide stable adhesion of basal keratinocytes to the underlying basement membrane. Once the assembly of HDs are initiated, the α6β4 integrin plays an essential role in mediating cell adhesion (Te Molder et al., 2021).

Moreover, filopodia adhesions have been identified as their own adhesion types with distinct protein composition and localisation either at filopodia tip, along filopodia shaft or at the base of filopodia. Filopodia adhesions can serve as precursors for nascent adhesions (Jacquemet et al., 2015; Jacquemet et al., 2019). Microscopy-based studies have shown that filopodia adhesions are enriched in Myosin10 (Myo10), kindlin, p130Cas and talin (Jacquemet et al., 2019).

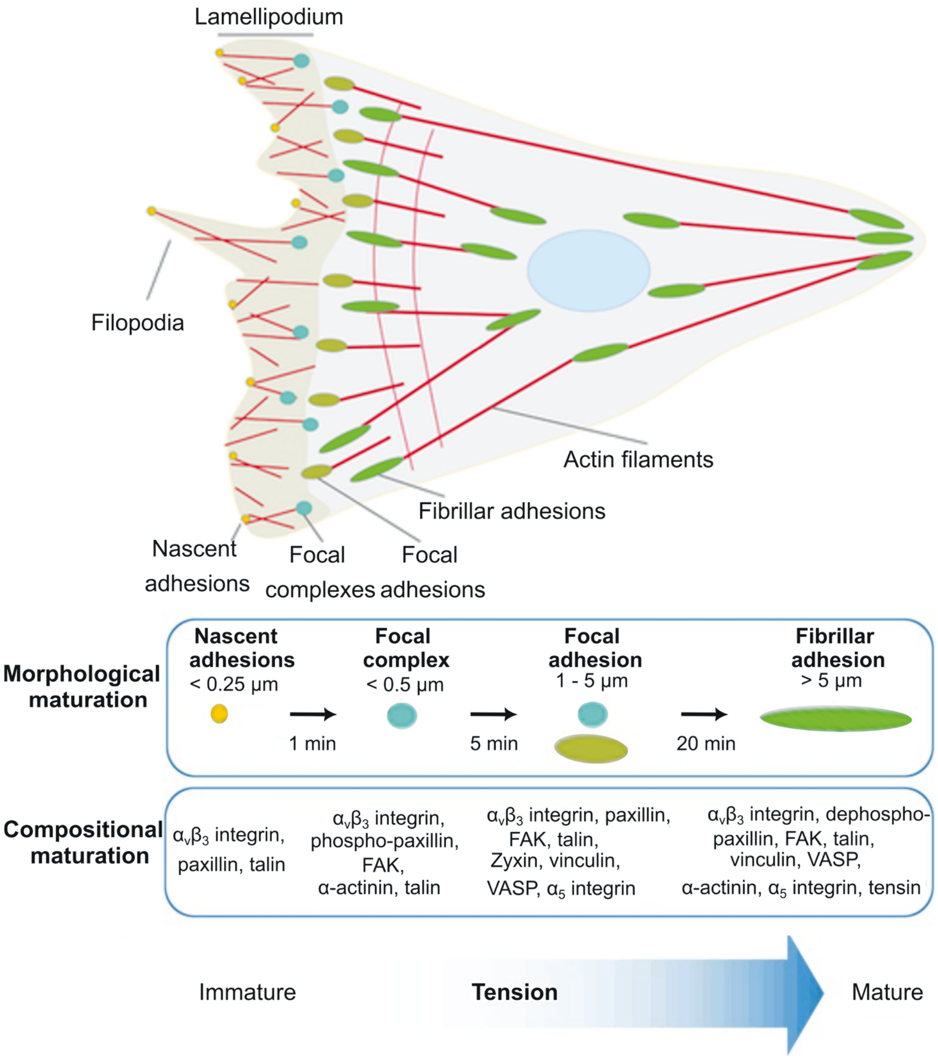

Figure 1. Protein composition and time scale of different stages of cell-ECM adhesions. Integrin-mediated matrix adhesions include nascent adhesions, focal complexes, focal adhesions and fibrillar adhesions. Nascent adhesions are dot-like adhesions formed at the early stages of interactions at the lamellipodia, which are sheet-like extensions at the leading edge of the migration cell. They are rich in tyrosine-phosphorylated paxillin and they are short-lived, but may transform into bigger focal complexes, which are also short-lived, associated with lamellipodial protrusions and can mature to focal adhesions. Focal adhesions form at the end of actin-containing stress fibres and have a longer lifetime. They have a lower level of phosphorylated paxillin in comparison to nascent adhesions, but contain other components such as vinculin. Fibrillar adhesions are under the centre of the cells and are highly stable and more mature than focal adhesions. They contain a high level of tensin and β1-integrins. Figure adapted with changes from (Koçer and Jonkheijm, 2018) and (Tabarin et al., 2014) and reproduced with permission from the publishers.

2.2.2 Focal complexes and focal adhesions

Nascent adhesions can either disassemble or continue the adhesion maturation process. The maturation into a focal complex and then into a focal adhesion (FA) is a mechanosensitive process, which in response to RhoA signalling, is induced by the actomyosin force generated in the lamella. The lamella contains contractile actin stress fibers (Ciobanasu et al., 2012). Actin-binding proteins such as talin and vinculin could act as mechanosensors, but the mechanisms by which proteins respond to actomyosin contractility and induce the assembly/disassembly of FAs is not yet well understood. Lavelin et al. demonstrated that the ROCK inhibitor Y-27632 releases intracellular actomyosin tension on integrin-based adhesion complexes. These mechanisms control tension-dependent adhesion stability in an ILK-dependent manner (Lavelin et al., 2013). Moreover, a recent study has found that the myosin-II filament formation needs to be locally activated by GEF-H1 in order for microtubule-driven focal adhesion disassembly to occur. The burst of actomyosin contractility triggers the disorganization of the focal adhesions (Aureille et al., 2023).

In the maturation process of a nascent adhesion, more adhesome proteins are recruited by membrane lipids or scaffold proteins modulated by phosphorylation or applied tension (Tabarin et al., 2014; Wehrle-Haller, 2012). Zaidal-Bar et al. systematically compared the composition of nascent adhesions and FAs by combined phase-contrast and fluorescence microscopy approaches for monitoring the incorporation of nine different focal adhesion proteins into focal complexes in endothelial cells. They showed that after talin is recruited in nascent adhesions, the maturation into FAs is accompanied by the accumulation of several proteins including vinculin, vasodilator-stimulated phosphoprotein (VASP), zyxin and α-actinin (Zaidel-Bar et al., 2003; Han et al., 2021b).

It is not entirely clear which components distinguish the focal complexes from focal adhesions, but it is known that integrin α5β1 as fibronectin receptor functions as a control hub for the intracellular focal adhesion machinery (Hynes, 2002; Zaidel-Bar et al., 2007). Super-resolution structured illumination microscopy (SR-SIM) image of NIH3T3 cell showed that αVβ3 integrin is able to bind fibronectin only in an extended-open conformation with higher mechanical load (Bachmann et al., 2020). Both α5β1 and tensin are enriched in fibrillar adhesions. The focal complexes at the periphery of migrating cells are regulated by Rac and Cdc42. The larger focal adhesions found both at the cell periphery and in the central part associated to stress fibres are regulated by Rho activity when cultured on rigid 2D surfaces (Wozniak et al., 2004).

One of the best-characterized cell-ECM adhesion types is the focal adhesion, which is found in adherent cells, e.g. in fibroblasts cultured on a rigid substrate (Wu, 2007). Focal adhesion mechanosensing includes recognizing and transferring the mechanical cues coming from the extracellular environment to the cellular cytoskeleton. In the focal adhesion, a complex structure including scaffolding, docking, and signalling proteins connects the ECM through integrin directly to the actin cytoskeleton (Martino et al., 2018; Wu, 2007). Signalling proteins at focal adhesions, e.g. Src, FAK and integrin-linked kinase (ILK), are crucial for transferring the mechanical information inside the cells. For example, integrin-mediated activation of Src and FAK can regulate Rho GTPases, which further regulate the organization of actin cytoskeleton (Seong et al., 2013).

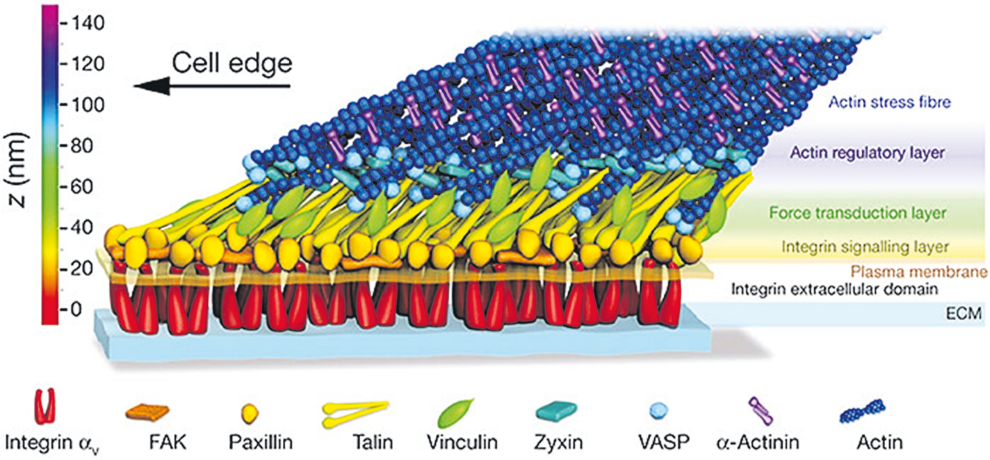

Figure 2. Schematic representation of focal adhesion molecular architecture. Integrins (red) are the transmembrane receptors attaching to the extracellular matrix (ECM) (blue). Talin (yellow) and other proteins linking integrin to the actin cytoskeleton. Figure from (Kanchanawong et al., 2010), reproduced with permission from the publisher.

Kanchanawong et al. demonstrated that focal adhesions contain a well-organized molecular architecture of the focal adhesion core region (height ~40 nm) containing partially overlapping protein strata, which separate integrin and actin (Figure 2) (Kanchanawong et al., 2010). They demonstrated that focal adhesion proteins are organized into three spatial and functional sections mediating interdependent functions: 1) the integrin signalling layer containing FAK and paxillin 2) a force transduction layer containing talin and vinculin, where talin is orientated diagonally, linking integrin to actin directly, and 3) the uppermost region of the actin regulatory layer containing vertically oriented VASP, zyxin and actin filaments (Figure 2).

2.2.2.1 Key components in the integrin-mediated cell-ECM focal adhesion

The integrin-mediated cell-ECM adhesion applies profound effects on the cell, including changes in cell shape, proliferation, differentiation, and survival by promoting integrin clustering and recruitment of other integrin-associated proteins to the integrin-rich adhesion sites (Wu, 2007). Focal adhesion kinase (FAK) is one of the first molecules recruited to the focal adhesion in response to external mechanical stimuli (Lachowski et al., 2018). One of the key signalling events is the phosphorylation of tyrosine, creating a docking site for the binding of SH2-containing proteins and regulating other kinases and phosphatases. The major kinases at focal adhesions are FAK and Src (Zamir and Geiger, 2001). When FAK is in an inactive conformation, the catalytic kinase domain is autoinhibited by the FERM domain, and the residue Y397 remains non-phosphorylated. When activated, the linker region is exposed and Y397 autophosphorylated. This provides a high affinity binding site for proteins such as Src. In addition, several other proteins such as paxillin, Crk and p130Cas act as signalling scaffolds for the components at the focal adhesion, creating a complex by combining kinases and substrates, leading to changes in the cell behaviour (Heim et al., 2017; Iwahara et al., 2004).

Paxillin is a 68 kDa protein with an N-terminal domain of 313 amino acids, containing several tyrosine and serine phosphorylation sites important in integrin-mediated signalling pathways. The C-terminal domain contains a focal adhesion targeting motif and four double zinc finger LIM domains, which act as binding site for tubulin and several uncharacterized serine/threonine kinases (Turner, 2000). Tyrosine phosphorylation of paxillin through the FAK/Src complex is important for its function as docking molecule in focal adhesion formation (Nakamura et al., 2000). Tyrosine phosphorylation at Tyr31 and Tyr118 is the key for binding of paxillin to other molecules, e.g. Crk (Petit et al., 2000). The interaction of paxillin and Crk is necessary for the localization of paxillin to focal adhesions and eventually influences the cell migration rate (Lamorte et al., 2003) with both increasing and decreasing effects (Yano et al., 2000).

An earlier study demonstrated that the collagen-induced phosphorylation of tyrosine 31 and 118 of paxillin is necessary for this paxillin-CrkII interaction. Inhibiting this interaction by a point mutation in either of the proteins resulted in reduced Nara Bladder Tumour II (NBT-II) cell locomotion on collagen. This effect can be rescued by overexpression of wild type paxillin (Petit et al., 2000). Paxillin as a signalling adaptor protein binds directly to the α4 cytoplasmic domain of integrin (Liu et al., 1999) regulated by α4 phosphorylation at Ser988 (Han et al., 2001). Paxillin binding to α4 was disrupted by an α4 (S998A) mutant, decreasing cell spreading in Jurkat T cells (Han et al., 2003).

Vinculin is a cytoplasmic actin-binding protein consisting of a 90 kDa N-terminal head, a short flexible proline-rich linker and a 27 kDa C-terminal rod-shaped tail. Vinculin is enriched in focal adhesions and adherent junctions and is essential for embryonic development, suggesting a critical functional role of vinculin in regulating integrin clustering, force generation and strength of adhesion (Isenberg et al., 1982).

Moreover, vinculin null cells are shown to be resistant to different apoptotic stimuli, showing that vinculin plays an important role in apoptosis signalling pathways (Subauste et al., 2004). Cells lacking vinculin are shown to be highly metastatic and motile. They also have increased survival due to upregulated activity of extracellular signal-regulated kinase (ERK), resulting from vinculin-mediated modulation of paxillin-FAK interaction. In vinculin null cells, expression of a vinculin fragment containing a paxillin binding site (amino acids 811-1066) suppressed ERK activity and restored apoptosis. Therefore, vinculin appears to control the accessibility of paxillin for FAK interaction and regulates cell survival and motility *via* ERK (Subauste et al., 2004).

Talin plays a prominent role in the focal adhesion formation and acts as a regulator of the inside-out integrin activation, that required for the initial link between integrin clusters and cytoskeleton (Calderwood et al., 1999; Tadokoro et al., 2003). Talin association with phosphatidylinositol phosphate kinase type Iγ (PIPKIγ) is known to regulate focal adhesion by synthesizing phosphatidylinositol-bisphosphate, PtdInsP2, for increasing integrin clustering (Di Paolo et al., 2002).

Kindlins are able to enhance talin-mediated integrin activation (Plow et al., 2009; Calderwood et al., 2013). Studies indicate that kindlins may bound to integrin prior to its activation, but the cooperation mechanism of integrin-bound kindlins with talin for integrin activation is not properly understood (Theodosiou et al., 2016; Bachir et al., 2014). A recent study investigated the contribution of talin, kindlin and actomyosin in integrin clustering using biomimetic *in vitro* system, made of giant unilamellar vesicles containing integrins (αIIbβ3) with purified talin1, kindlin2 and actomyosin. They demonstrated that talin and kindlin synergize to induce the formation of larger integrin clusters containing the three proteins. They also demonstrated that kindlin increases integrin-talin-actomyosin coupling (Pernier et al., 2023).

Kindlins are ~77kDa proteins adopting a FERM-like domain consisting of F1, F2 and F3 subdomains with a pleckstrin homology (PH) domain inserted into F2 domain. Similar to talin head, kindlin´s F3 subdomain binds to integrin β cytoplasmic tail (Harburger et al., 2009; Zhu et al., 2021). There are three kindlins known as kindlin1, kindlin2 and kindlin3, each encoded by separate genes. While kindlin2 is ubiquitously expressed, kindlin1 and kindlin3 are primarily expressed in epithelial and hematopoietic cells, respectively (Meves et al., 2009; Malinin et al., 2010). In addition, there are findings of kindlin3 expression in endothelial cells (Bialkowska et al., 2010) and some tumour cells (Sossey-Alaoui et al., 2014).

Each domain of kindlin mediate different binding events to regulate focal adhesion assembly. Kindlins are interacting with several signalling proteins and have an important role in transducing signals. For example, kindlin2 interact with integrin-linked kinase (ILK) (Fukuda et al., 2014), which then forms a complex with particularly interesting new cysteine and histidine-rich protein (PINCH) and parvin, forming the ILK-PINCH-parvin (IPP) complex. Moreover, IPP complex has an important role in connecting integrin to the actin cytoskeleton (Wickström et al., 2010a). There are also other kindlin interacting proteins such as actin-related proteins 2/3 (Arp2/3) and paxillin (Böttcher et al., 2017; Zhu et al., 2019). The binding affinities of the interactions are different indicating the dynamic nature of interactions during cell adhesion (Zhu et al., 2021).

2.2.2.2 Disassembly and turnover of adhesion in migrating cells

The FA assembly must be synchronized with FA disassembly to facilitate cell migration. Adhesion disassembly has been detected both at the leading age in the formation of new protrusions, and also at the cell rear in tail retraction. As new adhesions form at the leading edge, the adhesions at the base of a protrusion disassemble. These mechanisms are referred to turnover and the latter as disassembly. In addition, some of the adhesions are matured to larger and more stable structures (Webb et al., 2002; Webb et al., 2002).

In addition to microtubules, which are known to be involved in adhesion disassembly (Small and Kaverina, 2003), protein kinases and phosphatases have important role in the regulation of adhesion stability and turnover. Studies shown that cells lacking FAK or Src, migrate poorly and have larger adhesions (Webb et al., 2002; Alahari et al., 2002). Adhesion turnover seems to be regulated by interaction of FAK with Src, Crk and the adaptor protein Cas. In migrating cells it is also regulated by a complex Rac-associated proteins (Turner et al., 2001) and by mitogen-activated protein kinase ERK (Brahmbhatt and Klemke, 2003; Ridley et al., 2003). Besides to FAK, Src and other regulators of adhesion turnover, intracellular calcium level are involved in the disassembly of adhesions. Calcium channels can be opened for example from the tension generated by strong adhesion at the rear of the migratory cells (Lee et al., 1999). The possible targets for calcium are the calcium-regulated phosphatase calcineurin and the calcium-activated protease calpain, which is also activated by ERK. Calpain cleaves several adhesion proteins such as integrins, talin, vinculin and FAK (Glading et al., 2002; Ridley et al., 2003).

Studies indicated that the recruitment order of different adhesion proteins can affect adhesion fate for turnover and maturation. For example Laukaitis et al showed that at the cell rear, α-actinin and paxillin leave adhesions more or less at the same time although these molecules are recruited to the adhesion sites continuously (Laukaitis et al., 2001). In Rottner et al study, both paxillin and zyxin were found in the newly formed adhesions, although zyxin was shown to leave earlier than paxillin during adhesion disassembly at the rear (Rottner et al., 2001).

The rearmost adhesions in the fibroblasts, tether the cell firmly to the substratum developing a long tail to the site of anchorage. The tension exerted on the rear adhesions can be strong enough for breaking the linkage between integrin and actin cytoskeleton and contribute to detaching of the cells. This may result in substrate-bound integrins to be left behind as cell moves on. The same behaviour has been observed *in vivo* as well (Lauffenburger and Horwitz, 1996). During actin-based cell migration, myosin-II-motor-domain interacts with actin filament to retract cell rear. This retraction may also contribute to cell polarity, since as adhesions are released at the rear of the cell, the protrusion activity at cell front is increases (Cramer, 2013; Ridley et al., 2003).

2.2.3 Fibrillar adhesions

Short-lived peripheral nascent adhesions are replaced by actin-tethered focal adhesions, potentially further evolving into elongated, centrally located fibrillar adhesions with a size ranging from 1 µm to 10 µm in diameter (Zamir et al., 1999; Huveneers and Danen, 2009; Tabarin et al., 2014). These fibrillar adhesions are bound specifically to fibronectin *via* α5β1-integrins and mainly composed of thin actin cables crosslinked by proteins such as tensin 1 and tensin 3 (Pankov et al., 2000; Clark et al., 2010; Zamir and Geiger, 2001). Fibrillar adhesions are distinguished from focal adhesions by a high level of tensin and a low level or even absence of phosphotyrosine. They also do not attach to stress fibres or disassemble when the cytoskeletal force is relaxed (Katz et al., 2000). They are more centrally located and consist of extracellular fibronectin fibrils and are always aligned towards the long axis of the focal contacts (Zamir et al., 1999).

Previous research revealed that fibrillar adhesions are important structural components in fibroblasts and required for fibronectin fibrillogenesis, the formation of fibrils leading to the deposition of other matrix components such as collagens (Barber-Pérez et al., 2020). The formation of fibrillar adhesions is coupled to the mechanical parameters of the cell environment, such as stiffness, and might enable cells to adjust their matrix environment in response to changing physical conditions (Pankov et al., 2000; Barber-Pérez et al., 2020). Atherton et al demonstrated that fibrillar adhesion maturation is controlled by the interaction of talin R11 rod domain with the talin binding site in the tensin3. Moreover, vinculin indirectly associated to tensin3 through talin and acts to potentiate the tensin3 dependent fibrillar maturation (Atherton et al., 2022).

2.2.4 Podosomes and invadopodia

Podosomes and invadopodia appear as individual dot-like matrix contacts, which structurally and functionally are different from the adhesion structures mentioned in previous section. The most structurally distinguishing feature is their two-part architecture with a core of F-actin and actin-associated proteins, surrounded by a ring structure containing a plaque of proteins such as vinculin, paxillin and talin. The actin-rich core is not present in other cell-matrix adhesion structures. The ability of podosomes and invadopodia in engaging matrix degradation functionally separates them from other cell-matrix adhesion structures (Buccione et al., 2004; Geiger and Yamada, 2011; Linder and Kopp, 2005).

Podosomes are commonly found in normal cells such as in the monocyte lineage cells, e.g. macrophages and osteoclasts. They have also been found in other cell types such as endothelial cells, smooth muscle cells and in Src-transformed fibroblast (Linder and Kopp, 2005; Osiak et al., 2005). Invadopodia are found in some malignant cell types and fibroblasts transformed with viral oncogenes encoding a protein tyrosine kinase. Podosomes have a diameter of 0.5 – 1 µm, whereas invadopodia have a diameter of ~8 µm (Buccione et al., 2004; Linder and Kopp, 2005).

Different types of integrins are present in the podosomes and invadopodia of different cell types. For example, podosomes in epithelial cells contains α6β4, while in osteoclasts αvβ1, α2β1 and αvβ3 are recruited. Furthermore, α6β1, α3β1 and α5β1 are accumulated in the membrane fraction of lysyl oxidase (LOX) melanoma cells (Mueller et al., 1999). Podosomes have been described in Src-transformed cells containing variety of proteins including actin and c-Src. Src-dependent paxillin phosphorylation has been showed to be necessary for podosomes ring expansion (Gatesman et al., 2004; Badowski et al., 2008).

Substrate rigidity or stiffness has a key factor property on the formation of podosomes in different cell. For example, nontransformed fibroblasts ($\mathrm{RPTP}_{\alpha}^{+/+}$ mouse embryonic and REF52 rat) develop podosomes-like structures on fluid lipid surfaces containing RGD (Arg-Gly-Asp) peptides, although forming focal adhesions on rigid RGD glass surfaces (Yu et al., 2013). Another study showed that microvascular endothelial cells form more and larger podosomes on substrates with higher stiffness properties (20kPa) in comparison to substrate with low stiffness (2kPa) (Juin et al., 2013; Weber et al., 2022). Moreover, the integrin-ligand interaction is not needed for the formation of podosomes. This has been confirmed by a DNA-based tension sensors in THP-1 cells where it has been demonstrated that seeding cells on passivated surfaces, which block binding of integrins to ECM ligands, are dispensable for podosomes formation (Pal et al., 2022).

2.3 Integrins

Cells interact with their ECM microenvironment through several receptors, with integrins being the most important (Streuli, 2016). In humans, there are 18 α and eight β subunits, forming a range of αβ heterodimer transmembrane units. The members of this family also have been found widely in other mammals, chicken, zebrafish as well as in lower eukaryotes such as the fruit fly. The extracellular domain of α and β subunits contributes to the ligand-binding site of the heterodimer (Takada et al., 2007). The sequence arginine-glycine-aspartic acid (RGD) has been identified as a general integrin-binding motif, being an evolutionary conserved motif for integrin-mediated cell adhesion (Ruoslahti, 1996). The RGD motif was initially discovered in fibronectin (interaction with α5β1 or αv integrins), but was later found also in many other proteins, e. g. in vitronectin and laminin, regulating integrin-mediated cell migration, apoptosis, growth and differentiation (Ruoslahti, 1996; Barczyk et al., 2010).

Many integrins transmit mechanical forces bidirectionally between the ECM and the intracellular actomyosin cytoskeleton and therefore contribute to mechanotransduction. In mammals, the affinity of integrins for their ligands is regulated by cytoplasmic signals (inside-out signalling). The inside-out signalling brings αIIbβ3 and α2β1 integrins into the active conformation and is regulated by proteins such as talins, kindlins, filamins, migfilin, FAK, but also ILK (Honda et al., 2009). Upon binding to extracellular ligands, mammalian integrins transduce signals to the interior of the cell, leading to outside-in signalling, which further activates other signalling events. These events are complex and cell-specific, depending on other signalling receptors and signalling systems available in the cell (Barczyk et al., 2010; Giancotti and Ruoslahti, 1999). For example, intracellular adhesion molecules (ICAMs) are immunologically important integrin ligands. Integrin β1 was immunoprecipitated with ICAM5 from mouse brain (Ning et al., 2013) and ICAM1 was discovered as a ligand of the β2 integrin in lymphocytes (Rothlein et al., 1986).

In endothelial cells, leucocyte recruitment is mediated by clustering of high affinity integrins binding to ICAMs. These focal clusters themselves regulate outside-in integrin signals to affect functions such as cell migration (Takada et al., 2007). The central role of integrins as cell-matrix adhesion receptors (Bachmann et al., 2019) for tissue integrity and proper embryogenesis is already very well-known. Nevertheless, gene targeting technologies have made it possible to generate mice lacking specific integrins and provided additional insights into how integrins function in various diseases. For example, β3-integrin-deficient mice represented a model of the human Glanzmann thrombasthenia (GT) disease, which lead to prolonged bleeding and a defect in platelet aggregation (Hodivala-Dilke et al., 1999).

Molecules associated with the structure and signalling activity of integrin-mediated adhesions are called the integrin adhesome. It consists of over 200 scaffolding and signalling proteins, including various actin regulators and adaptor proteins. The mutation or dysregulation of adhesome components is often associated with human disease. For example, Horton et al. (Horton et al., 2016) investigated a set of 60 proteins commonly identified in isolated integrin adhesion complexes and examined their association with human disorders. They intensively studied the role of these consensus adhesome proteins and revealed their potential involvement in a large number of different diseases such as cancer, viral infections and autoimmune diseases. As the interest for personalized medicine is growing, the need for genomic and proteomic tools to identify disease-associated genes increases. In addition, experimental validation such as ex vivo culture-based model, is necessary to identify mutations and dysregulation activity of candidate genes (Winograd-Katz et al., 2014).

2.3.1 Integrin structure and activation

As previously mentioned, in mammals 24 different integrin heterodimers comprising of α and β subunits, which can be arranged into different subgroups based on their subunit composition and ligand-binding properties (Figure 3). Each integrin dimer has its own distinct characteristic binding affinities for different ECM proteins and other ligands such as the intercellular adhesion molecules (ICAMs) (Mezu-Ndubuisi and Maheshwari, 2021). This leads to the selective use of integrins as adhesion receptors in different cell types and tissues. The cytoplasmic tails of α-integrins vary in sequence and length, but they all share a common GFFKR motif, which is partially buried within the cell membrane, interacting with the transmembrane domain of the β subunit. In integrin dimers with α1, α2, α10, α11, αL, αX, αD and αE subunits, the extracellular ligand binding site is located in the αI-domain. Other α subunits do not have this domain, and they bind to their ligands through a homologous βI-domain in the β subunit. Eight of the heterodimers (αVβ1, αVβ3, αVβ5, αVβ6, αVβ8, α5β1, α8β1 and αIIbβ3) bind to the RGD motif with different affinity and ligand specificity (Figure 3) (Bachmann et al., 2019; Barczyk et al., 2010; Hynes, 2002).

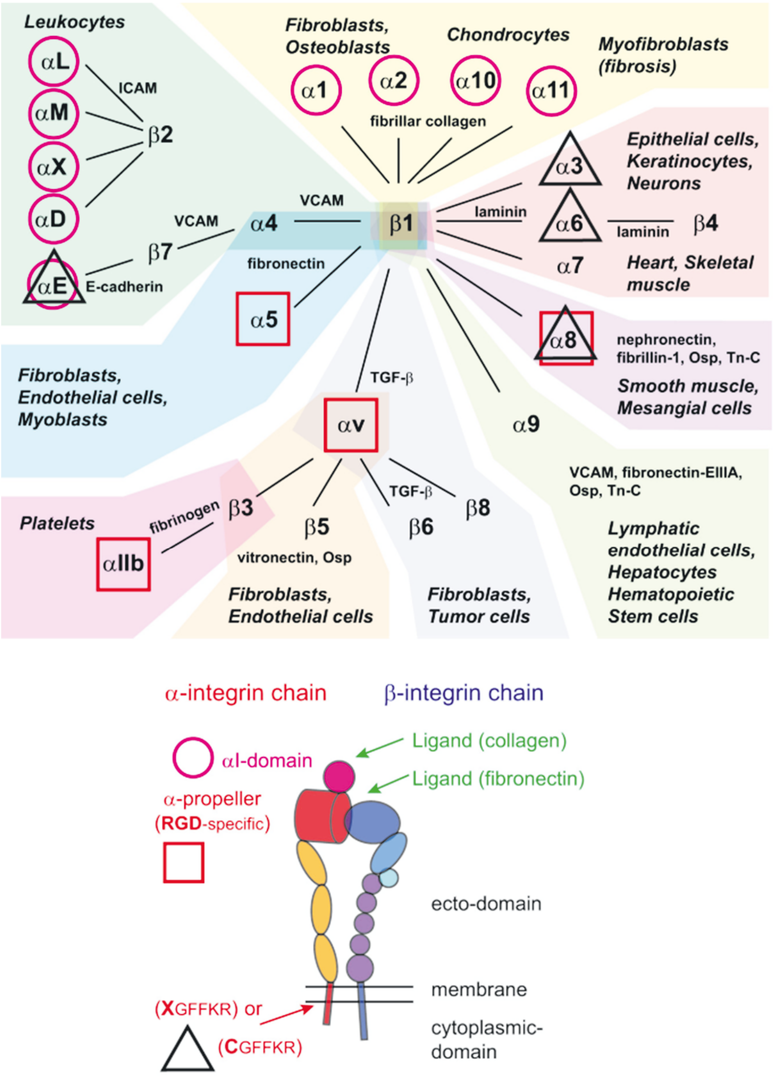

Figure 3. Integrin organization by their α- and β- subunits, their ligands, and cellular distributions. Integrins can be classified by their structural features, ligands as well as their tissue and cellular expression (Bachmann et al., 2019; Hynes, 2002). Integrins can be grouped into nine classes highlighted by different background colours. Highlighted are integrins an α-I domain (I; purple circle), RGD ligands (RGD; red square) and those with conserved GFFKR sequence in the membrane proximal section of a-subunit (black triangles indicating integrins with sequence deviating from CGFFKR). On the right an overview of integrin structure is given, indicating the location of the αI domain and the GFFKR sequence, respectively. The α-I domain integrins bind ligands such as collagen *via* their I domain. Other integrins bind ligands such as fibronectin in binding pockets formed by both α- and β-subunits. Figure from and reproduced from (Bachmann et al., 2019) with permission from the publishers.

In the absence of intra- or extracellular adaptors, integrins are in the inactive "bent" conformation (Figure 4). For example β2 integrin of leukocyte (Nishida et al., 2006) and αVβ3 and αIIbβ3 integrins in 293T cells (Takagi et al., 2002) have been shown to adopt bent conformation in their inactive state. The transmembrane domains are closely associated to support this structure, and the ectodomains of both α and β-integrins are bent towards plasma membrane. An interaction between the outer membrane clasp (glycine residues in the transmembrane helices of the α and β subunits) and the inner membrane clasp (ionic interaction between charged arginine and aspartate residues) stabilizes the inactive bent conformation. Even in this bent conformation, some integrins may be able to interact with ECM ligands with very low affinity, but the interaction of large ECM ligands with the binding sites is restricted (Lu et al., 2016; Bachmann et al., 2019). For instance, antibody Fab fragment mAb13 binds to the low affinity bent conformation of the β 1 integrin (Li et al., 2021).

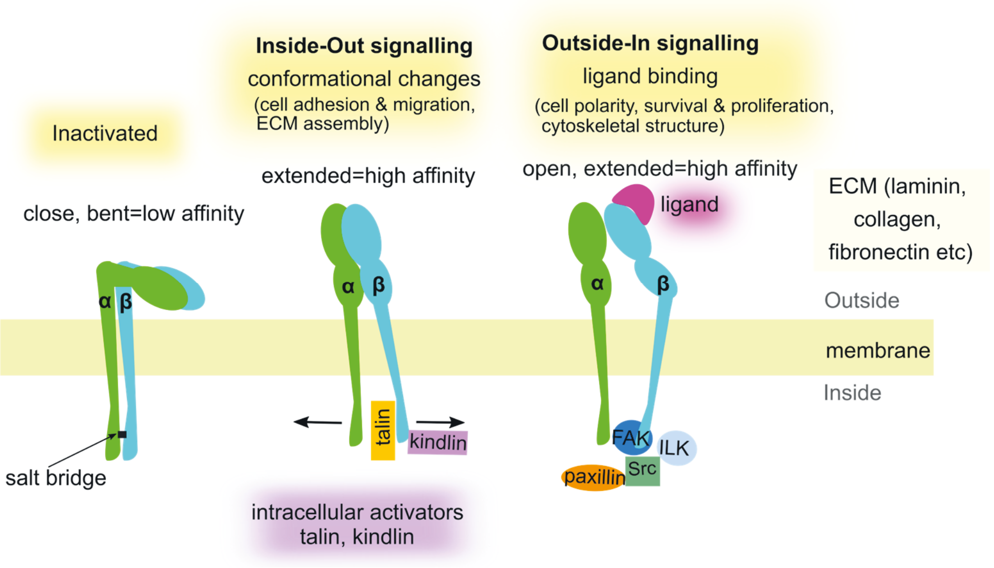

Figure 4. Schematic representation of integrin conformations at the membrane. An inactivated integrin heterodimer exists with a closed and bent conformation, stabilized by a salt bridge between the cytoplasmic domains. The bent conformation has very low ligand binding affinity. Intracellular activators such as kindlin and talin activate the inside-out signalling through binding to the β subunit, destabilizing the salt bridge between integrin subunits. This leads to an open and active conformation with increased ligand binding affinity. Integrin activation leads to intracellular signalling cascades and enables processes such as cell adhesion, cell migration and cell differentiation. The outside-in signalling and binding of ECM ligands such as laminin and fibronectin extracellularly results in a conformational change

to an open and extended (active) conformation with high ligand binding affinity. This leads to an intracellular signalling cascade contributing to cell polarity, cell differentiation and cytoskeleton structure. Figure adapted with changes from (Cheah and Andrews, 2018) and reproduced with permission from the publisher.

The activation process may be triggered by intracellular (talin, kindlin) or/and extracellular ligands (Figure 4), which lead to the extended form of the integrins. Talin contributes to mechanosensing and kindlin to the signalling process of integrin activation, both interacting with the cytosolic β-integrin tail domain in a cooperative manner (Theodosiou et al., 2016; Mezu-Ndubuisi and Maheshwari, 2021).

An important step in integrin activation is the separation of α and β subunits in the transmembrane and cytoplasmic tails and the physical connection to the actin cytoskeleton. The cytoplasmic tails of β-integrins contain two conserved phosphotyrosine binding (PTB) sequences, the membrane-proximal NPx(Y/F) and membrane-distal Nxx(Y/F) motifs, which are binding sites for talin and kindlin, respectively (Anthis et al., 2009; Li et al., 2017b). Deletion of the cytoplasmic tail or a targeted point mutation can decrease or eliminate integrin affinity for extracellular ligands, which perturbates the intracellular signalling pathways (Calderwood, 2004).

Although the mechanism of inside-out and outside-in signalling are described as separate processes, integrin activation is considered to be a dynamic equilibrium, with both intra- and extracellular factors contributing to the overall activation. In addition, the relative importance of these two mechanisms depends on the specific integrin heterodimer (Olsen and Ffrench-Constant, 2005). As example, the α5β1-integrin expressed in adherent fibroblast cells may be predominantly in its active state, while in resting platelets, αIIbβ3-integrins are mainly in inactive state (Chen et al., 2019). A recent study suggested that mechanical load applied on integrin influences its specificity towards ECM ligands. It was proposed that higher mechanical load on αVβ3 is necessary for fibronectin (Fn) binding, while vitronectin (Vn) is recognized by αVβ3-integrin under lower mechanical load (Bachmann et al., 2020).

2.4 Talin

Talin has been shown to be essential for integrin-based adhesion and signalling in mice (Monkley et al., 2000), *Caenorhabditis elegans* (Cram et al., 2003) and *Drosophila* (Brown et al., 2002) through direct binding to integrin and the actin filament, connecting the extracellular matrix with the intracellular actin cytoskeleton. Nowadays, even more studies address the physiological relevance of talin in different organisms and tissues, describing the consequence of talin mutation or loss and highlighting its importance in a broad variety of cell types and processes. In *Drosophila*, mutants affecting the gene encoding for talin, *rhea*, cause a blister phenotype of the wings (Brown et al., 2002). Talin1 also has been found to be necessary for cardiac Z-desk stabilization, endothelial cell integrity and cardiac function in zebrafish (Wu et al., 2015). The expression levels of both talin1 and talin2 are shown to correlate with tumorgenicity in human hepatocellular carcinoma (HCC) (Fang et al., 2016).

Talin exists in two isoforms; talin1 and talin2, that share 74% similarity of aa sequence, (Monkley et al., 2001) and it is probable that the identical regions in both isoforms conduct similar functions (Gough and Goult, 2018). Both talin1 and talin2 proteins are similar in size (talin1:2541aa; talin2:2540aa), and their major difference lies in the size of their genes, with the *TLN1* gene being ~30kb and the *TLN2* gene >200 kb due to a difference in intron size (Monkley et al., 2001). Talin1 is expressed in all tissues and especially highly expressed in hematopoietic and endothelial cells (Kopp et al., 2010). The expression of talin2 is more variable, but it is highly expressed in brain, cerebral cortex, cardiac muscle, skeletal muscle, and kidney (Debrand et al., 2009; Monkley et al., 2001). Talin2 can compensate the loss of talin1 under some conditions, but talin1 appears to be the dominant isoform (Zhang et al., 2008). Talin1 is critical for embryonic development in mice (Monkley et al., 2000), while talin2 knockout mice are viable and fertile, despite having a mild dystrophic phenotype. However, the survival of talin2 knockout pups to adulthood was challenging for unknown reason (Debrand et al., 2012). Although both talin isoforms have identical structures, my research focusses on talin1, and therefore in the following text talin refers to talin1 unless specified otherwise.

2.4.1 Talin structure: head FERM domain

Talin is a 270 kDa membrane-associated protein composed of 2541 amino acids, consisting of a 47 kDa N-terminal head and an elongated 220 kDa C-terminal tail domain (Burridge and Connell, 1983) (Figure 5). The head domain (residues 1-405) consists of an atypical FERM (**4**.1 protein, **e**zrin, **r**adixin, **m**oesin) domain containing four subdomains of F0, F1, F2 and F3, rather than the three subdomains found in most FERM proteins. Moreover, an unstructured loop inserted into the F1 subdomain is found in talin1 (Calderwood et al., 2002; Elliott et al., 2010). The first crystal structure of the talin1 head domain revealed an elongated structure rather than the cloverleaf structure reported for most FERM proteins (Elliott et al., 2010).

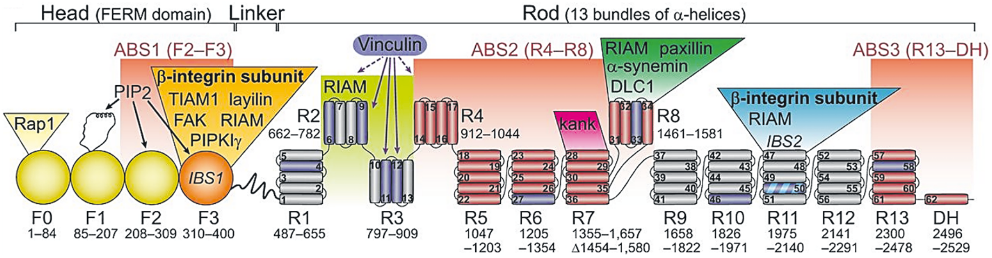

Figure 5. Domain structure of talin. The FERM domain of the talin head contains four subdomains F0, F1, F2 and F3, followed by a linker of 80 amino acids connecting to the rod (tail) of talin. The rod domain is a composite of 61 α-helices that are folded into 13 bundles called R1 to R13, each with four or five a-helices. The rod ends with a C-terminal dimerization helix (DH) (α-helix 62, also called dimerization domain DD). Vinculin binding sites (VBS) are shown with purple (dashed line arrows indicating binding to all other VBSs in the talin rod). The integrin binding site 1 (IBS1) is shown in orange. The a-helix 50 is shown in blue with purple stripes, indicating the integrin binding site 2 (IBS2) and VBS. Actin binding sites (ABS1, ABS2 and ABS3) are in red. Figure from (Klapholz and Brown, 2017) and reproduced with permission from the publisher.

The talin head F0 subdomain (residues 1-84) was revealed to be a ubiquitin-like fold; it is homologous to the head F1 subdomain. F0 is essential for β1-integrin activation and enhances the activation of the β3 integrin (Bouaouina et al., 2008; Goult et al., 2010). Talin´s F1 subdomain has a structure highly similar to the F0 subdomain, containing ubiquitin-like secondary structural elements with an additional unstructured loop. Upon talin activation and in contact with negatively charged membrane phospholipids, the F1 loop folds into a helix with positively charged amino acids, anchoring the talin F0F1 subdomain to the membrane. In addition, the F1 loop can interact with PIP2, which is essential for integrin activation (Goult et al., 2010).

The F2 and F3 subdomains contain positively charged amino acids, that bind to the negatively charged membrane lipids (Goult et al., 2010; Saltel et al., 2009). The F2 subdomain contains a positively charged surface called "membrane orientation patch" (MOP) (residues K256, K272, K274, and R277), which is important for membrane binding and integrin activation. Mutations in this region have been shown to disturb integrin activation (Anthis et al., 2009).

The actin binding site 1 (ABS1) located within the F2/F3 domain of the talin head (Lee et al., 2004) regulates actin polymerization through capping actin filaments (Ciobanasu et al., 2018). TheF3 subdomain of talin has structural similarity to a phosphotyrosine-binding (PTB) domain, and it binds the membrane-proximal NPxY motif of the β integrin cytoplasmic tail and stabilizes the active integrin conformation (Calderwood et al., 2002). Talin´s F3 has been shown to increase integrin activation, but for this binding to be effective, other talin subdomains are needed (Anthis et al., 2009). Nevertheless, previous studies have shown that both F2 and F3 are required for β3 integrin activation and clustering (Anthis et al., 2009; Saltel et al., 2009). The F3 domain can bind other ligands, including the Rap1-GTP interacting adapter molecule (RIAM) (Yang et al., 2014), FAK (Lawson et al., 2012), phosphatidylinositol 4-phosphate 5-kinase type-1 gamma (PIPKIγ) (Pereda et al., 2005), T-cell lymphoma invasion and metastasis inducing factor 1 (TIAM1) and Ras-related C3 botulinum toxin substrate 1-guanine nucleotide exchange factor (Rac1-GEF) (Wang et al., 2012).

2.4.2 Talin rod: structure and binding sites

The talin head and the C-terminal rod domain (tail) are separated by an unstructured region (~80 aa, 10kDa) (Rees et al., 1990). The talin rod comprises of amino acid residues 483-2541 and has fourteen subdomains, termed R1 to R13, and a dimerization domain (DD). The talin rod subdomains R1, R5 to R7 and R9 to R12 have a unique 5-helix topology suited for shearing force response, whereas the R2 to R4 subdomains are a cluster of 4-helix bundles and have an unzipping force response, meaning they resist rupture force less. In response to force, talin goes through a controlled unfolding behaviour of its rod subdomains, modulating interactions with its binding partners (Yan et al., 2015; Haining et al., 2016b; Hytönen and Vogel, 2008).

The rod contains up to eleven vinculin binding sites (VBS) (Gingras et al., 2005), two actin binding sites (ABS2: R4 to R8 and ABS3: R13-DD) and one integrin binding site (IBS2: R11) (Calderwood et al., 2013; Gingras et al., 2009; Hemmings et al., 1996) (Figure 5). Single molecule stretching experiments showed that the 4-helix bundles unfold at ~5-10 pN forces (Yan et al., 2015), while for the 5-helix domains a significantly larger force is required, suggesting the 4-helix domains are the first to unfold and expose their VBS sites (Rahikainen et al., 2017; Yan et al., 2015; Haining et al., 2016b). The unfolding of talin rod subdomains may result in the appearance of 3-helix intermediate state, which was proposed to be the most mechanically stable state for talin 4-helix subdomains (Mykuliak et al., 2018).

The talin rod subdomains are acting as binding sites for many other proteins, e.g. RIAM, which has binding sites with high affinity in the R2R3 bundles. RIAM is a RAP1 GTPase effector involved in the talin recruitment to the plasma membrane (Lee et al., 2009). In response to force-induced conformational changes, talin changes its binding partners. At low forces, RIAM is bound to talin R2-R3, reinforcing talin recruitment to the membrane, integrin activation and the assembly of nascent adhesions. At higher forces (~5 pN) (Yan et al., 2015), RIAM binding is disrupted by the unfolding of the R3 subdomain, resulting in a talin:vinculin complex, which directs the maturation of nascent adhesions into focal adhesions (Goult et al., 2013b; Rahikainen et al., 2017).

Not all 4-helix bundles will unfold at the same low force; some need a higher force for unfolding. The R2 subdomain has a hydrophobic interaction with the 5-helix R1 subdomain, which stabilizes it. The 4-helix R8 is inserted into a loop of the 5-helix R7 domain, creating a force-bearing 9-helix module (Yan et al., 2015).

This unique R7-R8 doublet domain is a hot spot for talin interactions. The R7 domain has an interaction site for the kidney ankyrin repeat-containing protein (KANK), which inhibits actin binding to ABS2, regulating talin activity and force transduction (Sun et al., 2016a). The R8 domain binds to tumour suppressor deleted in liver cancer 1 (DLC1), which interacts *via* an LD domain with talin and FAK (Li et al., 2011, 1). In addition, R8 competes with the vinculin rod for binding of α-synemin (a muscle intermediate filament protein) (Sun et al., 2008).

A recent study by Dahal et al (Dahal et al., 2022) showed that the R8 domain of talin can display a memory-dependent behaviour through repeated force cycles. By measuring the mechanical unfolding-refolding cycles of talin R8, the authors found out that the R8 domain binds to its ligand, DLC1, with much higher affinity.

The R11 domain contains an integrin binding site (IBS2) (Gingras et al., 2009), whose involvement in nascent adhesion formation has been suggested, based on mouse embryonic fibroblasts (MEFs) expressing only the talin rod alone being able to form nascent adhesion (Changede et al., 2015). Table 1 shows some of talin1´s binding partners and their functions, which we have investigated in our studies. This list, however, is far from complete, and many of the proposed or confirmed interactions are yet to be understood in detail.

Table 1. Binding partners of talin1 and their functions upon talin binding. PIP2: Phosphatidylinositol 4,5-bisphosphate. PDB: protein data bank.

Binding partner	Function	Binding site in talin1 /PDB	Reference
Rap1	Recruits talin to the cell membrane to regulate integrin activation	F0, F1 /6BA6	(Bromberger et al., 2019; Zhu et al., 2017)
PIP2	Induces conformation changes in talin, revealing integrin binding site	F2, F3 /6MSF	(Elliott et al., 2010; Chinthalapudi et al., 2018)
DLC1	Regulates RhoA signalling	R8 /5FZT	(Zacharchenko et al., 2016)
RIAM	Regulates RAP1 signalling, involved in integrin activation	F3, R2, R3 /2MWN	(Goult et al., 2013b; Yang et al., 2014)
Vinculin	Links the talin-integrin complex to the actin cytoskeleton; maturation of the integrin-talin complex to a more stable adhesion; participates in actin polymerization	Eleven binding sites within rod (Figure5)	(Gingras et al., 2005; Papagrigoriou et al., 2004; Chen et al., 2006)
Actin	Outside-in signalling through talin leads to the rearrangement of the actin cytoskeleton, maintaining the	F2, F3; R4, R5, R6, R7, R13-DD	(Parise, 1999; Haling et al., 2011)

	shape, structure and movement of the cell		
Integrin	Binds to the talin head domain to mediate the interactions between cytoskeleton and extracellular matrix	F1, F2, F3; R11	(Haling et al., 2011)
FAK	Regulates the dynamic of integrin adhesion by providing signalling and scaffolding functions	F2, F3	(Mitra et al., 2005; McLean et al., 2005; Chen et al., 1995)

The talin C-terminus contains a single α-helix (residues 2494-2541) (called dimerization domain [DD]; Figure 5) that mediates talin dimerization. (Gingras et al., 2008; Goldmann et al., 1994). Gingras et al (2008) reported the NMR structure of talin residues 2300-2482 (R13DD) resembling the HIP1R THATCH core domain. The common feature of THATCH domains is a helix at the C-terminus, that enhances actin binding by formation of a homodimer (Gingras et al., 2008). In talin, this site is the ABS3, and its engagement with actin mediates the initial adhesion complex assembly. Simultaneously, as the force is mediated through the rod, other cryptic binding sites such as vinculin binding sites in R3 (Yao et al., 2016) and R4-R8 (ABS2 site) will become unmasked, and RIAM is displaced. This process leads to the adhesion maturation and cell polarization, in which ABS2 plays a critical role (Atherton et al., 2015).

2.4.3 Regulation of talin function and mechanosensing properties

2.4.3.1 Talin conformation and autoinhibition

Energy-filtered electron microscopy revealed the talin protein to be a highly flexible protein with globular conformation, which adopts an elongated shape of 56 +/- 7 nm in length (Winkler et al., 1997). Talin conformation and localization are tightly regulated by mechanisms induced by signalling pathways, mechanical force, different interactors such as competitor proteins, and by limited proteolysis of talin by calpain2 (Calderwood et al., 2013; Yan et al., 2001). Structural studies using EM reconstruction of full-length talin and the known shapes of the individual domains and inter-domain angles as obtained from small angle X-ray scattering, suggested that the talin dimer adopts a compact conformation in which two talin rods form a donut-shaped structure, while the heads are packed in the centre of the donut (Goult et al., 2013b) (Figure 6). Talin's autoinhibited state is achieved by interaction between the talin F3 subdomain and the rod R9 domain masking the integrin-binding site of the F3 subdomain. PIP2, a negatively charged membrane lipid, tethers and activates talin *via* association with positively charged residues of the F2-F3 subdomains, while repelling the talin rod by an electrostatic "pull-push" process (Goult et al., 2013b; Song et al., 2012). A loose connection is suggested to exist between the head F2 subdomain and the rod R12, which is interrupted by PIP2 binding to its partners such as vinculin (Dedden et al., 2019). The auto-inhibited talin concept is compatible with the study by Banno et al. (Banno et al., 2012) where they observed that talin is abundant in the cytosol and associates with integrin in the plasma membrane in response to activation of Rap1A GTPase, the key regulator of integrin activation (Lee et al., 2009). Some other proteins such as calpain (Yan et al., 2001), RIAM (Han et al., 2006), and G protein Gα13 (Schiemer et al., 2016) are also known to relieve the talin autoinhibition.

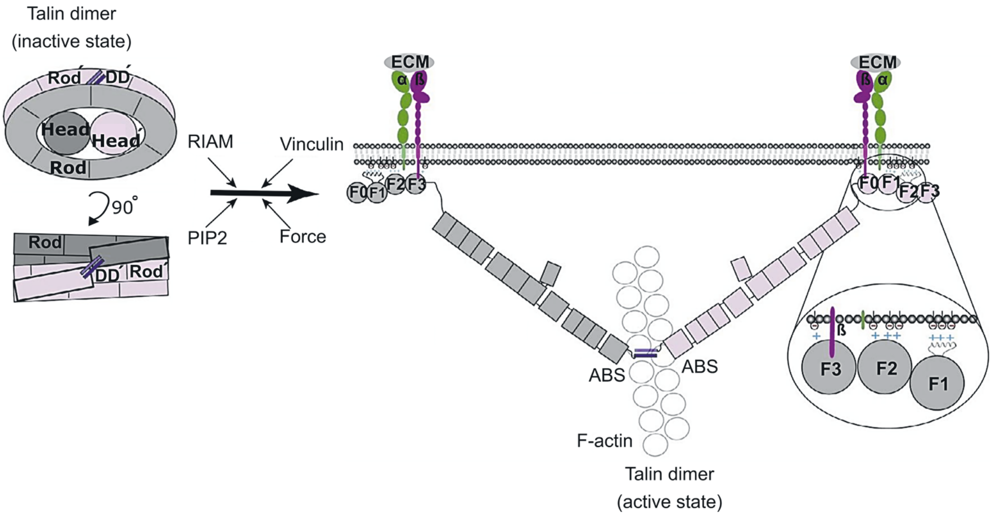

Figure 6. Schematic representation of active and inactive talin. The compact and inactive form of talin is a dimer. The talin rod forms a donut-shaped structure with the talin head filling the hole in the centre (left). Talin subunits are coloured as pink and grey, while blue colour is used for the dimerization helix. Upon activation, the talin dimer form an extended structure where the talin head F3 domain binds to the cytoplasmic domain of β-integrin subunits (purple), while residues on F1, F2 and F3 domains engage acidic membrane phospholipids. The C-terminal actin-binding site binds as a dimer to a single actin filament. Forces exerted on talin facilitate vinculin binding to the talin rod, stabilizing the

integrin/talin/actin complex. Figure from (Goult et al., 2013b) and reproduced with permission from the publisher.

Talin's autoinhibited conformation can be blocked by introducing a point mutation E1777A into R9, which leads to morphogenetic defects during fly development (Ellis et al., 2013). Disrupted autoinhibition has also been studied in mice carrying the E1770A mutation in talin1, causing delayed wound healing (Haage et al., 2018). These studies also demonstrated that more mature, stable focal adhesions with increased integrin activation were obtained in cells expressing talin with a defect in autoinhibition (Haage et al., 2018; Ellis et al., 2013).

Once talin is activated and force exerted on talin by actin, binding sites for vinculin are exposed as a result of mechanical unfolding of talin (Yao et al., 2016; Rio et al., 2009; Hytönen and Vogel, 2008) (Figure 6). Yao et al. revealed that in response to force, the talin R3 four-helix bundle, containing two VBS, is the first to unfold. As vinculin binds to partially unfolded R3, it prevents it from refolding. As mechanical load is reduced, talin can refold again, e. g. accelerating the dissociation of vinculin (Yao et al., 2016). This model was further supported by a study by Chakraborty et al (Chakraborty et al., 2022) where four threonine residues at the R3 hydrophobic core (at positions 809, 883, 867 and 901) were substituted by isoleucine and valine, resulting in the variant R3-IVVI. The four threonine residues in the hydrophobic core of the talin R3 domain make it mechanically the weakest domain of talin, with equilibrium folding dynamics at ~4-6 pN, while the modified version R3-IVVI unfolds at 9 pN, making it mechanically more stable (Yao et al., 2016; Haining et al., 2016b; Tapia-Rojo et al., 2020; Goult et al., 2013a). Inserting serine point mutations into the R3 domain instead makes the domain more sensitive for mechanotransduction at low forces (Rahikainen et al., 2017).

A study by Legate et al. showed that the removal of PIP2-producing PIP5KIγ had only partial and temporary impairing effect on talin-mediated adhesion sites (Legate et al., 2011), which suggests that additional pathways/factors regulating talin activity exist. One pathway involves the small GTPase Rap1 and its effector RIAM, which has been shown to sterically exclude the intramolecular F3/R9 interaction in the plasma membrane, promoting integrin activation (Lafuente et al., 2004; Lee et al., 2009; Yang et al., 2014).

Thus, the ability of talin to unfold is critical for the mechanosensory properties of talin, and it relies on talin's force-dependent interactions with other binding partners (Yao et al., 2016).

2.4.3.2 Talin-mediated integrin activation by Rap1A-RIAM

The two pathways of talin1 activation in which Rap1 plays a central role are 1) the direct activation of talin1 through direct binding of Rap1 to the talin1 F0 and F1 subdomains and 2) the indirect activation of talin1 through Rap1-mediated RIAM (Bivona et al., 2004). For talin to be recruited to integrin adhesion sites, Rap1 (a small GTPases) is activated by protein kinase C (Hilbi and Kortholt, 2017; Klapproth et al., 2015). Upon Rap1 activation, RIAM is recruited to talin1, which then provides an anchor for talin1. Yang et al. (Yang et al., 2014) showed that RIAM binds to the talin F3, R2, R3, R8 and R11 subdomains. This multisite binding could be involved in talin unfolding from its autoinhibited form (Wen et al., 2022; Han et al., 2006).

In leukocytes, RIAM is essential for inside-out activation of integrins (Klapproth et al., 2015), but not in platelets (Stritt et al., 2015), indicating the presence of alternative activation pathways. Lagarrigue et al. found that the Mig-10/RIAM/LPD protein-integrin-talin (MIT) complex forms the "sticky finger" to control cells migration route. A RIAM mutant defective in talin binding led to severe impairment of cell protrusion (Lagarrigue et al., 2015).

Chang et al. found evidence for FAK regulating RIAM through the phosphorylation of Tyr45 in the inhibitory segment (IN segment) of RIAM (Chang et al., 2019). Upon binding of integrins to the extracellular matrix, FAK plays an essential role in the outside-in signalling at focal adhesion (Giancotti and Ruoslahti, 1999), while RIAM is a known key regulator of inside-out signalling of integrins (Lagarrigue et al., 2016). In adherent cells, the cell edge and lamellipodium are rich in RIAM, which is subsequently reduced in mature adhesions due to competition for talin binding sites with other molecules such as vinculin. As vinculin stabilizes the adhesions and increases their ability to transmit forces, RIAM promotes lamellipodial protrusion (Lee et al., 2013). Moreover, RIAM overexpression has been shown to cause extensive lamellipodia formation and to induce actin polymerization. RIAM knockdown cells, in contrary, show reduced actin polymerization (Lafuente et al., 2004; Lagarrigue et al., 2016). In particular, RIAM is shown to be required for integrin activation in conventional T cells (Tconv cells), but not for regulatory T

(Treg cells), even though RIAM is expressed in Treg cells. *In vivo* studies in mice showed that loss of RIAM can cause a disorder such as inflammatory bowel disease (IBD) (Sun et al., 2021) by suppressing the integrin-mediated activation of Tconv cells (Klapproth et al., 2015).

While Rap1/talin and talin/membrane interactions act harmoniously on talin recruitment and integrin activation, mutations in the RIAM binding site of talin (in R3 and R8 subdomains) did not indicate any cooperative effect on integrin activity and function in fibroblasts (Bromberger et al., 2019). Bromberger et al study indicated that Rap1/talin pathway applies equally to all integrin classes while Rap1/RIAM/talin pathway is specific to β2 integrin. They showed that RIAM play a dominant role in β2 integrin function and the loss of RIAM resulted in strong defect in leukocyte adhesion ((Bromberger et al., 2021).

2.5 Talin in diseases

There are a few studies associating the integrin adaptor protein talin to diseases. A talin1 knockout is embryonic lethal in mice and associated with vascular defects in the embryo, resulting in a rapid-onset angiogenesis defect (Monkley et al., 2011). The high expression of talin2 compared to normal adjacent tissues has been confirmed in human breast cancer tissues (Wen et al., 2019). A high level of talin2 in cerebrospinal fluid of patients with postencephalitic epilepsy (PEE) has been detected, which might be connected to the development of drug-refractory PEE (RPEE) (Xiao et al., 2010). A heterozygous mutation S339L in talin2 was identified in patients with fifth finger camptodactyly, with equal severity between male and female patients. Camptodactyly is a non-traumatic, painless deformity characterized by permanent flexion contracture in one or both little finger joints (also called fifth finger) (Deng et al., 2016). Structural analysis suggested that S339 forms a hydrogen bond with E353 in talin2, contributing to affinity towards β1-integrin, while the S339L mutation completely disrupted its binding to the β-integrin tail (Yuan et al., 2017).

As previously mentioned, talin1 is ubiquitously expressed and required during the early development of mouse embryos, so this isoform may therefore possess higher potential to cause diseases. Table 2 shows diseases that have been linked to talin. The activation capacity of integrin αIIbβ3 was diminished in patients with

Myelodysplastic Syndromes. Förster resonance energy transfer (FRET) analysis identified low co-localization of talin1 to the β3-integrin subunit, where a general defect in integrin-dependent platelet aggregation was confirmed by platelet aggregation assay (Fröbel et al., 2013). Moreover, platelets isolated from conditional talin1-deficient mice were unable to activate integrin β3. As a consequence, the mice developed a severe hemostatic defect, but were completely resistant to arterial thrombosis (Nieswandt et al., 2007).

Furthermore, an *in vivo* study indicated the disruption of talin interaction with β3 to impair the activation of αIIbβ3 and to have potent antithrombotic effects in mice (Stefanini et al., 2014). Mice expressing the talin1 L325R mutant binds to integrin αIIbβ3, but does not activate it. Both talin-deficient and talin1 L325R platelets were deficient in retracting fibrin clots. However, in contrary to talin-deficient platelets, clot retraction in talin1 L325R platelets could be rescued by manganese (Mn^{2+}), indicating integrin activation and forming a functional link to the actin cytoskeleton (Haling et al., 2011).

Based on the list in Table 2, a common feature of all talin-associated disease types might be a mechanically unstable cell membrane related to the disruption in integrin activation. The severity of the cell´s functional defect is associated with the mutation type, the location of the mutation in talin and the associated ligand. Talin is abundant at the cell-ECM linkage and it is a key element in multiple signalling pathways leading to integrin activation. Talin-associated disorders can appear in various types of tissues. Talin1 is the only isoform expressed in hematopoietic and endothelial cells (Kopp et al., 2010), whereas talin2 isoform is highly expressed in cardiac muscles, brain tissue and skeletal muscles (Monkley et al., 2001). Fittingly, the effect of knockdown/knockout of each talin isoform is determined by its existence and abundance in that tissue. Additionally, the patient can be either heterozygous (Elefant et al., 2022; Turley et al., 2019) (Publication IV) or homozygous (Stefanini et al., 2014) for the talin mutant allele.

Table 2. Diseases associated with talin, their characteristics, other involved proteins/cause/subject.

Disease	Disease characteristic	Protein involved and cause /mutation	Subject (patient/tissue)	Reference
Endometriosis	Benign gynaecologic disease in which tissues resembling endometrium are present outside the uterus.	Increase in talin1 expression; low expression of N-cadherin, MMP-2, and integrin β3; high expression of E-cadherin.	Endometrial tissues collected from patients.	(Tang et al., 2021)
Colorectal cancer (CRC)	A heterogeneous disease with uncontrolled growth of cells within the colon or rectum.	Upregulated talin1 expression affects CRC cell invasiveness through the EMT signalling pathway.	Tissues and whole blood samples from 30 patients.	(Ji et al., 2021)
Hepatocellular carcinoma (HCC)	A primary tumour of the liver, which develops in chronic liver disease such as cirrhosis.	Downregulation of talin1 by decreasing activation of the ERK1/2 pathway.	HCC tissues from 36 patients.	(Chen et al., 2017)
Coronary artery disease (CAD)	Caused by plaque build-up in the wall of the arteries preventing /narrowing the supply of oxygen and nutrients to the heart.	High plasma levels of soluble talin1.	Plasma of 349 consecutive patients undergoing elective coronary angiography.	(Aoyama et al., 2020)
Coronary artery disease (CAD)	See previous	Downregulation of talin-1 leads to increased expression of miR-182-5p and miR-9-5p.	Serum samples collected from the blood of patients with CAD.	(Gholipour et al., 2022)
Prostate cancer	Uncontrolled growth of cells in the prostate gland.	Talin1 overexpression enhances prostate cancer cell adhesion & invasion by activating survival signals and conferring resistance to anoikis.	Human cell lines; human prostate specimens.	(Sakamoto et al., 2010)

Nasopharyngeal carcinoma (NPC)	A tumour arising from the epithelial cells that cover the surface of the nasopharynx.	Expression of talin-1 was upregulated on both mRNA and protein level.	NPC cell lines and clinical tissues.	(Xu et al., 2015)
Cardiac Z-disk destabilization	The impaired integrity of the Z-disks in the cardiomyocytes affected cardiac function.	Talin1 mutation fl02k; heart failure, brain haemorrhage, and diminished cardiac and vessel lumens.	Zebrafish	(Wu et al., 2015)
Cardiomyocyte remodelling	Changes in size, mass, geometry and function of the heart.	Continuous requirement of talin1 for cardiomyocyte remodelling during heart growth in Drosophila.	Drosophila cardiomyocyte.	(Bogatan et al., 2015)
Aortic dissection	An injury to the innermost layer of the aorta, causing blood flow between the layers and forcing them apart.	Downregulation of talin1.	Aortic fragments from ten patients.	(Wei et al., 2017)
Breast cancer	Uncontrolled growing of breast cells.	Overexpression of talin2.	32 breast cancer tissue specimens.	(Liang et al., 2018)
Dilated cardiomyopathy (DCM)	Heart muscle disease, where the heart chambers stretch, thin and grow larger.	Deletion of talin1 and 2 leads to β1-integrin reduction and heart failure.	Mice	(Manso et al., 2017)
Epilepsy	Brain disease where cluster of nerve cells signal abnormally, causing seizure.	Cerebrospinal fluid talin2 increase and serum–talin2 decrease in RPEE (drug-refractory PEE (postencephalitic epilepsy)) patients.	Blood and serum sample from 62 patients.	(Xiao et al., 2010)
Myelodysplastic syndrome (MDS)	Type of blood cancer in which immature blood cells in the bone marrow do not mature.	TLN1 overexpressed in the bone marrow plasma	Bone marrow plasma from patients with MDS-RS and MDS-EB ($n = 28$).	(Moura et al., 2022)
Multiple Sclerosis (MS)	A condition in which areas of the brain and spinal cord are damaged.	Overexpression of talin1 in the serum.	40 patients with MS.	(Muto et al., 2017)

Rheumatoid arthritis	A chronic inflammatory disease characterized by irreversible damage of the synovial-lined joints.	Talin1 overexpression.	Human plasma from five patients with rheumatoid arthritis (RA).	Zheng et al., 2009
Triple-negative breast cancer (TNBC)	A subgroup of breast tumour with high malignancy defined by lack of hormonal receptors.	Talin1 overexpression.	TCGA database and Shengjing Hospital cohort (171 patients).	Zhang et al., 2008)

2.5.1 Talin in cancer

Metastasis is a life-threatening multistep process of tumour cells spreading to a secondary site in the body, and it is responsible for the majority of cancer deaths (Sleeman et al., 2012). Cancer metastasis is a complex process involving the dissociation of tumour cells from the primary organ, degradation of the ECM, cell migration, apoptosis evasion, invasion of surrounding tissues, cell adhesion, movement, and colonization to different sites in the body. Upon detachment, most cells lose their ECM-mediated cell signalling, which eventually leads to anoikis (cell death caused by insufficient cell-ECM interaction). However, some cancer cells get the ability to survive without cell adhesion due to the activation of an anoikis resistance mechanism. Tumour cells control the anoikis pathway by the extrinsic death receptor pathway and the ECM/integrin-mediated cell survival pathway to escape detachment-induced apoptosis (Fornaro et al., 2001; Sakamoto and Kyprianou, 2010).

Sakamoto et al. provided evidence that talin1 might be responsible for the invasive and metastatic properties of a prostate cancer cell through the anoikis resistance mechanism (Sakamoto et al., 2010). In addition, they observed that talin1 overexpression enhanced prostate cancer cell migration by regulating cell survival signals *via* phosphorylation of focal adhesion complex proteins such as FAK and Src (Sakamoto et al., 2010). High expression of talin1 has been associated with the downregulation of miR-9 and contributes to the aggressive and metastasis in ovarian serous carcinoma (OSC) (Tang et al., 2013). Furthermore, the functional role of talin1 in regulating the tensional homeostasis in the adaptation of cell stiffness to changes in ECM stiffness in brain tumour glioblastoma multiforme (GBM) (Sen et al., 2012) and in hepatocellular carcinoma (HCC) (Kanamori et al., 2011) has been reported. In oral squamous cell carcinoma, talin1 overexpression has been shown to correlate with reduced overall survival in patients (Lai et al., 2011). Understanding the functional contribution of talin1 to cancer may provide new opportunities for therapeutic targeting of metastatic cancer cells.

2.5.1.1 Function of talin in cell-ECM interactions through integrin and possible mechanisms by which talin modulates cancer progression

Given the large number of talin interaction partners, there are various potential pathways how talin could contribute towards changes in inside-out integrin signalling. Talin as direct integrin activator can control cell adhesion, which is vital for migration and metastasis (Lu et al., 2022). Investigation of talin1 in prostate cancer progression to metastasis indicated that talin1 overexpression enhanced prostate cancer cell adhesion and migration by activating survival signals (*via* phosphorylation of focal adhesion complex proteins such as FAK, Src, and downstream activation of Serine/threonine kinases (AKTs)) and anoikis resistance (Sakamoto et al., 2010).

Invasive cancer cells express more dynamic focal adhesions with decreased adhesion strength and enhanced FA turnover (Bijian et al., 2013). The maturation of nascent adhesions to more stable focal adhesions may protect cancer cells from anoikis. It may assist the cell in migration by providing the anchorage in cellular traction or contrarily, it can restrict migration by keeping the cell in one place (Haining et al., 2016a; Sakamoto and Kyprianou, 2010). In another study analysing talin1 overexpression in prostate cancer cell lines, downregulation of miR-124 (a putative tumour suppressor reported in many carcinomas) was observed, suggesting that through integrins, both talin1 and miR-124 impaired cellular adhesion and motility. Thus, talin1 could be a novel player in the anti-metastatic signalling network of miR-124 (Zhang et al., 2015).

A direct binding interaction between Cyclin-dependent kinase-1 (CDK1; the master cell cycle regulator) and the talin rod R8 drives major morphological changes in adhesion during cell cycle progression and division (Gough et al., 2021). Furthermore, a study by Huang et al. showed that CDK5 (a cyclin-dependent protein kinase that is essential for cell migration in cancer metastasis) promotes tumour cell migration through the phosphorylation of talin Ser425 (Huang et al., 2009; Do and Lee, 2020). Talin head phosphorylation helps the assembly of the adhesion complex as well as the balance between assembly and disassembly of the complex (Huang et al., 2009; Wehrle-Haller, 2012; Zhu et al., 2021).

Without phosphorylation or in the absence of certain binding partners, talin remains in its autoinhibited form and does not bind to integrin. Jin et al. studied the activation of β1-integrin in prostate cancer cells and found that the phosphorylation of talin at residue S425 by p53-activated CdK5 as well as Rap1-activated RIAM and PIPKIγ led to the conformational change and activation of talin (Jin et al., 2015), which is required for the activation of downstream effectors involved in cell survival and migration (such as FAK, AKTs and Cas) (Jin et al., 2015). FAK is localized at focal adhesion, and it accumulates at the cytoplasmic tails of integrins (Kanchanawong et al., 2010). Integrin-FAK signalling activates signalling pathways through phosphorylation and protein-protein interactions. For example, autophosphorylation of FAK on Y397 is critical for binding of Src family kinases and the activation of signal transduction pathways (Toutant et al., 2002). Y925 on FAK is phosphorylated upon FAK-Src complex leading to the activation of the RAS-ERK signalling pathway (Shao et al., 2022; Zhao and Guan, 2009).

The talin-mediated integrin activation plays an important role in integrin-mediated signalling and the initiation of downstream survival pathways. These pathways lead to cell protection from anoikis, further resulting in cancer progression to metastasis *via* the AKT pathway (Desiniotis and Kyprianou, 2011) (Figure 7). The ability of integrin to induce FAK phosphorylation correlates with its ability to bind talin (Chen et al., 2009). Phosphorylation of FAK and paxillin, mediated by AKT/GSK-3β signalling, is shown to be required for neurite outgrowth induced by laminin. In brain, this process is essential in neuronal morphogenesis *in vivo* during cortical development (Chen et al., 2009). Paxillin, as a part of focal adhesion complex, is phosphorylated in response to growth factors such as platelet derived growth factor (PDGF) and epidermal growth factor (EGF). When integrins are activated by talin, increased paxillin phosphorylation is observed. This further leads to the direct interaction of kinases like FAK and integrin-linked kinase (ILK) with paxillin. FAK activates and recruits paxillin to the cell membrane, stimulating ERK and c-Jun NH(2)-terminal kinase (JNKs) in a PI3K/Akt-independent manner (Igishi et al., 1999). Either FAK or paxillin overexpression stimulates cancer cell migration on type IV collagen, which is ERK-dependent (Crowe and Ohannessian, 2004).

Li et al. 2016 found that a talin (T144A+T150A) mutation induced more extracellular signal-regulated kinase (ERK) expression, reducing cell adhesion (Li et al., 2016). Also, phosphatidylinositol 3 kinase (PI3K) and JUN N-terminal kinase (JNK) activation are required for growth factor-induced *in vitro* migration and invasion by human squamous cell carcinoma (SCC) cell lines (Tsang and Crowe, 1999). FAK tyrosine phosphorylation creates a strong binding site for SRC proto-oncogene non-receptor tyrosine kinase (Src), leading to the formation of stable FAK-Src complex.

This complex promotes the phosphorylation of many other substrates including paxillin and Cas family scaffolding protein (CAS), which are important in the reorganization of actin cytoskeleton and migration (Guarino, 2010).

Phosphatidylinositol-4,5-bisphosphate (PIP2) binding to talin leads to the activation of phosphatidylinositol phosphate kinase type Ic-90 (PIPKIc-90) phosphorylation by Src kinase. The activated Src induces a positive feedback by promoting PIP2 synthesis for further talin activation (Calderwood, 2004; Ratnikov et al., 2005).

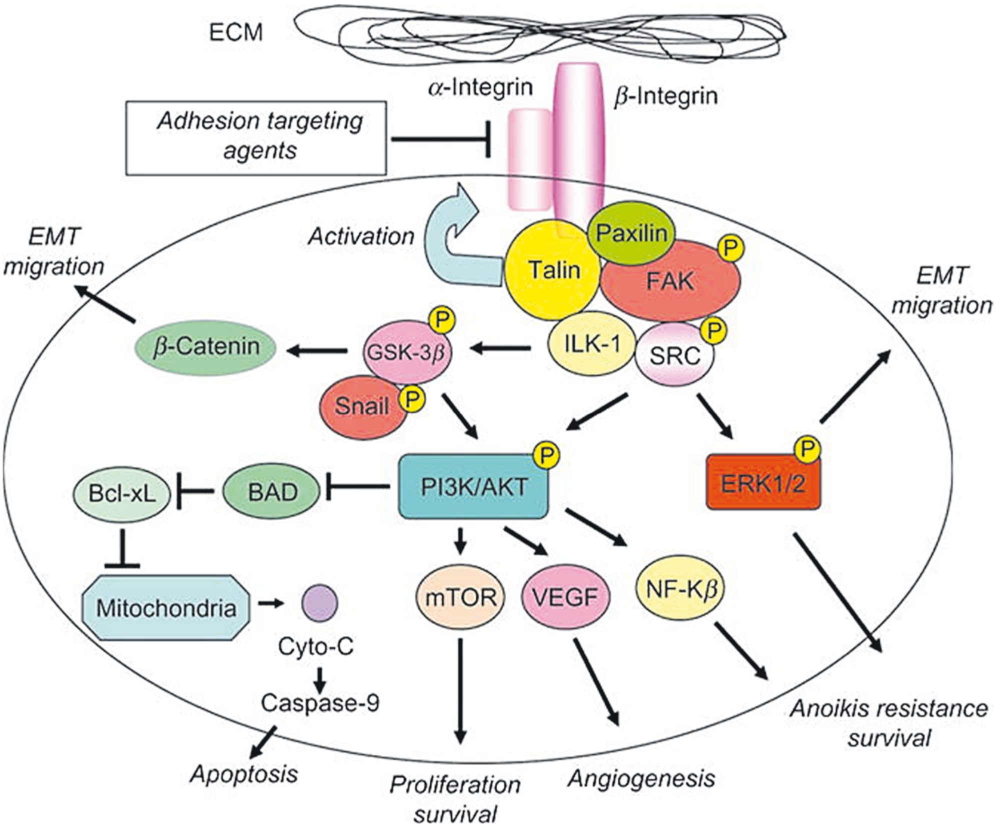

Figure 7. Talin activates integrins by formation and functional activation of a focal-adhesion complex, which induces multiple downstream signalling cascades. The focal adhesion complex components regulate the phosphorylation and activation of the PI3K/AKT survival pathway, resulting in increased angiogenesis, anoikis resistance, and survival. *Via* induction of EMT, ERK1/2 and GSK-3b are activated, promoting the migratory and invasive properties and the survival of tumour cells. ILK is a multifunctional molecule in cell-matrix and cell adhesion. Its catalytic activity has been questioned due to structural and functional issues and the exact molecular mechanism of signal transduction is left undetermined. Through its interaction with integrin, ILK combines functions of a scaffold protein and a

signal transducer to facilitate further protein recruitment within ILK-PINCH-Parvin (IPP) complex (Górska and Mazur, 2022). Figure from (Desiniotis and Kyprianou, 2011) and reproduced with permission from the publisher.

There are many publications demonstrating that within the focal adhesion plaque, ILK interacts with several other components of the formed complex involved in the suppression of apoptosis, cell survival and proliferation. These actions take place, for example, through the phosphorylation of protein kinase B (PKB/Akt) (Hemmings and Restuccia, 2012; Persad and Dedhar, 2003) and glycogen synthase kinase-3 (GSK-3) (Delcommenne et al., 1998; Persad and Dedhar, 2003). Phosphorylation of GSK-3 on Ser9 in a PI3K-dependent manner (Persad and Dedhar, 2003) by ILK results in the inhibition of the activity of GSK.3 (Delcommenne et al., 1998) resulting in the stabilization of β-catenin. When ILK is constitutively activated or overexpressed, it suppresses apoptosis and anoikis, promoting cell cycle progression, EMT and cell invasion (Persad and Dedhar, 2003; Persad et al., 2001).

The role of talin in integrin-linked kinase (ILK) recruitment to myotendinous junctions in mice has been reported by Conti et al. (Conti et al., 2009). The study by Zervas et al. shows that integrin and talin are important for ILK recruitment (Zervas et al., 2011). Based on the phenotypical characterization of cells expressing ILK mutants (such as E359K, K220M and V386G/T387G) in the "kinase" domain, ILK has been initially misclassified as a kinase (Wickström et al., 2010b; Bulus et al., 2021). Later, it has been classified as a pseudokinase devoid of catalytic activity and a central component of the intracellular ILK-pinch-parvin complex (IPP complex) (Ghatak et al., 2013) (Bulus et al., 2021).

A bioinformatic analysis of RNA-Seq data sets from The Cancer Genome Atlas (TCGA) has revealed a previously undocumented mRNA sequence in the *TLN1* gene (Gallego-Paez and Mauer, 2022). This sequence contains an additional exon, referred to as exon 17b, which is located between exons 17 and 18. A novel study by Gallego-Paez et al, has shown that exon 17b codes for an in-frame insertion of 17 amino acids into the first helix of the R2 helical bundle through differential pre-mRNA splicing analysis. Interestingly, this exon is already present in healthy tissue but is highly enriched in several subtypes of cancer, suggesting that it may play a role in cancer physiology controlled by TGF-β/SMAD3 signalling pathways(Gallego-Paez et al., 2023).

2.5.2 Talin in heart-associated diseases

Cardiomyocytes, the cells forming the heart muscle (cardiac muscle), are constantly subjected to high forces, so an appropriate linkage between cellular cytoskeleton and extracellular matrix is necessary for synchronized force distribution. Several intracellular proteins have been found to be crucial in this organized interaction between intracellular environment and ECM, including integrins and talins. Both talin isoforms are tightly regulated and expressed in cardiomyocytes. It was found that in the absence of talin2, talin1 is upregulated, maintaining normal cardiac structure and function. In contrast, the deletion of talin1 led to myocardial dysfunction and early death in mice (Manso et al., 2017). Studies in *Drosophila melanogaster* heart demonstrated that talin is required for the lumen formation of the heart (Vanderploeg and Jacobs, 2015) and continuous heart contractility (Bogatan et al., 2015).

Von Essen et al. studied the downregulation of *TLN1* expression in atherosclerotic plaques from 68 samples from carotid, aortic or femoral tissues. Their findings suggested that the downregulation of talin1 and vinculin causes disintegration of the tissue by loosening the cell-ECM interactions as well as remodelling of the tissue (von Essen et al., 2016). Other studies showed talin1 to be significantly downregulated in the media of aortic samples from patients with aortic dissection; this was associated with increased proliferation and migration of vascular smooth muscle cells (VSMC) (Cuesta et al., 2013; Wei et al., 2017). Moreover, the blood of patients with atherosclerotic diseases showed high soluble levels of talin 1 (sTalin1), associated with the presence and severity of coronary artery disease (CAD) (Aoyama et al., 2020).

The wall of blood vessels consists of three layers: the innermost tunica intima made of endothelial cells, the middle tunica media made of smooth muscle tissue, and the outermost tunica adventitia (or externa) (Milutinović et al., 2020) (Figure 8). Talin1 is expressed highly in vascular tissues (GTEx Consortium, 2015), particularly in endothelial cells as the only isoform (Monkley et al., 2011). During vascular development, the ECM provides important signalling cues, supporting the function of mature vessels by interacting with EC surface receptors (Hynes, 2007). The integrity of the endothelial cell (EC) layer, which is maintained *via* EC-EC and EC-ECM adhesions are pivotal for the proper function of the vascular barrier (Wallez and Huber, 2008) (Figure 8).

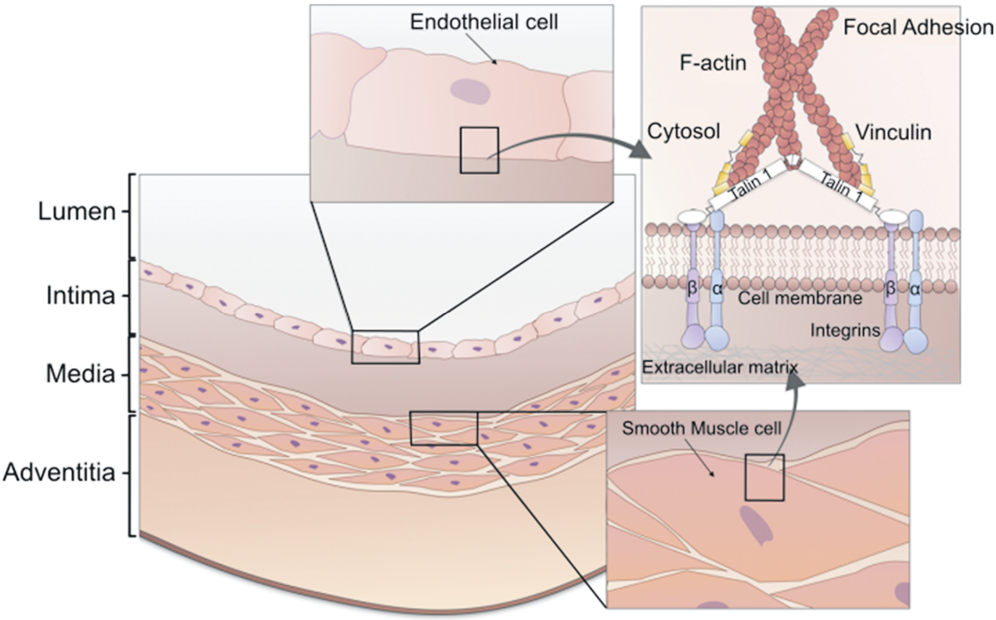

Figure 8. Talin1 is essential in vascular intimal and medial layers for cytoskeleton organization. Schematic representation of a normal coronary artery wall showing the intimal endothelial cell layer, the medial smooth muscle cells and the outer layer of adventitia. On the right, the focal adhesion complex showing talin1 as the core, linking F-actin to β-integrin. Figure adapted from (Turley et al., 2019) and reproduced with permission from the publishers.

Endothelial junctional proteins are important in vascular permeability, but also in tissue integrity (Wallez and Huber, 2008). As junctions form, EC undergo adhesional changes and initial focal contacts turn into focal adhesions (Kása et al., 2015).

Pulous et al. observed the phenomenon of integrin localization to the site of cell-cell junctions. Deletion of talin1 in endothelial cells reduced β1 integrin activation and disorganized adherent junctions, causing vascular death. Treatment of talin-deficient EC with β1 integrin rescued the EC barrier function, including the talin-dependent β1 integrin activation required for the maintenance of VE-cadherin organization and EC barrier function (Pulous et al., 2019).

Spontaneous coronary artery dissection (SCAD) is an important cause of myocardial infarction (=heart attack), affecting young, otherwise healthy, and predominantly female individuals lacking traditional risk factors for atherosclerotic coronary artery disease (Hayes et al., 2018). Figure 8 shows a sketch of a normal coronary artery wall, medial smooth muscle cells and intimal endothelial cells. Two hypotheses have been proposed to explain the pathophysiological process of SCAD: 1) after the development of an endothelial-intimal disruption, blood enters the subintimal space from the true lumen or 2) the disruption of traversing microvessels causes a hematoma (=clotted blood) (Hayes et al., 2020).

An exome study by Turley et al. conducted on familial and sporadic SCAD cases revealed talin1 as SCAD-associated gene. They identified rare heterozygous missense variants in talin1 in affected patients (Turley et al., 2019). Another study from the same group found in a genome-wide association study (GWAS), five genetic risk loci associated with SCAD. Talin1 was recognized to have indirect functional associations with phosphatase and actin regulator 1 (*PHACTR1)*, LDL receptor related protein 1 (*LRP1)* and fibrillin-1 (*FBN1)* (genes which previously linked to SCAD (*PHACTR1*) and vascular disorder (*LRP1* and *FBN1*) *via* actin and integrin (Turley et al., 2020).

It is necessary to review our current knowledge of the mechanosensitive talin molecule and to assess recent insights into talin´s structural and functional roles in the context of disease phenotypes as well as possible future areas of studies. Given the important role of talin in integrin-mediated cell attachment and its numerous binding partners, these aspects have been studied in this thesis using biochemical, cell culture and simulation methods.

3 AIMS OF THE STUDY

The aim of this dissertation was to investigate the molecular mechanisms of talin's involvement in organizing adhesions, stabilizing the integrin-actin linkage, and mediating integrin signalling. The specific aims were:

I. To understand the function of F1 loop within talin head and its interaction with the β3 integrin tail.

II. To reveal the physiologically functional and structurally stable talin head in a FERM-folded configuration in order to understand the regulation of cell-matrix adhesions.

III. To describe a pipeline approach of bioinformatics and wet laboratory experiments for crude characterization of talin1 mutants in order to evaluate their functional effects and potential pathogenicity.

IV. To uncover molecular consequences of the talin point mutation P229S found in a patient with multifaceted clinical symptoms.

4 MATERIALS AND METHODS

4.1 DNA expression constructs (I, II, III, IV)

The DNA constructs for expression of talin variants in the $TLN1^{-/-}TLN2^{-/-}$ mouse kidney fibroblast (MKF) cell line (Theodosiou et al., 2016) were subcloned into a modified pEGFP–C1 vector backbone (Clontech). All expression constructs contained C-terminal EGFP fluorescent protein to allow the analysis of subcellular protein localization and comparison of expression levels at single cell level. Point mutations were introduced into talin expression plasmids by GeneScript gene synthesis service and verified by DNA sequencing. Table 3 shows the expression constructs used in this thesis and from our unpublished data.

Table 3. The expression construct used in studies I, II, III and IV. *each point/hybrid mutation has been studied as separate construct. ¤ constructs from unpublished study.

Expression construct	Residues	Mutations	Study
Talin-1 head	1-405	-	I, II
Talin-1 head mutant*	1-405	del30, (del37/GAG), (T144E/T150E), 151-154AAAA, R194E, (R194E/D222K)	I
Talin-1 head	1-435		I, II
Talin-1 head	206-405		I
Talin-1 head	1-400		II
Talin-1 head (WT & mutant)	1-490	P229S	IV
Minitalin (WT & mutant)	1-490+2296-2541	P229S	IV
Talin-1	1-2541+EGFP	-	III, IV
Talin-1 mutant*	1-2541+EGFP	P229L, I392N, V577D, A893E, R1368W, Y1389C,	III

		L1539P, S1750F, E1770Q, D2086V, L2509P	
ΔR13–DD	1–2299+EGFP		III
ΔDD	1–2493+EGFP		III
Talin-1 mutant*	1-2541+EGFP	P229S, R297H, T585M, P942L, A1219V, R1241W, S1333T, V1964I, A2013T, T2098M, V2440E	IV, ¤

4.2 Cell lines and cell culture methods (III, IV)

The Tln1-/-Tln2-/- MKF cell line (talin-null MKF) was a kind gift from Dr. Carsten Grashoff, Max Plank Institute of Biochemistry, Germany. This cell line has been previously described by Theodosiou et al. (Theodosiou et al., 2016). The cell line was maintained in high-glucose DMEM supplemented with 10% FBS and 1% GlutaMax (Thermo Fisher Scientific, USA). Starvation medium contained 0.2% FBS. Cells were cultured using standard cell culture methods in a 37 °C incubator with 5% CO_2. All cells used in this work were regularly verified to be free of mycoplasma.

Talin-null MKF cells were transfected with the Neon electroporation transfection system according to the manufacturer's instructions (Thermo Fisher Scientific, USA). For all plasmid constructs, 6 μg of endotoxin-free plasmid DNA was used per 10^6 cells. 1400 V 30 ms, 1 pulse electroporation parameters were used to transfect talin-null MEF cells. Transfected cells were allowed to recover for 24 h before they were used in any experiments.

Human Umbilical Vein Endothelial Cells (HUVEC) were purchased from PromoCell (#C12208, lot447Z015) and cultured in EGM™-2 Endothelial Cell Growth Medium-2 BulletKit™ (Lonza, #CC-3162) containing supplements and growth factors (#CC-4176). The medium was changed every 2-3 days and cells were used at passage 3-6. The cells were regularly inspected for the absence of mycoplasma.

To evaluate the effect of talin point mutations on the cell behaviour, siRNA targeting the endogenous talin1 was constructed (HuTln1_siRNA_4367_4391: Sense: 5'CCAAGAACGGAAACCUGCCAGAGUUU3'; Antisense: 5'AACUCUGGC

AGGUUUCCGUUCUUGGUU3' (Horizon discovery LTD) and used for all subsequent experiments. A universal Stealth siRNA (Silencer TM siRNA; ThermoFisher; Catalog#4390843) was used as negative control. HUVEC were trypsinized, washed with 1x PBS before electroporation. The Neon transfection system (1350 v, 30 ms, 1 pulse) was used for the co-transfection of HUVEC cells with tln1-siRNA (1μM) and the talin1 point mutation expression plasmid. 20 μg of endotoxin-free plasmid DNA was used for 2x10^6 cells in the electroporation process.

4.3 Sample preparation for microscope imaging and western blot (III, IV)

For immunofluorescence (IF) staining, clean and sterile coverslips were coated with 10 μg/ml gelatin affinity-purified human fibronectin (Fn) for 1 h at 37 °C and washed twice with sterile PBS. Tln1-/-Tln2-/- MKF cells were transfected with talin expression plasmids and allowed to recover for 24 h. Transfected cells were trypsinized, and plated on the fibronectin-coated coverslips for 24 h, after which cells were fixed with 4% PFA for 20 minutes at room temperature (RT). Fixed cells were washed twice with PBS and permeabilized with 0.2 % Triton X-100 in PBS for 5 minutes at RT. Both primary and secondary antibodies were diluted in 0.1 % Triton X-100, 1.5 % BSA in PBS. Fixed cells were first incubated with the primary antibody for 1 h, washed with PBS (3 x 10 min), followed by incubation with the secondary antibody for 1 h and washes with PBS (3 x 10 min). The immunostained coverslips were stored at +4 °C in PBS or were mounted with Prolong mounting reagent (Thermo Fisher Scientific, USA).

For Western blotting, transfected cells were cultivated for 24 h and lysed with RIPA buffer supplemented with protease inhibitor cocktail (Sigma-Aldrich lot#126M4016V). After centrifugation, cell lysates were separated on SDS-PAGE. A wet blot system was used to transfer the separated protein from gel onto a polyvinylidene fluoride (PVDF) membrane. The antibodies and dilutions used are presented in Table 4.

Table 4. Antibodies used in the studies III and IV.

Antibody	Manufacturer	Dilution	Study
Vinculin	Merck, clone hVIN, V9131, RRID:AB_477629	1:100 IF/ 1:1000 WB	III, IV
FAK–pY397	Abcam, ab81298 [EP2160Y], RRID:AB_1640500	1:100 IF/ 1:1000 WB	III, IV
FAK (clone 77)	BD Biosciences, 610088	1:1000 WB	III
DLC–1 (H–260)	Santa Cruz Biotechnology, sc–32931	1:100 IF	III
Integrin β1 (D6S1W)	Cell Signaling Technology, #34971	1:100 IF	IV
Integrin β1–chain CD29, clone 9EG7	BD Pharmingen (Cat:553715)	1:200 IF	III, IV
Paxillin	BD Biosciences, 349/Paxillin, 610051, RRID:AB_397463	1:100 IF/ 1:1000 WB	III, IV
GFP	Sicgen AB0020–200	1:1000 WB	III, IV
Actin	Millipore, MAB 1501R, RRID: AB_2223041	1:2000 WB	III, IV
Alexa Fluor 568 phalloidin	Life Technologies	1:40 IF	III, IV
Alexa Fluor 568 goat anti–rabbit IgG	Life Technologies, A11011	1:200 IF	III, IV
Alexa Fluor 568 goat anti–mouse IgG	Molecular Probes, A11004	1:200 IF	III, IV
Alexa Fluor 594 goat anti–rat	Life Technologies	1:200 IF	IV

4.4 Microscopy methods (III, IV)

4.4.1 Live cell imaging for cell migration and wound closure assays (III, IV)

Transfected Tln1-/-Tln2-/- MKF cells were allowed to recover for 24 h, after which they were trypsinized and plated onto human fibronectin and/or human vitronectin (10 μg/ml) coated well-plate at low confluency. Cells were allowed to attach for 90 minutes before changing the medium to remove dead and not-transfected cells. The plate was transferred into the prewarmed EVOS FL auto microscope (ThermoFisher Scientific) equipped with a humidification chamber and on-stage incubator. The temperature was set to 37 °C, compressed air and 5% CO_2 lines were also connected. Live cells imaging was performed for 12 h at 5 min intervals. The resulting image sequences were analysed with ImageJ (Fiji) (Schneider et al., 2012) and MTrackJ plugin (Meijering et al., 2012).

For wound closure assay, transfected cells were cultured at high confluency (90 %) for 48 hours after which the wound was created by scraping with a 100 μl pipette tip. Cells were washed to remove dead and detached cells. The wound closure was imaged by EVOS FL auto microscopy and the traveling distance of cells within 12 h analysed with ImageJ.

4.4.2 Confocal microscopy (III, IV)

Protein co-localization analysis in single cells was performed using paraformaldehyde (PFA)-fixed and immunostained samples imaged either with a Zeiss CellObserverZ1 equipped with 63×/1.4, WD 0.19 mm oil immersion objective, an LSM780 confocal unit (Carl Zeiss Microscopy) (III) or with a Zeiss LSM800 laser scanning confocal microscope, mounted on inverted Zeiss Axio Observer.Z1 (Zeiss, Oberkochen, Germany) using Plan-Apochromat 63×/1.40, WD 0.19 mm oil immersion objective (IV). All imaging parameters were kept constant for the quantitative image analysis by ImageJ. During analysis processing, maximum intensity projection was used to convert the image stacks into single image. For the quantification of adhesion-localized protein intensity, 5–10 adhesion sites per cell were selected based on the EGFP-talin channel (Figure 9a), and each selection was copied to the red fluorescence channel (Figure 9b), followed by measurement of intensities from both channels using ImageJ. The background was assessed in the same way from areas near adhesion sites (Figure 9c, d). The background intensities were subtracted from the measured adhesion protein intensities for each channel.

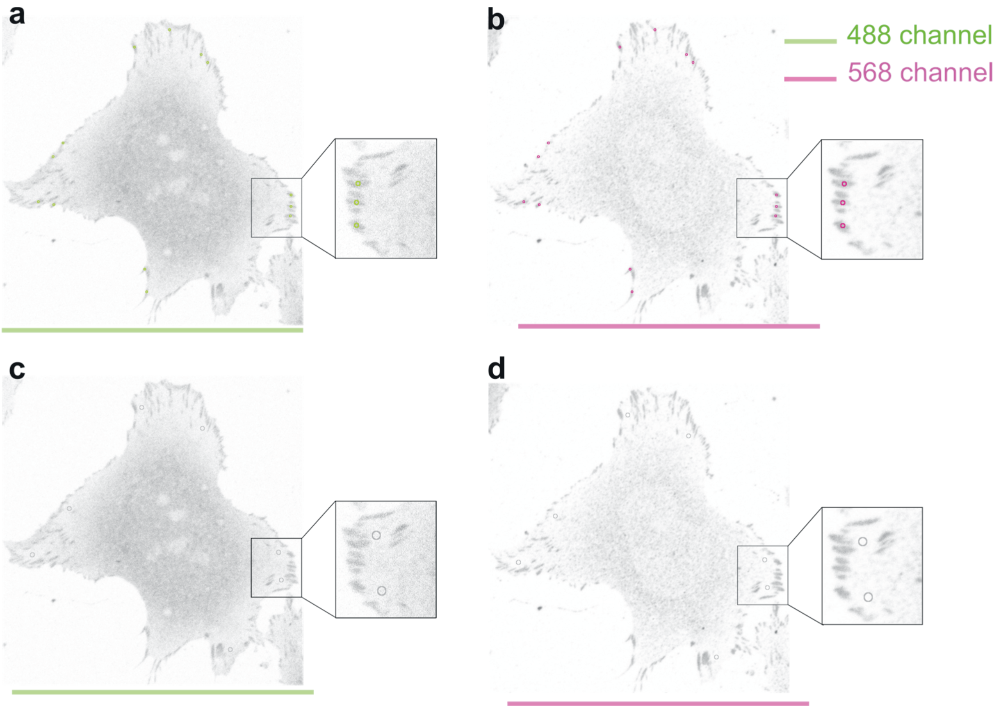

Figure 9. Schematic representation of the quantification of adhesion-localized protein intensity. Here an example of a cell transfected with WT talin1 protein (GFP, 488 nm channel) and immunostained with the total paxillin (red, 568 nm channel). a) Three adhesion sites were selected on the talin (GFP) channel using the ImageJ selection tool of 8-pixel size (green circles) and the intensities were measured. b) The same selected areas from the talin channel were copied to the red channel (magenta circles) and again the intensities were measured. c) Background selection using ImageJ selection tool of 16-pixel size (grey circles) near to the selected adhesion sites. The intensities were measured d) The same selected background areas (grey circles) on the red channel again and the intensities were measured.

For the quantification of adhesion number and size (Publication IV), samples immunostained against paxillin were used. The paxillin single channel image was used with raw data without any pre-processing. An 8-bit image was created to convert it to a greyscale binary image. The peripheral area of the cell was selected using free-hand tool in ImageJ. The "analyse particles" command with the pre-defined parameters (size = 0.2–5 µm2, circularity = 0–1) was used to scan the thresholded (binary) image for adhesion sites and to quantify their number, size, and total area.

4.5 Bioinformatics methods

The bioinformatics methods used in the studies were carried out completely by my colleagues, mostly by PhD Sampo Kukkurainen (Publication I and II) and PhD Vasyl Mykuliak (Publications III and IV). They have been described in detail in the original publications and are summarized briefly in this chapter. The bioinformatic screening tools for determination of deleterious effects of talin1 mutations were performed by myself under my supervisor´s guidance and advice from my bioinformatician colleagues.

4.5.1 Molecular dynamics (I, III, IV)

In publication I we studied the conformation of talin head and its integrin binding in the context of 100 % 1,2-dioleoyl-sn-glycero-3-phosphocholine (DOPC) and DOPC:PIP2 (9:1) bilayers in 150 mM KCl and transferable intermolecular potential with 3 points (TIP3P) water with counter ions added to neutralize the charge of the system using GROMACS 4.5.5 (Hess et al., 2008) and OPLS force field (Jorgensen et al., 1996). Control simulations of the talin head alone in 150 mM KCl were run with isotropic pressure coupling. Control simulations were run with the wild-type talin head (1-405), the F1-F2 interface mutant (1-405 R194E) and the F1-F2 interface charge inversion double mutant (1-405 R194E, D222K) for 100 ns. The simulation for talin1 (1-405 R194E) was run using GROMACS 4.6.6. Using the same setting, three 200 ns simulations of the wild-type talin head and three 200 ns simulations of a F1-loop-deleted (del30) talin head were run with GROMACS 2018.1.

In publications III and IV, the RCSB PDB structures were used as starting conformations for the MD simulations. We used 3IVF for F2–F3 (residues 208–398) (Elliott et al., 2010), 2H7E for F3 (residues 309–405) (Wegener et al., 2007), 1SJ8 for R1 (residues 487–656) (Papagrigoriou et al., 2004), 2L7A for R3 (residues 796–909) (Goult et al., 2013b), 2X0C for R7–R8 and R7 (residues 1352–1457, 1585–1659) (Gingras et al., 2010), 2KBB for R9 (residues 1655–1822) (Goult et al., 2009), 3DYJ for R11 (residues 1975–2140) (Gingras et al., 2009) and 2QDQ for the DD domain (residues 2494–2541) (Gingras et al., 2008). Equilibrium MD simulations were performed using GROMACS (Abraham et al., 2015) at the Sisu supercomputer, CSC, Finland. Alchemical free energy calculations were prepared using PMX (Gapsys et al., 2015) and performed with GROMACS at Puhti supercomputer, CSC, Finland.

4.5.2 Prediction of the deleterious effect of TLN-1 mutation (III)

Talin1 variation data were obtained from the COSMIC (Catalogue of Somatic Mutations In Cancer) database (January 2017) with the reported recurrence for each mutation. We identified 368 talin-1 mutations, from which 258 missense mutations were further filtered using several bioinformatics tools to study and predict the consequences of the mutations in more details. We went through the aa sequence in talin1 and explored the structural information available in the protein data bank (PDB). These PDB structures were selected in our analysis: 3IVF (Elliott et al., 2010), 4F7G (Song et al., 2012), 1SJ7 (Papagrigoriou et al., 2004), 2L7A (Goult et al., 2013b), 2X0C (Gingras et al., 2010), 2KBB (Goult et al., 2009), 3DYJ (Gingras et al., 2009) and 2QDQ (Gingras et al., 2008). The position and location (of each point mutation on the talin domains (whether on surface or buried) were examined using PyMol software by visual observation of the position of the mutation.

To classify the variants into pathogenic, neutral, and unknown, the PON-P2 tool freely available at http://structure.bmc.lu.se/PON–P2/ (Niroula et al., 2015) was used. To evaluate the severity and the degree of evolutionary conservation of each mutation the BLOSUM 62 matrix (Henikoff and Henikoff, 1992) and ConSurf (https://consurf.tau.ac.il/) (Ashkenazy et al., 2016) tools were used, respectively. The amino acid substitution matrices CBSM60 was used to analyse the sequence–structure relationship of the protein (Liu and Zheng, 2006). We also investigated the location of the known ligand-binding sites and the substitution of hydrophobic with hydrophilic amino acids and vice versa.

Based on the location of each mutation, they were classified into six group and given a position code between zero and one as follow: surface (0.4), buried (1), on a loop (0.2), on a linker but buried (1), between the helices buried (0), and on the dimerisation domain (0.8). A polarity change code of one was given when the amino acid was mutated from hydrophilic residue to hydrophobic residue or vice versa. We used the formula $n_1X1+n_2X2+\ldots+n_nXn$ (n is the scoring coefficient and X is the variable) to calculate the total score by giving different scoring coefficients in nine iteration. Each time, we generated a list of mutations with the highest score on the top of the list. Finally, we generated a list of top ten mutations which appeared frequently after each iteration. Using this method, we selected ten talin mutations for further analysis.

4.6 Biochemical and biophysical characterization

4.6.1 Recombinant protein production and purification (I, III)

In publication I, talin1 head domains (Table 3) were cloned into the pTrcHis-C vector (ThermoFisher Scientific, Carlsbad, CA), which includes an N-terminal hexahistidine tag followed by Xpress epitope and Enterokinase cleavage site (MGGSHHHHHHGMASMTGGQQMGRDLYDDDDKDRWIRPRA). The plasmids were introduced into *E. coli* BL21-Star cells (Thermo Fisher Scientific). Bacteria were cultured in LB-medium containing 100 µg/ml ampicillin at 37 °C and induced by 1 mM IPTG for protein expression for 5 h. After homogenization using Emulsiflex C3, the clarified cell lysate was applied into a HisTrap FF 5 ml affinity column (GE healthcare) using an Äkta purifier.

The His-tagged proteins were purified according to the manufacturer instructions, using 20 mM sodium phosphate buffer containing 1 M NaCl and 20 mM imidazole pH 7.4 as binding buffer and binding buffer with 700 mM imidazole as elution buffer in a gradient purification method. Eluted fractions were analysed by SDS-PAGE and the fractions containing the protein of interest were collected for further purification using an ion exchange chromatography method (IEX) considering the calculated isoelectric point (pI) value of the protein (using ProtParam Expasy tool, freely available at: https://web.expasy.org/protparam/) to select the correct column and buffers. The HiTrap SP FF 1ml columns (GE Healthcare) using 50 mM sodium phosphate buffer pH 7.5 with a linear NaCl gradient from 20 mM to 1 M NaCl.

The GST-tagged integrin constructs (WT-β3: GST–GSKLLITIH-DRKEFAKFEEERARAKWDTANNPLYKEATSTFTNITYRGT; and the GST-β3-VE: GST–GSKLLITIHDRKEFAKFEEERARAKWVENPLYKEATS-TFTNITYRGT) were expressed using *E. coli* BL21-Star cells and similar conditions as for the talin head constructs. The purifications were performed with Glutathione

Sepharose (GE Healthcare 4 Fast Flow) using 50 mM Tris-HCl pH 8, and 20 mM reduced glutathione as eluent.

In publication III, segments of cDNA encoding for talin1 (Table 3) were introduced into a modified pHis vector to create N-terminal His6-tagged constructs. The His6-tag is separated from the talin fragment by an eleven-residue linker: SSSGPSASGTG. Mutagenesis was performed using QuikChange II Site–Directed Mutagenesis kit. Talin constructs were expressed in *E. coli* BL21(DE3) cells and induced with 0.1 mM IPTG at 18 °C overnight. Protein purification was performed in the same way as in publication II and according to the column manufacture instructions. In all cases, the sequence of the plasmid was confirmed by capillary Sanger sequencing before the protein production and expression.

4.6.2 Size exclusion chromatography with static light scattering (I, III)

In publication I, the static light scattering (SLS) method in combined with size exclusion chromatography (SEC) was used to determine the molecular weight (MW) of the proteins. The instrument contained a Malvern Zetasizer (μV) (Malvern Instruments Ltd., Worcestershire, UK) and a liquid chromatography (CBM-20A, Shimadzu Corporation, Kyoto, Japan) equipped with autosampler (SIL-20A), UV–VIS (SPD-20A), and a fluorescence detector (RF-20Axs). For the determination of protein concentration, the UV absorption intensity at 280 nm was measured using the right angle light scattering (RALS) technique. Data were processed using Lab Solution Version 5.51 (Shimadzu Corporation) and OmniSec 4.7 (Malvern Instrument Ltd) software. Talin protein samples (50 μg) were injected using the autosampler on a Superdex 200 5/150 column (GE Healthcare, Uppsala, Sweden). 50 mM NaH_3PO_4, 150 mM NaCl pH 7.2 was used as running buffer. The molecular weight for each sample was determined by calibrating the light scattering detector based on the monomeric peak of BSA.

In publication III, the purified talin constructs were analysed by a SEC-MALS at a concentration of 100 μM at room temperature (RT). Eluted proteins were analysed with Viscotek SEC–MALS 9 and Viscotek RI detector VE3580 (Malvern Panalytical).

4.6.3 Differential Scanning Calorimetry (DSC) (I)

To measure the temperature transition midpoint (Tm) and calorimetric heat change associated with unfolding (ΔH), each sample was first degassed, and concentrations were measured by NanoDrop. Samples were analysed using the VP-DSC instrument (MicroCal, Malvern Instruments Ltd) with protein concentrations of ~0.2 mg/ml. Samples were heated from 20 °C to 130 °C at a scanning rate of 2 °C/min. The feedback mode was set to low and filter period was 5 s. The baseline was subtracted, and the Levenberg-Marquardt non-linear least-squares method was applied using MicroCal Origin 7.0 software (MicroCal, Malvern Instrument Ltd).

4.6.4 Biosensor analysis for talin-integrin interaction (I)

In publication I, binding of the GST-tagged integrin to different His-tagged talin head constructs was measured using Fortebio Octet RED384 instrument (Pall Life Science) using Ni-NTA sensors. Sensors were pre-wetted with the running buffer (50 mM NaH_3PO_4, 150 mM NaCl pH 7.2) in order to get baseline prior to immobilization, using an operating temperature at 27 °C and a stirring speed of 1000 rpm throughout the experiment. His-tagged talin was immobilized on the sensor via EDC/NHS (1-Ethyl-3-(3-dimethylaminopropyl/N-Hydroxysuccinimide) carbodiimide coupling. The remaining activated groups were quenched by 1 M ethanolamine pH 8.5. Talin-integrin binding was measured at five different GST-integrin concentrations of 20, 80, 320, 1250 and 5000 nM. The data was analysed by GraphPad Prism 5.02 (GraphPad Software, La Jolla, CA). The binding signals were normalized within each group of GST-β3 and GST-β3-VE.

The background data from the GST control (without integrin peptide) was subtracted from all datasets and the data were normalized to the wild-type talin head at a GST-integrin concentration of 1250 nM. A linear regression analysis assuming one site-specific binding was carried out in GraphPad Prism 5.02 (GraphPad Software, La Jolla, CA).

5 SUMMARY OF THE RESULTS

5.1 Talin head is required to bind and regulate integrin activation and clustering

At the early steps of the cell adhesion, talin regulates integrin activation and clustering through direct interactions *via* its head domain. Publication I focus on the structural analysis of the talin head, the identification of the intersubdomain interactions as well as interactions between the C-terminal lysine motif of the F3 subdomain with the β3-integrin. Publication II focuses on the long loop within the F1 subdomain, aiming to understand how the loop regulates β integrin activation and clustering.

5.1.1 F1 loop in integrin activation and clustering in a FERM-folded talin head structure (I, II)

Previously, it has been shown that talin F3 binds to the NPLY motif of integrin β3 (García-Alvarez et al., 2003). Furthermore, it has been shown that the talin F2-F3 fragment alone is not sufficient to activate the α5β1-integrin, when measured by assessing soluble fibronectin binding (Bouaouina et al., 2008). However, in the presence of Mn^{2+} and when cells are cultured on a vitronectin-coated surface αvβ3, integrin clustering has been induced by the F2-F3 fragment alone (Saltel et al., 2009). We analysed the clustering of the β3-integrin in a physiological Mn^{2+}-independent manner in the presence of a fluorescently labelled talin head and kindlin1 in B16F1 melanoma cells. We found that the complete talin head domain (1-435) alone enhanced the β3-integrin clustering (Figure S1D in publication I). The co-expression of kindlin1 with talin head further increased the integrin β3 clustering to the same level as in the presence of Mn^{2+}, but this was not observed in the case of co-expression of kindlin1 with the talin F2-F3 fragment (Figure 1b in Publication I). This confirmed the previously known fact that the talin F0-F1 subdomains are required for the kindlin1-mediated integrin clustering, but are dispensable when Mn^{2+} is used to activate integrins.

Furthermore, the long loop in the F1 subdomain (38 residues in talin, residues 139-177) has been shown to be important for integrin activation (Goult et al., 2010; Bouaouina et al., 2012; Xing et al., 2006). Complete deletion of the F1 loop (residues 139-168; del30), or replacement of residues 134-170 with Gly-Ala-Gly (del37/GAG) to yield a loop similar in sequence and equal in length to *Dictyostelium* TalB (Figure 2G, H and Figure S1 in publication I), both yielded a defect in integrin β3 activation and clustering in B16F1 cells (Figure 2F, H, I in publication I). To narrow down the contributing area within the loop, the deletion of the central part of the loop (del 17) and the replacement of the residues 151-154 (LLRD) with alanines (151-154AAAA), preserving the length and net charge of the loop, were performed. Cells expressing these talin mutations did not show proper integrin activation or clustering (Figure 2F in publication I), suggesting that the central part residues 151-154 (LLRD) are important for F1 loop function.

Based on these results, we decided to create a model where the talin head is rotated at its F1-F2 linker to create a compact FERM-like folded domain. The structural stability and the potential lipid interaction of this model was explored by MD simulations including the lipid membrane and the integrin αIIβ3 transmembrane and cytoplasmic domains. In this suggested compact conformation, the lipid interaction sites of the F2 and F3 subdomains are oriented towards the lipid membrane where F3 is in contact with the F1 subdomain and the F1 loop is in close proximity to the integrin binding site, creating altogether a FERM-like triangular assembly (Figure 10a).

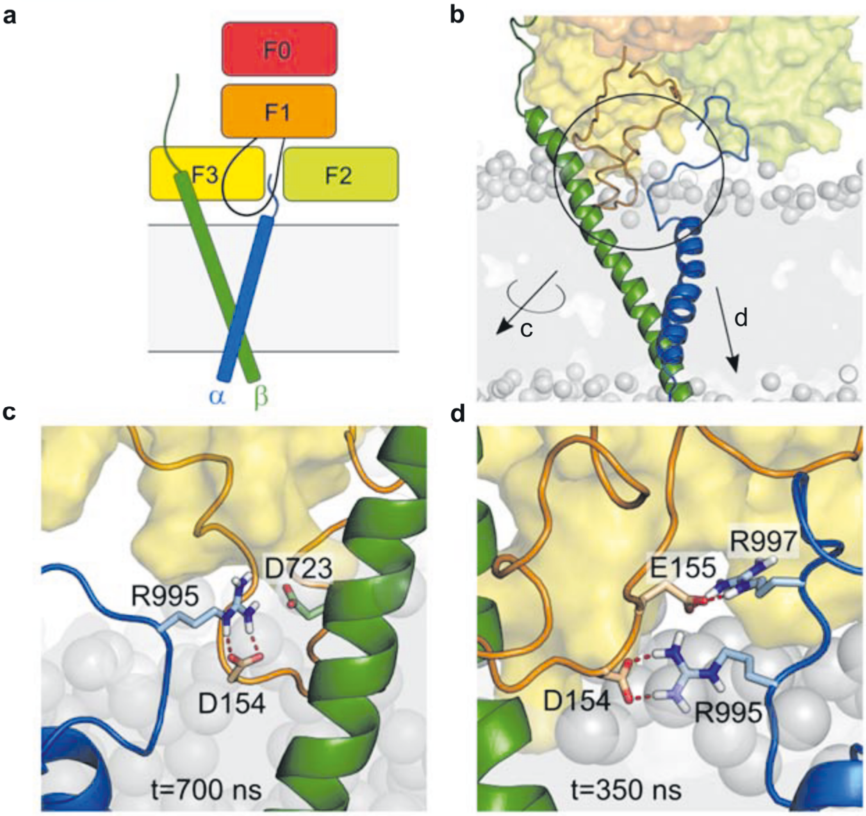

Figure 10. The residues D154 and E155 in the F1 loop are critical for integrin β3 clustering. A,b) Schematic representation (a) and in an MD simulation manner (b) of the F1 loop position. C) MD simulation indicate that the residue D154 in the F1 loop interferes with the R995-D723 salt bridge of integrin αIIbβ3, forming a more stable salt bridge between F1 loop and R995 in αIIbβ3. d) MD simulation indicated a salt bridge between the residue E155 in the F1 loop and R995 in αIIbβ3. Figure adapted from publication I.

Further investigating our MD simulation data, we found that the residue D154 in the talin F1 loop is competing with the residue D723 of β3-integrin for binding to the residue R995 of αIIb integrin (Figure 10b, c). As the D154A mutation alone did not influence the integrin clustering in cells, we also targeted the nearby residue E155 (Figure 10b, d). The combination of D154A + E155A was found to be harmful to the integrin clustering (Figure 3E in publication I).

To gain more insight into the conformation and interactions of the F1 loop, we analysed the interface between F2 and F3 subdomains. In a solvent-exposed model, we found a potential binding patch consisting of the residues Leu314 in F3 and

Gly226 in F2 subdomains for interaction with the F1 loop. In addition, a potential flexibility of the residues in F1 loop was exposed in the solvent-exposed model. For example, the residue K149 in F1 loop interacts both with K268 in the F2 and K320 in the F3 subdomain. This suggests that the F1 loop can bind to the region of the F3 domain relevant to integrin binding and clustering, indicating a gatekeeper function for the F1 loop.

Moreover, we showed that kindlin1 can replace Mn^{2+}, mediating integrin β3 clustering induced by the full length talin head, but not induced by the F2-F3 fragment of the talin head. Upon removal of flexible loop within talin head F1 subdomain, kindlin1 and talin head -mediated integrin clustering was lost. Moreover, the removal of the poly lysine motif (residues 401 to 405), led to a loss of integrin β3 clustering even in the presence of kindlin. This indicates of a mechanism by which talin-kindlin complex activates and clusters integrins.

5.1.2 Crystal structure revealed the C-terminal poly-lysine motif to mediate FERM conformation and to tightly associate with the N-P-L-Y motif of the β3-integrin (II)

To get an overall view on the talin head structure, we performed negative-stain transmission electron microscopy (TEM) and crystallography. None of the analysed TEM images or crystallography data supported the elongated model for the t1-405 revealed earlier (residues 1-400 without F1 loop; PDB ID 3IVF (Elliott et al., 2010) (Figure 11a)). We further explored the intersubdomain interaction network maintaining the FERM conformation (Figure 11a, b). As shown in Figure 11b, a network of salt bridges and hydrogen bonds connecting the talin head subdomains is formed, that is likely responsible for the stability of the FERM conformation. We investigated the role of the F3 subdomain C-terminal poly-lysine motif and found that B16F1 melanoma cells transfected with the poly-lysine truncated version of the talin head (residues 1-400) showed significantly reduced integrin activation and clustering (Figure 2E in publication II). These findings suggest that the compact FERM-like talin conformation and the C-terminal lysine motif in the F3 subdomain are both required for talin-induced integrin activation and clustering.

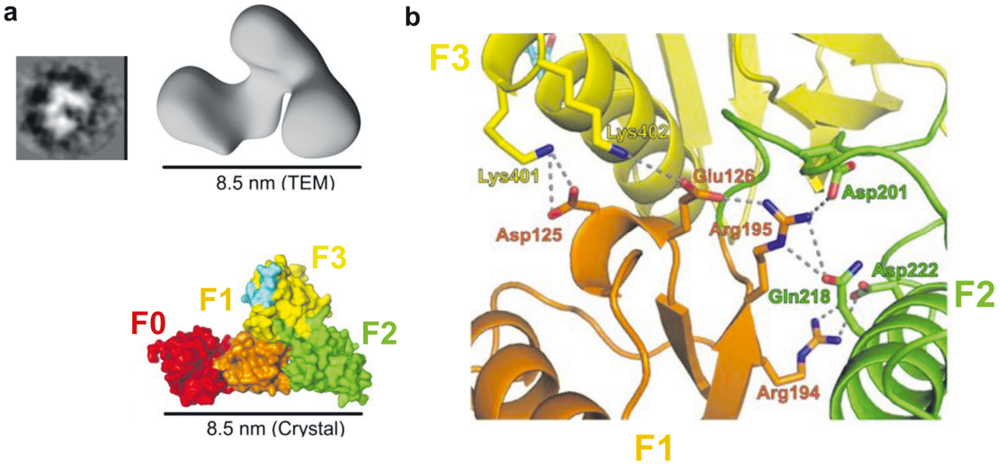

Figure 11. Crystal structure of talin head in a FERM-folded configuration. a) A 2D view of negatively stained talin head (residues 1-405) captured by TEM (up left). A 3D TEM volume of talin head (residues 1-405) (up right). Surface representation of the talin head (residues 1-405) in the crystal structure (down). b) Intersubdomain interaction network in the talin FERM domain. Hydrogen bond interactions are shown by dotted lines. Figure adapted from publication I and II.

5.2 Point mutations in talin disrupt cell adhesion stabilization and contributes to diseases (III, IV)

Publications III and IV study how point mutations in talin1 contribute to human diseases. In publication III, we investigated cancer-associated talin1 point mutations found in the COSMIC database using bioinformatic tools. The top ten selected point mutations with a high probability of affecting cell function were investigated further by MD simulations, cell migration, invasion, and proliferation assays and with biochemical analyses to learn about the structure-function relationship of mutated talins. In publication IV, a novel talin variant identified in a young patient was studied by biochemical and cell culture methods. In our unpublished study, talin point mutations found in patients with spontaneous artery dissection (SCAD) were investigated using similar methods.

5.2.1 Talin point mutations destabilize the structural stability of talin (III, IV)

The effect of point mutations on talin structure and stability was investigated by MD simulation. To predict free energy changes in subdomain stability, non-equilibrium alchemical MD simulations were conducted (Table 5). According to this analysis, the strongest destabilisation effect was observed for the mutations V577D in R1 (52.15 ± 13.71 kJ/mol), I392N in F3 (38.28 ± 1.27 kJ/mol) and Y1389C in R7 (20.60 ± 4.09 kJ/mol). Weaker, but still significant destabilisation was observed for the mutations D2086V in R11 (12.96 ± 0.82 kJ/mol), R1368W in R7 (12.63 ± 0.27 kJ/mol), A893E in R3 (10.5 ± 1.91 kJ/mol), (publication III) and V2440E in R13 (-11.22 ± 0.66 kJ/mol) (unpublished data). Other mutations showed only mild stabilisation/destabilisation effects, which did not cause significant changes in the subdomain stability. The MD simulation suggested a mild, but consistent destabilization of the P229S point mutation by 5.6 +- 2.2 kJ/mol for F2-F3 interaction energy, which did not cause major changes in protein conformation. We did not detect any similar effect for P229L (0.1 +-1.2 kJ/mol) (Publication IV).

Table 5. Analysis of free energy changes in protein stability upon mutation. ¤unpublished data.

Mutation	Subdomain	Location	ΔΔG, kJ/mol	STD	Study
R297H	F2	surface	2.91	0.16	¤
I392N	F3	buried	38.28	1.27	III
V577D	R1	buried	52.15	13.71	III
T582M	R1	surface	-4.27	0.90	¤
A893E	R3	buried	10.50	1.91	III
A1219V	R6	buried	-0.44	0.81	¤
R1241W	R6	surface	6.67	1.98	¤
S1333T	R6	surface	3.57	0.54	¤
R1368W	R7	surface	12.63	0.27	III
Y1389C	R7	buried	20.60	4.09	III
S1750F	R9	buried	2.28	2.33	III
E1770Q	R9	surface	-4.17	0.35	III
V1964I	R10	buried	0.05	1.23	¤
A2013T	R11	surface	0.43	0.90	¤
D2086V	R11	surface	12.96	0.82	III
T2098M	R11	buried	-5.14	3.64	¤
V2440E	R13	surface	-11.22	0.66	¤

The mutation isoleucine to asparagine at residue 392 (I392N) in the F3 subdomain strongly destabilized the domains' stability (Publication III). Our MD simulation data indicated that by exchange of the hydrophobic isoleucine to hydrophilic asparagine, a water molecule penetrated inside the F3 subdomain and made the structure unstable (Figure 12a).

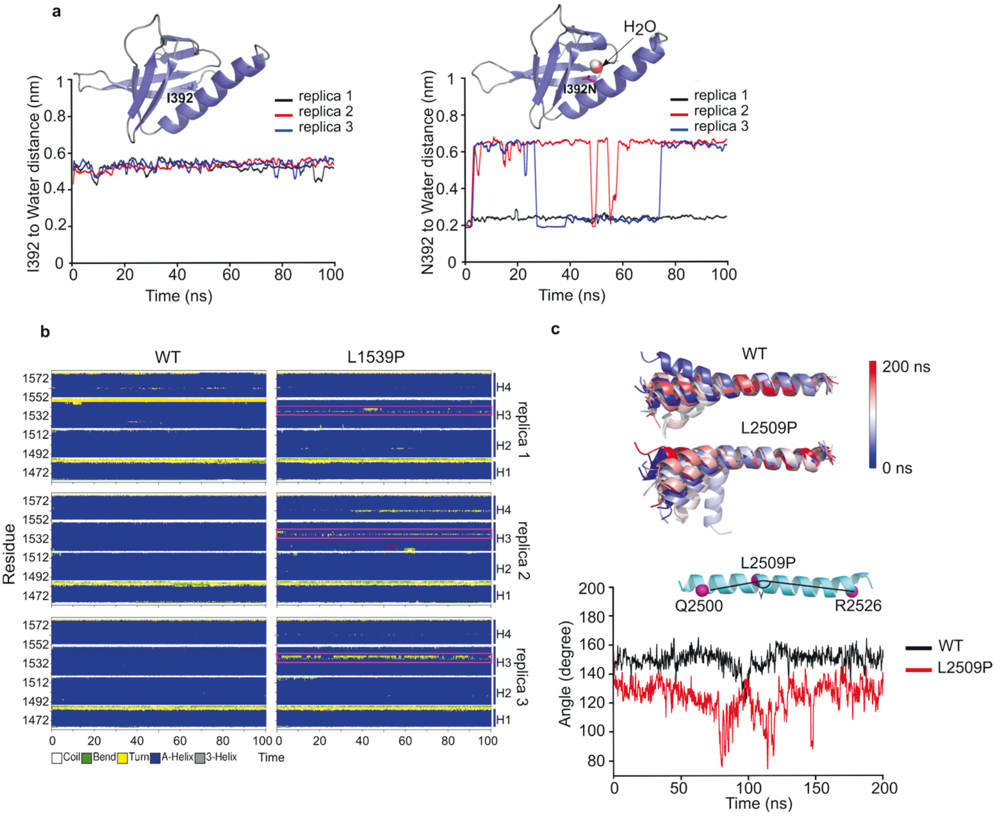

Figure 12. MD simulation analysis of the effects of cancer–associated mutations on talin domains. a) Structure snapshots of the F3 subdomains of WT and I392N mutant. The residue 392 and a water molecule inside the F3 domain in the I392N mutant simulation are shown. The plots show the distance between the residue 392 side chain and the closest water molecule as function of the MD simulation time in WT (left) and I392N mutant (right). The distance of~0.6 nm in the WT indicates that the closest water molecule is located at the F3 surface, while in the I392N mutant the distance of ~0.2 nm indicates that the nearest water molecule has penetrated the F3 fold. b) Secondary structure analysis of the R8 subdomain in WT and L1539P mutant suggested that the mutation breaks the helix 3 (highlighted by a magenta box). c) MD simulation for the L2509P mutation in the dimerization domain (DD) showing increased flexibility of the domain in comparison to the WT (upper). Superposition was performed using C-alpha atoms of residues 2510 to 2529. The angle (γ) in L2509P mutant and WT in a single helix measured as a function of time (showed in the helix with cyanide colour). Figure adapted from publication III.

The point mutation of leucine to proline at positions 1539 and 2509 strongly destabilized the subdomain structures of R8 and dimerization domain (DD), respectively. Secondary structure analysis of the helix 3 in R8 revealed that the L1539P mutation effectively breaks the structure of the helix 3 in the R8 subdomain compared to the WT (Figure 12b). MD for R7-R8 WT and R7-R8 L1539P indicated the increased flexibility of the R8 subdomain caused by proline. The L2509P mutation in the dimerization domain breaks its helical structure and causes high flexibility (Figure 12c).

5.2.2 Clear impact of the point mutation on the cell shape and migratory ability was detected

Having demonstrated by MD simulations that most of the point mutations could structurally destabilize talin subdomains, we next wanted to determine whether those point mutations in talin contribute to migratory/invasive characteristics, proliferation, and ligand binding in cell models (publications III, IV). Previous studies showed that talin triggers the inside-out integrin activation pathway by direct interaction of the F3 subdomain with the β-integrin cytoplasmic tail (Anthis et al., 2009). Based on this information, we expected to detect behavioural changes in cells transfected with the I392N variant. Our results indicated a high migration rate of 0.82 μm/min in cells transfected with I392N compared to cells transfected with WT talin-1 (0.65 μm/min) (Figure 13a) (publication III). As metastasis requires cell invasion in addition to migration, we also utilised a Boyden chamber with a Matrigel layer to explore the contribution of the point mutation on the migratory ability of the MKF cells through Matrigel. As with migration, the I392N significantly increased the cell invasion ability through Matrigel in comparison to WT, leading to a ~40 % larger invaded area.

The analysis of the MD simulations for the L2509P mutation located in the dimerisation domain showed a high flexibility of the mutated helix (Figure 12C and Figure 2e in publication III). Cells transfected with the full length talin containing L2509P possessed a significantly low ability to migrate (0.37 μm/min) in comparison with WT (0.63 μm/min) (Figure 13a) and showed severe morphological changes, resulting in a round cell shape (Figure 13b) (Publication III).

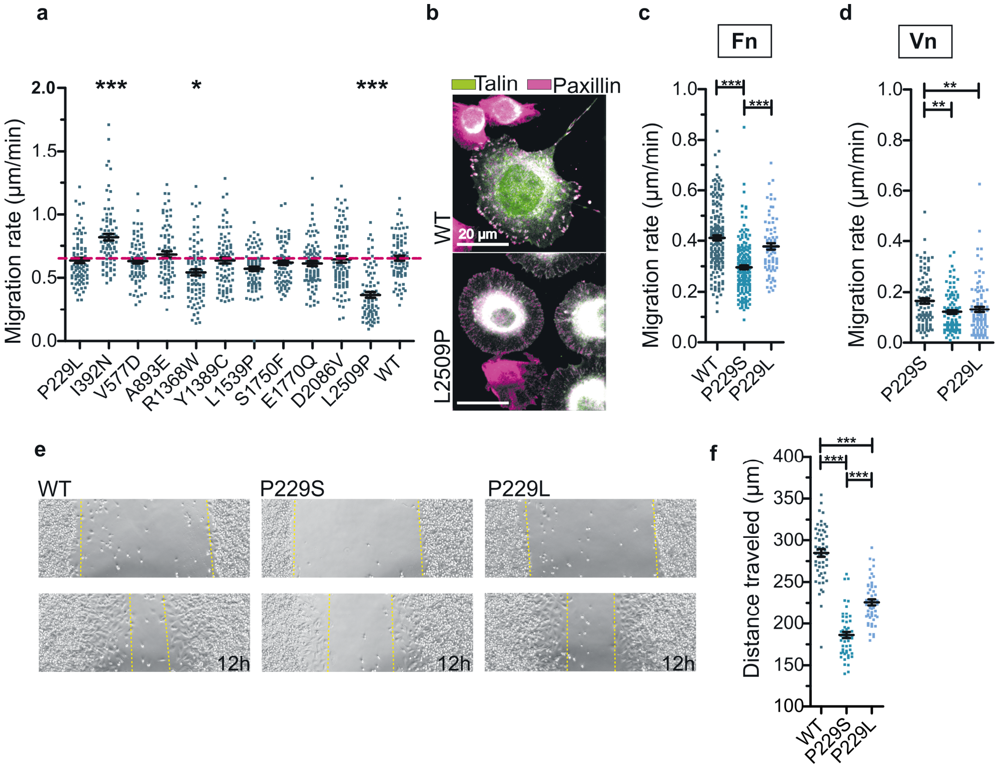

Figure 13. Talin mutations affect cell migration and cell morphology. Random migration speed (µm/min) analysed from time-lapse images of cells transfected with the talin constructs on fibronectin (Fn)-coated surface (Publication I). Significantly increased and decreased migration speed was detected for cells transfected with I392N and L2509P, respectively, in comparison to WT-transfected cells. In addition, cells transfected with R1368W showed decreased migration speed in comparison to WT. n ~ 80 cells pooled from three independent experiments. The statistical significance of the results analysed in comparison to talin1 WT by one-way ANOVA and Bonferroni test: *P<0.05, **P<0.01, ***P<0.001. The results are normalized to talin1 WT b) SUM projections of z–stacks of TLN1–/–TLN2–/– mouse kidney fibroblasts expressing WT (upper) and L2509P (lower) variants showed a circular phenotype for L2509P-transfected cells in comparison to the WT transfected cells. Cells immunolabeled against paxillin. Scale bar is 25 µm. (Publication I). c, d) Random migration analysis of the cells transfected with full-length talin WT, P229S and P229L on fibronectin (Fn)-coated surface (c) or on vitronectin-(Vn) coated surface (d), n ~ 95 cells pooled from three independent experiments. (Publication IV). e) Representative images of the wound closure assay for cells transfected with full-length talin WT, P229S and P229L at 0 h (upper) and after 12 h (lower). f) The distance travelled (µm) by the cells to close the wound was calculated by analysing the scratched area at 0 h and 12 h. n ~ 25 scratches from three independent experiments. The statistical analysis in (c), (d) and (f) was done using t-test Mann–Whitney *P < 0.05, **P < 0.01, ***P < 0.001. Data represent the mean values with SEM. Figure adapted from publication III and IV.

In Publication IV, we investigated MKF cells transfected with full-length P229S talin1, which had a slightly larger surface area with higher circularity compared to WT transfected cells. Random migration analysis of the cells expressing P229S talin1 variant was investigated on fibronectin- (Figure 13c) and vitronectin- (Figure 13d) coated surfaces, showing a significant decrease in migration rate in the case of P229S (~0.29 μm/min) compared to WT (~0.41 um/min). Furthermore, a scratch assay indicated a delay in wound closure in cells expressing P229S, with cells travelling only three-quarters of the distance of talin1 WT expressing cells (Figure 13e, f). We used the variant P229L from previous study (publication III) as a control in these experiments and noticed P229S to have a clear negative effect on cell migratory capacity even in comparison to the P229L variant (0.38 μm/min).

Since many cell types express both talin1 and talin2 phenotypes, we aimed to show the dominative effect of talin1 L2509P. We co-transfected MKF cells with full-length talin1 L2509P and talin2 WT. As control we co-transfected MKF cells with full-length talin1WT and talin2 WT. The results showed significantly slower cell movement (0.39 μg/min) for cells containing L2509P, even in the presence of talin2 WT, when compared to cells co-transfected with full-length wild type of both talin isoforms (0.49 μm/min) (Figure 7c in publication III).

Next, we wanted to understand the mechanism behind the effect of L2509P on cell behaviour, resembling cells expressing talin with a deletion of the whole dimerization domain. We engineered a series of talin1 truncated constructs with deletion in the c-terminus: ΔDD (1–2493) and ΔR13-DD (1-2299). Cell morphology and behaviour transfected with these newly engineered constructs were compared to the talin1 full length WT and talin1 full length L2509P. The results showed the same changes in morphology with L2509P, ΔDD and ΔR13-DD with loss of i) adhesion maturation and ii) localization of FA components in all of them (Figure 14).

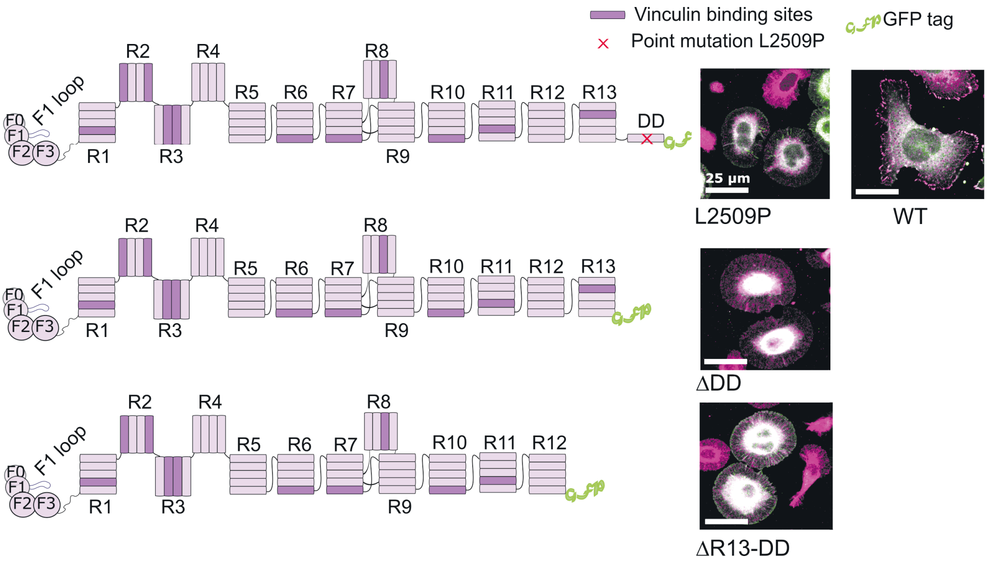

Figure 14. The talin1 L2509P point mutation has the same effect on cell morphology as the deletion of the whole dimerization domain. On the left, schematic representations of the point mutation L2509P in full-length talin (upper) and the truncations; ΔDD (middle) and ΔR13-DD (lower). On the right, SUM projections of z–stacks of TLN1–/–TLN2–/– mouse kidney fibroblast cells expressing full length WT talin1 (upper right), L2509P (upper left), and talin1-truncated constructs ΔDD (middle) and ΔR13–DD (lower). Cells were immunolabeled against vinculin. No clear localisation of vinculin was evident with any of the mutants. Scale bars are 25 µm. Figure adapted from publication III.

5.2.3 Talin1 point mutation I392N disrupt ligand binding and adhesion signalling

We evaluated whether the cancer-associated talin1 point mutation I392N, locating close to a known integrin binding site in F3 (PDB:2H7D) (Wegener et al., 2007), has an impact on the co-localization with integrin and its activation. Indeed, we found that with the mutant the level of activated β1-integrin was reduced significantly (~53%) in comparison to the WT (Figure 15a, b). L1539P is also located near to the DLC-1 binding site, and we were thus interested to quantify the amount of DLC-1 within the adhesion sites. We found that the DLC-1 level was attenuated by ~42% in comparison to the WT (Figure 15c).

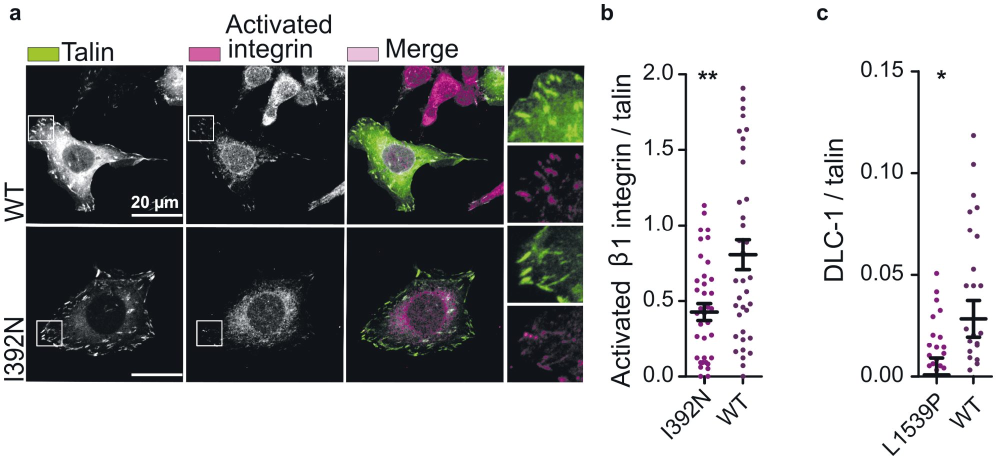

Figure 15. Talin1 point mutations alter the interaction and colocalization of talin with activated β1-integrin and DLC-1. a) Representative confocal immunofluorescence images of the co-localisation of talin and integrin and the organization of activated integrin β1 in cells transfected with full length talin WT and I392N. SUM projections of z-stacks of cells expressing GFP-tagged talin-1 (WT and/or point mutated) and immunolabeled against integrin CD29 or DLC-1, and ~ 30 cells per label have been analysed. b) Data obtained from the co-localization analysis of talin and integrin and the organization of activated integrin CD29 in the cells transfected with full length talin WT and I392N. c) Data obtained from the co-localization analysis of talin and integrin and the organization of the DLC-1 in the cells transfected with full length talin WT and L1539P. The statistical significance of all results was analysed by one-way ANOVA and Bonferroni test: $^*P < 0.05$, $^{**}P < 0.01$, $^{***}P < 0.001$. Scale bars are 25 µm, zoom-in square size is 12.5 µm × 12.5 µm. Figure adapted from publication III.

A significant defect in migratory ability was seen in cells transfected with full length talin1 carrying the mutation P229S in both random migration and collective cell migration assays in comparison to the WT (Figure 13c, d, e, f). To understand whether the variant P229S also interrupts adhesion signalling, we assessed the adhesion maturation by the co-localization of the adhesion signalling molecules pFAK, paxillin and β1-integrin. In full length versions of talin1 WT and P229S, no clear differences were seen in the co-localization of these focal adhesion markers. We hypothesized that a potential difference could be best visible in the early phase of adhesion maturation and then become diminished with the adhesion plaque growth. As the P229S variant situated in the F2 subdomain of the talin head, we engineered a mini-talin version (described in (Rahikainen et al., 2019)), for both WT and variant, which contains the head and the actin binding site R13-DD. For comparison, we also engineered a construct of only talin1 head for the WT and variant (Figure 16a, b). By assessing the co-localization of the pFAK, paxillin PY31 and activated β1-integrin, we saw a significant decrease in the levels of these adhesion markers in mini-talin P229S compared to mini-talin WT (Figure 16c).

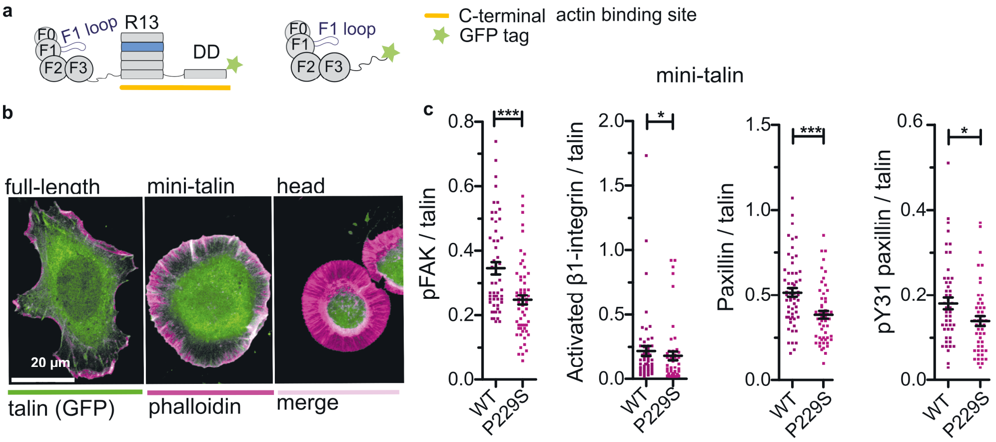

Figure 16. The point mutation P229S in minitalin causes early cell spreading and integrin mediated cell signalling. a) Schematic representation of the mini-talin (left) and talin head (right). b) Representative images of TLN1−/-TLN2−/− cells expressing full-length talin, mini-talin and talin head. Phalloidin staining is used to visualize the actin cytoskeleton. c) pTyr397 FAK/talin, activated β1-integrin/talin and total paxillin/talin and pY31 paxillin intensities ratios for the cells transfected with WT mini-talin or mini-talin P229S. n ~ 50 cells pooled from three independent experiments. The statistical analysis was done by Mann–Whitney t-test *$P < 0.05$, **$P < 0.01$, ***$P < 0.001$. Data represent the mean values with SEM. Figure adapted from publication III.

5.3 Biochemical characterization of talin proteins (I, II, III, IV)

Recombinant talin head forms (publications I, II) were characterized by size exclusion chromatography, differential scanning calorimetry (DSC), and biosensor analysis to determine their molecular weight, melting temperature and interaction with integrin. Chromatography analysis revealed a similar molecular size and hydrodynamic radius for the talin head full length mutants, suggesting that manipulation of the F1 loop did not change the folding of the protein. According to our DSC analysis, removing the F1 loop had a slight stabilizing effect indicated as higher melting temperature (Table 6). In the t1-405 (151-154AAAA) mutant, despite the presence of the full-size F1-loop, a decreased binding to the β3-integrin was seen in comparison to the F1-loop deleted construct, indicating that the F1 loop interferes with β3-integrin binding to some extent. The phosphomimetic F1 loop mutant talin

1-2541(T144E, T150E) activated β1-integrin less efficiently compared to wild type talin 1-2541 (Figure 6A in publication I), which also was consistent with reduced β3-integrin binding *in vitro* (Table 6).

Table 6. Characterization of talin head forms by high performance size exclusion chromatography (HPLC) obtaining retention volume (V_{ret} ml), molecular weight (MW_{SLS}) using static light scattering (SLS). R(h) is the hydrodynamic radius obtained from dynamic light scattering technique. Differential scanning calorimetry (DSC) was used for calculating melting temperature (T_m). Binding of integrin WT- β3 was quantified using an Octet biosensor to obtain the approximated Gibbs free energy of binding (ΔG_{app}) in $kJmol^{-1}$. $MW_{theor.}$ is the theoretical molecular weight of the talin construct (Publication I, II).

		HPLC			DSC	BLI WT-β3
talin	**$MW_{theor.}$**	**V_{ret}**	**MW_{SLS}**	**R(h) in DLS**	**T_m**	**$\Delta G_{app.}$**
t1-405	51.4	1.80	66.9	4.62 ±0.35	54.2 ±0.1	-27.1
t1-405 (del30)	47.8	1.90	65.3	4.48 ±0.30	55.4 ±0.1	-27.9
t1-405 (del37/GAG)	47.1	1.88	64.9	4.48 ±0.37	57.0 ±0.3	-29.1
t1-405 (T144E, T150E)	51.5	1.80	68.6	4.55 ±0.28	54.2 ±0.5	-24.1
t1-405 (T144E, T150E)	51.2	1.80	67.7	4.59 ±0.35	54.2 ±0.2	-26.3
T206-405	27.7	2.13	33.2	3.30 ±0.30	56.2 ±0.4	-40.3

In addition, the deletion of either the F0-F1 subdomains (t206-405) or only the F1 loop (t1-405 (del30)) enhanced talin head binding to the wild-type β3-integrin, but the phosphomimetic mutations (T144E, T150E) in the F1 loop reduced this binding, which suggests that the phosphorylation of the F1 loop can regulate the β3-F3 interactions.

In publication III, we selected the point mutations I392N, R1368W, Y1389C, L1539P and L2509P for further biochemical characterization. The recombinant protein expression of talin head WT and I392N (1-405) resulted in the purification of two separate fragment in the case of I392N. This suggest that destabilization of F3 leads to exposure of proteolytically sensitive regions. The R7-R8 fragment (1355-

1652) was used to investigate R1368W, Y1389C and L1539P mutations. In all three cases, *E. coli* protein expression was successful and no structural effect in the secondary structure was observed in comparison to the R7-R8 WT. However, the thermal melting point of R7-R8 Y1389C decreased to 45.5 °C in comparison to the R7-R8 WT (52 °C), indicating a lower thermal stability (Figure 17a). In addition, size exclusion chromatography showed that the R7-R8 Y1389C is able to bind two vinculin head (Vd1) molecules (Figure 6c in publication III), indicating a destabilization caused by the Y1389C mutation making the vinculin binding site (VBS) in R7 more accessible. In the control analysis, the wild-type R7-R8 showed binding of only one vinculin head (Figure 6c in publication III).

A previous study showed the contribution of the talin dimerization ability for F-actin binding, where a series of tested mutations were able to markedly reduce actin binding (Gingras et al., 2008). To better understand the physiochemical behaviour of the L2509P mutant, we designed the R13-DD WT (2300-2541) and R13-DD L2509P for protein expression in *E. coli*. Size exclusion chromatography with Multi-Angle Light Scattering (SEC-MALS) results showed the mutant to run as a monomer, confirming the disruption in talin dimerization (Figure 17b).

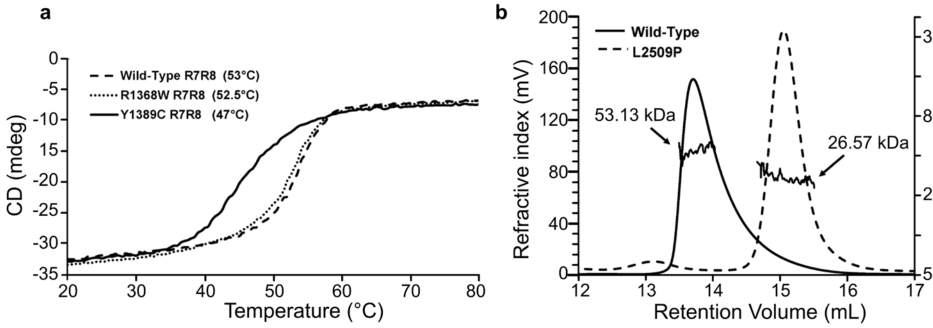

Figure 17. Influence of talin1 point mutations on the biophysical properties of the talin1 fragment. a) Melting temperature curves for each protein are shown. b) SEC–MALS analysis of R13–DD WT and R13–DD L2509P, showing that the R13–DD L2509P is monomeric. The molecular weight obtained from MALS is shown for each peak. Figure adapted from publication III.

6 DISCUSSION

6.1 FERM-folded talin induced integrin activation

Integrins and their activation are essential for the development and functioning of multicellular animals due to their key role in cell adhesion, cell migration and differentiation. Integrins are also critical in different pathological events such as inflammation, thrombosis, and tumour metastasis (Lowell and Mayadas, 2012). The activation of integrin is driven by intracellular association with talin and other ligands such as kindlin, stimulating inside-out integrin activation. This pathway is induced by interaction of RAP1-interacting-adapter-molecule (RIAM) with the talin head to mediate the translocation of talin to the plasma membrane (Wynne et al., 2012; Chang et al., 2014).

How does talin/integrin interaction lead to activation of integrin? A study using nuclear magnetic resonance (NMR) spectroscopic technique suggested the interaction between talin F3 and the membrane-proximal (MP) domain of β-tail region (Ulmer et al., 2003). Structural studies indicated that the mutations R358A and W359A in the F3 domain reduced talin F2-F3 biding to the integrin β3 tail (García-Alvarez et al., 2003). Functional studies of these two mutations in a cell model using HUVEC indicated that they either inhibit integrin binding (W359A) or its activation (L352R) (Kopp et al., 2010). Integrin β3 is connected by a salt bridge to the αIIb domain controlling integrin activation (Hughes et al., 1996; Anthis and Campbell, 2011). A study suggested that the putative salt bridge between αIIb(R995) and β3(D723) is disrupted by F3-MP interaction, which could prevent the formation of the salt bridge (Gottschalk, 2005). Our MD simulations suggested a direct talin-integrin contact mediated by residue D154 in the F1 loop, which competed with the residue D723 of β3 for binding to the residue R995 of αIIb (Figure 3 A-C in publication I). This finding suggests that talin contributes to integrin activation by catalysing the dissociation of integrin subunits *via* direct interaction.

There are tens of proteins binding directly to the short cytoplasmic tail of β-integrin, indicating a significant overlap between adaptor binding sites (Bachmann et al., 2019). Three distinct binding sites are preferred for most adaptors. 1) the HDRK/R motif 2) the NPxY motif and 3) the NxxY motif. The HDRK motif in β3 (HDRR in β1 and β5) binds to the Src-family kinase Fyn, FAK, skelemin and paxillin. In the inactive state of integrins, a salt bridge forms between the aspartate (D) residue in HDRK and the arginine (R) residue in the α-integrin tail of GFKR motif, which stabilizes the inactive state of the integrins. Nevertheless, the significance of the salt bridge depends on the integrins involved (Legate and Fässler, 2009). Interestingly, a previous study showed that mice expressing β1-integrin lacking the aspartate in the HDRK motif showed a normal phenotype (Czuchra et al., 2006), while a mutation in the arginine residue of the GFFKR motif in α4-integrin caused an abnormal phenotype (Imai et al., 2008). In addition, *in vitro* peptide binding studies have demonstrated additional sequences at the N-terminus of HDRK, which are activated and accessible upon integrin activation (Legate and Fässler, 2009). Even though some adaptors bind specifically to a specific site of integrin, for instance to the membrane-proximal NPxY motif, many other adaptors are non-selective. Some of the adapters can bind to several different integrin tails, e. g. adaptors binding to membrane-distal NxxY motifs. These adapter proteins experience sequence diversity: This sequence in β3-integrin is NITY and in β1-integrin NPKY (Calderwood et al., 2003).

Phosphorylation of the NxxY motifs acts as switch in favour of PTB-containing domains. For example, Oxley et al (Oxley et al., 2008) shown that while talin binds to a non-phosphorylated β3-integrin tail, upon phosphorylation of the Y773-residue in the NPxY motif DOK1 binds tightly, outcompeting talin from binding.

The importance of the talin head F1 loop has been emphasized in a previous study where it was proposed to either work through a "fly-casting mechanism" (Goult et al., 2010; Shoemaker et al., 2000) or *via* binding cationic regions of talin on the F2 and F3 subdomains to the membrane, where also the F1 loop associates (Kalli et al., 2013). When the F1 loop encounters a cluster of negatively charged phospholipids, it adopts a folded helical structure and residues on one side of the helix are bound to the membrane. This folding process causes a decrease in the apparent length of the loop, dragging the F1 subdomain closer to the membrane (Goult et al., 2010). As F1 brings the whole talin head closer to the membrane, also the interaction of F2 and F3 with acidic membrane phospholipids is facilitated. Our study showed that phosphomimetic mutations (T144E, T150E) in the F1 loop activated β1-integrin less efficiently, which was consistent with reduced talin head binding to the integrin β3 (publication I). Our results observed with the loss of kindlin-mediated control of integrin clustering by T144A/T150A mutations in the F1 loop are consistent with the results observed by (Katzemich et al., 2019) for the T152A mutant in *Drosophila,* indicating a link between the phosphorylation state of the F1 loop and kindlin. The phosphorylation of the F1 loop at T144/T150 may disrupt the membrane association of the talin head either by reducing the overall positive charge in the loop or by disrupting the helical formation of the loop (Goult et al., 2010).

A reduction in integrin activation and clustering caused by the phosphorylation of the F1 loop suggests that the F1 loop indeed controls integrin function (publication I). In all our talin-integrin-lipid simulations we noticed that the L152 residue of the LLRD151-154 of the F1 loop can enter into the hydrophobic core of the membrane. The LLRD stretch might help to guide the L154 or E155 residues to the membrane and even directly interact with integrin at the inner membrane clasp, suggesting that the F1 subdomain, and particularly the F1 loop, acts as "gate keeper" at the initial talin-integrin association step (Figure 4 in publication I).

6.1.1 The compact FERM-folded talin head

FERM domains are found in different proteins contributing to cellular signalling, and many of them function as adaptor proteins, such as FAK, JAK, kindlin and talin. They are located at the cytoplasmic plasma membrane with some variations in the linker region and loop insertions. Common to all FERM-like proteins is a cloverleaf conformation (Fehon et al., 2010). Based on C-terminally truncated versions of the talin head, Elliot et al. (Elliott et al., 2010) suggested three separate folded domains (F1, F2, F3) of the talin head in a compact cloverleaf structure, with the F0 domain packed against F1. It has been reported that the FERM domain of talin had a linear arrangement of four subdomains rather than a cloverleaf arrangement (Elliott et al., 2010; Campbell, 2010; Pearson et al., 2000). Our crystal structure of the talin-integrin interface revealed that the F3 α1-helix at the C-terminus (poly-lysine motif) interacts with F1, creating a groove for the accommodation of the integrin β3 N-P-L-Y motif. Further, the position of the F3 α1-helix was found to differ in F2-F3 or F3-only constructs, which potentially influences the integrin/ligand affinity (publication II). A study on the talin2 head domain (residues 1-400) revealed a semi-cloverleaf arrangement of the F0-F1-F2 subdomains in comparison to the canonical F1-F2-F3 FERM-like cloverleaf fold (Rangarajan et al., 2020). We noticed that the talin2 construct used in this study (1-403) was based on the linear form of the talin1 head structure (1-400) and was therefore also missing the C-terminal basic residues (i.e. the poly-lysine motif).

Our particle shape analysis of the full talin head (1-406) by EM revealed that the talin head adopts the FERM-folded configuration, but not the linear form (publication II). Crosslinking and SAXS data also suggested the compact FERM folding of the talin head with the F1 loop next to the integrin-binding site in the talin F3 subdomain (K316, K324 and L325) (Figure 5B in Publication I). In addition, we found that our FERM-folded talin head structure is compatible with the talin full length cryo-EM structure (PDB ID 6R9T) published by Dedden et al. (Dedden et al., 2019). Despite the F0-F1 segment of the talin head missing in the cryo-EM model (PDB ID 6R9T), the F2-F3 segment from our structure superimposed perfectly to the cryo-EM model without any structural conflict of our F0-F1 segment accommodation in the model (Figure S4D in Publication II).

In order for talin to control the outside-in and inside-out signalling of integrin, it folds into a canonical FERM configuration, providing a scaffold where talin binds to β-integrins, while stabilizing their activated state in a kindlin-dependent manner. It is interesting to notice that the talin and kindlin binding sites on the β3 tail are only about eight residues apart. As the full length talin head is tightly associated with the NPLY motif in β3-integrin, it restricts the flexibility of the proceeding kindlin-binding motif. So, when integrin binds simultaneously to talin and kindlin, a considerable interaction may also take place between talin and kindlin, forming a trimeric complex of β-integrin:talin:kindlin (Lu et al., 2022). Modification in either of these trimeric components may impact integrin signalling. We demonstrated that talin´s conserved FERM domain motifs at the F1-F2 interface (R194-D222, Q218) and the poly-lysine motif at the C-terminus of the F3 subdomain are important for sufficient integrin activation and clustering in collaboration with kindlin (Publication II).

There are still some questions to be answered, such as whether the FERM fold of the talin head is stable in solution and what controls its organization. Molecular modelling might solve the details, but most likely a multidisciplinary approach is needed to understand this complex process in detail, as demonstrated for example by Haining et al. 2016, who successfully combined the predictions of molecular dynamics simulations with atomic force microscopy to analyse mechanical stability of the talin rod domains (Haining et al., 2016b).

6.2 Effect of mutations on the structure and function of talin and its contribution to human diseases

The pathogenesis of numerous diseases such as angiogenesis, inflammation or infectious diseases involves integrin dysregulation. As examples, leukocyte adhesion deficiency (LAD) and Glanzmann's thrombasthenia are caused by multiple mutations in the β2 and αIIb/β3-integrins, respectively (Wickström et al., 2011). Integrins are not constantly active and in their inactive state do not bind ligands; instead their activity is regulated by a process called inside-out signalling. Cytoplasmic factors interacting with the cytoplasmic portion of the β-integrin tail initiate integrin activation (Gahmberg et al., 2009). Talin1 is recruited to integrins as primary transducer of mechanotransduction signals in both directions, inside-out and outside-in, influencing the composition of the actin network and focal adhesion (Anthis and Campbell, 2011; Schmidt et al., 1999; Zhang et al., 1996). Therefore, it can be expected that a talin variant causing a defect in integrin activation would also impact on all functions of integrin, such as cell adhesion, migration, invasion (publication I, III and IV) and apoptosis (Klann et al., 2017).

We studied the effect of talin1 point mutations on essential cellular behaviours such as cell movement, invasion, proliferation and interactions with other adhesion molecules. The point mutation I392N originally found from pancreatic carcinoma (screened from COSMIC database) had a pronounced effect on cell migration and invasion. Our results showed a clear decrease in the amount of integrin in the talin-rich adhesion sites of fibroblast cells with the mutant protein compared to the WT (Figure 15a, b). A study by Isenberg et al proposed that the amino acids 385-406 of the F3 helix form a potential membrane-anchoring domain with I392 as one of the residues inserting into the lipid bilayer (Isenberg et al., 2002), mediating integrin activation (Li et al., 2017a). Protein expression of the I392N variant in our biochemical experiments failed, indicating a folding defect in the C-terminal part of the protein.

R1368W, Y1389C and L1539P are point mutations situated in the R7-R8 subdomains, that were found in the top ten list of our COSMIC database screening results (Publication III). MD simulations suggested a transient interaction between the R7 and R8 subdomains over the course of 100 ns. Our MD simulation results further suggested, that the R1368W mutant in the R7 domain might enhance interaction between the R7 and R8 domains (Supplementary figure S2a, b in

Publication III). A previous study indicated a cooperative function of the R7-R8 domains, with R8 locating outside the force transduction and being protected by R7 from mechanical stress (Yao et al., 2016). In addition, most of the crystal structures obtained for the R7-R8 indicate an open conformation with limited contacts between the domains (Zacharchenko et al., 2016; Gingras et al., 2010; Chang et al., 2014). However, a crystal structure obtained by Cowell et al. from TLNRD1 (PDB:6XZ4) (Cowell et al., 2021), revealed a close association of the R7-R8 domains, supporting our findings that the two subdomains could interact. There are binding sites for multiple molecules (such as KANK1, DLC1, RIAM, paxillin and vinculin) in both domains (Yao et al., 2016). One possibility is that the interaction between R7 and R8 domains reduces the accessibility of ligand binding sites on the domains, which affects cell behaviour by disturbing the localization of FA proteins within the adhesion (Figure 4b, c in Publication III).

However, we found that the binding affinity of the R7-R8 R1368W mutant for KANK1 was not altered and instead was comparable with WT, suggesting that the cellular effect from this mutant was not due to an alteration in a known function of R7. As the role of the interaction is not fully clear and further investigations need to be done, it remains possible that the dynamics of the R7 and R8 domains are altered by the R1368W mutation, causing the cellular phenotype observed in our experiment (Figure 13a).

Our gel filtration analysis showed that R7-R8 R1368W binds a single Vd1 molecule, while R7-R8 Y1389C was able to bind two Vd1 molecules (Publication III). Previous studies suggested that the VBS in R7 is one of the hardest to expose (Gingras et al., 2010), but can be stretch-activated (Yao et al., 2016). The R7-R8 Y1389C mutation seemed to destabilise the R7 helical bundle and therefore to allow vinculin binding more easily in the absence of force. Reduced R7 stability causes a "butterfly" effect on R8 stability, which indirectly leads to signalling defects caused *via* perturbances of R8 (Haining et al., 2018). Facilitating the formation of talin-vinculin pre-complexes necessary for efficient adhesion maturation and additional actin recruitment *via* vinculin could also have a direct effect on FA dynamics (Han et al., 2021a). This could affect actomyosin contractility and Rho/ROCK signalling, which have been shown to regulate cell proliferation (Kümper et al., 2016).

The colocalization of L1539P with DLC-1 in fibroblast cells transfected with this mutant was significantly decreased compared to WT talin, although we observed similar protein expression levels (Figure 15c). DLC-1 is known as a tumour suppressor (Durkin et al., 2007) containing an LD-like motif, that mediates the complete tumour suppressor activity *via* interaction with talin (Li et al., 2017a). The residue D470 in DLC-1 makes a direct contact with the positively charged side chain of K1530 and K1544 in talin R8 (Zacharchenko et al., 2016). Moreover, the R7-R8 fragment carrying the mutation L1539P was difficult to produce as a recombinant protein, suggesting that this mutation destabilised the corresponding talin domain.

One of the most interesting talin1 mutations in publication III was the L2509P point mutation situated at the dimerization domain of talin1. This mutation resulted in an unpolarised and non-migratory cell phenotype in addition to a lack of mature FAs and actin contacts on the cell surface. Interestingly, the same phenotype was observed after complete removal of the dimerisation domain (ΔDD) or actin binding site (ΔR13DD) (Figure 14). A previous study showed that the linkage between the C-terminal actin-binding site, ABS3, and actin is necessary for cell polarisation (Rahikainen et al., 2019), a process dependent on talin dimerisation (Goult et al., 2013b). Wang et al. detected cell cycle deficiency and the absence of pY397 FAK in talin-depleted epithelial cells, which could be rescued with the expression of a C-terminal talin fragment (Wang et al., 2011). Our biochemical results indicate that the R13-DD L2509P mutant causes the complete loss of dimerisation compared to the R13-DD WT (Figure 17b).

6.3 Why to investigate talin1?

The contribution of talin to cancer progression is recognized more and more. 368 talin1 mutations were found in the COSMIC database in January 2017, from which 258 missense mutations were chosen for further screening using bioinformatic tools. During the time until the acceptance of the study for publication in November 2020, ~670 more cancer-associated talin1 mutations have been added to the COSMIC database, with ~420 being missense mutations. Until September 2022, ~85 more mutations have been added to the list. However, the total number of talin1 cancer-associated missense mutations and the recurrence of the selected top ten missense mutations remain unchanged in the last years. Nevertheless, new talin1 point mutations have been found to be associated with other diseases, e. g. the mutation P229S discovered from the whole exome sequencing of a young patient with multifaceted illness (publication IV).

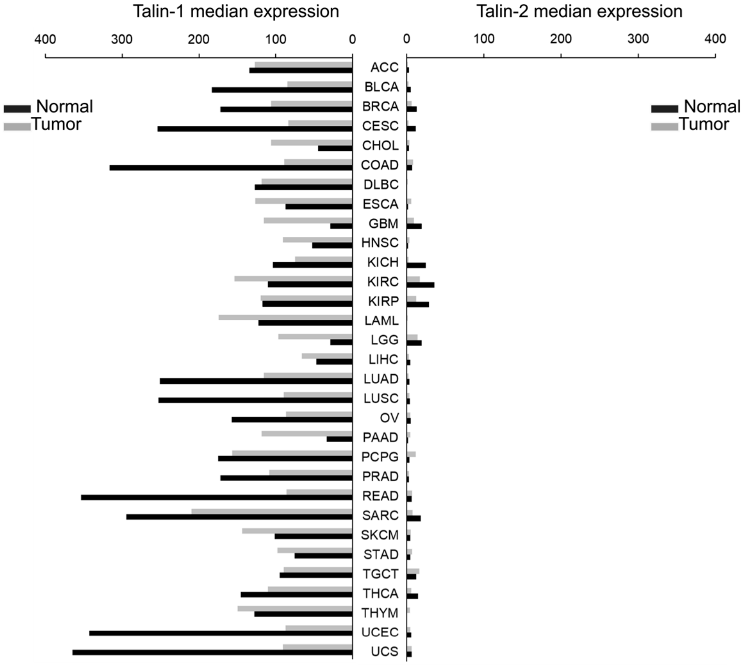

ACC Adrenocortical carcinoma
BLCA Bladder Urothelial Carcinoma
BRCA Breast invasive carcinoma
CESC Cervical squamous cell carcinoma and endocervical adenocarcinoma
CHOL Cholangiocarcinoma
COAD Colon adenocarcinoma
DLBC Lymphoid Neoplasm Diffuse Large B-cell Lymphoma
ESCA Esophageal carcinoma
GBM Glioblastoma multiforme
HNSC Head and Neck squamous cell carcinoma
KICH Kidney Chromophobe
KIRC Kidney renal clear cell carcinoma
KIRP Kidney renal papillary cell carcinoma
LAML Acute Myeloid Leukemia
LGG Brain Lower Grade Glioma
LIHC Liver hepatocellular carcinoma
LUAD Lung adenocarcinoma
LUSC Lung squamous cell carcinoma
MESO Mesothelioma
OV Ovarian serous cystadenocarcinoma
PAAD Pancreatic adenocarcinoma
PCPG Pheochromocytoma and Paraganglioma
PRAD Prostate adenocarcinoma
READ Rectum adenocarcinoma
SARC Sarcoma
SKCM Skin Cutaneous Melanoma
STAD Stomach adenocarcinoma
TGCT Testicular Germ Cell Tumours
THCA Thyroid carcinoma
THYM Thymoma
UCEC Uterine Corpus Endometrial Carcinoma
UCS Uterine Carcinosarcoma
UVM Uveal Melanoma

Figure 18. Talin1 and talin2 gene expression profiles across tumour and paired normal samples. Expression levels are taken from the GEPIA database. At the time of analysis GEPIA contained 9662 tumour and 5540 normal samples across 33 cancer types.

The two isoforms of talin have different expression patterns (Debrand et al., 2009; Gough and Goult, 2018). Talin1 is expressed almost in all tissues, while talin2 has lower expression levels and more variability between tissues. We investigated the overall expression levels of the two talin isoforms on the GEPIA (gene expression profiling interactive analysis) server (Tang et al., 2017), finding that talin1 expression levels differ more between different cancers and their counterpart healthy tissues than those of talin2 (Figure 18). We found the highest overexpression to be associated with glioblastomas (GBM; > 300%), brain gliomas (LGG; > 300%) and pancreatic adenocarcinomas (PAAD; > 300%). In contrast, the most drastic talin1 downregulation was seen in uterine carcinoma (UCS; −25%) and endometrial carcinoma of the uterine (UCEC; –25%).

6.4 The coordinated interaction of talin, integrin and the membrane is essential for integrin activation and focal adhesion formation

The talin F3 domain forms a unique and well-defined complex with the membrane proximal region of the β-integrin tail, which is important for the molecular recognition required for integrin activation. The mutation L325R in talin F3 caused an altered cell functionality, completely inhibiting integrin β3 activation and leading to hemostasis in mouse. The W359A mutation had a decreasing effect on integrin activation in platelets, protecting mice from thrombosis (Stefanini et al., 2014). Having this in mind, Bouaouina et al. proved that neither talin F3 nor F2-F3 on their own are sufficient for full integrin β1 activation, and the entire talin head F0-F3 (including the F1-loop (publication I)) is required for the maximal integrin activation (Bouaouina et al., 2008). The F2-F3 domain has been reported to be important due to its membrane orientation patch (MOP), which binds tightly to the plasma membrane (Figure 19a, b). This patch comprises of the residues K256, K272, K274 and R277.

Anthis et al. reported that upon F3 domain binding to integrin, the F2-F3 module rotates at a 20° rotation angle to engage the MOP at the plasma membrane (Figure 19c). This rotation stabilizes the active conformation of integrin. Therefore, mutations in the MOP region alter or prevent integrin activation (Anthis et al., 2009).

We hypothesized that the talin1 P229S point mutation (publication IV) disturbs the coupling between F2-F3 domains, resulting in perturbed rotation of F2 to engage talin1 head with membrane. We believe that the decoupling of membrane binding and integrin binding disrupt the regulation of integrin activation, when the P229S mutation is present in talin1. Moreover, our biophysical studies of the protein's F2-F3 subdomain suggest that the P229S mutation causes a subtle loss of synergy between the F2-F3 domains, manifesting in minor disruptions of cellular processes.

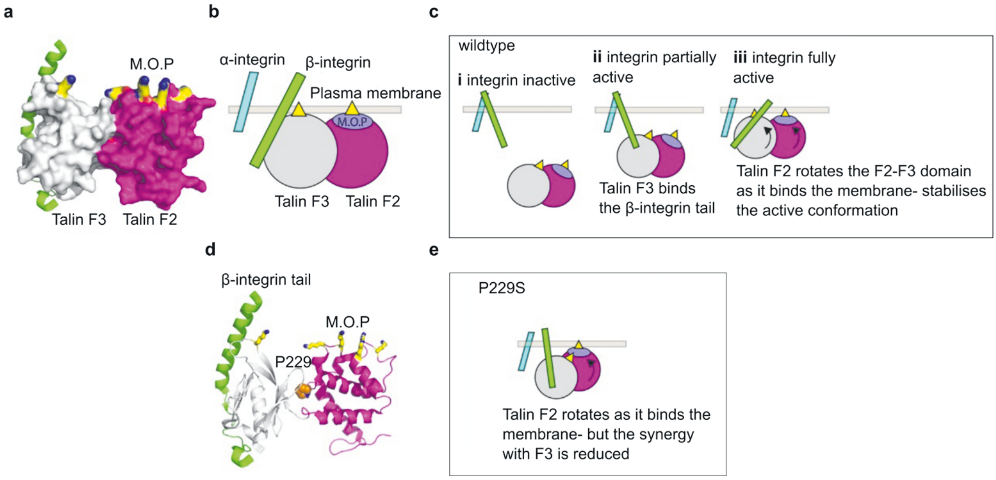

Figure 19. Proposed model for P229 function in the synergistic coordination of the talin-integrin-plasma membrane interactions. a,b) Surface representation of the F2-F3 subdomains showing P229 to be buried in the F2-F3 interface. The negatively charged plasma membrane is shown to illustrate the tripartite interaction between talin F2-F3 (a), β-integrin and the plasma membrane, that needs to occur for robust integrin activation (b). c) Model of the integrin activation process mediated *via* the F2-F3 domains, based on the model proposed by (Anthis et al., 2009). (i) Integrins exist in an inactive state in the absence of talin binding. (ii, iii) The F2-F3 double domain module inextricably links integrin binding to membrane binding. To simultaneously optimize the interactions of both F3-integrin and F2-membrane, the F2-F3 module needs to undergo a 20° rotation, and this torque (iii) is thought to help lock integrin in the active conformation. d) Cartoon of the F2-F3 domains bound to the β-integrin cytoplasmic domain (green). The location of proline 229 (orange) in the interface between F2 and F3 is shown. The basic residues in the membrane orientation patch (MOP) on F2 (yellow) are highlighted. e) The P229S mutation disrupts the tight apposition of F2 and F3 and uncouples the tight interplay between integrin and membrane binding. With the two domains able to move independently, the optimization of the F2-membrane interface no longer exerts torque onto the F3–integrin interaction, perturbing the tight regulation of the talin-mediated integrin dynamics.

However, at the organismal level, we envision that the P229S variant impacts all integrin processes that are talin-dependent and thus interrupt the fine-tuned balance of integrin dynamics. Our case study patient (publication IV) experienced multiple immune system-related defects, which could be explained by disturbed integrin function. Indeed, cell biology experiments revealed a decrease in activated β1-integrin levels within cell adhesions caused by the mutation (Figure 16). Our case study emphasizes the mutation P229S as a variant of uncertain significance due to lack of evidence explaining the multitude symptoms of the patient. Therefore, additional cases with similar variants need to be identified to confirm the association with disease. In any case, our study emphasizes the central role of talin as a link between cytoskeleton and extracellular environment.

Here we have proved the important role of talin as a link between integrin and cytoskeleton, controlling cell movement and regulating interactions with other adhesome components. Although we have progressed in the study of structure-function of talin, also revealed new questions for future research, for example: What are the similarities and differences in the roles of talin in different cell lines? How does talin function when cells experience different environments, such as soft or stiff tissue?

One of the broader challenges in our study was to understand talin role in its physiological context. The simplified 2D surfaces has been commonly used in microscopy and although it has been criticized, it still provide underlying principles and insights to understand talin´s function in more complex *in vivo* system. The tools and approaches which reflex or make it possible to study cell function in more physiological context or in living organism are becoming more available, for example the possibilities are reviewed by Allen et al (Allen et al., 2023). A deeper understanding using new methods might be necessary to effectively treat human diseases.

7 CONCLUSIONS AND FUTURE ASPECTS

Talin binding to the cytoplasmic tail of β-integrin and the role of talin in integrin activation has provided an important focus point in research aiming to understand the regulation of cell adhesion, cell migration and assembly of the ECM.

The central novel conclusions in this thesis can be presented as following:

- The F1 loop in the talin head domain directly interacts with β3-integrin and contributes to integrin clustering. This interaction was confirmed by MD simulations and chemical crosslinking.
- The talin head possesses structural flexibility, and the C-terminal poly-lysine motif of the F3 domain mediates an interdomain contact within the talin head, supporting a compact tertiary structure. This conformation has a significant role in integrin activation and clustering.
- Bioinformatic tools enabled us to systematically explore hundreds of talin-associated mutations from human disease-associated databases to identify the most prominent mutants causing functional defects.
- A point mutation in talin can have drastic effects on the most vital cell functions such as migration and proliferation by interfering with integrin activation and ligand interactions.

Changes in talin expression have been associated with several diseases, thus it is quite possible that talin mutations predisposing to various diseases will be detected in the future. The results of my PhD thesis may be valuable for the development of bioinformatic, biochemical and cell biology methods helping to characterize novel mutants.

8 REFERENCES

Abraham, M. J., Murtola, T., Schulz, R., Páll, S., Smith, J. C., Hess, B. and Lindahl, E. (2015). GROMACS: High performance molecular simulations through multi-level parallelism from laptops to supercomputers. *SoftwareX* **1–2**, 19–25.

Alahari, S. K., Reddig, P. J. and Juliano, R. L. (2002). Biological aspects of signal transduction by cell adhesion receptors. *Int. Rev. Cytol.* **220**, 145–184.

Allen, S. L., Elliott, B. T., Carson, B. P. and Breen, L. (2023). Improving physiological relevance of cell culture: the possibilities, considerations, and future directions of the ex vivo coculture model. *Am. J. Physiol. - Cell Physiol.* **324**, C420–C427.

Anthis, N. J. and Campbell, I. D. (2011). The tail of integrin activation. *Trends Biochem. Sci.* **36**, 191–198.

Anthis, N. J., Wegener, K. L., Ye, F., Kim, C., Goult, B. T., Lowe, E. D., Vakonakis, I., Bate, N., Critchley, D. R., Ginsberg, M. H., et al. (2009). The structure of an integrin/talin complex reveals the basis of inside-out signal transduction. *EMBO J.* **28**, 3623–3632.

Aoyama, M., Kishimoto, Y., Saita, E., Ikegami, Y., Ohmori, R., Nakamura, M., Kondo, K. and Momiyama, Y. (2020). High Plasma Levels of Soluble Talin-1 in Patients with Coronary Artery Disease. *Dis. Markers* **2020**, 2479830.

Ashkenazy, H., Abadi, S., Martz, E., Chay, O., Mayrose, I., Pupko, T. and Ben-Tal, N. (2016). ConSurf 2016: an improved methodology to estimate and visualize evolutionary conservation in macromolecules. *Nucleic Acids Res.* **44**, W344-350.

Atherton, P., Stutchbury, B., Wang, D.-Y., Jethwa, D., Tsang, R., Meiler-Rodriguez, E., Wang, P., Bate, N., Zent, R., Barsukov, I. L., et al. (2015). Vinculin controls talin engagement with the actomyosin machinery. *Nat. Commun.* **6**, 10038.

Atherton, P., Konstantinou, R., Neo, S. P., Wang, E., Balloi, E., Ptushkina, M., Bennett, H., Clark, K., Gunaratne, J., Critchley, D., et al. (2022). Tensin3 interaction with talin drives the formation of fibronectin-associated fibrillar adhesions. *J. Cell Biol.* **221**, e202107022.

Aureille, J., Barnett, S. F. H., Arnal, I., Lafanechère, L., Low, B. C., Kanchanawong, P., Mogilner, A. and Bershadsky, A. D. (2023). Focal adhesions are controlled by microtubules through local contractility regulation. 2023.04.17.535593.

Bachir, A. I., Zareno, J., Moissoglu, K., Plow, E. F., Gratton, E. and Horwitz, A. R. (2014). Integrin-associated complexes form hierarchically with variable stoichiometry in nascent adhesions. *Curr. Biol. CB* **24**, 1845–1853.

Bachmann, M., Kukkurainen, S., Hytönen, V. P. and Wehrle-Haller, B. (2019). Cell Adhesion by Integrins. *Physiol. Rev.* **99**, 1655–1699.

Bachmann, M., Schäfer, M., Mykuliak, V. V., Ripamonti, M., Heiser, L., Weißenbruch, K., Krübel, S., Franz, C. M., Hytönen, V. P., Wehrle-Haller, B., et al. (2020). Induction of ligand promiscuity of αVβ3 integrin by mechanical force. *J. Cell Sci.* **133**, jcs242404.

Badowski, C., Pawlak, G., Grichine, A., Chabadel, A., Oddou, C., Jurdic, P., Pfaff, M., Albigès-Rizo, C. and Block, M. R. (2008). Paxillin Phosphorylation Controls Invadopodia/Podosomes Spatiotemporal Organization. *Mol. Biol. Cell* **19**, 633–645.

Banno, A., Goult, B. T., Lee, H., Bate, N., Critchley, D. R. and Ginsberg, M. H. (2012). Subcellular localization of talin is regulated by inter-domain interactions. *J. Biol. Chem.* **287**, 13799–13812.

Barber-Pérez, N., Georgiadou, M., Guzmán, C., Isomursu, A., Hamidi, H. and Ivaska, J. (2020). Mechano-responsiveness of fibrillar adhesions on stiffness-gradient gels. *J. Cell Sci.* **133**, jcs242909.

Barczyk, M., Carracedo, S. and Gullberg, D. (2010). Integrins. *Cell Tissue Res.* **339**, 269–280.

Bear, J. E. and Haugh, J. M. (2014). Directed migration of mesenchymal cells: where signaling and the cytoskeleton meet. *Curr. Opin. Cell Biol.* **30**, 74–82.

Bialkowska, K., Ma, Y.-Q., Bledzka, K., Sossey-Alaoui, K., Izem, L., Zhang, X., Malinin, N., Qin, J., Byzova, T. and Plow, E. F. (2010). The integrin co-activator Kindlin-3 is expressed and functional in a non-hematopoietic cell, the endothelial cell. *J. Biol. Chem.* **285**, 18640–18649.

Bijian, K., Lougheed, C., Su, J., Xu, B., Yu, H., Wu, J. H., Riccio, K. and Alaoui-Jamali, M. A. (2013). Targeting focal adhesion turnover in invasive breast cancer cells by the purine derivative reversine. *Br. J. Cancer* **109**, 2810–2818.

Bivona, T. G., Wiener, H. H., Ahearn, I. M., Silletti, J., Chiu, V. K. and Philips, M. R. (2004). Rap1 up-regulation and activation on plasma membrane regulates T cell adhesion. *J. Cell Biol.* **164**, 461–470.

Bogatan, S., Cevik, D., Demidov, V., Vanderploeg, J., Panchbhaya, A., Vitkin, A. and Jacobs, J. R. (2015). Talin Is Required Continuously for Cardiomyocyte Remodeling during Heart Growth in Drosophila. *PloS One* **10**, e0131238.

Bonnans, C., Chou, J. and Werb, Z. (2014). Remodelling the extracellular matrix in development and disease. *Nat. Rev. Mol. Cell Biol.* **15**, 786–801.

Böttcher, R. T., Veelders, M., Rombaut, P., Faix, J., Theodosiou, M., Stradal, T. E., Rottner, K., Zent, R., Herzog, F. and Fässler, R. (2017). Kindlin-2 recruits paxillin and Arp2/3 to promote membrane protrusions during initial cell spreading. *J. Cell Biol.* **216**, 3785–3798.

Bouaouina, M., Lad, Y. and Calderwood, D. A. (2008). The N-terminal domains of talin cooperate with the phosphotyrosine binding-like domain to activate beta1 and beta3 integrins. *J. Biol. Chem.* **283**, 6118–6125.

Bouaouina, M., Goult, B. T., Huet-Calderwood, C., Bate, N., Brahme, N. N., Barsukov, I. L., Critchley, D. R. and Calderwood, D. A. (2012). A conserved lipid-binding loop in the kindlin FERM F1 domain is required for kindlin-mediated αIIbβ3 integrin coactivation. *J. Biol. Chem.* **287**, 6979–6990.

Brahmbhatt, A. A. and Klemke, R. L. (2003). ERK and RhoA differentially regulate pseudopodia growth and retraction during chemotaxis. *J. Biol. Chem.* **278**, 13016–13025.

Bromberger, T., Zhu, L., Klapproth, S., Qin, J. and Moser, M. (2019). Rap1 and membrane lipids cooperatively recruit talin to trigger integrin activation. *J. Cell Sci.* **132**, jcs235531.

Bromberger, T., Klapproth, S., Rohwedder, I., Weber, J., Pick, R., Mittmann, L., Min-Weißenhorn, S. J., Reichel, C. A., Scheiermann, C., Sperandio, M., et al. (2021). Binding of Rap1 and Riam to Talin1 Fine-Tune β2 Integrin Activity During Leukocyte Trafficking. *Front. Immunol.* **12**, 702345.

Brown, N. H., Gregory, S. L., Rickoll, W. L., Fessler, L. I., Prout, M., White, R. A. H. and Fristrom, J. W. (2002). Talin is essential for integrin function in Drosophila. *Dev. Cell* **3**, 569–579.

Buccione, R., Orth, J. D. and McNiven, M. A. (2004). Foot and mouth: podosomes, invadopodia and circular dorsal ruffles. *Nat. Rev. Mol. Cell Biol.* **5**, 647–657.

Bulus, N., Brown, K. L., Mernaugh, G., Böttcher, A., Dong, X., Sanders, C. R., Pozzi, A., Fässler, R. and Zent, R. (2021). Disruption of the integrin-linked kinase (ILK) pseudokinase domain affects kidney development in mice. *J. Biol. Chem.* **296**, 100361.

Burridge, K. and Connell, L. (1983). Talin: a cytoskeletal component concentrated in adhesion plaques and other sites of actin-membrane interaction. *Cell Motil.* **3**, 405–417.

Calderwood, D. A. (2004). Integrin activation. *J. Cell Sci.* **117**, 657–666.

Calderwood, D. A., Zent, R., Grant, R., Rees, D. J., Hynes, R. O. and Ginsberg, M. H. (1999). The Talin head domain binds to integrin beta subunit cytoplasmic tails and regulates integrin activation. *J. Biol. Chem.* **274**, 28071–28074.

Calderwood, D. A., Yan, B., Pereda, J. M., Alvarez, B. G., Fujioka, Y., Liddington, R. C. and Ginsberg, M. H. (2002). The phosphotyrosine binding-like domain of talin activates integrins. *J. Biol. Chem.* **277**, 21749–21758.

Calderwood, D. A., Fujioka, Y., Pereda, J. M., García-Alvarez, B., Nakamoto, T., Margolis, B., McGlade, C. J., Liddington, R. C. and Ginsberg, M. H. (2003). Integrin beta cytoplasmic domain interactions with phosphotyrosine-binding domains: a structural prototype for diversity in integrin signaling. *Proc. Natl. Acad. Sci. U. S. A.* **100**, 2272–2277.

Calderwood, D. A., Campbell, I. D. and Critchley, D. R. (2013). Talins and kindlins: partners in integrin-mediated adhesion. *Nat. Rev. Mol. Cell Biol.* **14**, 503–517.

Campbell, I. D. (2010). The talin FERM domain is not so FERM. *Struct. Lond. Engl. 1993* **18**, 1222–1223.

Carmona-Fontaine, C., Matthews, H. and Mayor, R. (2008). Directional cell migration in vivo: Wnt at the crest. *Cell Adhes. Migr.* **2**, 240–242.

Case, L. B. and Waterman, C. M. (2015). Integration of actin dynamics and cell adhesion by a three-dimensional, mechanosensitive molecular clutch. *Nat. Cell Biol.* **17**, 955–963.

Caswell, P. T. and Zech, T. (2018). Actin-Based Cell Protrusion in a 3D Matrix. *Trends Cell Biol.* **28**, 823–834.

Chakraborty, S., Chaudhuri, D., Banerjee, S., Bhatt, M. and Haldar, S. (2022). Direct observation of chaperone-modulated talin mechanics with single-molecule resolution. *Commun. Biol.* **5**, 1–14.

Chang, Y.-C., Zhang, H., Franco-Barraza, J., Brennan, M. L., Patel, T., Cukierman, E. and Wu, J. (2014). Structural and mechanistic insights into the recruitment of talin by RIAM in integrin signaling. *Struct. Lond. Engl. 1993* **22**, 1810–1820.

Chang, Y.-C., Su, W., Cho, E.-A., Zhang, H., Huang, Q., Philips, M. R. and Wu, J. (2019). Molecular basis for autoinhibition of RIAM regulated by FAK in integrin activation. *Proc. Natl. Acad. Sci. U. S. A.* **116**, 3524–3529.

Changede, R., Xu, X., Margadant, F. and Sheetz, M. P. (2015). Nascent Integrin Adhesions Form on All Matrix Rigidities after Integrin Activation. *Dev. Cell* **35**, 614–621.

Cheah, M. and Andrews, M. R. (2018). Integrin Activation: Implications for Axon Regeneration. *Cells* **7**, 20.

Chen, H. C., Appeddu, P. A., Parsons, J. T., Hildebrand, J. D., Schaller, M. D. and Guan, J. L. (1995). Interaction of focal adhesion kinase with cytoskeletal protein talin. *J. Biol. Chem.* **270**, 16995–16999.

Chen, H., Choudhury, D. M. and Craig, S. W. (2006). Coincidence of actin filaments and talin is required to activate vinculin. *J. Biol. Chem.* **281**, 40389–40398.

Chen, Z.-L., Haegeli, V., Yu, H. and Strickland, S. (2009). Cortical deficiency of laminin gamma1 impairs the AKT/GSK-3beta signaling pathway and leads to defects in neurite outgrowth and neuronal migration. *Dev. Biol.* **327**, 158–168.

Chen, P., Lei, L., Wang, J., Zou, X., Zhang, D., Deng, L. and Wu, D. (2017). Downregulation of Talin1 promotes hepatocellular carcinoma progression through activation of the ERK1/2 pathway. *Cancer Sci.* **108**, 1157–1168.

Chen, Y., Ju, L. A., Zhou, F., Liao, J., Xue, L., Su, Q. P., Jin, D., Yuan, Y., Lu, H., Jackson, S. P., et al. (2019). An integrin αIIbβ3 intermediate affinity state mediates biomechanical platelet aggregation. *Nat. Mater.* **18**, 760–769.

Chinthalapudi, K., Rangarajan, E. S. and Izard, T. (2018). The interaction of talin with the cell membrane is essential for integrin activation and focal adhesion formation. *Proc. Natl. Acad. Sci.* **115**, 10339–10344.

Ciobanasu, C., Faivre, B. and Le Clainche, C. (2012). Actin dynamics associated with focal adhesions. *Int. J. Cell Biol.* **2012**, 941292.

Ciobanasu, C., Wang, H., Henriot, V., Mathieu, C., Fente, A., Csillag, S., Vigouroux, C., Faivre, B. and Le Clainche, C. (2018). Integrin-bound talin head inhibits actin filament barbed-end elongation. *J. Biol. Chem.* **293**, 2586–2596.

Clark, K., Howe, J. D., Pullar, C. E., Green, J. A., Artym, V. V., Yamada, K. M. and Critchley, D. R. (2010). Tensin 2 modulates cell contractility in 3D collagen gels through the RhoGAP DLC1. *J. Cell. Biochem.* **109**, 808–817.

Conti, F. J., Monkley, S. J., Wood, M. R., Critchley, D. R. and Müller, U. (2009). Talin 1 and 2 are required for myoblast fusion, sarcomere assembly and the maintenance of myotendinous junctions. *Development* **136**, 3597–3606.

Cowell, A. R., Jacquemet, G., Singh, A. K., Varela, L., Nylund, A. S., Ammon, Y.-C., Brown, D. G., Akhmanova, A., Ivaska, J. and Goult, B. T. (2021). Talin rod domain-containing protein 1 (TLNRD1) is a novel actin-bundling protein which promotes filopodia formation. *J. Cell Biol.* **220**, e202005214.

Cram, E. J., Clark, S. G. and Schwarzbauer, J. E. (2003). Talin loss-of-function uncovers roles in cell contractility and migration in C. elegans. *J. Cell Sci.* **116**, 3871–3878.

Cramer, L. P. (2013). Mechanism of cell rear retraction in migrating cells. *Curr. Opin. Cell Biol.* **25**, 591–599.

Crowe, D. L. and Ohannessian, A. (2004). Recruitment of focal adhesion kinase and paxillin to beta1 integrin promotes cancer cell migration via mitogen activated protein kinase activation. *BMC Cancer* **4**, 18.

Cuesta, F., Zubiri, I., Maroto, A. S., Posada, M., Padial, L. R., Vivanco, F., Alvarez-Llamas, G. and Barderas, M. G. (2013). Deregulation of smooth muscle cell cytoskeleton within the human atherosclerotic coronary media layer. *J. Proteomics* **82**, 155–165.

Czuchra, A., Meyer, H., Legate, K. R., Brakebusch, C. and Fässler, R. (2006). Genetic analysis of β1 integrin "activation motifs" in mice. *J. Cell Biol.* **174**, 889–899.

Dahal, N., Sharma, S., Phan, B., Eis, A. and Popa, I. (2022). Mechanical regulation of talin through binding and history-dependent unfolding. *Sci. Adv.* **8**, eabl7719.

Dang, I. and Gautreau, A. (2018). Random Migration Assays of Mammalian Cells and Quantitative Analyses of Single Cell Trajectories. *Methods Mol. Biol. Clifton NJ* **1749**, 1–9.

Debrand, E., El Jai, Y., Spence, L., Bate, N., Praekelt, U., Pritchard, C. A., Monkley, S. J. and Critchley, D. R. (2009). Talin 2 is a large and complex gene encoding multiple transcripts and protein isoforms. *FEBS J.* **276**, 1610–1628.

Debrand, E., Conti, F. J., Bate, N., Spence, L., Mazzeo, D., Pritchard, C. A., Monkley, S. J. and Critchley, D. R. (2012). Mice carrying a complete deletion of the talin2 coding sequence are viable and fertile. *Biochem. Biophys. Res. Commun.* **426**, 190–195.

Dedden, D., Schumacher, S., Kelley, C. F., Zacharias, M., Biertümpfel, C., Fässler, R. and Mizuno, N. (2019). The Architecture of Talin1 Reveals an Autoinhibition Mechanism. *Cell* **179**, 120-131.e13.

Delcommenne, M., Tan, C., Gray, V., Rue, L., Woodgett, J. and Dedhar, S. (1998). Phosphoinositide-3-OH kinase-dependent regulation of glycogen synthase kinase 3 and protein kinase B/AKT by the integrin-linked kinase. *Proc. Natl. Acad. Sci. U. S. A.* **95**, 11211–11216.

Desiniotis, A. and Kyprianou, N. (2011). Significance of talin in cancer progression and metastasis. *Int. Rev. Cell Mol. Biol.* **289**, 117–147.

Di Paolo, G., Pellegrini, L., Letinic, K., Cestra, G., Zoncu, R., Voronov, S., Chang, S., Guo, J., Wenk, M. R. and De Camilli, P. (2002). Recruitment and regulation of phosphatidylinositol phosphate kinase type 1 gamma by the FERM domain of talin. *Nature* **420**, 85–89.

Do, P. A. and Lee, C. H. (2020). The Role of CDK5 in Tumours and Tumour Microenvironments. *Cancers* **13**, 101.

Durkin, M. E., Yuan, B.-Z., Zhou, X., Zimonjic, D. B., Lowy, D. R., Thorgeirsson, S. S. and Popescu, N. C. (2007). DLC-1:a Rho GTPase-activating protein and tumour suppressor. *J. Cell. Mol. Med.* **11**, 1185–1207.

Elefant, N., Nikolopoulou, P. A., Papadaki, V. V., Oz-Levi, D., Rouni, G., Sion-Sarid, R., Edwards, W. J., Arapatzi, C., Yanovsky-Dagan, S., Cowell, A. R., et al. (2022). Talin1 dysfunction is genetically linked to systemic capillary leak syndrome. 2022.10.17.22280833.

Elliott, P. R., Goult, B. T., Kopp, P. M., Bate, N., Grossmann, J. G., Roberts, G. C. K., Critchley, D. R. and Barsukov, I. L. (2010). The Structure of the talin head reveals a novel extended conformation of the FERM domain. *Struct. Lond. Engl. 1993* **18**, 1289–1299.

Ellis, S. J., Goult, B. T., Fairchild, M. J., Harris, N. J., Long, J., Lobo, P., Czerniecki, S., Van Petegem, F., Schöck, F., Peifer, M., et al. (2013). Talin autoinhibition is required for morphogenesis. *Curr. Biol. CB* **23**, 1825–1833.

Fang, K.-P., Dai, W., Ren, Y.-H., Xu, Y.-C., Zhang, S.-M. and Qian, Y.-B. (2016). Both Talin-1 and Talin-2 correlate with malignancy potential of the human hepatocellular carcinoma MHCC-97 L cell. *BMC Cancer* **16**, 45.

Fehon, R. G., McClatchey, A. I. and Bretscher, A. (2010). Organizing the cell cortex: the role of ERM proteins. *Nat. Rev. Mol. Cell Biol.* **11**, 276–287.

Fornaro, M., Manes, T. and Languino, L. R. (2001). Integrins and prostate cancer metastases. *Cancer Metastasis Rev.* **20**, 321–331.

Friedl, P. (2004). Prespecification and plasticity: shifting mechanisms of cell migration. *Curr. Opin. Cell Biol.* **16**, 14–23.

Fröbel, J., Cadeddu, R.-P., Hartwig, S., Bruns, I., Wilk, C. M., Kündgen, A., Fischer, J. C., Schroeder, T., Steidl, U. G., Germing, U., et al. (2013). Platelet proteome analysis reveals integrin-dependent aggregation defects in patients with myelodysplastic syndromes. *Mol. Cell. Proteomics MCP* **12**, 1272–1280.

Fukuda, K., Bledzka, K., Yang, J., Perera, H. D., Plow, E. F. and Qin, J. (2014). Molecular basis of kindlin-2 binding to integrin-linked kinase pseudokinase for regulating cell adhesion. *J. Biol. Chem.* **289**, 28363–28375.

Gahmberg, C. G., Fagerholm, S. C., Nurmi, S. M., Chavakis, T., Marchesan, S. and Grönholm, M. (2009). Regulation of integrin activity and signalling. *Biochim. Biophys. Acta* **1790**, 431–444.

Gallego-Paez, L. M. and Mauer, J. (2022). DJExpress: An Integrated Application for Differential Splicing Analysis and Visualization. *Front. Bioinforma.* **2**, 786898.

Gallego-Paez, L. M., Edwards, W. J. S., Chanduri, M., Guo, Y., Koorman, T., Lee, C.-Y., Grexa, N., Derksen, P., Yan, J., Schwartz, M. A., et al. (2023). TLN1 contains a cancer-associated cassette exon that alters talin-1 mechanosensitivity. *J. Cell Biol.* **222**, e202209010.

Gapsys, V., Michielssens, S., Seeliger, D. and Groot, B. L. (2015). pmx: Automated protein structure and topology generation for alchemical perturbations. *J. Comput. Chem.* **36**, 348–354.

García-Alvarez, B., Pereda, J. M., Calderwood, D. A., Ulmer, T. S., Critchley, D., Campbell, I. D., Ginsberg, M. H. and Liddington, R. C. (2003). Structural determinants of integrin recognition by talin. *Mol. Cell* **11**, 49–58.

Gatesman, A., Walker, V. G., Baisden, J. M., Weed, S. A. and Flynn, D. C. (2004). Protein kinase Calpha activates c-Src and induces podosome formation via AFAP-110. *Mol. Cell. Biol.* **24**, 7578–7597.

Geiger, B. and Yamada, K. M. (2011). Molecular Architecture and Function of Matrix Adhesions. *Cold Spring Harb. Perspect. Biol.* **3**, a005033.

Geiger, B., Bershadsky, A., Pankov, R. and Yamada, K. M. (2001). Transmembrane crosstalk between the extracellular matrix--cytoskeleton crosstalk. *Nat. Rev. Mol. Cell Biol.* **2**,.

Ghatak, S., Morgner, J. and Wickström, S. A. (2013). ILK: a pseudokinase with a unique function in the integrin–actin linkage. *Biochem. Soc. Trans.* **41**, 995–1001.

Gholipour, A., Shakerian, F., Zahedmehr, A., Irani, S., Mowla, S. J. and Malakootian, M. (2022). Downregulation of Talin-1 is associated with the increased expression of miR-182-5p and miR-9-5p in coronary artery disease. *J. Clin. Lab. Anal.* **36**, e24252.

Giancotti, F. G. and Ruoslahti, E. (1999). Integrin signaling. *Science* **285**, 1028–1032.

Gingras, A. R., Ziegler, W. H., Frank, R., Barsukov, I. L., Roberts, G. C. K., Critchley, D. R. and Emsley, J. (2005). Mapping and consensus sequence identification for multiple vinculin binding sites within the talin rod. *J. Biol. Chem.* **280**, 37217–37224.

Gingras, A. R., Bate, N., Goult, B. T., Hazelwood, L., Canestrelli, I., Grossmann, J. G., Liu, H., Putz, N. S. M., Roberts, G. C. K., Volkmann, N., et al. (2008). The structure of the C-terminal actin-binding domain of talin. *EMBO J.* **27**, 458–469.

Gingras, A. R., Ziegler, W. H., Bobkov, A. A., Joyce, M. G., Fasci, D., Himmel, M., Rothemund, S., Ritter, A., Grossmann, J. G., Patel, B., et al. (2009). Structural determinants of integrin binding to the talin rod. *J. Biol. Chem.* **284**, 8866–8876.

Gingras, A. R., Bate, N., Goult, B. T., Patel, B., Kopp, P. M., Emsley, J., Barsukov, I. L., Roberts, G. C. K. and Critchley, D. R. (2010). Central region of talin has a unique fold that binds vinculin and actin. *J. Biol. Chem.* **285**, 29577–29587.

Glading, A., Lauffenburger, D. A. and Wells, A. (2002). Cutting to the chase: calpain proteases in cell motility. *Trends Cell Biol.* **12**, 46–54.

Goldmann, W. H., Bremer, A., Häner, M., Aebi, U. and Isenberg, G. (1994). Native talin is a dumbbell-shaped homodimer when it interacts with actin. *J. Struct. Biol.* **112**, 3–10.

Górska, A. and Mazur, A. J. (2022). Integrin-linked kinase (ILK): the known vs. the unknown and perspectives. *Cell. Mol. Life Sci.* **79**, 100.

Gottschalk, K.-E. (2005). A coiled-coil structure of the alphaIIbbeta3 integrin transmembrane and cytoplasmic domains in its resting state. *Struct. Lond. Engl. 1993* **13**, 703–712.

Gough, R. E. and Goult, B. T. (2018). The tale of two talins - two isoforms to fine-tune integrin signalling. *FEBS Lett.* **592**, 2108–2125.

Gough, R. E., Jones, M. C., Zacharchenko, T., Le, S., Yu, M., Jacquemet, G., Muench, S. P., Yan, J., Humphries, J. D., Jørgensen, C., et al. (2021). Talin mechanosensitivity is modulated by a direct interaction with cyclin-dependent kinase-1. *J. Biol. Chem.* **297**, 100837.

Goult, B. T., Bate, N., Anthis, N. J., Wegener, K. L., Gingras, A. R., Patel, B., Barsukov, I. L., Campbell, I. D., Roberts, G. C. K. and Critchley, D. R. (2009). The structure of an interdomain complex that regulates talin activity. *J. Biol. Chem.* **284**, 15097–15106.

Goult, B. T., Bouaouina, M., Elliott, P. R., Bate, N., Patel, B., Gingras, A. R., Grossmann, J. G., Roberts, G. C. K., Calderwood, D. A., Critchley, D. R., et al. (2010). Structure of a double ubiquitin-like domain in the talin head: a role in integrin activation. *EMBO J.* **29**, 1069–1080.

Goult, B. T., Zacharchenko, T., Bate, N., Tsang, R., Hey, F., Gingras, A. R., Elliott, P. R., Roberts, G. C. K., Ballestrem, C., Critchley, D. R., et al. (2013a). RIAM and vinculin binding to talin are mutually exclusive and regulate adhesion assembly and turnover. *J. Biol. Chem.* **288**, 8238–8249.

Goult, B. T., Xu, X.-P., Gingras, A. R., Swift, M., Patel, B., Bate, N., Kopp, P. M., Barsukov, I. L., Critchley, D. R., Volkmann, N., et al. (2013b). Structural studies on full-length talin1 reveal a compact auto-inhibited dimer: implications for talin activation. *J. Struct. Biol.* **184**, 21–32.

GTEx Consortium (2015). Human genomics. The Genotype-Tissue Expression (GTEx) pilot analysis: multitissue gene regulation in humans. *Science* **348**, 648–660.

Guarino, M. (2010). Src signaling in cancer invasion. *J. Cell. Physiol.* **223**, 14–26.

Haage, A., Goodwin, K., Whitewood, A., Camp, D., Bogutz, A., Turner, C. T., Granville, D. J., Lefebvre, L., Plotnikov, S., Goult, B. T., et al. (2018). Talin Autoinhibition Regulates Cell-ECM Adhesion Dynamics and Wound Healing In Vivo. *Cell Rep.* **25**, 2401-2416.e5.

Haeger, A., Wolf, K., Zegers, M. M. and Friedl, P. (2015). Collective cell migration: guidance principles and hierarchies. *Trends Cell Biol.* **25**, 556–566.

Haining, A. W. M., Lieberthal, T. J. and Del Río Hernández, A. (2016a). Talin: a mechanosensitive molecule in health and disease. *FASEB J. Off. Publ. Fed. Am. Soc. Exp. Biol.* **30**, 2073–2085.

Haining, A. W. M., Essen, M., Attwood, S. J., Hytönen, V. P. and Del Río Hernández, A. (2016b). All Subdomains of the Talin Rod Are Mechanically Vulnerable and May Contribute To Cellular Mechanosensing. *ACS Nano* **10**, 6648–6658.

Haining, A. W. M., Rahikainen, R., Cortes, E., Lachowski, D., Rice, A., Essen, M., Hytönen, V. P. and Del Río Hernández, A. (2018). Mechanotransduction in talin through the interaction of the R8 domain with DLC1. *PLoS Biol.* **16**, e2005599.

Haling, J. R., Monkley, S. J., Critchley, D. R. and Petrich, B. G. (2011). Talin-dependent integrin activation is required for fibrin clot retraction by platelets. *Blood* **117**, 1719–1722.

Han, J., Rose, D. M., Woodside, D. G., Goldfinger, L. E. and Ginsberg, M. H. (2003). Integrin alpha 4 beta 1-dependent T cell migration requires both phosphorylation and dephosphorylation of the alpha 4 cytoplasmic domain to regulate the reversible binding of paxillin. *J. Biol. Chem.* **278**, 34845–34853.

Han, J., Lim, C. J., Watanabe, N., Soriani, A., Ratnikov, B., Calderwood, D. A., Puzon-McLaughlin, W., Lafuente, E. M., Boussiotis, V. A., Shattil, S. J., et al. (2006). Reconstructing and deconstructing agonist-induced activation of integrin alphaIIbbeta3. *Curr. Biol. CB* **16**, 1796–1806.

Han, S. J., Azarova, E. V., Whitewood, A. J., Bachir, A., Guttierrez, E., Groisman, A., Horwitz, A. R., Goult, B. T., Dean, K. M. and Danuser, G. (2021a). Talin-vinculin precomplex drives adhesion maturation by accelerated force transmission and vinculin recruitment. 735183.

Han, S. J., Azarova, E. V., Whitewood, A. J., Bachir, A., Guttierrez, E., Groisman, A., Horwitz, A. R., Goult, B. T., Dean, K. M. and Danuser, G. (2021b). Pre-complexation of talin and vinculin without tension is required for efficient nascent adhesion maturation. *eLife* **10**, e66151.

Harburger, D. S., Bouaouina, M. and Calderwood, D. A. (2009). Kindlin-1 and -2 Directly Bind the C-terminal Region of β Integrin Cytoplasmic Tails and Exert Integrin-specific Activation Effects. *J. Biol. Chem.* **284**, 11485–11497.

Hayes, S. N., Kim, E. S. H., Saw, J., Adlam, D., Arslanian-Engoren, C., Economy, K. E., Ganesh, S. K., Gulati, R., Lindsay, M. E., Mieres, J. H., et al. (2018). Spontaneous Coronary Artery Dissection: Current State of the Science: A Scientific Statement From the American Heart Association. *Circulation* **137**, e523–e557.

Hayes, S. N., Tweet, M. S., Adlam, D., Kim, E. S. H., Gulati, R., Price, J. E. and Rose, C. H. (2020). Spontaneous Coronary Artery Dissection: JACC State-of-the-Art Review. *J. Am. Coll. Cardiol.* **76**, 961–984.

Heim, J. B., Squirewell, E. J., Neu, A., Zocher, G., Sominidi-Damodaran, S., Wyles, S. P., Nikolova, E., Behrendt, N., Saunte, D. M., Lock-Andersen, J., et al. (2017). Myosin-1E interacts with FAK proline-rich region 1 to induce fibronectin-type matrix. *Proc. Natl. Acad. Sci. U. S. A.* **114**, 3933–3938.

Hemmings, B. A. and Restuccia, D. F. (2012). PI3K-PKB/Akt pathway. *Cold Spring Harb. Perspect. Biol.* **4**, a011189.

Hemmings, L., Rees, D. J., Ohanian, V., Bolton, S. J., Gilmore, A. P., Patel, B., Priddle, H., Trevithick, J. E., Hynes, R. O. and Critchley, D. R. (1996). Talin contains three actin-binding sites each of which is adjacent to a vinculin-binding site. *J. Cell Sci.* **109 (Pt 11)**, 2715–2726.

Henikoff, S. and Henikoff, J. G. (1992). Amino acid substitution matrices from protein blocks. *Proc. Natl. Acad. Sci. U. S. A.* **89**, 10915–10919.

Henning Stumpf, B., Ambriović-Ristov, A., Radenovic, A. and Smith, A.-S. (2020). Recent Advances and Prospects in the Research of Nascent Adhesions. *Front. Physiol.* **11**, 574371.

Hess, B., Kutzner, C., Spoel, D. and Lindahl, E. (2008). GROMACS 4: Algorithms for Highly Efficient, Load-Balanced, and Scalable Molecular Simulation. *J. Chem. Theory Comput.* **4**, 435–447.

Hilbi, H. and Kortholt, A. (2017). Role of the small GTPase Rap1 in signal transduction, cell dynamics and bacterial infection. *Small GTPases* **10**, 336–342.

Hodivala-Dilke, K. M., McHugh, K. P., Tsakiris, D. A., Rayburn, H., Crowley, D., Ullman-Culleré, M., Ross, F. P., Coller, B. S., Teitelbaum, S. and Hynes, R. O. (1999). Beta3-integrin-deficient mice are a model for Glanzmann thrombasthenia showing placental defects and reduced survival. *J. Clin. Invest.* **103**, 229–238.

Honda, S., Shirotani-Ikejima, H., Tadokoro, S., Maeda, Y., Kinoshita, T., Tomiyama, Y. and Miyata, T. (2009). Integrin-linked kinase associated with integrin activation. *Blood* **113**, 5304–5313.

Horton, E. R., Humphries, J. D., James, J., Jones, M. C., Askari, J. A. and Humphries, M. J. (2016). The integrin adhesome network at a glance. *J. Cell Sci.* **129**, 4159–4163.

Huang, C., Rajfur, Z., Yousefi, N., Chen, Z., Jacobson, K. and Ginsberg, M. H. (2009). Talin Phosphorylation by Cdk5 regulates Smurf1-mediated talin head ubiquitination and cell migration. *Nat. Cell Biol.* **11**, 624–630.

Hughes, P. E., Diaz-Gonzalez, F., Leong, L., Wu, C., McDonald, J. A., Shattil, S. J. and Ginsberg, M. H. (1996). Breaking the Integrin Hinge: A DEFINED STRUCTURAL CONSTRAINT REGULATES INTEGRIN SIGNALING (*). *J. Biol. Chem.* **271**, 6571–6574.

Huveneers, S. and Danen, E. H. J. (2009). Adhesion signaling - crosstalk between integrins, Src and Rho. *J. Cell Sci.* **122**, 1059–1069.

Hynes, R. O. (2002). Integrins: Bidirectional, Allosteric Signaling Machines. *Cell* **110**, 673–687.

Hynes, R. O. (2007). Cell-matrix adhesion in vascular development. *J. Thromb. Haemost. JTH* **5 Suppl 1**, 32–40.

Hynes, R. O. (2009). The extracellular matrix: not just pretty fibrils. *Science* **326**, 1216–1219.

Hytönen, V. P. and Vogel, V. (2008). How Force Might Activate Talin's Vinculin Binding Sites: SMD Reveals a Structural Mechanism. *PLoS Comput. Biol.* **4**, e24.

Igishi, T., Fukuhara, S., Patel, V., Katz, B. Z., Yamada, K. M. and Gutkind, J. S. (1999). Divergent signaling pathways link focal adhesion kinase to mitogen-activated protein kinase cascades. Evidence for a role of paxillin in c-Jun NH(2)-terminal kinase activation. *J. Biol. Chem.* **274**, 30738–30746.

Imai, Y., Park, E. J., Peer, D., Peixoto, A., Cheng, G., Andrian, U. H., Carman, C. V. and Shimaoka, M. (2008). Genetic perturbation of the putative cytoplasmic membrane-proximal salt bridge aberrantly activates alpha(4) integrins. *Blood* **112**, 5007–5015.

Isenberg, G., Leonard, K. and Jockusch, B. M. (1982). Structural aspects of vinculin-actin interactions. *J. Mol. Biol.* **158**, 231–249.

Isenberg, G., Doerhoefer, S., Hoekstra, D. and Goldmann, W. H. (2002). Membrane fusion induced by the major lipid-binding domain of the cytoskeletal protein talin. *Biochem. Biophys. Res. Commun.* **295**, 636–643.

Iwahara, T., Akagi, T., Fujitsuka, Y. and Hanafusa, H. (2004). CrkII regulates focal adhesion kinase activation by making a complex with Crk-associated substrate, p130Cas. *Proc. Natl. Acad. Sci. U. S. A.* **101**, 17693–17698.

Jaalouk, D. E. and Lammerding, J. (2009). Mechanotransduction gone awry. *Nat. Rev. Mol. Cell Biol.* **10**, 63–73.

Jacquemet, G., Hamidi, H. and Ivaska, J. (2015). Filopodia in cell adhesion, 3D migration and cancer cell invasion. *Curr. Opin. Cell Biol.* **36**, 23–31.

Jacquemet, G., Stubb, A., Saup, R., Miihkinen, M., Kremneva, E., Hamidi, H. and Ivaska, J. (2019). Filopodome Mapping Identifies p130Cas as a Mechanosensitive Regulator of Filopodia Stability. *Curr. Biol. CB* **29**, 202-216.e7.

Ji, L., Jiang, F., Cui, X. and Qin, C. (2021). Talin1 knockdown prohibits the proliferation and migration of colorectal cancer cells via the EMT signaling pathway. *Oncol. Lett.* **22**, 682.

Jin, J.-K., Tien, P.-C., Cheng, C.-J., Song, J. H., Huang, C., Lin, S.-H. and Gallick, G. E. (2015). Talin1 phosphorylation activates β1 integrins: a novel mechanism to promote prostate cancer bone metastasis. *Oncogene* **34**, 1811–1821.

Juin, A., Planus, E., Guillemot, F., Horakova, P., Albiges-Rizo, C., Génot, E., Rosenbaum, J., Moreau, V. and Saltel, F. (2013). Extracellular matrix rigidity controls podosome induction in microvascular endothelial cells. *Biol. Cell* **105**, 46–57.

Kalli, A. C., Campbell, I. D. and Sansom, M. S. P. (2013). Conformational changes in talin on binding to anionic phospholipid membranes facilitate signaling by integrin transmembrane helices. *PLoS Comput. Biol.* **9**, e1003316.

Kanamori, H., Kawakami, T., Effendi, K., Yamazaki, K., Mori, T., Ebinuma, H., Masugi, Y., Du, W., Nagasaka, K., Ogiwara, A., et al. (2011). Identification by differential tissue proteome analysis of talin-1 as a novel molecular marker of progression of hepatocellular carcinoma. *Oncology* **80**, 406–415.

Kanchanawong, P., Shtengel, G., Pasapera, A. M., Ramko, E. B., Davidson, M. W., Hess, H. F. and Waterman, C. M. (2010). Nanoscale architecture of integrin-based cell adhesions. *Nature* **468**, 580–584.

Kása, A., Csortos, C. and Verin, A. D. (2015). Cytoskeletal mechanisms regulating vascular endothelial barrier function in response to acute lung injury. *Tissue Barriers* **3**, e974448.

Katz, B. Z., Zamir, E., Bershadsky, A., Kam, Z., Yamada, K. M. and Geiger, B. (2000). Physical state of the extracellular matrix regulates the structure and molecular composition of cell-matrix adhesions. *Mol. Biol. Cell* **11**, 1047–1060.

Katzemich, A., Long, J. Y., Panneton, V., Fisher, L. A. B., Hipfner, D. and Schöck, F. (2019). Slik phosphorylation of Talin T152 is crucial for proper Talin recruitment and maintenance of muscle attachment in Drosophila. *Dev. Camb. Engl.* **146**, dev176339.

Klann, J. E., Remedios, K. A., Kim, S. H., Metz, P. J., Lopez, J., Mack, L. A., Zheng, Y., Ginsberg, M. H., Petrich, B. G. and Chang, J. T. (2017). Talin Plays a Critical Role in the Maintenance of the Regulatory T Cell Pool. *J. Immunol. Baltim. Md 1950* **198**, 4639–4651.

Klapholz, B. and Brown, N. H. (2017). Talin – the master of integrin adhesions. *J. Cell Sci.* **130**, 2435–2446.

Klapproth, S., Sperandio, M., Pinheiro, E. M., Prünster, M., Soehnlein, O., Gertler, F. B., Fässler, R. and Moser, M. (2015). Loss of the Rap1 effector RIAM results in leukocyte adhesion deficiency due to impaired β2 integrin function in mice. *Blood* **126**, 2704–2712.

Koçer, G. and Jonkheijm, P. (2018). About Chemical Strategies to Fabricate Cell-Instructive Biointerfaces with Static and Dynamic Complexity. *Adv. Healthc. Mater.* **7**, e1701192.

Kopp, P. M., Bate, N., Hansen, T. M., Brindle, N. P. J., Praekelt, U., Debrand, E., Coleman, S., Mazzeo, D., Goult, B. T., Gingras, A. R., et al. (2010). Studies on the morphology and spreading of human endothelial cells define key inter- and intramolecular interactions for talin1. *Eur. J. Cell Biol.* **89**, 661–673.

Kümper, S., Mardakheh, F. K., McCarthy, A., Yeo, M., Stamp, G. W., Paul, A., Worboys, J., Sadok, A., Jørgensen, C., Guichard, S., et al. (2016). Rho-associated kinase (ROCK) function is essential for cell cycle progression, senescence and tumorigenesis. *eLife* **5**, e12994.

Lachowski, D., Cortes, E., Robinson, B., Rice, A., Rombouts, K. and Del Río Hernández, A. E. (2018). FAK controls the mechanical activation of YAP, a transcriptional regulator required for durotaxis. *FASEB J. Off. Publ. Fed. Am. Soc. Exp. Biol.* **32**, 1099–1107.

Ladoux, B. and Nicolas, A. (2012). Physically based principles of cell adhesion mechanosensitivity in tissues. *Rep. Prog. Phys. Phys. Soc. G. B.* **75**, 116601.

Lafuente, E. M., Puijenbroek, A. A. F. L., Krause, M., Carman, C. V., Freeman, G. J., Berezovskaya, A., Constantine, E., Springer, T. A., Gertler, F. B. and Boussiotis, V. A. (2004). RIAM, an Ena/VASP and Profilin ligand, interacts with Rap1-GTP and mediates Rap1-induced adhesion. *Dev. Cell* **7**, 585–595.

Lagarrigue, F., Vikas Anekal, P., Lee, H.-S., Bachir, A. I., Ablack, J. N., Horwitz, A. F. and Ginsberg, M. H. (2015). A RIAM/lamellipodin-talin-integrin complex forms the tip of sticky fingers that guide cell migration. *Nat. Commun.* **6**, 8492.

Lagarrigue, F., Kim, C. and Ginsberg, M. H. (2016). The Rap1-RIAM-talin axis of integrin activation and blood cell function. *Blood* **128**, 479–487.

Lai, M.-T., Hua, C.-H., Tsai, M.-H., Wan, L., Lin, Y.-J., Chen, C.-M., Chiu, I.-W., Chan, C., Tsai, F.-J. and Jinn-Chyuan Sheu, J. (2011). Talin-1 overexpression defines high risk for aggressive oral squamous cell carcinoma and promotes cancer metastasis. *J. Pathol.* **224**, 367–376.

Lämmermann, T. and Sixt, M. (2009). Mechanical modes of "amoeboid" cell migration. *Curr. Opin. Cell Biol.* **21**, 636–644.

Lamorte, L., Rodrigues, S., Sangwan, V., Turner, C. E. and Park, M. (2003). Crk associates with a multimolecular Paxillin/GIT2/beta-PIX complex and promotes Rac-dependent relocalization of Paxillin to focal contacts. *Mol. Biol. Cell* **14**, 2818–2831.

Lauffenburger, D. A. and Horwitz, A. F. (1996). Cell migration: a physically integrated molecular process. *Cell* **84**, 359–369.

Laukaitis, C. M., Webb, D. J., Donais, K. and Horwitz, A. F. (2001). Differential dynamics of alpha 5 integrin, paxillin, and alpha-actinin during formation and disassembly of adhesions in migrating cells. *J. Cell Biol.* **153**, 1427–1440.

Lavelin, I., Wolfenson, H., Patla, I., Henis, Y. I., Medalia, O., Volberg, T., Livne, A., Kam, Z. and Geiger, B. (2013). Differential effect of actomyosin relaxation on the dynamic properties of focal adhesion proteins. *PloS One* **8**, e73549.

Lawson, C., Lim, S.-T., Uryu, S., Chen, X. L., Calderwood, D. A. and Schlaepfer, D. D. (2012). FAK promotes recruitment of talin to nascent adhesions to control cell motility. *J. Cell Biol.* **196**, 223–232.

Lee, J., Ishihara, A., Oxford, G., Johnson, B. and Jacobson, K. (1999). Regulation of cell movement is mediated by stretch-activated calcium channels. *Nature* **400**, 382–386.

Lee, H.-S., Lim, C. J., Puzon-McLaughlin, W., Shattil, S. J. and Ginsberg, M. H. (2009). RIAM activates integrins by linking talin to ras GTPase membrane-targeting sequences. *J. Biol. Chem.* **284**, 5119–5127.

Lee, H.-S., Anekal, P., Lim, C. J., Liu, C.-C. and Ginsberg, M. H. (2013). Two modes of integrin activation form a binary molecular switch in adhesion maturation. *Mol. Biol. Cell* **24**, 1354–1362.

Legate, K. R. and Fässler, R. (2009). Mechanisms that regulate adaptor binding to β-integrin cytoplasmic tails. *J. Cell Sci.* **122**, 187–198.

Legate, K. R., Takahashi, S., Bonakdar, N., Fabry, B., Boettiger, D., Zent, R. and Fässler, R. (2011). Integrin adhesion and force coupling are independently regulated by localized PtdIns(4,5)2 synthesis. *EMBO J.* **30**, 4539–4553.

Li, G., Du, X., Vass, W. C., Papageorge, A. G., Lowy, D. R. and Qian, X. (2011). Full activity of the deleted in liver cancer 1 (DLC1) tumor suppressor depends on an LD-like motif that binds talin and focal adhesion kinase (FAK). *Proc. Natl. Acad. Sci. U. S. A.* **108**, 17129–17134.

Li, Y., Luo, X., Sun, Y., Cui, Z., Liu, Y., Liu, R. and Guo, X. (2016). High Stoichiometry Phosphorylation of Talin at T144/T150 or S446 Produces Contrasting Effects on Calpain-mediated Talin Cleavage and Cell Migration. *J. Cancer* **7**, 1645–1652.

Li, A., Guo, Q., Wei, A., Zhou, Y. and Hu, W. (2017a). Role of the Helix in Talin F3 Domain (F3 Helix) in Talin-Mediated Integrin Activation. *Cell Biochem. Biophys.* **75**, 79–86.

Li, H., Deng, Y., Sun, K., Yang, H., Liu, J., Wang, M., Zhang, Z., Lin, J., Wu, C., Wei, Z., et al. (2017b). Structural basis of kindlin-mediated integrin recognition and activation. *Proc. Natl. Acad. Sci. U. S. A.* **114**, 9349–9354.

Li, J., Yan, J. and Springer, T. A. (2021). Low-affinity integrin states have faster ligand-binding kinetics than the high-affinity state. *eLife* **10**, e73359.

Liang, Y., Chen, H., Ji, L., Du, J., Xie, X., Li, X. and Lou, Y. (2018). Talin2 regulates breast cancer cell migration and invasion by apoptosis. *Oncol. Lett.* **16**, 285–293.

Linder, S. and Kopp, P. (2005). Podosomes at a glance. *J. Cell Sci.* **118**, 2079–2082.

Liu, X. and Zheng, W.-M. (2006). An amino acid substitution matrix for protein conformation identification. *J. Bioinform. Comput. Biol.* **4**, 769–782.

Liu, S., Thomas, S. M., Woodside, D. G., Rose, D. M., Kiosses, W. B., Pfaff, M. and Ginsberg, M. H. (1999). Binding of paxillin to α4 integrins modifies integrin-dependent biological responses. *Nature* **402**, 676–681.

Lock, J. G., Jones, M. C., Askari, J. A., Gong, X., Oddone, A., Olofsson, H., Göransson, S., Lakadamyali, M., Humphries, M. J. and Strömblad, S. (2018). Reticular adhesions are a distinct class of cell-matrix adhesions that mediate attachment during mitosis. *Nat. Cell Biol.* **20**, 1290–1302.

Lowell, C. A. and Mayadas, T. N. (2012). Overview-studying integrins in vivo. *Methods Mol. Biol. Clifton NJ* **757**, 369–397.

Lu, P., Takai, K., Weaver, V. M. and Werb, Z. (2011). Extracellular matrix degradation and remodeling in development and disease. *Cold Spring Harb. Perspect. Biol.* **3**, a005058.

Lu, Z., Mathew, S., Chen, J., Hadziselimovic, A., Palamuttam, R., Hudson, B. G., Fässler, R., Pozzi, A., Sanders, C. R. and Zent, R. (2016). Implications of the differing roles of the β1 and β3 transmembrane and cytoplasmic domains for integrin function. *eLife* **5**, e18633.

Lu, F., Zhu, L., Bromberger, T., Yang, J., Yang, Q., Liu, J., Plow, E. F., Moser, M. and Qin, J. (2022). Mechanism of integrin activation by talin and its cooperation with kindlin. *Nat. Commun.* **13**, 2362.

Malinin, N. L., Plow, E. F. and Byzova, T. V. (2010). Kindlins in FERM adhesion. *Blood* **115**, 4011–4017.

Manso, A. M., Okada, H., Sakamoto, F. M., Moreno, E., Monkley, S. J., Li, R., Critchley, D. R. and Ross, R. S. (2017). Loss of mouse cardiomyocyte talin-1 and talin-2 leads to β-1 integrin reduction, costameric instability, and dilated cardiomyopathy. *Proc. Natl. Acad. Sci. U. S. A.* **114**, E6250–E6259.

Martino, F., Perestrelo, A. R., Vinarský, V., Pagliari, S. and Forte, G. (2018). Cellular Mechanotransduction: From Tension to Function. *Front. Physiol.* **9**, 824.

Martins, G. G. and Kolega, J. (2006). Endothelial cell protrusion and migration in three-dimensional collagen matrices. *Cell Motil. Cytoskeleton* **63**, 101–115.

Mayor, R. and Etienne-Manneville, S. (2016). The front and rear of collective cell migration. *Nat. Rev. Mol. Cell Biol.* **17**, 97–109.

McLean, G. W., Carragher, N. O., Avizienyte, E., Evans, J., Brunton, V. G. and Frame, M. C. (2005). The role of focal-adhesion kinase in cancer - a new therapeutic opportunity. *Nat. Rev. Cancer* **5**, 505–515.

Mecham, R. P. (2001). Overview of extracellular matrix. *Curr. Protoc. Cell Biol.* **Chapter 10**, Unit 10.1.

Meves, A., Stremmel, C., Gottschalk, K. and Fässler, R. (2009). The Kindlin protein family: new members to the club of focal adhesion proteins. *Trends Cell Biol.* **19**, 504–513.

Mezu-Ndubuisi, O. J. and Maheshwari, A. (2021). The role of integrins in inflammation and angiogenesis. *Pediatr. Res.* **89**, 1619–1626.

Mierke, C. T. (2015). Physical view on migration modes. *Cell Adhes. Migr.* **9**, 367–379.

Milutinović, A., Šuput, D. and Zorc-Pleskovič, R. (2020). Pathogenesis of atherosclerosis in the tunica intima, media, and adventitia of coronary arteries: An updated review. *Bosn. J. Basic Med. Sci.* **20**, 21–30.

Mitra, S. K., Hanson, D. A. and Schlaepfer, D. D. (2005). Focal adhesion kinase: in command and control of cell motility. *Nat. Rev. Mol. Cell Biol.* **6**, 56–68.

Monkley, S. J., Zhou, X. H., Kinston, S. J., Giblett, S. M., Hemmings, L., Priddle, H., Brown, J. E., Pritchard, C. A., Critchley, D. R. and Fässler, R. (2000). Disruption of the talin gene arrests mouse development at the gastrulation stage. *Dev. Dyn. Off. Publ. Am. Assoc. Anat.* **219**, 560–574.

Monkley, S. J., Pritchard, C. A. and Critchley, D. R. (2001). Analysis of the mammalian talin2 gene TLN2. *Biochem. Biophys. Res. Commun.* **286**, 880–885.

Monkley, S. J., Kostourou, V., Spence, L., Petrich, B., Coleman, S., Ginsberg, M. H., Pritchard, C. A. and Critchley, D. R. (2011). Endothelial cell talin1 is essential for embryonic angiogenesis. *Dev. Biol.* **349**, 494–502.

Moura, A. A., Bezerra, M. J. B., Martins, A. M. A., Borges, D. P., Oliveira, R. T. G., Oliveira, R. M., Farias, K. M., Viana, A. G., Carvalho, G. G. C., Paier, C. R. K., et al. (2022). Global Proteomics Analysis of Bone Marrow:

Establishing Talin-1 and Centrosomal Protein of 55 kDa as Potential Molecular Signatures for Myelodysplastic Syndromes. *Front. Oncol.* **12**, 833068.

Mueller, S. C., Ghersi, G., Akiyama, S. K., Sang, Q. X., Howard, L., Pineiro-Sanchez, M., Nakahara, H., Yeh, Y. and Chen, W. T. (1999). A novel protease-docking function of integrin at invadopodia. *J. Biol. Chem.* **274**, 24947–24952.

Muto, M., Mori, M., Liu, J., Uzawa, A., Uchida, T., Masuda, H., Ohtani, R., Sugimoto, K. and Kuwabara, S. (2017). Serum soluble Talin-1 levels are elevated in patients with multiple sclerosis, reflecting its disease activity. *J. Neuroimmunol.* **305**, 131–134.

Mykuliak, V. V., Haining, A. W. M., von Essen, M., del Río Hernández, A. and Hytönen, V. P. (2018). Mechanical unfolding reveals stable 3-helix intermediates in talin and α-catenin. *PLoS Comput. Biol.* **14**, e1006126.

Nakamura, K., Yano, H., Uchida, H., Hashimoto, S., Schaefer, E. and Sabe, H. (2000). Tyrosine phosphorylation of paxillin alpha is involved in temporospatial regulation of paxillin-containing focal adhesion formation and F-actin organization in motile cells. *J. Biol. Chem.* **275**, 27155–27164.

Nieswandt, B., Moser, M., Pleines, I., Varga-Szabo, D., Monkley, S., Critchley, D. and Fässler, R. (2007). Loss of talin1 in platelets abrogates integrin activation, platelet aggregation, and thrombus formation in vitro and in vivo. *J. Exp. Med.* **204**, 3113–3118.

Ning, L., Tian, L., Smirnov, S., Vihinen, H., Llano, O., Vick, K., Davis, R. L., Rivera, C. and Gahmberg, C. G. (2013). Interactions between ICAM-5 and β1 integrins regulate neuronal synapse formation. *J. Cell Sci.* **126**, 77–89.

Niroula, A., Urolagin, S. and Vihinen, M. (2015). PON-P2: prediction method for fast and reliable identification of harmful variants. *PloS One* **10**, e0117380.

Nishida, N., Xie, C., Shimaoka, M., Cheng, Y., Walz, T. and Springer, T. A. (2006). Activation of Leukocyte β2 Integrins by Conversion from Bent to Extended Conformations. *Immunity* **25**, 583–594.

Olsen, I. M. and Ffrench-Constant, C. (2005). Dynamic regulation of integrin activation by intracellular and extracellular signals controls oligodendrocyte morphology. *BMC Biol.* **3**, 25.

Osiak, A.-E., Zenner, G. and Linder, S. (2005). Subconfluent endothelial cells form podosomes downstream of cytokine and RhoGTPase signaling. *Exp. Cell Res.* **307**, 342–353.

Oxley, C. L., Anthis, N. J., Lowe, E. D., Vakonakis, I., Campbell, I. D. and Wegener, K. L. (2008). An integrin phosphorylation switch: the effect of beta3 integrin tail phosphorylation on Dok1 and talin binding. *J. Biol. Chem.* **283**, 5420–5426.

Pal, K., Tu, Y. and Wang, X. (2022). Single-Molecule Force Imaging Reveals That Podosome Formation Requires No Extracellular Integrin-Ligand Tensions or Interactions. *ACS Nano* **16**, 2481–2493.

Paluch, E. K. and Raz, E. (2013). The role and regulation of blebs in cell migration. *Curr. Opin. Cell Biol.* **25**, 582–590.

Paluch, E. K., Nelson, C. M., Biais, N., Fabry, B., Moeller, J., Pruitt, B. L., Wollnik, C., Kudryasheva, G., Rehfeldt, F. and Federle, W. (2015). Mechanotransduction: use the force(s). *BMC Biol.* **13**, 47.

Pankov, R., Cukierman, E., Katz, B.-Z., Matsumoto, K., Lin, D. C., Lin, S., Hahn, C. and Yamada, K. M. (2000). Integrin Dynamics and Matrix Assembly: Tensin-Dependent Translocation of α5β1 Integrins Promotes Early Fibronectin Fibrillogenesis. *J. Cell Biol.* **148**, 1075–1090.

Papagrigoriou, E., Gingras, A. R., Barsukov, I. L., Bate, N., Fillingham, I. J., Patel, B., Frank, R., Ziegler, W. H., Roberts, G. C. K., Critchley, D. R., et al. (2004). Activation of a vinculin-binding site in the talin rod involves rearrangement of a five-helix bundle. *EMBO J.* **23**, 2942–2951.

Parise, L. V. (1999). Integrin alpha(IIb)beta(3) signaling in platelet adhesion and aggregation. *Curr. Opin. Cell Biol.* **11**, 597–601.

Pearson, M. A., Reczek, D., Bretscher, A. and Karplus, P. A. (2000). Structure of the ERM protein moesin reveals the FERM domain fold masked by an extended actin binding tail domain. *Cell* **101**, 259–270.

Pereda, J. M., Wegener, K. L., Santelli, E., Bate, N., Ginsberg, M. H., Critchley, D. R., Campbell, I. D. and Liddington, R. C. (2005). Structural basis for phosphatidylinositol phosphate kinase type Igamma binding to talin at focal adhesions. *J. Biol. Chem.* **280**, 8381–8386.

Pernier, J., Cardoso Dos Santos, M., Souissi, M., Joly, A., Narassimprakash, H., Rossier, O., Giannone, G., Helfer, E., Sengupta, K. and Le Clainche, C. (2023). Talin and kindlin cooperate to control the density of integrin clusters. *J. Cell Sci.* **136**, jcs260746.

Persad, S. and Dedhar, S. (2003). The role of integrin-linked kinase (ILK) in cancer progression. *Cancer Metastasis Rev.* **22**, 375–384.

Persad, S., Troussard, A. A., McPhee, T. R., Mulholland, D. J. and Dedhar, S. (2001). Tumor suppressor PTEN inhibits nuclear accumulation of beta-catenin and T cell/lymphoid enhancer factor 1-mediated transcriptional activation. *J. Cell Biol.* **153**, 1161–1174.

Petit, V., Boyer, B., Lentz, D., Turner, C. E., Thiery, J. P. and Vallés, A. M. (2000). Phosphorylation of tyrosine residues 31 and 118 on paxillin regulates cell migration through an association with CRK in NBT-II cells. *J. Cell Biol.* **148**, 957–970.

Plow, E. F., Qin, J. and Byzova, T. (2009). Kindling the flame of integrin activation and function with kindlins. *Curr. Opin. Hematol.* **16**, 323–328.

Pora, A., Yoon, S., Windoffer, R. and Leube, R. E. (2019). Hemidesmosomes and Focal Adhesions Treadmill as Separate but Linked Entities during Keratinocyte Migration. *J. Invest. Dermatol.* **139**, 1876-1888.e4.

Pulous, F. E., Grimsley-Myers, C. M., Kansal, S., Kowalczyk, A. P. and Petrich, B. G. (2019). Talin-Dependent Integrin Activation Regulates VE-Cadherin Localization and Endothelial Cell Barrier Function. *Circ. Res.* **124**, 891–903.

Rahikainen, R., Essen, M., Schaefer, M., Qi, L., Azizi, L., Kelly, C., Ihalainen, T. O., Wehrle-Haller, B., Bastmeyer, M., Huang, C., et al. (2017). Mechanical stability of talin rod controls cell migration and substrate sensing. *Sci. Rep.* **7**, 3571.

Rahikainen, R., Öhman, T., Turkki, P., Varjosalo, M. and Hytönen, V. P. (2019). Talin-mediated force transmission and talin rod domain unfolding independently regulate adhesion signaling. *J. Cell Sci.* **132**, jcs226514.

Rangarajan, E. S., Primi, M. C., Colgan, L. A., Chinthalapudi, K., Yasuda, R. and Izard, T. (2020). A distinct talin2 structure directs isoform specificity in cell adhesion. *J. Biol. Chem.* **295**, 12885–12899.

Rappel, W.-J. and Edelstein-Keshet, L. (2017). Mechanisms of Cell Polarization. *Curr. Opin. Syst. Biol.* **3**, 43–53.

Ratnikov, B. I., Partridge, A. W. and Ginsberg, M. H. (2005). Integrin activation by talin. *J. Thromb. Haemost. JTH* **3**, 1783–1790.

Rees, D. J., Ades, S. E., Singer, S. J. and Hynes, R. O. (1990). Sequence and domain structure of talin. *Nature* **347**, 685–689.

Ridley, A. J., Schwartz, M. A., Burridge, K., Firtel, R. A., Ginsberg, M. H., Borisy, G., Parsons, J. T. and Horwitz, A. R. (2003). Cell Migration: Integrating Signals from Front to Back. *Science* **302**, 1704–1709.

Rio, A., Perez-Jimenez, R., Liu, R., Roca-Cusachs, P., Fernandez, J. M. and Sheetz, M. P. (2009). Stretching single talin rod molecules activates vinculin binding. *Science* **323**, 638–641.

Ross, T. D., Coon, B. G., Yun, S., Baeyens, N., Tanaka, K., Ouyang, M. and Schwartz, M. A. (2013). Integrins in mechanotransduction. *Curr. Opin. Cell Biol.* **25**, 613–618.

Rothlein, R., Dustin, M. L., Marlin, S. D. and Springer, T. A. (1986). A human intercellular adhesion molecule (ICAM-1) distinct from LFA-1. *J. Immunol. Baltim. Md 1950* **137**, 1270–1274.

Rottner, K., Krause, M., Gimona, M., Small, J. V. and Wehland, J. (2001). Zyxin is not colocalized with vasodilator-stimulated phosphoprotein (VASP) at lamellipodial tips and exhibits different dynamics to vinculin, paxillin, and VASP in focal adhesions. *Mol. Biol. Cell* **12**, 3103–3113.

Ruoslahti, E. (1996). RGD and other recognition sequences for integrins. *Annu. Rev. Cell Dev. Biol.* **12**, 697–715.

Sakamoto, S. and Kyprianou, N. (2010). Targeting anoikis resistance in prostate cancer metastasis. *Mol. Aspects Med.* **31**, 205–214.

Sakamoto, S., McCann, R. O., Dhir, R. and Kyprianou, N. (2010). Talin1 promotes tumor invasion and metastasis via focal adhesion signaling and anoikis resistance. *Cancer Res.* **70**, 1885–1895.

Saltel, F., Mortier, E., Hytönen, V. P., Jacquier, M.-C., Zimmermann, P., Vogel, V., Liu, W. and Wehrle-Haller, B. (2009). New PI(4,5)P2- and membrane proximal integrin-binding motifs in the talin head control beta3-integrin clustering. *J. Cell Biol.* **187**, 715–731.

Schiemer, J., Bohm, A., Lin, L., Merrill-Skoloff, G., Flaumenhaft, R., Huang, J.-S., Le Breton, G. C. and Chishti, A. H. (2016). Gα13 Switch Region 2 Relieves Talin Autoinhibition to Activate αIIbβ3 Integrin. *J. Biol. Chem.* **291**, 26598–26612.

Schmidt, J. M., Zhang, J., Lee, H. S., Stromer, M. H. and Robson, R. M. (1999). Interaction of talin with actin: sensitive modulation of filament crosslinking activity. *Arch. Biochem. Biophys.* **366**, 139–150.

Sen, S., Ng, W. P. and Kumar, S. (2012). Contributions of talin-1 to glioma cell-matrix tensional homeostasis. *J. R. Soc. Interface* **9**, 1311–1317.

SenGupta, S., Parent, C. A. and Bear, J. E. (2021). The principles of directed cell migration. *Nat. Rev. Mol. Cell Biol.* **22**, 529–547.

Seong, J., Wang, N. and Wang, Y. (2013). Mechanotransduction at focal adhesions: from physiology to cancer development. *J. Cell. Mol. Med.* **17**, 597–604.

Shao, S., Piao, L., Guo, L., Wang, J., Wang, L., Wang, J., Tong, L., Yuan, X., Zhu, J., Fang, S., et al. (2022). Tetraspanin 7 promotes osteosarcoma cell invasion and metastasis by inducing EMT and activating the FAK-Src-Ras-ERK1/2 signaling pathway. *Cancer Cell Int.* **22**, 183.

Shoemaker, B. A., Portman, J. J. and Wolynes, P. G. (2000). Speeding molecular recognition by using the folding funnel: the fly-casting mechanism. *Proc. Natl. Acad. Sci. U. S. A.* **97**, 8868–8873.

Sleeman, J. P., Christofori, G., Fodde, R., Collard, J. G., Berx, G., Decraene, C. and Rüegg, C. (2012). Concepts of metastasis in flux: the stromal progression model. *Semin. Cancer Biol.* **22**, 174–186.

Small, J. V. and Kaverina, I. (2003). Microtubules meet substrate adhesions to arrange cell polarity. *Curr. Opin. Cell Biol.* **15**, 40–47.

Song, X., Yang, J., Hirbawi, J., Ye, S., Perera, H. D., Goksoy, E., Dwivedi, P., Plow, E. F., Zhang, R. and Qin, J. (2012). A novel membrane-dependent on/off switch mechanism of talin FERM domain at sites of cell adhesion. *Cell Res.* **22**, 1533–1545.

Sossey-Alaoui, K., Pluskota, E., Davuluri, G., Bialkowska, K., Das, M., Szpak, D., Lindner, D. J., Downs-Kelly, E., Thompson, C. L. and Plow, E. F. (2014). Kindlin-3 enhances breast cancer progression and metastasis by activating Twist-mediated angiogenesis. *FASEB J. Off. Publ. Fed. Am. Soc. Exp. Biol.* **28**, 2260–2271.

Stefanini, L., Ye, F., Snider, A. K., Sarabakhsh, K., Piatt, R., Paul, D. S., Bergmeier, W. and Petrich, B. G. (2014). A talin mutant that impairs talin-integrin binding in platelets decelerates αIIbβ3 activation without pathological bleeding. *Blood* **123**, 2722–2731.

Streuli, C. H. (2016). Integrins as architects of cell behavior. *Mol. Biol. Cell* **27**, 2885–2888.

Stritt, S., Wolf, K., Lorenz, V., Vögtle, T., Gupta, S., Bösl, M. R. and Nieswandt, B. (2015). Rap1-GTP–interacting adaptor molecule (RIAM) is dispensable for platelet integrin activation and function in mice. *Blood* **125**, 219–222.

Subauste, M. C., Pertz, O., Adamson, E. D., Turner, C. E., Junger, S. and Hahn, K. M. (2004). Vinculin modulation of paxillin-FAK interactions regulates ERK to control survival and motility. *J. Cell Biol.* **165**, 371–381.

Sun, N., Critchley, D. R., Paulin, D., Li, Z. and Robson, R. M. (2008). Identification of a repeated domain within mammalian alpha-synemin that interacts directly with talin. *Exp. Cell Res.* **314**, 1839–1849.

Sun, Z., Lambacher, A. and Fässler, R. (2014). Nascent adhesions: from fluctuations to a hierarchical organization. *Curr. Biol. CB* **24**, R801-803.

Sun, Z., Tseng, H.-Y., Tan, S., Senger, F., Kurzawa, L., Dedden, D., Mizuno, N., Wasik, A. A., Thery, M., Dunn, A. R., et al. (2016a). Kank2 activates talin, reduces force transduction across integrins and induces central adhesion formation. *Nat. Cell Biol.* **18**, 941–953.

Sun, Z., Guo, S. S. and Fässler, R. (2016b). Integrin-mediated mechanotransduction. *J. Cell Biol.* **215**, 445–456.

Sun, H., Lagarrigue, F., Wang, H., Fan, Z., Lopez-Ramirez, M. A., Chang, J. T. and Ginsberg, M. H. (2021). Distinct integrin activation pathways for effector and regulatory T cell trafficking and function. *J. Exp. Med.* **218**, e20201524.

Tabarin, T., Pageon, S. V., Bach, C. T. T., Lu, Y., O'Neill, G. M., Gooding, J. J. and Gaus, K. (2014). Insights into adhesion biology using single-molecule localization microscopy. *Chemphyschem Eur. J. Chem. Phys. Phys. Chem.* **15**, 606–618.

Tadokoro, S., Shattil, S. J., Eto, K., Tai, V., Liddington, R. C., Pereda, J. M., Ginsberg, M. H. and Calderwood, D. A. (2003). Talin Binding to Integrin ß Tails: A Final Common Step in Integrin Activation. *Science* **302**, 103–106.

Takada, Y., Ye, X. and Simon, S. (2007). The integrins. *Genome Biol.* **8**, 215.

Takagi, J., Petre, B. M., Walz, T. and Springer, T. A. (2002). Global Conformational Rearrangements in Integrin Extracellular Domains in Outside-In and Inside-Out Signaling. *Cell* **110**, 599–611.

Tang, H., Yao, L., Tao, X., Yu, Y., Chen, M., Zhang, R. and Xu, C. (2013). miR-9 functions as a tumor suppressor in ovarian serous carcinoma by targeting TLN1. *Int. J. Mol. Med.* **32**, 381–388.

Tang, X., Li, Q., Li, L. and Jiang, J. (2021). Expression of Talin-1 in endometriosis and its possible role in pathogenesis. *Reprod. Biol. Endocrinol. RBE* **19**, 42.

Tapia-Rojo, R., Alonso-Caballero, Á. and Fernández, J. M. (2020). Talin folding as the tuning fork of cellular mechanotransduction. *Proc. Natl. Acad. Sci.* **117**, 21346–21353.

Te Molder, L., de Pereda, J. M. and Sonnenberg, A. (2021). Regulation of hemidesmosome dynamics and cell signaling by integrin α6β4. *J. Cell Sci.* **134**, jcs259004.

Theodosiou, M., Widmaier, M., Böttcher, R. T., Rognoni, E., Veelders, M., Bharadwaj, M., Lambacher, A., Austen, K., Müller, D. J., Zent, R., et al. (2016). Kindlin-2 cooperates with talin to activate integrins and induces cell spreading by directly binding paxillin. *eLife* **5**, e10130.

Toutant, M., Costa, A., Studler, J.-M., Kadaré, G., Carnaud, M. and Girault, J.-A. (2002). Alternative splicing controls the mechanisms of FAK autophosphorylation. *Mol. Cell. Biol.* **22**, 7731–7743.

Tsang, D. K. and Crowe, D. L. (1999). The mitogen activated protein kinase pathway is required for proliferation but not invasion of human squamous cell carcinoma lines. *Int. J. Oncol.* **15**, 519–523.

Turley, T. N., Theis, J. L., Sundsbak, R. S., Evans, J. M., O'Byrne, M. M., Gulati, R., Tweet, M. S., Hayes, S. N. and Olson, T. M. (2019). Rare Missense Variants in TLN1 Are Associated With Familial and Sporadic Spontaneous Coronary Artery Dissection. *Circ. Genomic Precis. Med.* **12**, e002437.

Turley, T. N., O'Byrne, M. M., Kosel, M. L., Andrade, M., Gulati, R., Hayes, S. N., Tweet, M. S. and Olson, T. M. (2020). Identification of Susceptibility Loci for Spontaneous Coronary Artery Dissection. *JAMA Cardiol.* **5**, 929–938.

Turner, C. E. (2000). Paxillin and focal adhesion signalling. *Nat. Cell Biol.* **2**, E231-236.

Turner, C. E., West, K. A. and Brown, M. C. (2001). Paxillin-ARF GAP signaling and the cytoskeleton. *Curr. Opin. Cell Biol.* **13**, 593–599.

Ulmer, T. S., Calderwood, D. A., Ginsberg, M. H. and Campbell, I. D. (2003). Domain-specific interactions of talin with the membrane-proximal region of the integrin beta3 subunit. *Biochemistry* **42**, 8307–8312.

Uray, I. P. and Uray, K. (2021). Mechanotransduction at the Plasma Membrane-Cytoskeleton Interface. *Int. J. Mol. Sci.* **22**, 11566.

Vafaei, S., Saeednejad Zanjani, L., Habibi Shams, Z., Naseri, M., Fattahi, F., Gheytanchi, E., Alemrajabi, M., Ebrahimi, M. and Madjd, Z. (2020). Low expression of Talin1 is associated with advanced pathological features in colorectal cancer patients. *Sci. Rep.* **10**, 17786.

Vanderploeg, J. and Jacobs, J. R. (2015). Talin is required to position and expand the luminal domain of the Drosophila heart tube. *Dev. Biol.* **405**, 189–201.

von Essen, M., Rahikainen, R., Oksala, N., Raitoharju, E., Seppälä, I., Mennander, A., Sioris, T., Kholová, I., Klopp, N., Illig, T., et al. (2016). Talin and vinculin are downregulated in atherosclerotic plaque; Tampere Vascular Study. *Atherosclerosis* **255**, 43–53.

Wallez, Y. and Huber, P. (2008). Endothelial adherens and tight junctions in vascular homeostasis, inflammation and angiogenesis. *Biochim. Biophys. Acta* **1778**, 794–809.

Wang, P., Ballestrem, C. and Streuli, C. H. (2011). The C terminus of talin links integrins to cell cycle progression. *J. Cell Biol.* **195**, 499–513.

Wang, S., Watanabe, T., Matsuzawa, K., Katsumi, A., Kakeno, M., Matsui, T., Ye, F., Sato, K., Murase, K., Sugiyama, I., et al. (2012). Tiam1 interaction with the PAR complex promotes talin-mediated Rac1 activation during polarized cell migration. *J. Cell Biol.* **199**, 331–345.

Webb, D. J., Parsons, J. T. and Horwitz, A. F. (2002). Adhesion assembly, disassembly and turnover in migrating cells -- over and over and over again. *Nat. Cell Biol.* **4**, E97-100.

Weber, K., Hey, S., Cervero, P. and Linder, S. (2022). The circle of life: Phases of podosome formation, turnover and reemergence. *Eur. J. Cell Biol.* **101**, 151218.

Wegener, K. L., Partridge, A. W., Han, J., Pickford, A. R., Liddington, R. C., Ginsberg, M. H. and Campbell, I. D. (2007). Structural basis of integrin activation by talin. *Cell* **128**, 171–182.

Wehrle-Haller, B. (2012). Assembly and disassembly of cell matrix adhesions. *Curr. Opin. Cell Biol.* **24**, 569–581.

Wei, X., Sun, Y., Wu, Y., Zhu, J., Gao, B., Yan, H., Zhao, Z., Zhou, J. and Jing, Z. (2017). Downregulation of Talin-1 expression associates with increased proliferation and migration of vascular smooth muscle cells in aortic dissection. *BMC Cardiovasc. Disord.* **17**, 162.

Wen, Z., Liang, Y., Deng, S., Zou, L., Xie, X., Yang, J. and Wu, Y. (2019). Talin2 regulates invasion of human breast cancer MDA-MB-231 cells via alteration of the tumor microenvironment. *Oncol. Lett.* **17**, 4835–4842.

Wen, L., Lyu, Q., Ley, K. and Goult, B. T. (2022). Structural Basis of β2 Integrin Inside-Out Activation. *Cells* **11**, 3039.

Wickström, S. A., Lange, A., Montanez, E. and Fässler, R. (2010a). The ILK/PINCH/parvin complex: the kinase is dead, long live the pseudokinase! *EMBO J.* **29**, 281–291.

Wickström, S. A., Lange, A., Hess, M. W., Polleux, J., Spatz, J. P., Krüger, M., Pfaller, K., Lambacher, A., Bloch, W., Mann, M., et al. (2010b). Integrin-linked kinase controls microtubule dynamics required for plasma membrane targeting of caveolae. *Dev. Cell* **19**, 574–588.

Wickström, S. A., Radovanac, K. and Fässler, R. (2011). Genetic analyses of integrin signaling. *Cold Spring Harb. Perspect. Biol.* **3**, a005116.

Winkler, J., Lünsdorf, H. and Jockusch, B. M. (1997). Energy-filtered electron microscopy reveals that talin is a highly flexible protein composed of a series of globular domains. *Eur. J. Biochem.* **243**, 430–436.

Winograd-Katz, S. E., Fässler, R., Geiger, B. and Legate, K. R. (2014). The integrin adhesome: from genes and proteins to human disease. *Nat. Rev. Mol. Cell Biol.* **15**, 273–288.

Wozniak, M. A., Modzelewska, K., Kwong, L. and Keely, P. J. (2004). Focal adhesion regulation of cell behavior. *Biochim. Biophys. Acta* **1692**, 103–119.

Wu, C. (2007). Focal adhesion: a focal point in current cell biology and molecular medicine. *Cell Adhes. Migr.* **1**, 13–18.

Wu, Q., Zhang, J., Koh, W., Yu, Q., Zhu, X., Amsterdam, A., Davis, G. E., Arnaout, M. A. and Xiong, J.-W. (2015). Talin1 is required for cardiac Z-disk stabilization and endothelial integrity in zebrafish. *FASEB J. Off. Publ. Fed. Am. Soc. Exp. Biol.* **29**, 4989–5005.

Wynne, J. P., Wu, J., Su, W., Mor, A., Patsoukis, N., Boussiotis, V. A., Hubbard, S. R. and Philips, M. R. (2012). Rap1-interacting adapter molecule (RIAM) associates with the plasma membrane via a proximity detector. *J. Cell Biol.* **199**, 317–330.

Xiao, Z., Shen, L., Chen, D., Wang, L., Xi, Z., Xiao, F. and Wang, X. (2010). Talin 2 concentrations in cerebrospinal fluid in patients with epilepsy. *Clin. Biochem.* **43**, 1129–1132.

Xing, B., Thuppal, S., Jedsadayanmata, A., Du, X. and Lam, S. C.-T. (2006). TA205, an anti-talin monoclonal antibody, inhibits integrin-talin interaction. *FEBS Lett.* **580**, 2027–2032.

Xu, Y.-F., Ren, X.-Y., Li, Y.-Q., He, Q.-M., Tang, X.-R., Sun, Y., Shao, J.-Y., Jia, W.-H., Kang, T.-B., Zeng, M.-S., et al. (2015). High expression of

Talin-1 is associated with poor prognosis in patients with nasopharyngeal carcinoma. *BMC Cancer* **15**, 332.

Yan, B., Calderwood, D. A., Yaspan, B. and Ginsberg, M. H. (2001). Calpain Cleavage Promotes Talin Binding to the β3Integrin Cytoplasmic Domain*. *J. Biol. Chem.* **276**, 28164–28170.

Yan, J., Yao, M., Goult, B. T. and Sheetz, M. P. (2015). Talin Dependent Mechanosensitivity of Cell Focal Adhesions. *Cell. Mol. Bioeng.* **8**, 151–159.

Yang, J., Zhu, L., Zhang, H., Hirbawi, J., Fukuda, K., Dwivedi, P., Liu, J., Byzova, T., Plow, E. F., Wu, J., et al. (2014). Conformational activation of talin by RIAM triggers integrin-mediated cell adhesion. *Nat. Commun.* **5**, 5880.

Yano, H., Uchida, H., Iwasaki, T., Mukai, M., Akedo, H., Nakamura, K., Hashimoto, S. and Sabe, H. (2000). Paxillin alpha and Crk-associated substrate exert opposing effects on cell migration and contact inhibition of growth through tyrosine phosphorylation. *Proc. Natl. Acad. Sci. U. S. A.* **97**, 9076–9081.

Yao, M., Goult, B. T., Klapholz, B., Hu, X., Toseland, C. P., Guo, Y., Cong, P., Sheetz, M. P. and Yan, J. (2016). The mechanical response of talin. *Nat. Commun.* **7**, 11966.

Yu, C., Rafiq, N. B. M., Krishnasamy, A., Hartman, K. L., Jones, G. E., Bershadsky, A. D. and Sheetz, M. P. (2013). Integrin-matrix clusters form podosome-like adhesions in the absence of traction forces. *Cell Rep.* **5**, 1456–1468.

Yuan, Y., Li, L., Zhu, Y., Qi, L., Azizi, L., Hytönen, V. P., Zhan, C.-G. and Huang, C. (2017). The molecular basis of talin2's high affinity toward β1-integrin. *Sci. Rep.* **7**, 41989.

Yue, B. (2014). Biology of the extracellular matrix: an overview. *J. Glaucoma* **23**, S20-23.

Zacharchenko, T., Qian, X., Goult, B. T., Jethwa, D., Almeida, T. B., Ballestrem, C., Critchley, D. R., Lowy, D. R. and Barsukov, I. L. (2016). LD Motif Recognition by Talin: Structure of the Talin-DLC1 Complex. *Struct. Lond. Engl. 1993* **24**, 1130–1141.

Zaidel-Bar, R., Ballestrem, C., Kam, Z. and Geiger, B. (2003). Early molecular events in the assembly of matrix adhesions at the leading edge of migrating cells. *J. Cell Sci.* **116**, 4605–4613.

Zaidel-Bar, R., Itzkovitz, S., Ma'ayan, A., Iyengar, R. and Geiger, B. (2007). Functional atlas of the integrin adhesome. *Nat. Cell Biol.* **9**, 858–867.

Zamir, E. and Geiger, B. (2001). Molecular complexity and dynamics of cell-matrix adhesions. *J. Cell Sci.* **114**, 3583–3590.

Zamir, E., Katz, B. Z., Aota, S., Yamada, K. M., Geiger, B. and Kam, Z. (1999). Molecular diversity of cell-matrix adhesions. *J. Cell Sci.* **112 (Pt 11)**, 1655–1669.

Zervas, C. G., Psarra, E., Williams, V., Solomon, E., Vakaloglou, K. M. and Brown, N. H. (2011). A central multifunctional role of integrin-linked kinase at muscle attachment sites. *J. Cell Sci.* **124**, 1316–1327.

Zhang, J., Robson, R. M., Schmidt, J. M. and Stromer, M. H. (1996). Talin can crosslink actin filaments into both networks and bundles. *Biochem. Biophys. Res. Commun.* **218**, 530–537.

Zhang, X., Jiang, G., Cai, Y., Monkley, S. J., Critchley, D. R. and Sheetz, M. P. (2008). Talin depletion reveals independence of initial cell spreading from integrin activation and traction. *Nat. Cell Biol.* **10**, 1062–1068.

Zhang, W., Mao, Y.-Q., Wang, H., Yin, W.-J., Zhu, S.-X. and Wang, W.-C. (2015). MiR-124 suppresses cell motility and adhesion by targeting talin 1 in prostate cancer cells. *Cancer Cell Int.* **15**, 49.

Zhao, J. and Guan, J.-L. (2009). Signal transduction by focal adhesion kinase in cancer. *Cancer Metastasis Rev.* **28**, 35–49.

Zheng, X., Wu, S.-L., Hincapie, M. and Hancock, W. S. (2009). Study of the human plasma proteome of rheumatoid arthritis. *J. Chromatogr. A* **1216**, 3538–3545.

Zhu, L., Yang, J., Bromberger, T., Holly, A., Lu, F., Liu, H., Sun, K., Klapproth, S., Hirbawi, J., Byzova, T. V., et al. (2017). Structure of Rap1b bound to talin reveals a pathway for triggering integrin activation. *Nat. Commun.* **8**, 1744.

Zhu, L., Liu, H., Lu, F., Yang, J., Byzova, T. V. and Qin, J. (2019). Structural Basis of Paxillin Recruitment by Kindlin-2 in Regulating Cell Adhesion. *Struct. Lond. Engl. 1993* **27**, 1686-1697.e5.

Zhu, L., Plow, E. F. and Qin, J. (2021). Initiation of focal adhesion assembly by talin and kindlin: A dynamic view. *Protein Sci. Publ. Protein Soc.* **30**, 531–542.

Zuidema, A., Wang, W. and Sonnenberg, A. (2020). Crosstalk between Cell Adhesion Complexes in Regulation of Mechanotransduction. *BioEssays News Rev. Mol. Cell. Dev. Biol.* **42**, e2000119.

9 ORIGINAL PUBLICATIONS

PUBLICATION
I

The F1 loop of the talin head domain acts as a gatekeeper in integrin activation and clustering

Kukkurainen, S., Azizi, L., Zhang, P., Jacquier, M. C., Baikoghli, M., von Essen, M., Tuukkanen, A., Laitaoja, M., Liu, X., Rahikainen, R., Orłowski, A, Jänis, J., Määttä, J.A.E., Varjosalo, M., Vattulainen, I., Róg, T., Svergun, D., Cheng, R.H., Wu, J., Hytönen, V.P., Wehrle-Haller, B.

Journal of Cell Science. 2020 Oct 12;133(19):jcs239202
doi: 10.1242/jcs.239202

© 2020. Published by The Company of Biologists Ltd | Journal of Cell Science (2020) 133, jcs239202. doi:10.1242/jcs.239202

RESEARCH ARTICLE

The F1 loop of the talin head domain acts as a gatekeeper in integrin activation and clustering

Sampo Kukkurainen[1,2], Latifeh Azizi[1,2,*], Pingfeng Zhang[3,*], Marie-Claude Jacquier[4,*], Mo Baikoghli[5], Magdaléna von Essen[1,2], Anne Tuukkanen[6,7], Mikko Laitaoja[8], Xiaonan Liu[9], Rolle Rahikainen[1,2], Adam Orłowski[9], Janne Jänis[8], Juha A. E. Määttä[1,2], Markku Varjosalo[9], Ilpo Vattulainen[10,11], Tomasz Róg[10,11], Dmitri Svergun[6], R. Holland Cheng[5], Jinhua Wu[3], Vesa P. Hytönen[1,2,‡,§] and Bernhard Wehrle-Haller[4,‡,§]

ABSTRACT

Integrin activation and clustering by talin are early steps of cell adhesion. Membrane-bound talin head domain and kindlin bind to the β integrin cytoplasmic tail, cooperating to activate the heterodimeric integrin, and the talin head domain induces integrin clustering in the presence of Mn^{2+}. Here we show that kindlin-1 can replace Mn^{2+} to mediate β3 integrin clustering induced by the talin head, but not that induced by the F2–F3 fragment of talin. Integrin clustering mediated by kindlin-1 and the talin head was lost upon deletion of the flexible loop within the talin head F1 subdomain. Further mutagenesis identified hydrophobic and acidic motifs in the F1 loop responsible for β3 integrin clustering. Modeling, computational and cysteine crosslinking studies showed direct and catalytic interactions of the acidic F1 loop motif with the juxtamembrane domains of α- and β3-integrins, in order to activate the β3 integrin heterodimer, further detailing the mechanism by which the talin–kindlin complex activates and clusters integrins. Moreover, the F1 loop interaction with the β3 integrin tail required the newly identified compact FERM fold of the talin head, which positions the F1 loop next to the inner membrane clasp of the talin-bound integrin heterodimer.

This article has an associated First Person interview with the first author of the paper.

KEY WORDS: Activation, Cell adhesion, Clustering, Integrin, Molecular dynamics, Talin

INTRODUCTION

Cells spread, adhere and move with the help of integrins. Integrins are allosterically regulated heterodimeric transmembrane receptors forming 24 distinct combinations of α- and β-integrins in mammals (Hynes, 2002; Bachmann et al., 2019). Cytoplasmic adaptor proteins, along with extracellular divalent cations and tensional forces, affect integrin conformation and interactions with extracellular ligands (Sun et al., 2016; Bachmann et al., 2019). One of the key intracellular adaptors is talin, a large, modular protein that binds and activates integrins with its N-terminal head domain, while connecting them to actin fibers via its C-terminal rod domain, which harbors binding sites for further adaptor and signaling molecules required to form cell–matrix adhesion complexes (Sun et al., 2016; Haining et al., 2016). Humans have two talins, talin-1 and talin-2, which have 76% amino acid sequence identity. Of these two talin forms, talin-1 is ubiquitously expressed and is critical for cell adhesion and morphogenesis (Monkley et al., 2000, 2011; Calderwood et al., 2013; Ellis et al., 2013), whereas talin-2 is highly expressed in brain and striated muscle (Senetar and McCann, 2005; Senetar et al., 2007; Debrand et al., 2012). Hereafter, the term talin refers to talin-1.

The talin N-terminal head domain (defined by calpain II cleavage at residues 433–435) contains two ubiquitin-like subdomains (F0 and F1), an acyl-coenzyme A-binding protein-like subdomain (F2) and a phosphotyrosine binding-like integrin-binding subdomain (F3) (Roberts and Critchley, 2009), followed by a calpain II processable linker (residues 406–481) (Rees et al., 1990). The C-terminal rod domain (residues 482–2541) is composed of 13 α-helical bundles that bind actin filaments and adaptor proteins, and a C-terminal helix involved in talin dimerization (Roberts and Critchley, 2009; Gingras et al., 2008; Calderwood et al., 2013). Association with phosphatidylinositol (4,5)-bisphosphate (PIP2)-containing membranes regulates talin activity and integrin binding by competing with auto-inhibitory rod bundle–head domain interactions (Goksoy et al., 2008; Saltel et al., 2009; Goult et al., 2013; Zhang et al., 2016). The talin head domain is a FERM domain by homology (residues 84–405), and talin-1 has been crystallized in a linear arrangement of the subdomains (Elliott et al., 2010; Chinthalapudi et al., 2018). A talin-2 structure adopting a novel cloverleaf-like conformation was presented recently (Rangarajan et al., 2020).

In addition to talin, knockout studies of kindlin-1, -2 and -3 (also known as FERMT1, 2 and 3, respectively), as well as studies of patients with kindlin-3 deficiencies have shown that kindlins are also required for integrin activation and clustering (Montanez et al., 2008; Moser et al., 2008; Qu et al., 2011; Theodosiou et al., 2016). However, in most experimental settings, endogenous kindlin is present in cells, and hence integrins can be activated by talin head overexpression (Tadokoro et al., 2003). Integrins can also be allosterically activated by ligand binding and manganese (Mn^{2+})

---

[1]Faculty of Medicine and Health Technology, Tampere University, Arvo Ylpön katu 34, FI-33520 Tampere, Finland. [2]Fimlab Laboratories, Biokatu 4, FI-33520 Tampere, Finland. [3]Molecular Therapeutics Program, Fox Chase Cancer Center, Philadelphia, PA 19111, USA. [4]Department of Cell Physiology and Metabolism, University of Geneva, Centre Médical Universitaire, Rue Michel-Servet 1, 1211 Geneva 4, Switzerland. [5]Department of Molecular and Cellular Biology, University of California, 1 Shields Ave, Davis, CA 95616, USA. [6]EMBL Hamburg c/o DESY, European Molecular Biology Laboratory, Notkestrasse 85, 22607 Hamburg, Germany. [7]European Bioinformatics Institute (EMBL-EBI), European Molecular Biology Laboratory, Wellcome Genome Campus, Hinxton, Cambridgeshire CB10 1SD, UK. [8]Department of Chemistry, University of Eastern Finland, P.O. Box 111, FI-80101 Joensuu, Finland. [9]Proteomics Unit, Institute of Biotechnology, University of Helsinki, FI-00014 Helsinki, Finland. [10]Computational Physics Laboratory, Tampere University, FI-33520 Tampere, Finland. [11]Department of Physics, University of Helsinki, P.O. Box 64, FI-00014 Helsinki, Finland.
[*,‡]These authors contributed equally to this work

[§]Authors for correspondence (Bernhard.Wehrle-Haller@unige.ch; Vesa.Hytonen@tuni.fi)

S.K., 0000-0002-0635-784X; P.Z., 0000-0001-5985-4914; M.v.E., 0000-0002-2412-6316; M.V., 0000-0002-1340-9732; I.V., 0000-0001-7408-3214; J.W., 0000-0001-5913-0633; V.P.H., 0000-0002-9357-1480; B.W., 0000-0002-1159-1147

Handling Editor: Michael Way
Received 12 September 2019; Accepted 31 July 2020

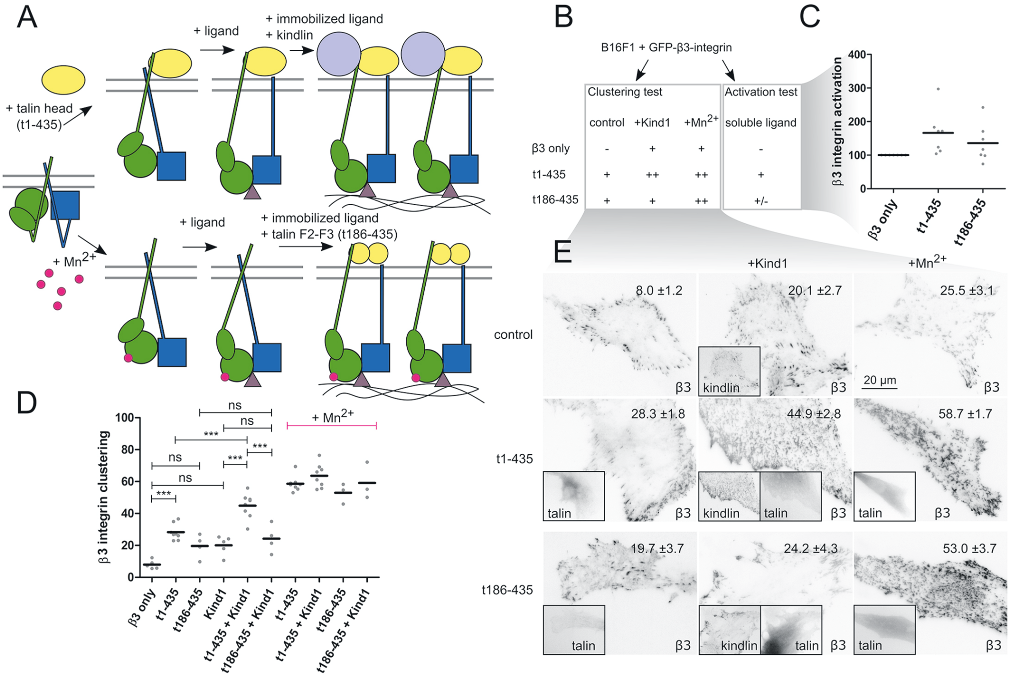

	Clustering test control	 +Kind1	 +Mn2+	Activation test soluble ligand
β3 only	-	+	+	-
t1-435	+	++	++	+
t186-435	+	+	++	+/-

Fig. 1. The complete talin head cooperates with kindlin to activate αvβ3 integrin. Integrin activation and clustering by the complete (subdomains F0–F3, residues 1–435) or partial talin head (subdomains F2–F3, residues 186–435) in B16F1 cells co-transfected with β3–GFP integrin are visualized schematically in (A) and presented as a table in (B). In A: green, α-integrin; blue, β-integrin; yellow, talin head domain; light blue, kindlin; purple triangle, integrin ligand; pink sphere, manganese ion. In B, the scoring for clustering is as follows: - (clustering index 0-10), + (10-30), ++ (>30). Scoring for activation: - (basal level), +/- (activation increase <50%), + (activation increase >50%). Kind1, kindlin-1. (C) Integrin activation assay. Soluble RGD-ligand (SKI-7) binding to B16F1 cells co-transfected with β3–GFP integrin and complete and partial CFP-labeled talin head (t1–435, *n*=7 experiments; t186–435, *n*=7). The control cells (β3 only, *n*=7 experiments) expressed β3–GFP integrin. Dots indicate activation indices (percentage relative to the control), and lines indicate mean values. Variation between the groups was determined using a one-way ANOVA [*F*(2,18)=3.04]. Despite the differences in the mean activation levels, the variance analysis revealed no significant difference. (D) β3–GFP integrin clustering assay. Clustering indices and mean values are shown. The differences in clustering efficiency were analyzed by one-way ANOVA [*F*(9,46)=48.99, *P*<0.0001] and Tukey's multiple comparison test. ****P*<0.001; ns, not significant. Among the Mn^{2+}-treated groups (magenta), no significant differences in β3–GFP integrin clustering efficiency were found. The numbers of experiments (15–25 cells evaluated per experiment) in the non-Mn^{2+}-treated group were: β3 only, *n*=5; t1–435, *n*=8; t186–435, *n*=4; Kind1, *n*=5; t1–435+Kind1, *n*=8; and t186–435+Kind1, *n*=4. For the manganese-treated group the numbers of experiments were: t1–435, *n*=8; t1–435+Kind1, *n*=8; t186–435, *n*=3; and t186–435+Kind1, *n*=3. (E) TIRF images (kindlin-1, β3 integrin) and epifluorescence of transfected talin head constructs showing the representative integrin phenotypes, along with clustering indices (mean±s.d.). For Mn^{2+} alone, images are representative of *n*=5 experiments. Scale bar: 20 µm.

(Mould et al., 1995; Eng et al., 2011) (Fig. 1A). Upon binding to bent integrins on the cell surface, Mn^{2+} switches integrins to an extended conformation, allowing interaction with immobilized extracellular ligands, leading to integrin clustering in a talin-head-dependent manner (Cluzel et al., 2005; Saltel et al., 2009; Changede et al., 2015; Bachmann et al., 2019). For this talin-head-dependent integrin clustering to occur, an acidic (D723/E726), membrane-proximal motif in β3 integrins interacts with basic residues (K316/K324) in the talin F3 subdomain, while other basic residues of the F2 and F3 subdomains interact with acidic membrane lipids, such as PIP2 (Anthis et al., 2009; Saltel et al., 2009). The talin head subdomains F2 and F3 (referred to collectively as F2–F3) are hence sufficient for activation of αIIbβ3 integrin, as recorded using the PAC-1 antibody in detached cells (Tadokoro et al., 2003), but fail to activate α5β1 integrin, when probed with a fibronectin fragment (Bouaouina et al., 2008). This suggests that, at least in the latter case, the entire talin head domain is needed for the binding of soluble ligand. Importantly, when kindlin-1 and kindlin-2 are completely removed from cells, talin no longer activates integrins and cells do not spread (Theodosiou et al., 2016). In addition, Rap1 (RAP1A and RAP1B in mammals) binding to the F0 and/or F1 subdomains of the talin head has been proposed to recruit talin to the plasma membrane, contributing to integrin activation and Rap1-mediated cell–matrix adhesion (Camp et al., 2018; Katzemich et al., 2019; Gingras et al., 2019). Thus, talin, Rap1 and kindlin play important roles in the integrin activation step, while kindlin also induces clustering of activated integrins (Feigelson et al., 2011; Schmidt et al., 2011; Feng et al., 2012; Ye et al., 2013).

The F1 subdomains of both talins and kindlins contain a long loop (38 residues in talin) that binds to negatively charged membrane lipids (Goult et al., 2010; Bouaouina et al., 2012). The talin F1 loop is important for αIIbβ3- and α5β1-integrin activation, but not for β1 integrin binding to talin (Goult et al., 2010; Bouaouina et al., 2008). Charge inversion of basic residues in the talin F1 loop inhibits cell spreading (Elliott et al., 2010), membrane association of the F1 subdomain and integrin activation (Goult et al., 2010). Nevertheless, the F2–F3 subdomains alone bind efficiently to membranes, and the F0–F1 subdomains do not further enhance this interaction (Moore et al., 2012). In addition, the F1 loop is reportedly flexible and does not form stable contacts within the talin head, and its removal has not been found to affect the structure of the folded subdomains (Elliott et al., 2010). Thus, it is not fully clear how the F1 loop contributes to talin-head-induced integrin activation, since it also acts downstream of the Rap1-mediated mechanism of integrin activation and membrane recruitment (Gingras et al., 2019). Nevertheless, it appears to be a site of important posttranslational modifications, because phosphorylation of the F1 loop at T144 and T150 has been associated with reduced membrane binding (Goult et al., 2010), and also affects talin recruitment to muscle attachment sites in *Drosophila* (Katzemich et al., 2019).

Talin is, so far, the only FERM family protein that has not been shown to fold into a conserved cloverleaf-like shape, and current models propose that the membrane recruitment of the talin head domain in an F1 loop- and Rap1-dependent manner is the key to integrin activation. Here, we validated the FERM fold of the full-length talin head by small-angle X-ray scattering and used molecular dynamics (MD) analysis to evaluate the functional role of the F1 loop in integrin activation. We show that the F1 loop interacts with the β integrin cytoplasmic tail and interferes with the inner membrane clasp via conserved acidic residues, leading to integrin activation and clustering in a talin- and kindlin-mediated manner. Taken together, our data support a new mechanism for kindlin- and talin-induced integrin activation, in which the FERM-folded talin head tightly interacts with the β integrin tail and projects the F1 loop to act as a gatekeeper to control the talin–integrin association and regulate the activation and clustering of integrins.

RESULTS

Talin F1 loop is required for integrin activation and clustering

The talin head can induce integrin activation (as measured by soluble ligand binding) and integrin clustering (Tadokoro et al., 2003; Goult et al., 2010; Cluzel et al., 2005) (Fig. 1A). However, we found that the integrin-binding F2–F3 fragment of the talin head (t186–435), when probed with a soluble, RGD-containing snake venom (SKI-7; Ballestrem et al., 2001), did not efficiently activate β3 integrin (Fig. 1B,C). Similarly, the talin F2–F3 fragment is reportedly not sufficient to induce α5β1 integrin activation, when measured by soluble fibronectin binding (Bouaouina et al., 2008), whereas it activates αIIbβ3 integrin when probed with the multivalent PAC-1 IgM antibody (Calderwood et al., 2002; Tadokoro et al., 2003; Bouaouina et al., 2008). On the other hand, the talin head F2–F3 fragment induces αvβ3 integrin clustering on vitronectin-coated surfaces in the presence of Mn^{2+} (Saltel et al., 2009). Because integrin activation and clustering are tightly interlinked (Bunch, 2009), the conformational activation of the extracellular domain of integrins by Mn^{2+} may therefore mask the physiological role of the intracellular adaptors in the regulation of the integrin function at the cell surface.

In order to develop a more physiological Mn^{2+}-independent test that also takes into account the role of kindlin in integrin activation (Ma et al., 2008; Moser et al., 2009; Harburger et al., 2009), and therefore its potential influence on integrin clustering, we analyzed the clustering of β3 integrin with a C-terminal GFP tag (β3–GFP integrin) in the presence of fluorescently labeled talin head and kindlin-1 in B16F1 melanoma cells spread on serum-coated glass coverslips (Fig. 1B,C,D) (Saltel et al., 2009). The degree of clustering of integrin receptors was calculated from TIRF images, by determining the percentage of the cell area covered with integrin clusters (Fig. 1E). The complete talin head domain (t1–435) enhanced β3–GFP integrin clustering ($P<0.001$), but the co-expression of kindlin-1 with the talin head and β3–GFP integrin was needed for increasing the integrin clustering further ($P<0.001$) to a level similar to that observed with the talin head and Mn^{2+}. Interestingly, kindlin-1 did not enhance talin F2–F3-mediated clustering, whereas this did occur when Mn^{2+} was used for integrin activation (Saltel et al., 2009) (Fig. 1D,E). Importantly, co-expression of talin head and kindlin-1 was critical for full clustering. Although the exact role of kindlin in the integrin activation process is still unknown (Rognoni et al., 2016), kindlin-mediated integrin clustering requires the presence of the talin F0–F1 subdomains. In addition, the large loop insert in the F1 subdomain is a feature of talins and kindlins, and has been shown to be important for integrin activation by both adaptors (Goult et al., 2010; Bouaouina et al., 2012). Because antibody interference of the talin–integrin association using an F1 loop-directed monoclonal antibody, Ta205 (Xing et al., 2006), suggested proximity of the F1 loop to the integrin-binding F3 subdomain in the talin head, we decided to further investigate the role of the talin F1 loop in kindlin-1-assisted integrin clustering by assaying a series of loop deletions. In addition, we created a model of a FERM-folded talin head domain, containing the F1 loop, to study the biological role of the F1 loop *in silico* (Fig. 2).

We completely removed the talin F1 loop using two different strategies: by deleting residues 139–168 (del30), as was done for the previously published elongated structures of the talin head (Goult et al., 2010; Elliott et al., 2010), and by replacing residues 134–170 with a Gly-Ala-Gly stretch (del37/GAG) to yield a loop similar in sequence and equal in length to *Dictyostelium* TalB (Fig. 2G,H; Fig. S1). Both loop deletions led to defects in β3 integrin activation and clustering (Fig. 2F,H,I), but enhanced β3 integrin binding *in vitro* (Tables S1, S2). We then further narrowed down the deletion to the central part of the loop (del17), and replaced the residues 151–154 (LLRD) with four alanines (151–154AAAA), preserving the length, the previously identified cluster of basic residues (Goult et al., 2010) and the net charge of the loop. Neither of the mutants showed significant integrin activation (Fig. 2F), and the 151–154AAAA mutation alone was sufficient to decrease clustering as compared to the wild-type head domain (t1–435), suggesting that the central stretch of residues 151–154 (LLRD) is important for the functions of the F1 loop. Despite the presence of a full-size F1 loop, the 151–154AAAA mutant displayed decreased *in vitro* binding to β3 integrin compared to that of the F1 loop deletion mutants, and this was even slightly lower than measured for the wild-type F1 loop (Table S2). These data suggest that the F1 loop interferes with β3 integrin binding to the talin head, to some extent, but at the same time appears to stimulate integrin activation and clustering.

Modeling of the F1 loop into the compact talin FERM fold

Because all talin head structures published so far lack the F1 loop, we decided to create a F1 loop-containing talin head model based on the compact FERM fold and then explored its structural stability and potential lipid interactions using MD simulations. Compared to the existing extended crystal structure of the talin head [t1–400(del139–168/del30); PBD ID 3IVF] (Elliott et al., 2010), our talin model is rotated at its F1–F2 linker to yield a compact FERM domain (Fig. 2E), similar to the recently published crystallographic structure of kindlin-2 (PDB ID 5XPY) (Li et al., 2017). The F1 domain loop

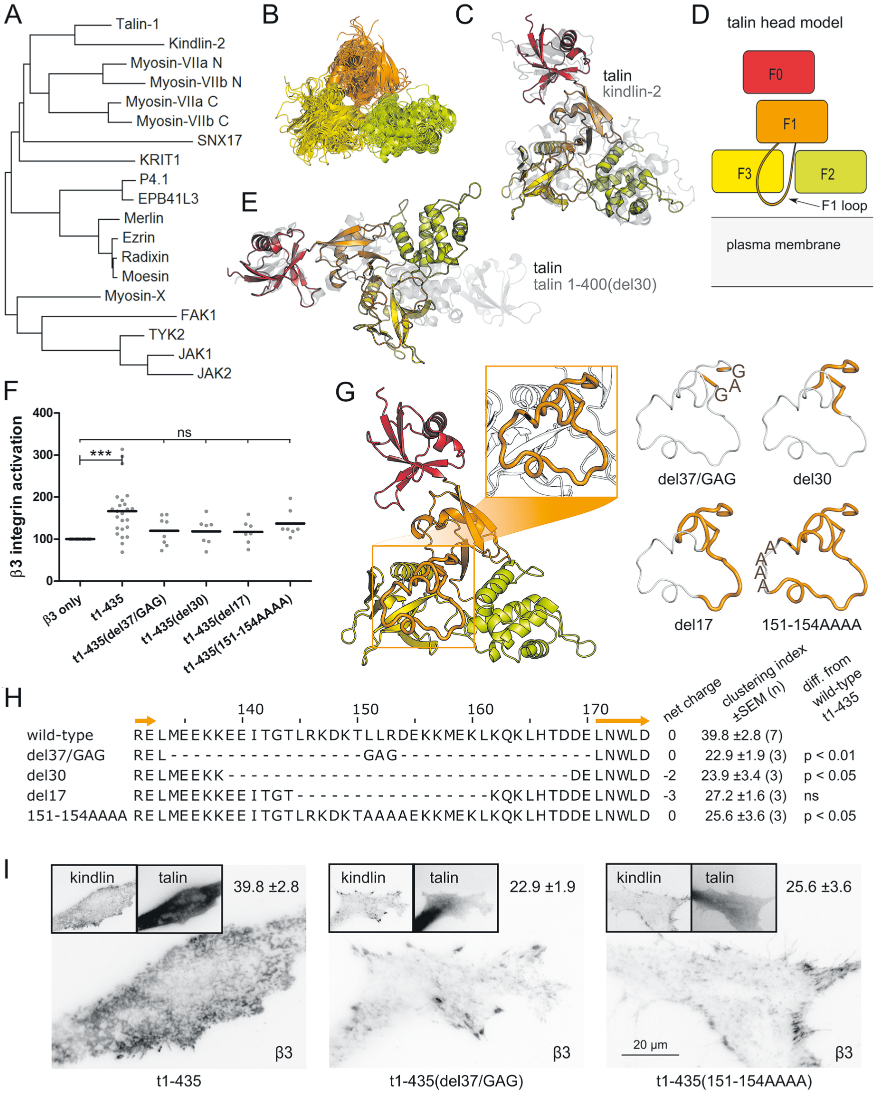

		net charge	clustering index ±SEM (n)	diff. from wild-type t1-435
wild-type	RELMEEKKEEITGTLRKDKTLLRDEKKMEKLKQKLHTDDELNWLD	0	39.8 ±2.8 (7)	
del37/GAG	REL-----------------GAG-----------------LNWLD	0	22.9 ±1.9 (3)	$p < 0.01$
del30	RELMEEKK------------------------------DELNWLD	-2	23.9 ±3.4 (3)	$p < 0.05$
del17	RELMEEKKEEITGT-----------------KQKLHTDDELNWLD	-3	27.2 ±1.6 (3)	ns
151-154AAAA	RELMEEKKEEITGTLRKDKTAAAAEKKMEKLKQKLHTDDELNWLD	0	25.6 ±3.6 (3)	$p < 0.05$

Fig. 2. See next page for legend.

conformation, adopted from a talin F1 subdomain NMR structure (PDB ID 2KC2) (Goult et al., 2010), is clearly different from the conformation of the F1 loop of kindlin-2. Similiar to the F1 loop in our talin model, the kindlin F1 loop is in contact with the F3 and F2 subdomains; however, the kindlin F1 loop is very long (~125 residues) compared to the talin loop (~40 residues).

Transmembrane and cytoplasmic domains of αIIbβ3 integrin and a lipid membrane were included in the MD simulation (Table S3). The talin head model remained in a stable FERM domain fold in all simulations except one, in which the F1–F2 interface slightly opened after 0.42 µs of simulation (PIP-A simulation; see Table S3). Generally, the F1, F2 and F3 subdomains remained in the FERM-like triangular assembly, with the F1 and F3 subdomains in contact and the F1 loop in close proximity to the integrin-binding site in the F3 subdomain throughout the 0.5–1 µs simulations. In this compact conformation, the talin head sat on the lipid membrane surface with lipid interaction sites in the F2 and F3 subdomains and in the F1 loop (Fig. S1). Whereas the F1 loop of an isolated F1 domain is

Fig. 2. The talin head contains a FERM domain composed of F1, F2 and F3 subdomains, and a loop within the F1 subdomain is important for β3–GFP integrin activation and clustering. (A) Talin FERM domain similarity to known FERM domains from the proteins detailed Table S6 analyzed using the ProbCons algorithm (Do et al., 2005) via JalView (Waterhouse et al., 2009), and visualized as maximum likelihood tree calculated using MEGA7 (Kumar et al., 2016). P4.1, protein 4.1 (also known as ERB41). (B) The structures of the same FERM domains aligned in PyMOL (Schrodinger). (C) We constructed a FERM-folded talin head model, shown here superimposed with the crystal structure of kindlin-2 (Li et al., 2017) (gray) and revealed to be essentially identical to the FERM-folded structure (P.Z., L.A., S.K. et al., unpublished). (D) In addition to the F1, F2 and F3 subdomains of a FERM domain, talin contains an extra ubiquitin-like subdomain F0 and a loop of more than 30 residues inserted in the F1 subdomain. Subdomains F2, F3 and the F1 loop possess acidic lipid binding activities (Anthis et al., 2009; Saltel et al., 2009; Goult et al., 2010). (E) Comparison of the FERM-folded talin head model and the extended crystal structure of talin 1–400(del139–168) (gray; PDB ID 3IVF; Elliott et al., 2010). (F) Integrin activation assay. Soluble ligand (SKI-7) binding to B16F1 cells transfected with β3–GFP integrin and different CFP-labeled talin head versions. Dots indicate activation indices (percentage relative to the control), and lines indicate mean values. β3 only, $n=26$; t1–435, $n=24$; t1–435(del37/GAG), $n=8$; t1–435(del30), $n=7$; t1–435(del17), $n=7$; and t1–435(151–154AAAA), $n=7$. Variation between the groups was determined by one-way ANOVA [$F(5,73)=7.527$, $P<0.0001$] and Tukey's multiple comparison test, showing no significant difference (ns) between groups except for β3 only versus t1–435 (***$P\leq0.001$). (G) Localization of the F1 loop within the FERM domain model. The deleted loop regions (thin, gray backbone) are shown within the F1 loop (orange, thick backbone) on the right. The amino acid sequences of the F1 loop truncations are shown in H, presenting the F1 subdomain residues 131–175 of wild-type talin-1. β3–GFP integrin clustering indices of t1–435 talin head and its loop-modified forms are given next to the sequence alignment. Variation between groups was assessed with a one-way ANOVA [$F(5,16)=8.967$, $P=0.0003$] and Tukey's multiple comparison test (with 15–25 cells analyzed per experiment) to calculate the P-values indicated in the figure. The t1–435 only condition was used as control (mean±s.e.m.: 15.6±2.9, $n=3$). (I) Representative TIRF (kindlin-1, β3 integrin) and epifluorescence (talin) images, and mean±s.e.m. β3–GFP integrin clustering indices, of the wild-type talin head t1–435 and two loop-modified talin head forms are shown. Scale bar: 20 µm.

highly flexible (Goult et al., 2010), the compact, FERM-folded talin head stabilized the F1 loop conformation, with conserved regions of the loop contributing to interactions with integrin, talin head and lipids, as summarized in Fig. S1.

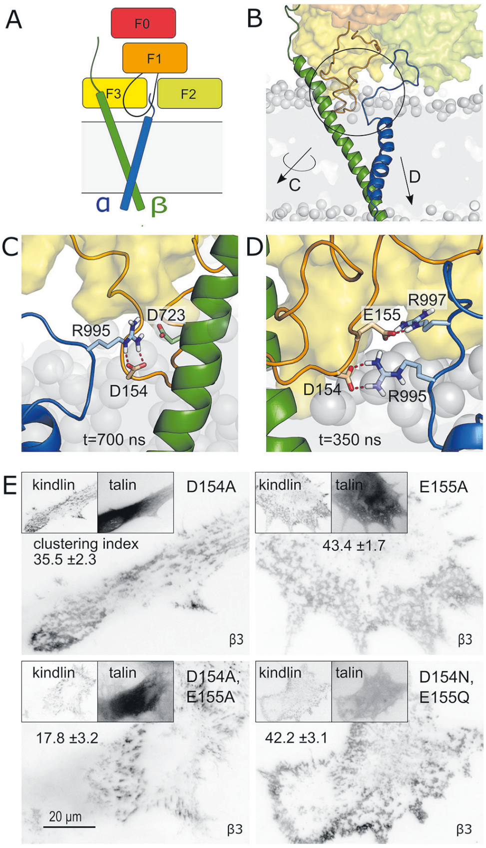

Fig. 3. The F1 loop residues D154 and E155 are critical for β3–GFP integrin clustering. The position of the F1 loop, α- and β-integrin subunits are shown in a schematic manner (A) and in an MD simulation (B). The circled region is shown expanded in C and D (arrows). (C) The D154 residue in the F1 loop interfered with the R995–D723 salt bridge of the integrin αIIbβ3 dimer at the cytoplasm–membrane border in all MD simulations, and a stable salt bridge between talin F1 loop and αIIb R995 was formed. The image is a snapshot from the PIP-B simulation (nomenclature explained in Table S3) at t=700 ns. (D) Salt bridge formation between F1 loop residue E155 and αIIb integrin R997 was observed in three simulations. The image is a snapshot from the no-PIP-B simulation at t=350 ns. (E) Representative TIRF (kindlin-1, β3 integrin) and epifluorescence (talin) images and mean±s.e.m. β3–GFP integrin clustering indices for cells expressing the indicated mutant variants of the talin head domain. Statistical significance was assessed using a one-way ANOVA [$F(4,19)=9.258$, $P=0.0003$] and Tukey's multiple comparison test. Integrin clustering efficiency was significantly compromised in cells expressing t1–435(D154A,E155A) compared to cells expressing wild-type t1–435 talin head ($P<0.001$), whereas the other mutants did not significantly differ from t1–435. The numbers of experiments analyzed were: t1–435, $n=10$; t1–435(D154A), $n=3$; t1–435(E155A), $n=4$; t1–435 (D154A,E155A), $n=4$; and t1–435 (D154N,E155Q), $n=3$; 15–25 cells analyzed per experiment. Scale bar: 20 µm.

Talin F1 loop interacts directly with the inner membrane clasp of integrins

A salt bridge connects the αIIb and β3 integrin chains as part of the inner membrane clasp that controls integrin activation (Hughes et al., 1996; Anthis and Campbell, 2011). In the MD simulations, the talin F1 loop residue D154 competed with D723 of β3 integrin for binding to R995 of αIIb integrin (Fig. 3A–C), and a D154–R995 salt bridge formed after 3–180 ns (mean±s.d. distance between charged groups 3.5±0.3 Å). As a consequence, the contact between D723 and R995 was lost in all talin–integrin–lipid simulations (charged group distance 6.3±2.1 Å), whereas in control simulations without talin, the D723–R995 contacts were more stable (charged group distance 4.8±0.8 Å).

Based on the MD simulations, we hypothesized that a D154A substitution could block integrin clustering in cells. However, D154A had no significant effect on clustering (Fig. 3E), and closer inspection of the simulation data revealed an additional salt bridge connecting the F1 loop residue E155 with the αIIb integrin residue R997 in three out of four simulations (charged group distance 3.8±0.8 Å, $n=3$ simulations), suggesting that either of the D154 and E155 residues might interact with αIIb integrin (Fig. 3D). Indeed, although a single E155A mutation had no effect on clustering, replacement of both D154 and E155 with alanine residues was as harmful to integrin clustering as the complete deletion of the F0–F1 subdomains. In contrast, replacement with asparagine and glutamine (D154N, E155Q) preserved wild-type-like integrin clustering (Fig. 3E).

A previous report has shown that the combined charge inversion of adjacent R153E and K156E residues, as well as that of R146E, prevented lipid interaction of the F1 domain, as well as integrin activation in the context of the talin head domain (Goult et al., 2010). We therefore also tested talin head mutants R153A (LLR^{153}D-LLAD) and L151A, L152A, D154A (LLR^{153} D-AARA), to detect potential interference of integrin clustering. Similarly to the individual D154A mutant, both of these mutants showed normal talin-induced integrin clustering (Fig. S1C), suggesting that membrane binding of the F1 loop is shared by multiple basic residues, as is the potential to activate and cluster integrins by the acidic motif.

Both molecular modeling and integrin clustering assays thus suggested that acidic residues in the F1 loop regulated β3 integrin activation and clustering. To assess whether this regulation takes place via direct interaction of the talin F1 loop with the integrin heterodimer in living cells, we introduced cysteine residues into sites along the inner membrane clasp of β3 integrin and along the mid-part of the F1 loop. We avoided the mutation of residues directly involved in the stabilization of the inner membrane clasp, such as D723 and R995, which might have modified the integrin activation and clustering state independently of kindlin and talin. COS7 cells were transfected with plasmids encoding mouse αv integrin (also known as ITGAV) and human kindlin-1, along with cysteine-mutated talin heads and β3 integrins. To prevent palmitoylation of these newly added cysteines, cells were incubated overnight with bromopalmitate prior to permeabilization with saponin. During saponin permeabilization, cysteine thiol groups were oxidized with copper phenanthroline to promote covalent integrin–talin binding via intermolecular disulfide bonds within integrin–talin complexes persisting in the cells during the permeabilization and oxidation treatment (Fig. 4A). After cell extraction, covalently linked proteins were subsequently identified using non-reduced SDS–PAGE followed by western blotting. Of the five different integrin mutants tested, only the β3(H722C) and β3(I719C) integrin variants yielded covalent heterodimers with the t1–435(L152C) and t1–435(D154C) talin head mutants, representing a restricted subset of the five different F1 loop variants tested (Fig. 4B–E; Fig. S2). In addition, β3(H722C) formed a heterodimer with t1–435(L151C). It is important to note that in the extended talin head conformation (Elliott et al., 2010), the F1 loop and integrin would not reach sufficiently close proximity for disulfide bonding, whereas the FERM-like conformation would enable the observed contacts between the F1 loop and the β3 integrin, and would therefore also explain an interference of the F1 loop with β3 integrin binding to the F3 domain *in vitro* (Table S2).

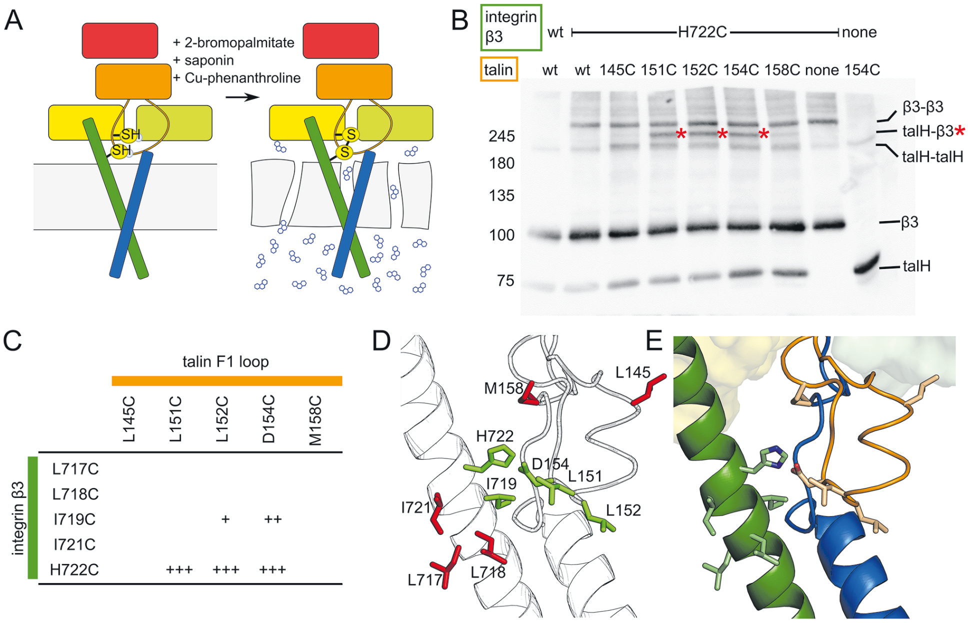

Fig. 4. The F1 loop directly interacts with β3 integrin in COS7 cells. (A) Schematic diagram of the cysteine mapping procedure. Cysteine-mutated CFP–talin head and β3–GFP integrin, as well as RFP–kindlin-1 and unlabeled αv integrin were overexpressed in COS7 cells. The cells were treated with 2-bromopalmitate to prevent cysteine palmitoylation, the membrane was permeabilized with saponin and oxidizing conditions were introduced by treating the cells with phenanthroline, allowing neighboring cysteines in the cytoplasm (above the membrane) to form disulfide bridges. Blue small molecules represent phenanthroline. (B) Representative anti-GFP western blot showing either wild-type (wt) or H722C β3 integrin crosslinking to wt or cysteine-mutated talin heads (talH). Talin–integrin heterodimers in the L151C, L152C and D154C lanes are highlighted with asterisks. (C) Disulfide bonding efficiencies between talin (horizontal) and integrin residues (vertical). (D) The target residues of cysteine mapping in integrin and talin are shown as sticks. Disulfide-bonding residues are shown in green and non-bonding residues in red. (E) Colored representation of D, cysteine-mutated residues from integrin (green) and the F1 loop of talin (orange) are shown as sticks.

The F1 loop is in contact with the FERM-folded talin head

In order to obtain further insight into the role and position of the F1 loop in the compact FERM-folded talin structure, we closely analyzed the interface between subdomains F2 and F3 (Fig. 5A). In previously published talin head structures that either did not include the F0 and F1 domains (Anthis et al., 2009) or showed the elongated talin head fold (Elliott et al., 2010), the F2–F3 domains are closely associated and linked together by a salt bridge connecting E269 and K345. However, this salt bridge was not present in our FERM-based model, or in the FERM-folded talin head structure (P.Z., L.A., S.K. et al., unpublished). This led to large solvent-exposed surfaces in the model, which were centered around a solvent-exposed Leu314 in the F3 subdomain and Gly226 in the F2 subdomain, forming potential surfaces for interaction with the F1 loop (Fig. 5A). Indeed, observations of our MD simulations suggested stable hydrophobic and charge–charge interactions of C-terminal F1 loop residues with both the F3 (Fig. 5B) and F2 subdomain surfaces (Fig. 5C).

To investigate whether such F1 loop interactions with the F2 and F3 subdomains would be stable, and whether they contribute significantly to domain–domain interactions within the talin head, we applied two mass spectrometry methods to study the compactness and subdomain interactions of the talin head in

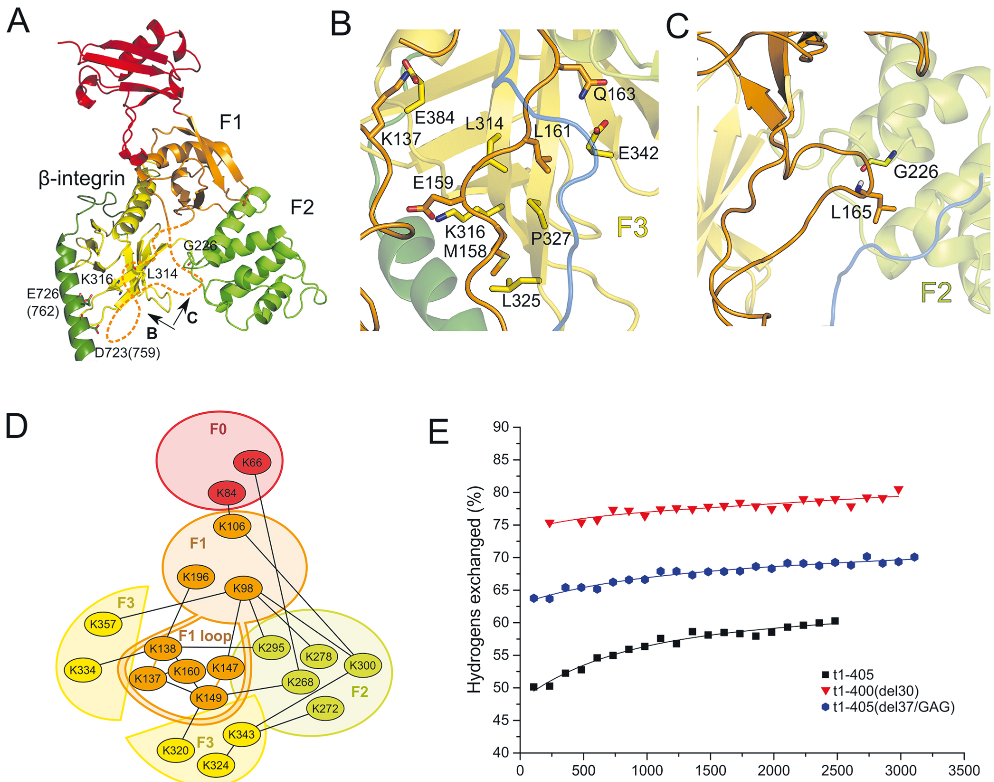

Fig. 5. The F1 loop interacts with F2 and F3 subdomains in the FERM-folded talin head. (A) Overlay of the FERM-folded talin head model with talin-2(F3)–β1D integrin tail (Anthis et al., 2009), fitted at the F3 domain. Please note the gap between F2 and F3 domains with exposed hydrophobic residues such as L314 in F3, or short side chains like G226 in F2 (talin-1 numbering). The missing F1 loop in these structures is indicated by a dotted orange line. Acidic residues in the membrane-proximal domain of β1D integrin known to participate in the inner membrane clasp are numbered as in β3- and β1D-integrins (brackets). Arrows denote regions shown in B and C, as indicated. (B) Interface of F3 with F1 loop from the MD simulation, showing hydrophobic side-chain matching and reciprocal charge distributions. (C) View of the F2–F1 loop interface with anchored L165 sidechain in the F2 subdomain. Please note the trace of the α integrin cytoplasmic tail in blue. (D) Lysine–lysine crosslinking of talin head t1–405. Disuccinimidyl suberate crosslinking followed by trypsin treatment and mass spectrometry analysis showed short distance (linker length ∼1 nm) interactions within the talin head subdomains and F1 loop. The crosslinks are shown as black lines. The proximity of residues K137 and K138, and K147 and K149, in the F1 loop is highlighted with orange lines. Only a single molecular weight was detected for each crosslink, except K272–K343, which was identified via two different peptides. Please note the crosslinks of K149 from the F1 loop with both the F2 residue K268 and F3 residue K320, demonstrating proximity of the F1 loop to both F2 and F3 subdomains. (E) Hydrogen–deuterium exchange mass spectrometry analysis comparing the solvent accessibility of residues in the intact talin head t1–405 and in two F1 loop-deleted forms, measured as percentage of hydrogens exchanged as a function of time. The red curve shows data for the t1–400(del30) construct, representing the elongated talin head, while the blue curve represents the loop-deleted FERM-folded talin head.

solution. Firstly, we characterized the inter-subdomain interactions in the talin head by crosslinking lysine residues using disuccinimidyl suberate (DSS). Monomeric talin head was separated from its oligomeric species by electrophoresis, then trypsinized and analyzed by mass spectrometry. The analysis confirmed that the F1 loop readily interacts with the F1, F2 and F3 subdomains (Fig. 5D; Table S4). However, a further classification of the crosslinks was difficult, because the potential flexibility of the F1 loop may dynamically sample the subdomain surfaces to induce multiple crosslinks from one given loop residue. For example, K149, which in our F1 loop model was solvent exposed, formed crosslinks with both K268 from the F2 subdomain and K320 from the F3 subdomain (Fig. 5D; Table S4). The latter crosslink further suggests that the F1 loop can indeed contact regions of the F3 domain that are otherwise relevant for β integrin binding to talin (Anthis et al., 2009) and integrin clustering (Saltel et al., 2009), indicative of a gatekeeper function for the F1 loop.

Secondly, because the crosslinking approach provided limited information about the specific positions of the F1 loop, we analyzed the compactness of three talin head forms using hydrogen–deuterium exchange mass spectrometry (HDX-MS). The HDX-MS profiles of the talin head variants t1–405, t1–400(del30) and t1–405(del37/GAG) showed major differences in their deuterium intake versus exchange time (Fig. 5E). The native form containing an intact F1 loop (t1–405) clearly showed the lowest HDX rate among the talin forms (up to ∼60% in 2500 s), and had a population of very rapidly exchanging (burst phase) hydrogens, which represented labile side-chain or non-hydrogen-bonded, solvent-exposed backbone hydrogens. In addition, ∼40% of all hydrogens in t1–405 were tightly hydrogen bonded or located in the hydrophobic core and were not exchanged within 1 h of reaction time. The HDX rate was, however, clearly faster for the loop-deleted form t1–405(del37/GAG) and even faster for t1–400(del30), which corresponds to the construct that formed the extended talin head structure during crystallization. Thus, the results suggest that the F1 loop is an integral part of the talin head structure, where it covers parts of the F2 and F3 domains. On the other hand, the C-terminal lysines, absent in the tl–400(del30) construct, may connect the F3 and F1 subdomains, thereby stabilizing the compact structure. Whereas the removal of the F1 loop results in new solvent-exposed talin residues, moderately increasing the HDX rates, the additional C-terminal truncation of the talin head (t1–400) induces an open and flexible structure that is reflected by a further considerable increase in HDX rates (Fig. 5E).

Lastly, we studied the t1–405, t1–405(del30) and t1–405(del37/GAG) talin head variants using small-angle X-ray scattering (Fig. S3). Inline size exclusion chromatography was utilized to ensure monodisperse scattering data derived only from monomers. Kratky analysis indicated that all of the talin forms studied were partially flexible, with t1–405(del37/GAG) being slightly more compact than the other forms (Fig. S3E). To account for the apparent flexibility of talin in solution, we analyzed the talin head solution conformation using the Ensemble Optimization Method (Eom) (Tria et al., 2015). In this analysis, the Eom program generated a pool of talin head domain models from the individual subdomain 3D structures (PDB ID 3IVF; Elliott et al., 2010) with the missing F1 loop and linkers *ab initio*-modeled as dummy residues. The program then selected an ensemble of conformations that best fitted the scattering data using a genetic algorithm, and this conformational ensemble was represented by a few conformations. The analysis suggested that most of the talin head molecules in the samples were in a FERM-like conformation (Fig. S3). Moreover, the calculated conformational ensembles of all the talin head forms showed narrow R_g distributions, and again the t1–405(del37/GAG) was observed to be more compact than the other talin head forms or a random pool (Fig. S3). The results thus propose that FERM-shaped talin head folds are the major constituent of the talin samples, irrespective of the presence or absence of the F1 loop.

The F1 loop is critical both in the talin head and in full-length talin

All of our cell biological experiments reported thus far were carried out with the talin head domains in a β3 integrin context. Talin head alone does not become autoinhibited and, hence, is more potent in integrin activation and clustering than full-length talin (Goksoy et al., 2008; Saltel et al., 2009). However, the head domain alone is not properly coupled to the cytoskeleton (Cluzel et al., 2005), because two of the three actin-binding sites in the talin protein are located in the rod domain (Hemmings et al., 1996). To analyze the function of the F1 loop within the complete protein, we expressed wild-type (t1–2541), loop-deleted [t1–2541(del37/GAG)] and point-mutated talins in talin-1$^{-/-}$ talin-2$^{-/-}$ mouse kidney fibroblast cells (Theodosiou et al., 2016) and detected the extended and activated forms of β1 integrin by FACS using the conformation-specific 9EG7 monoclonal antibody. Whereas no 9EG7 staining was detected on talin-null cells, the expression of wild-type talin t1–2541 protein rescued the 9EG7 staining to levels comparable to those in talin-floxed cells (data not shown). The loop-deleted talin t1–2541(del37/GAG) only partially activated β1 integrins, comparable to the effects of an R358A talin mutant [t1–2541(R358A)], which reportedly reduces β3 integrin binding (García-Alvarez et al., 2003). The loop deletion was, however, less harmful to integrin activation than the membrane-proximal β integrin binding site mutant t1–2541(K316E,K324E) (Saltel et al., 2009) (Fig. 6A). Furthermore, the previously proposed phosphomimetic F1 loop mutant t1–2541(T144E,T150E) activated β1 integrin less efficiently than wild-type t1–2541, which is also consistent with the reduced β3 integrin binding of a talin head construct of this mutant *in vitro* (Table S2). In contrast, the phosphorylation-deficient variant t1–2541(T144A,T150A) behaved like wild-type talin in the β1 integrin activation assay (Fig. 6A), and showed kindlin-1-independent integrin clustering in B16F1 cells (Fig. S1D). This suggests that the loop structure and integrin activation function is modulated by phosphorylation at these residues.

Thus, the loop deletion in full-length talin impaired the activation of β1 integrin in suspended cells. Although the ‘inside-out’ activation by loop-deleted talin works poorly in this situation, tension from integrin attachment to a rigid fibronectin-coated surface may still provide ‘outside-in’ activation of integrins, leading to integrin clustering and cell spreading. Indeed, on a rigid and saturated fibronectin substrate, besides a reduction in cell spreading area, talin-knockout cells expressing wild-type or F1 loop-deleted talin (t1–2541) constructs spread comparably (data not shown).

To explore cell spreading in a more natural setting, we used cell-derived 3D fibronectin-containing matrices. After an incubation of 6 h, cells expressing loop-deleted talin had an area of 870±335 μm^2 (mean±s.d.), whereas cells expressing the intact talin form had spread out to an area of 1359±503 μm^2 (Fig. 6B,C). Intriguingly, cells expressing wild-type talin formed longer ‘fibrillar-like’ adhesions, whereas in cells transfected with loop-deleted t1–2541(del37/GAG) talin, adhesions were shorter (Fig. 6D). Thus, β1 integrin activation was partially inhibited by the loop deletion, affecting cell spreading in complex 3D matrices and the elongation of adhesions along 3D extracellular matrix fibrils.

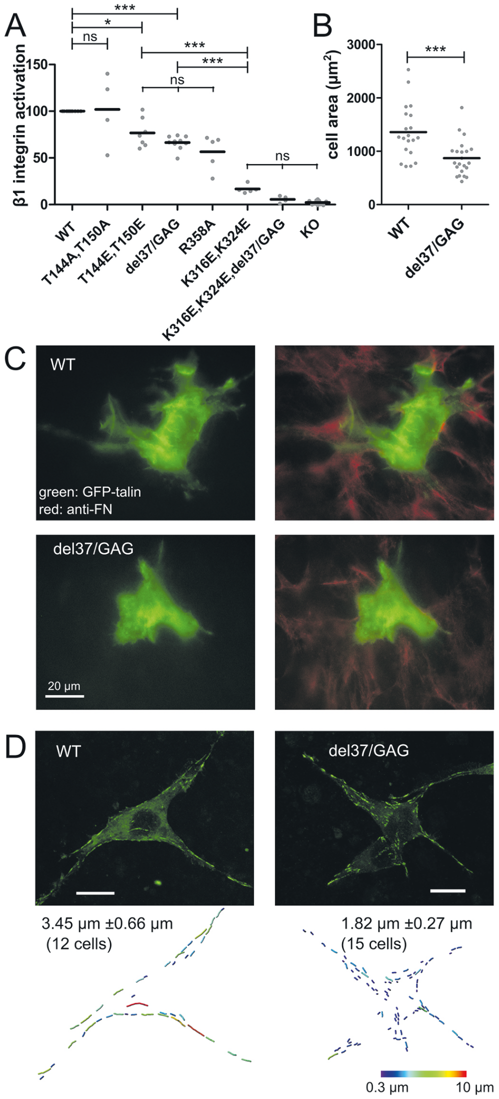

Fig. 6. F1 loop-deleted full-length talin rescues integrin activation in talin-knockout cells, but both integrin activation and adhesion maturation are impaired. (A) Activation of β1 integrin by wild-type (WT) and F1 loop-deleted full-length talin. Talin knockout cells (KO, $n=10$), and cells expressing talin constructs with an N-terminal GFP tag (WT, $n=10$; del37/GAG, $n=10$; T144E T150E, $n=7$; T144A T150A, $n=4$; R358A, $n=5$; K316E K324E, $n=5$; and K316E K324E+del37/GAG, $n=4$). The activation indices were normalized to GFP-tagged wild-type talin. Normalized activation indices are shown as points, with the mean indicated by a line. Statistical analysis was carried out using a one-way ANOVA [$F(7,47)=66.13$, $P<0.0001$] and Tukey's multiple comparison test. (B) Spreading of talin-knockout cells expressing the wild-type ($n=42$ cells) and F1 loop-deleted ($n=30$) full-length talin on a 3D matrix. Cell area was measured at 6 h. Lines indicate the mean values. Statistical analysis was carried out using an unpaired two-tailed t-test [$t(40)=3.740$, $P=0.0006$]. (C) Cell spreading and fibronectin remodeling in 3D culture. Representative talin-knockout cells expressing the indicated talin variants are shown. Red, anti-fibronectin; green, GFP–talin. (D) Top: two representative talin-knockout cells expressing the wild-type and loop-deleted GFP-labeled full-length talins are shown. Green, GFP–talin. Bottom: average single adhesion lengths (mean±s.e.m.) of the indicated number of cells, along with individual adhesions for the representative cells, color-coded by length of adhesions as determined using the Imaris software (Bitplane, Zürich, Switzerland). Scale bars: 20 µm. $^{*}P\leq0.05$; $^{***}P\leq0.001$; ns, not significant.

DISCUSSION

Talin plays a key role in integrin-mediated cell–matrix interactions. The function of the F1 loop in the talin head domain has been found important in previous studies, where it was proposed that it either worked through a fly-cast mechanism (Goult et al., 2010) or by continuing the lipid-binding ridge of the F3 and F2 subdomains towards the N-terminal part of an extended form of the talin head domain (Kalli et al., 2013). The reduction of integrin activation and clustering by phosphorylation of F1 loop residues (Fig. 6; Goult et al., 2010) may indeed suggest that differential membrane interaction of the F1 loop controls integrin function. Similarly the loss of kindlin-mediated control of integrin clustering by T144A/T150A substitutions in the F1 loop (Fig. S1D) is consistent with altered muscle attachment site remodeling observed for a T152A mutant in *Drosophila* (Katzemich et al., 2019), and may also indicate a link between kindlin and the phosphorylation state of the F1 loop. However, independent of the regulation of the talin–membrane interaction, the identification of conserved acidic residues critical for integrin activation and clustering that are localized immediately adjacent to the inner membrane clasp reveals a much more direct way of controlling integrin activation and clustering than by differential membrane recruitment of the talin head.

The crosslinking and SAXS data suggest that the head domain of talin assumes a compact FERM fold, which positions the talin F1 loop next to the integrin-binding site in the F3 subdomain of talin (K316, K324 and L325; see Fig. 5B). This site in talin interacts with the membrane proximal acidic (Saltel et al., 2009) and hydrophobic (Wegener et al., 2007) integrin-activity regulating motif D^{723}R[K/R]EFAKF to take a central role in the β1- and β3-integrin activation and clustering process regulated by talin and kindlin. Selected acidic residues of the F1 loop appear to target the positively charged juxtamembrane residues in the integrin α subunit thereby interfering with the inner membrane clasp and inhibiting α–β subunit association in order to stabilize the extended conformation of the integrin. The recently reported binding of the Rap1 adaptor to the talin F1 or F0 subdomains (Zhu et al., 2017; Bromberger et al., 2018; Lagarrigue et al., 2018; Gingras et al., 2019) might, in turn, help to stabilize the orientation and membrane tethering of the FERM-folded talin head in order to strategically position the F1 loop and to regulate integrin activation in an F1 loop-dependent manner (Gingras et al., 2019).

While talin and kindlin binding to integrins rearranges the integrin juxtamembrane- and ecto-domains, talin itself is also regulated through conformational changes (Goksoy et al., 2008; Song et al., 2012; Goult et al., 2013; Ye et al., 2016). Our results suggest that additional subtle regulations of the talin–integrin interface may take place within the talin head. The deletion of either the entire F0–F1 subdomains or only the F1 loop enhanced talin head binding to wild-type β3 integrin, whereas phosphomimetic mutations (T144E, T150E) in the F1 loop reduced this binding (Table S2), suggesting that the phosphorylation of the F1 loop can regulate β3–F3 interactions. Accordingly, the phosphomimetic T144E, T150E mutations impaired β1 integrin activation by full-length talin (Fig. 6A) and β3 integrin clustering by the talin head (Fig. S1D). Moreover, the mutagenesis of T144 and T150 (T144A, T150A) enhanced integrin clustering independent of additional kindlin-1 expression. In contrast, both the neutral F1 loop mutant (151–154AAAA) and the mutant with increased net charge (D154A, E155A) clustered integrin poorly (Figs 2F,G and 3E), suggesting that the F1 loop has functions beyond charge interactions with membrane lipids. We observed that the L152 residue of the LLRD151–154 region can stretch and enter into the hydrophobic core of the membrane in all talin–integrin–lipid simulations (Fig. S1A). The LLRD stretch may thus help to guide the D154 or E155 residues to membranes and even to interact directly with integrin at the level of the inner membrane clasp (Fig. 4). The F1 subdomain, and the F1 loop in particular, may therefore function as a gatekeeper in raising the threshold for initial talin–integrin association, while promoting the stability of the unclasped, activated form of the bound integrin heterodimers.

This model is particularly interesting in the light of mechanical tension exerted on the integrin bond. When the talin head induces integrin activation and clustering in a low-force regime, the presence of the F1 loop is required for maintaining the conformational changes of cell-surface-exposed integrins for rapid binding of soluble ligands (inside-out activation). In contrast, when integrins are exposed to mechanical forces, such as those encountered within a rigid 3D matrix scaffold, the integrin catch bond is able to maintain the extracellular domain in a ligand-bound conformation, reducing the requirement for the F1 loop to keep the integrin activated. Therefore, the equilibrium between different integrin conformations at the cell surface, and their functional roles, could be regulated by the F1 loop and the affinity of the talin head for the integrin. Thus, the different types of ECM adhesion and differential remodeling capacity of the extracellular matrix, as recently shown for the β1A- and β1D-integrin splice variants (Soto-Ribeiro et al., 2019), could be explained by different affinities for the talin head domain (Anthis et al., 2010) as well as changes in integrin signaling capacities that potentially affect talin F1 loop residues (Katzemich et al., 2019).

In conclusion, structural and mutational analysis shows that the conformation of the talin head in solution adopts the shape of a FERM domain. In cells, the talin F1 loop directly interacts with residues of the inner membrane clasp of integrins, enabled by the specific projection of the F1 loop from a compact FERM-folded talin head. The FERM configuration of talin provides a scaffold that allows the docking of upstream integrin regulators such as Rap1, in order to position the F1 loop for the talin-dependent regulation of β integrin activation and clustering (Fig. S4). This integrin activation process is assisted by a kindlin-dependent mechanism that leads to integrin clustering, which is required for efficient linkage of integrins to the actin cytoskeleton, and by regulation of integrin signaling, which in turn can be modulated by the phosphorylation state of the F1 loop of talin.

MATERIALS AND METHODS

Protein production

Talin head domains (Table S1) were expressed using the pTrcHis C vector (Thermo Fisher Scientific, Carlsbad, CA), which includes an N-terminal hexahistidine tag (MGGSHHHHHHGMASMTGGQQMGRDLYDDDDKDRWIRPRA). The sequence-confirmed plasmids were introduced into *E. coli* BL21-Star cells (Thermo Fisher Scientific). Bacteria were cultured in LB medium containing 100 µg/ml of ampicillin at 37°C. IPTG (1 mM) was used to induce protein expression at an optical density of 0.4, and cells were harvested after 5 h of incubation. *E. coli* extracts were prepared by homogenization (Emulsiflex C3) in 20 mM $NaPO_4$ pH 7.4, 1 M NaCl and 20 mM imidazole. Clarified lysates were applied to a HisTrap FF 5 ml affinity column (GE Healthcare) using an ÄKTA purifier (GE Healthcare). Talin head domains were eluted from columns using 20 mM sodium phosphate buffer pH 7.4 containing 1 M NaCl with gradually increasing imidazole concentration (20–700 mM). Eluted fractions were analyzed by SDS–PAGE and Coomassie staining and were pooled when appropriate. Furthermore, talin head domains were purified using a HiTrap SP FF 1 ml column (GE Healthcare) after dilution (1:10) in 50 mM $NaPO_4$, 20 mM NaCl, pH 7.2 buffer. Elution was performed by preparing a linear NaCl gradient with 50 mM $NaPO_4$, 1 M NaCl pH 7.2 buffer.

GST–β3-integrin-tail fusion constructs (WT-beta3, GST–GSKLLITIHDRKEFAKFEEERARAKWDTANNPLYKEATSTFTNITYRGT; and beta3-VE, GST–GSKLLITIHDRKEFAKFEEERARAKWVENPLYKEATSTFTNITYRGT) were expressed in *E. coli* BL21-Star cells using a similar approach. Cells were lysed by homogenization (Emulsiflex C3) in phosphate-buffered saline (PBS) pH 7.4 buffer, and proteins were purified with Glutathione Sepharose (GE Healthcare 4 Fast Flow) using buffer containing 50 mM Tris-HCl pH 8 and 20 mM reduced glutathione as eluent. Eluted fractions were analyzed with SDS–PAGE, Coomassie staining, and western blotting using mouse anti-GST B-14 (Santa Cruz) and goat anti-mouse antibodies. Fractions containing the desired proteins were dialyzed into 50 mM sodium phosphate buffer, pH 7.2, containing 150 mM NaCl and stored at −20°C.

The homogeneity of the purified proteins was evaluated using dynamic light scattering (Malvern Zetasizer ZS). The purified talin proteins were also subjected to high-resolution mass spectrometric analysis. The mass spectra indicated that the protein samples were pure and homogeneous, and the determined accurate masses were in a full agreement with those calculated from the sequences.

Mass spectrometry

Talin head molecular weight determination and hydrogen–deuterium exchange mass spectrometry experiments were performed on a Bruker Apex-Qe FT-ICR instrument (Bruker Daltonics, Billerica, MA), equipped with an Apollo-II ESI source and an actively shielded 12-T superconducting magnet. First, all talin samples were buffer exchanged into 200 mM ammonium acetate (pH 7) using Sephadex G-25 columns (PD-10; GE Healthcare Life Sciences). The protein concentrations were determined by absorbance at 280 nm using sequence-derived extinction coefficients. The samples were further diluted with acetonitrile:water (50:50 v/v) containing 1% acetic acid to a final concentration of 1–10 µM. The produced protein ions were accumulated in the collision cell for 100 ms and transferred to the Infinity ICR cell for trapping, broadband (*m/z* 500–3000) excitation and detection. For each spectrum, a total of 200 time-domain transients (1 MWord) were co-added. All mass spectra were externally calibrated by using ESI-L Tuning Mix calibration mixture (Agilent Technologies). The spectral acquisition and data post-processing were accomplished using Bruker DataAnalysis 4.4 software. Neutral, most abundant protein masses were obtained through a standard charge deconvolution and compared to those calculated from the protein sequences (Table S1).

Hydrogen–deuterium exchange

In hydrogen–deuterium exchange mass spectrometry (HDX-MS) experiments, all talin samples were first buffer-exchanged to 200 mM ammonium acetate (pH 7) by using Sephadex G-25 columns (PD-10; GE Healthcare Life Sciences). The protein concentrations were determined by absorbance at 280 nm using sequence-derived extinction coefficients. The determined protein concentrations varied between 5 and 50 µM. Native HDX-MS measurements were subsequently performed by diluting 40 µl of each protein stock solution with 160 µl of D_2O (99.9% D) to initiate HDX. Therefore, the maximum theoretical deuterium intake was 80%. In order to obtain sufficient spectral intensities for the least concentrated talin samples, greater dilution factors could not be used. After mixing, the samples were immediately delivered to a 250 µl Hamilton glass syringe and continuously infused (1.5 µl/min) to the ESI source using a syringe pump. The ESI-generated ions were accumulated in the collision cell and transferred to the Infinity ICR cell for trapping, broadband (*m/z* 1000–5000) excitation and detection. All ion source and ion transmission parameters were optimized for native MS experiments. The HDX mass spectra were measured in an automated fashion by 125-s intervals (the first spectrum was acquired after a period of 107.5 s to ensure that the spray current had been stabilized) up to ∼1 h. For each spectrum, a total of 40 time-domain transients were co-added and fast-Fourier transformed prior to magnitude calculation. Each recorded transient had only a 128-kWord data size (equal to the transient length of ∼0.11 s) to increase the time-resolution of the experiments (at the expense of spectral resolution). The final transformed data were downsampled to 32 kWord using Gaussian multiplication to improve peak shapes and allow straightforward peak centroid location, and finally charge deconvoluted. The control experiments (0% D) were performed by diluting the protein samples with H_2O instead; these experiments were performed with two different time-domain data sizes (128 and 1024 kWord), the latter providing isotopically resolved spectra for a more accurate molecular mass determination. All mass spectra were externally calibrated by using ESI-L Tuning Mix calibration mixture (Agilent Technologies). The spectral acquisition and data processing was accomplished using Bruker XMASS 7.0.8 software.

The data analysis for HDX-MS experiments was as follows. The maximum theoretical number of exchangeable hydrogens (D_{max}) in each protein construct was calculated as: $D_{\mathrm{max}}=3n_{\mathrm{Arg}}+2n_{\mathrm{Lys}}+2n_{\mathrm{Gln}}+2n_{\mathrm{Asn}}+n_{\mathrm{His}}+n_{\mathrm{Ser}}+n_{\mathrm{Thr}}+n_{\mathrm{Cys(SH)}}+n_{\mathrm{Tyr}}+n_{\mathrm{Asp}}+n_{\mathrm{Glu}}+n_{\mathrm{total}}+n_{\mathrm{charge}}-n_{\mathrm{Pro}}-1$, where n_{Xxx} is the number of the respective residue in the sequence, n_{total} is the total number of residues (counting for backbone amide hydrogens) and n_{charge} is the average number of charges in the observed protein ions. The relative deuterium intake (% D) at each time point was calculated as $\%\ D=(m_{\mathrm{D}}-m_{\mathrm{H}})/(0.80\times D_{\mathrm{max}})$, where m_{D} and m_{H} are the masses of the deuterated and undeuterated protein samples, respectively. For each time point, the HDX reaction time (t_{react}) was calculated as $t_{\mathrm{react}}=(t_{\mathrm{start}}-t_{\mathrm{end}})/2$, in which t_{start} and t_{end} are the starting and ending time points of the spectral acquisition. This calculation assumes roughly linear deuterium intake for the given time window. Finally, % D was plotted against t_{react}, and the data were fitted with a kinetic model of three exponential terms, representing fast, slow and very slow exchanging hydrogens. The fitting was accomplished using OriginPro 15 software (OriginLab Corporation).

Disuccinimidyl suberate crosslinking

A talin head sample (t1–405, 1 mg ml^{-1} in $NaPO_4$ pH 7.2 and 150 mM NaCl) was crosslinked with 50× molar excess of disuccinimidyl suberate (DSS) according to the manufacturer's instructions (Thermo Fisher Scientific). The crosslinked talin particles were separated by electrophoresis on a Bolt 4–12% Bis-Tris Plus gel (Thermo Fisher Scientific). The ∼50 kDa bands were excised, and peptides were extracted from the gel slices by in-gel digestion according to methods previously described (O'Connell and Stults, 1997). Cysteine bonds were reduced with 0.045 M dithiothreitol (DTT; D0632 Sigma-Aldrich) for 20 min at 37°C, followed by alkylation with 10 mM iodoacetamide (57670 Fluka, Sigma-Aldrich) at room temperature. The proteins were then digested to peptides using sequencing-grade modified trypsin (V5113, Promega) at 37°C overnight. After quenching with 10% trifluoroacetic acid (TFA), the peptides were desalted by C18 reversed-phase spin columns according to the manufacturer's instructions (Harvard Apparatus). The eluted peptide sample was dried in vacuum centrifuge and reconstituted to a final volume of 30 µl buffer containing 0.1% TFA in 1% acetonitrile (ACN).

Liquid chromatography–mass spectrometry (LC-MS) analysis was performed on an EASY-nLC 1000 system (Thermo Fisher Scientific) connected to a Q-Exactive mass spectrometer (Thermo Fisher Scientific) with nano electrospray ionization sprayer (Thermo Fisher Scientific). In detail, peptides were eluted and separated with a C18 pre-column (Acclaim PepMap 100, 75 µm×2 cm, 3 µm, 100 Å; Thermo Fisher Scientific) and analytical column (Acclaim PepMap RSLC, 50 µm×15 cm, 2 µm, 100 Å; Thermo Fisher Scientific), using a 60 min buffer gradient ranging from 5 to 35% buffer B, followed by a 5 min gradient from 35 to 80% buffer B and 10 min gradient from 80 to 100% buffer B at a flow rate of 300 nl/min (buffer A: 0.1% formic acid in 98% HPLC grade water and 2% ACN; buffer B: 0.1% formic acid in 98% ACN and 2% water). For direct LC-MS analysis, 4 µl peptide sample was injected to the LC-MS/MS and analyzed. Data-dependent FTMS acquisition was in positive ion mode for 80 min. A full scan (200–2000 *m/z*) was performed with a resolution of 70,000, followed by top10 CID-MS2 ion trap scans with resolution of 17,500. Dynamic exclusion was set for 30 s.

The search engine pLink (v2.3.3; http://pfind.ict.ac.cn/software/pLink) (Lu et al., 2015) was used to identify the intra-protein crosslinked peptides. The precursor mass tolerance was set at 10 ppm and 0.05 Da for the fragment mass tolerance, and the FDR was set to <1% at spectral level. All spectra of putative crosslinked peptides were manually controlled before positive identification. The extended and FERM conformations were compared in terms of inter-residue distances of the identified crosslinks using MNXL analysis (Bullock et al., 2016).

Analytical light scattering

Proteins were analyzed using a liquid chromatography instrument (CBM-20A, Shimadzu Corporation, Kyoto, Japan) equipped with an autosampler (SIL-20A), UV-VIS (SPD-20A) and a fluorescence detector (RF-20Axs). Molecular weight was determined using size-exclusion chromatography with a Malvern Zetasizer µV instrument (Malvern Instruments Ltd, Worcestershire, UK) measuring inline Static Light Scattering (SLS) and Dynamic Light Scattering (DLS). Data were processed using Lab Solution Version 5.51 (Shimadzu Corporation) and OmniSec 4.7 (Malvern Instruments Ltd) software. Samples (50 µg) were injected into the column (Superdex 200 Increase 5/150, GE Healthcare, Uppsala, Sweden) using the autosampler. The column was equilibrated with 50 mM Na_3PO_4 pH 7.2, 150 mM NaCl running buffer. The measurements were run with a flow rate of 0.1 ml/min at 20°C. BSA was used for calibration of the system to calculate molecular weight from the measured SLS intensity.

Differential scanning calorimetry

Talin samples were analyzed using the VP-DSC instrument (MicroCal, Malvern Instruments Ltd) with protein concentrations of ∼0.2 mg/ml in 50 mM NaH_2PO_4 pH 7.2, 150 mM NaCl containing 1 mM EDTA and 1 mM DTT. Concentrations were measured before the analysis by NanoDrop using a theoretical molar extinction coefficient calculated using ProtParam software. Samples were stored at 4°C prior to analysis. Solutions were degassed prior to measurements. Samples were heated from 20°C to 130°C at a scanning rate of 2°C/min. Feedback mode was set to low, and the filter period was 5 s. Temperature transition midpoint (T_{m}) and calorimetric heat change (ΔH) were obtained by subtracting the baseline and applying the Levenberg–Marquardt non-linear least-squares method to the data using MicroCal Origin 7.0 software (MicroCal, Malvern Instruments Ltd).

Biosensor analysis of talin–integrin interactions

Biosensor analysis was carried out on a ForteBio Octet RED384 instrument (Pall Life Sciences) using Ni-NTA sensors following a strategy similar to the one described by Pinon et al. (2014). Samples or buffers were prepared into 96- or 384-well plates at a volume of 200 µl or 80 µl per well, respectively. Sensors were pre-wetted with buffer (50 mM Na_3PO_4 pH 7.2, 150 mM NaCl) in order to obtain baseline measurements prior to protein immobilization. An operating temperature of 27°C and a stirring speed of 1000 rpm were used throughout the experiment. Sensors were chemically activated by immersion in 0.05 M EDC [1-Ethyl-3-(3-dimethylaminopropyl)carbodiimide] and 0.1 M NHS (*N*-Hydroxysuccinimide) in water for 100 s. Different talin head mutant samples (50 µg/ml) were immobilized on the sensor's surface for 300 s. The excess sulfo-NHS esters were quenched by 1 M ethanolamine pH 8.5 for 100 s. Serially diluted GST–β3-integrin-tail fusion proteins were applied on the talin-coated sensors in concentrations of 20, 80, 320, 1250 and 5000 nM to obtain the relative affinity of talin to GST–β3. Each concentration of GST–β3-integrin-tail fusion protein binding to the sensor was measured for 300 s before moving on to a higher concentration.

Talin–wild-type β3 integrin (WT-β3) and talin–high-affinity β3 integrin (VE-β3) binding data from Octet biosensor (20, 80, 320, 1250, and 5000 nM) were treated as follows: background (GST control) was subtracted, and all the data were normalized to t1–405 at concentration 1250 nM to allow comparison between experiments. The normalized data were analyzed by linear regression analysis in GraphPad Prism 5.02 (GraphPad Software, La Jolla, CA), assuming one-site specific binding. Bmax was set to 8.6 for WT-β3 binding data and to 1.265 for VE-β3 binding data.

Protein modeling and molecular dynamics

Integrin-αIIb (residues 955–1008) and -β3 (residues 684–762) were modeled as described by Orłowski et al. (2015). A FERM-like fold for the talin head domain was generated using the experimental structures of talin F0, F1, F2, and F3 subdomains [PDB IDs 3IVF (Elliott et al., 2010), 2KC2, 2KMA (Goult et al., 2010) and 2H7E (Wegener et al., 2007)]. The F1, F2 and F3 subdomains were arranged into a FERM-like fold using merlin as a template (PDB ID 1H4R; Kang et al., 2002). The model was prepared in an iterative process of homology modeling, manual adjusting of contacts, energy minimizations and short molecular dynamics simulations (up to 23 ns). The loop missing from the crystallographic structure of talin head, residues 139–168, was added to the FERM fold by selecting the least clashing conformer from the NMR structure of talin F1 subdomain (PDB ID 2KC2; conformer 8). Modeling of the integrin dimer has been described previously (Orłowski et al., 2015). MODELLER (Šali and Blundell, 1993) was used for protein modeling. Quality assessment of the talin–integrin complex used for the molecular dynamics simulations with MolProbity (Chen et al., 2010) gave a MolProbity score of 1.71 (89th percentile) and a clash score of 0.61 (99th percentile).

Molecular dynamics simulations were run at 310 K using Gromacs 4.5.5 (Van Der Spoel et al., 2005) and the OPLS force field (Jorgensen et al., 1996) in 0.15 M KCl and TIP3P water using a setup described previously (Orłowski et al., 2015). The simulated systems are described in Table S3. The resulting MD data has been deposited into IDA research data storage and can be accessed via https://ida.fairdata.fi/s/NOT_FOR_PUBLICATION_AfayjpjdWxyL.

Cell lines

Mouse melanoma B16F1 cells (initially obtained from Garth L. Nicolson, Texas M.D. Anderson Cancer Center, Houston, TX) (Ballestrem et al., 1996) and COS7 cells (ATCC CRL-1651) were cultured in DMEM, 10% fetal calf serum (FCS) and antibiotics and passaged by trypsin treatment as described previously (Cluzel et al., 2005). Talin-1$^{-/-}$ talin-2$^{-/-}$ cells were obtained from Reinhard Fässler, Max Planck Institute of Biochemistry, Martinsried, Germany (Theodosiou et al., 2016), and cultured in DMEM, containing 10% FCS and antibiotics. At each passage, substrate-adhering cells were detached with trypsin treatment and combined with suspended cells, prior to dilution and resuspension in new culture medium.

DNA constructs

Wild-type and mutant human talin1 head domain constructs used for mammalian cell transfection were cloned in pcDNA3 [Invitrogen (Thermo Fischer V79020)] as N-terminal cyan fluorescent protein (CFP) fusion proteins, following standard molecular biology protocols, and confirmed by automated DNA sequencing (Saltel et al., 2009). His-tagged human talin1 head domain constructs were cloned into pTrcHis C vector. GFP-tagged talin1 full-length constructs were cloned into pcDNA3 as an N-terminal tagged human–mouse chimera comprising the human head domain (Saltel et al., 2009) and the mouse rod domain (kindly provided by Anna Huttenlocher, University of Wisconsin–Madison, WI). N-terminal TagRFP-labeled human kindlin-1 (kindly provided by Drs Hongquan Zhang and Staffan Strömblad, Karolinska Institutet, Sweden) was cloned into pcDNA3. Wild-type and VE-mutant forms of the GST–β3-integrin cytoplasmic tail constructs have been described previously (Pinon et al., 2014). C-terminal GFP-tagged mouse β3 integrin constructs were cloned in pcDNA3 and the linker region modified by two additional amino acids, in comparison to previously used constructs (old linker, SPVAT; new linker, DGSPVAT). The DG-linker variant performed identically in β3 integrin spreading assays (Pinon et al., 2014), but showed slightly better clustering behavior in response to co-transfected kindlin-1 constructs (data not shown). A non-tagged mouse αv-integrin construct was amplified by PCR from a mouse placenta cDNA and cloned into pcDNA3 using the following primers (forward, 5′-ATTATGGATCCACCATGGCTGCTCCCGGGCG-CCTGCT-3′; reverse: 5′-ATATTAGGGCCCTCAGGTTTCAGAGTTCC-TT-3′) as described previously (Wiedle et al., 1999).

Transfections

Adherent (B16F1, COS7) or non-adherent cells (talin knockout), were transfected in 6-well culture dishes with the JET PEi transfection reagent (Polyplus-transfection) according to the manufacturer's protocol. For multiple transfections, different vector DNAs were mixed at equimolar concentrations. For adherent cells, the transfection mixture was removed and replaced with fresh medium after 6 h. For talin-knockout cells, the transfection mixture was left on the cells.

Integrin clustering analysis

After 6 h in transfection mixture, melanoma B16F1 cells were detached using trypsin-EDTA and plated on ethanol-sterilized glass-bottom dishes in FCS-containing culture medium. After 48 h on the FCS-coated glass surface, cells were either fixed directly, or after 20 min exposure to 0.5 mM Mn^{2+} in DMEM containing FCS, with 4% PFA (paraformaldehyde in PBS) for 10 min. Cells were subsequently immerged in PBS for total internal fluorescence microscopy. Integrin clustering analysis was then performed from TIRF images according to methods reported by Saltel et al. (2009). In brief, after background removal, an arbitrary threshold that allowed clustered and membrane-inserted integrins to be distinguished was used to quantify the area exhibiting integrin clusters relative to the total cell surface.

Integrin activation assay

48 h after transfection, mouse melanoma B16F1 cells were detached using non-enzymatic cell-dissociation solution (SIGMA C5788), and talin-knockout cells were collected using trypsin-EDTA, as described above, in culture medium. Cells were then washed twice in PBS containing 0.5 mg/ml BSA and split into two equal populations. Antibody staining or soluble-ligand incubation was performed on ice in PBS containing 0.5 mg/ml BSA. For one cell population, the total amount of cell-surface integrin was revealed by staining with either a hamster anti-β1-integrin antibody (clone HM β1-1; 550530, Pharmingen, BD) or hamster anti-β3-integrin antibody (anti-mouse CD61, clone 2C9.G2; 553344, Pharmingen, BD). The other cell population was stained with a conformation-specific rat monoclonal antibody (rat anti-mouse CD29, clone 9EG7, 553715, Pharmingen, BD) to detect the extended form of the β1 integrin (Lenter et al., 1993), or incubated with an RGD-containing fusion protein of the snake venom disintegrin (kistrin) and the first Ig domain of CD31 (SKI-7), followed by incubation with a rat anti-CD31 monoclonal antibody (GC51) as described previously (Saltel et al., 2009). Subsequent detection of the conformation-specific antibody or the bound β3 integrin ligand SKI-7–GC51 complex were achieved using PE-labeled affinity-purified anti-hamster antibody (127-115-160; Jackson ImmunoResearch Europe), or $F(ab')_2$ fragments of goat anti-rat antibodies, respectively and analyzed in an Accuri flow cytometer. Integrin activation was determined by the ratio of the signal between the activation-specific and total integrin-binding antibodies as described in Saltel et al. (2009).

Cell-derived matrix

To prepare cell-derived matrix in ethanol-sterilized glass-bottom dishes, the dishes were coated for 60 min at 37°C with 0.2% gelatin in PBS then washed three times in PBS. The gelatin coating was fixed for 30 min in 1% glutaraldehyde, washed in PBS and blocked with 1 M glycine in PBS for 20 min, both at room temperature. After washing in PBS and equilibration in DMEM containing 10% FCS for 30 min at 37°C, 3T3 cells were plated at 50,000 cells/cm^2 and incubated until they reached confluency (typically, 1 day). The medium – DMEM containing 10% FCS, antibiotics and ascorbic acid at 50 µg/ml – was then changed daily. After 7 days of culture, the wells were washed with PBS and incubated in extraction buffer at 37°C (20 mM NH_4OH containing 0.5% Triton X-100 in PBS) for periods of 2 min. DNA of lysed cells was removed by DNAseI (Amersham, 10 U/ml final) treatment in PBS containing 0.5 mM Mg^{2+} and 1 mM Ca^{2+} at 37°C for 30 min. After gentle washing with PBS containing 0.5 mM Mg^{2+} and 1 mM Ca^{2+}, the cell-derived matrix was blocked in DMEM containing 10% FCS for 30 min at 37°C, prior to seeding with talin-knockout cells transfected with GFP–talin constructs. After incubation for 6 h, invaded and spread cells were fixed in 4% PFA in PBS for 10 min and subsequently imaged in PBS by confocal or epifluorescence microscopy.

Cysteine crosslinking

COS7 cells were transfected in a 6-well plate using JetPEi reagent (1.5 µl; Polyplus-transfection) containing 0.3 µg of mouse αv integrin expression vector, 0.3 µg of mRFP–kindlin-1 vector, 0.3 µg of wild-type or cysteine-mutated β3–GFP integrin constructs (all in pcDNA3) and 0.3 µg of wild-type or cysteine-mutated CFP–talin head constructs, as described above. After 1 d, the culture medium was supplemented with 20 µg/ml 2-bromopalmitate for an additional 17 h, in order to prevent palmitoylation of juxtamembrane cysteine residues. Prior to cell extraction, cells were oxidized for 10 min at 4°C in 400 µl of DMEM medium containing 200 µM CuSO$_4$, 100 µM phenanthroline and 0.02% saponin. Cells were lysed after gentle removal of the oxidation solution in 300 µl of Tris-buffered saline containing 2% Triton X-100, 0.1% NP40, 5 mM N-ethylmaleimide, 1 mM PMSF and protease inhibitors at 1 µg/ml (chymotrypsin, leupeptine, aprotinin and pepstatin; Sigma) for 10 min at 4°C. 40 µl of the lysate was subsequently run on an SDS–PAGE gel (6%) under non-reducing conditions, then transferred to nitrocellulose and revealed using a mouse monoclonal anti-GFP antibody (clone B34, MMS-118R, LOT/147936001; Covance, Berkeley, CA) according to standard protocols. Analysis of the cysteine-crosslinked samples by 2D-SDS–PAGE (non-reduced/reduced) was performed as follows. The sample to be analysed in 2D was run alongside a pre-stained molecular weight marker on a 6% SDS–PAGE gel under non-reducing conditions. The sample band and part of the marker were then cut from the gel and placed on top of the stacking gel of a 10% SDS–PAGE gel. The gel slice was then overlaid with 1× sample buffer containing reducing agents. SDS–PAGE was stopped for 10 min once the front had just passed the gel slice, in order to reduce the included samples, and subsequently resolved. Transfer to nitrocellulose and anti-GFP detection was then performed as described above.

Small-angle X-ray scattering

Small angle X-ray scattering (SAXS) data for talins t1–405, t1–405(del30) and t1–405(del37/GAG) were collected at the P12 beamline at the PETRA III storage ring (EMBL Hamburg/DESY, Hamburg) (Blanchet et al., 2015). Analysis was performed on the monomeric fraction of the sample, as separated by in-line size exclusion chromatography. 100 µl of talin head in a concentration of 4.8–7.6 mg/ml in 50 mM sodium phosphate (pH 7.2) containing 150 mM NaCl was injected onto a Superdex 200 10/300 GL column with a flow rate of 0.25 ml/min. From the column, the sample flowed through the right-angle light-scattering detector at 26°C and through the SAXS sample cell at 10°C. SAXS data were collected on a Pilatus 2 M detector at a 3-m distance from the sample cell, at a wavelength of 1.24 Å, covering the momentum transfer range of $0.025<s<4.8$ Å^{-1}. Data were collected at 1-s intervals with an exposure time of 995 ms. The details of the experiment and data analyses are described in Table S5. The SAXS data has been deposited in the Small Angle Scattering Biological Data Bank and can be accessed at https://www.sasbdb.org/project/796/.

Statistics

Statistical analyses were carried out in GraphPad Prism 5.02 for Windows (GraphPad Software, La Jolla, CA). All clustering data were analyzed using one-way analysis of variance (ANOVA) and a Tukey's multiple comparison test for differences between the groups. The cell spreading data in Fig. 6B were analyzed using a two-tailed, unpaired *t*-test.

Acknowledgements

Ritva Romppanen, Ulla Kiiskinen, Niklas Kähkönen, Tatiana Fomekong and Monica Julio-Barreto are acknowledged for excellent technical help, and Michael Bachmann for help in figure preparations. Hongquan Zhang and Staffan Strömblad (Karolinska Institutet, Sweden) kindly provided the kindlin-1 construct. CSC – IT Center for Science Ltd. is acknowledged for computational resources, and Biocenter Finland is acknowledged for infrastructure support.

Competing interests

The authors declare no competing or financial interests.

Author contributions

Conceptualization: S.K., J.J., M.V., V.P.H., B.W.-H.; Methodology: S.K., L.A., P.Z., M.-C.J., M.v.E., A.T., M.L., X.L., A.O., J.J., J.A.E.M., M.V., I.V., T.R., D.S., J.W., V.P.H., B.W.-H.; Software: A.O., T.R., D.S.; Validation: S.K., A.T., D.S., J.W., V.P.H., B.W.-H; Formal analysis: S.K., M.-C.J., M.v.E., A.T., R.R., A.O., T.R., J.W., V.P.H.; Investigation: M.B., R.H.C., S.K., L.A., P.Z., M.-C.J., M.v.E., A.T., M.L., X.L., R.R., A.O., J.J., J.A.E.M., T.R., V.P.H., B.W.-H.; Resources: J.J., I.V., D.S., J.W., V.P.H., B.W.-H.; Data curation: S.K., L.A., P.Z., M.-C.J., M.v.E., A.T., X.L., R.R., M.V., T.R., V.P.H., B.W.-H.; Writing - original draft: S.K., V.P.H., B.W.-H.; Writing - review & editing: S.K., L.A., P.Z., M.v.E., A.T., X.L., R.R., A.O., J.J., J.A.E.M., M.V., I.V., T.R., J.W., V.P.H., B.W.-H.; Visualization: S.K., P.Z., J.J., T.R., B.W.-H.; Supervision: R.H.C., J.J., M.V., I.V., T.R., D.S., J.W., V.P.H., B.W.-H.; Project administration: J.W., V.P.H., B.W.-H.; Funding acquisition: V.P.H., B.W.-H.

Funding

We acknowledge Academy of Finland (grant number 290506) for research funding. This work was granted access to the HPC resources of EPCC made available within the Distributed European Computing Initiative by the PRACE-2IP, receiving funding from the European Community's Seventh Framework Programme (FP7/2007–2013) under grant agreement number RI-283493. S.K. was supported by the Tampere Graduate Program in Biomedicine and Biotechnology. B.W.-H. and M.-C.J. were supported by a grant from the Schweizerischer Nationalfonds zur Förderung der Wissenschaftlichen Forschung (31003A_166384).

Data availability

Molecular dynamics data have been deposited into IDA research data storage and can be accessed via https://etsin.fairdata.fi/dataset/4bf3cf43-49f4-4898-bf38-0381552c3fd2. Small-angle x-ray scattering data have been deposited in the Small Angle Scattering Biological Data Bank, and can be accessed via https://www.sasbdb.org/project/796/.

Supplementary information

Supplementary information available online at
https://jcs.biologists.org/lookup/doi/10.1242/jcs.239202.supplemental

References

Anthis, N. J. and Campbell, I. D. (2011). The tail of integrin activation. *Trends Biochem. Sci.* **36**, 191-198. doi:10.1016/j.tibs.2010.11.002

Anthis, N. J., Wegener, K. L., Ye, F., Kim, C., Goult, B. T., Lowe, E. D., Vakonakis, I., Bate, N., Critchley, D. R., Ginsberg, M. H. et al. (2009). The structure of an integrin/talin complex reveals the basis of inside–out signal transduction. *EMBO J.* **28**, 3623-3632. doi:10.1038/emboj.2009.287

Anthis, N. J., Wegener, K. L., Critchley, D. R. and Campbell, I. D. (2010). Structural diversity in integrin/talin interactions. *Structure* **18**, 1654-1666. doi:10.1016/j.str.2010.09.018

Bachmann, M., Kukkurainen, S., Hytönen, V. P. and Wehrle-Haller, B. (2019). Cell Adhesion by Integrins. *Physiol. Rev.* **99**, 1655-1699. doi:10.1152/physrev.00036.2018

Ballestrem, C., Wehrle-Haller, B. and Imhof, B. A. (1996). Actin dynamics in living mammalian cells. *J. Cell Sci.* **111**, 1649-1658.

Ballestrem, C., Hinz, B., Imhof, B. A. and Wehrle-Haller, B. (2001). Marching at the front and dragging behind. *J. Cell Biol.* **155**, 1319-1332. doi:10.1083/jcb.200107107

Blanchet, C. E., Spilotros, A., Schwemmer, F., Graewert, M. A., Kikhney, A., Jeffries, C. M., Franke, D., Mark, D., Zengerle, R., Cipriani, F. et al. (2015). Versatile sample environments and automation for biological solution X-ray scattering experiments at the P12 beamline (PETRA III, DESY). *J. Appl. Crystallogr.* **48**, 431-443. doi:10.1107/S160057671500254X

Bouaouina, M., Lad, Y. and Calderwood, D. A. (2008). The N-terminal domains of talin cooperate with the phosphotyrosine binding-like domain to activate β1 and β3 integrins. *J. Biol. Chem.* **283**, 6118-6125. doi:10.1074/jbc.M709527200

Bouaouina, M., Goult, B. T., Huet-Calderwood, C., Bate, N., Brahme, N. N., Barsukov, I. L., Critchley, D. R. and Calderwood, D. A. (2012). A conserved lipid-binding loop in the kindlin FERM F1 domain is required for kindlin-mediated αIIbβ3 integrin coactivation. *J. Biol. Chem.* **287**, 6979-6990. doi:10.1074/jbc.M111.330845

Bromberger, T., Klapproth, S., Rohwedder, I., Zhu, L., Mittmann, L., Reichel, C. A., Sperandio, M., Qin, J. and Moser, M. (2018). Direct Rap1/Talin1 interaction regulates platelet and neutrophil integrin activity in mice. *Blood.* **132**, 2754-2762. doi:10.1182/blood-2018-04-846766

Bullock, J. M. A., Schwab, J., Thalassinos, K. and Topf, M. (2016). The importance of non-accessible crosslinks and solvent accessible surface distance in modeling proteins with restraints from crosslinking mass spectrometry. *Mol. Cell. Proteomics* **15**, 2491-2500. doi:10.1074/mcp.M116.058560

Bunch, T. A. (2009). Integrin αIIbβ3 activation in chinese hamster ovary cells and platelets increases clustering rather than affinity. *J. Biol. Chem.* **285**, 1841-1849. doi:10.1074/jbc.M109.057349

Calderwood, D. A., Yan, B., de Pereda, J. M., Alvarez, B. G., Fujioka, Y., Liddington, R. C. and Ginsberg, M. H. (2002). The phosphotyrosine binding-like domain of talin activates integrins. *J. Biol. Chem.* **277**, 21749-21758. doi:10.1074/jbc.M111996200

Calderwood, D. A., Campbell, I. D. and Critchley, D. R. (2013). Talins and kindlins: partners in integrin-mediated adhesion. *Nat. Rev. Mol. Cell Biol.* **14**, 503-517. doi:10.1038/nrm3624

Camp, D., Haage, A., Solianova, V., Castle, W. M., Xu, Q. A., Lostchuck, E., Goult, B. T. and Tanentzapf, G. (2018). Direct binding of Talin to Rap1 is required for cell-ECM adhesion in Drosophila. *J. Cell Sci.* **131**, jcs225144. doi:10.1242/jcs.225144

Changede, R., Xu, X., Margadant, F. and Sheetz, M. P. (2015). Nascent integrin adhesions form on all matrix rigidities after integrin activation. *Dev. Cell.* **35**, 614-621. doi:10.1016/j.devcel.2015.11.001

Chen, V. B., Arendall, W. B., III, Headd, J. J., Keedy, D. A., Immormino, R. M., Kapral, G. J., Murray, L. W., Richardson, J. S. and Richardson, D. C. (2010). *MolProbity* : all-atom structure validation for macromolecular crystallography. *Acta Crystallogr. Sect. D Biol. Crystallogr.* **66**, 12-21. doi:10.1107/S0907444909042073

Chinthalapudi, K., Rangarajan, E. S. and Izard, T. (2018). The interaction of talin with the cell membrane is essential for integrin activation and focal adhesion formation. *Proc. Natl. Acad. Sci. USA* **115**, 10339-10344. doi:10.1073/pnas.1806275115

Cluzel, C., Saltel, F., Lussi, J., Paulhe, F., Imhof, B. A. and Wehrle-Haller, B. (2005). The mechanisms and dynamics of αvβ3 integrin clustering in living cells. *J. Cell Biol.* **171**, 383-392. doi:10.1083/jcb.200503017

Debrand, E., Conti, F. J., Bate, N., Spence, L., Mazzeo, D., Pritchard, C. A., Monkley, S. J. and Critchley, D. R. (2012). Mice carrying a complete deletion of the talin2 coding sequence are viable and fertile. *Biochem. Biophys. Res. Commun.* **426**, 190-195. doi:10.1016/j.bbrc.2012.08.061

Do, C. B., Mahabhashyam, M. S. P., Brudno, M. and Batzoglou, S. (2005). ProbCons: Probabilistic consistency-based multiple sequence alignment. *Genome Res.* **15**, 330-340. doi:10.1101/gr.2821705

Elliott, P. R., Goult, B. T., Kopp, P. M., Bate, N., Grossmann, J. G., Roberts, G. C. K., Critchley, D. R. and Barsukov, I. L. (2010). The structure of the talin head reveals a novel extended conformation of the FERM domain. *Structure* **18**, 1289-1299. doi:10.1016/j.str.2010.07.011

Ellis, S. J., Goult, B. T., Fairchild, M. J., Harris, N. J., Long, J., Lobo, P., Czerniecki, S., Van Petegem, F., Schöck, F., Peifer, M. et al. (2013). Talin autoinhibition is required for morphogenesis. *Curr. Biol.* **23**, 1825-1833. doi:10.1016/j.cub.2013.07.054

Eng, E. T., Smagghe, B. J., Walz, T. and Springer, T. A. (2011). Intact α_{IIb} β_3 integrin is extended after activation as measured by solution X-ray scattering and electron microscopy. *J. Biol. Chem.* **286**, 35218-35226. doi:10.1074/jbc.M111.275107

Feigelson, S. W., Grabovsky, V., Manevich-Mendelson, E., Pasvolsky, R., Shulman, Z., Shinder, V., Klein, E., Etzioni, A., Aker, M. and Alon, R. (2011). Kindlin-3 is required for the stabilization of TCR-stimulated LFA-1:ICAM-1 bonds critical for lymphocyte arrest and spreading on dendritic cells. *Blood* **117**, 7042-7052. doi:10.1182/blood-2010-12-322859

Feng, C., Li, Y.-F., Yau, Y.-H., Lee, H.-S., Tang, X.-Y., Xue, Z.-H., Zhou, Y.-C., Lim, W.-M., Cornvik, T. C., Ruedl, C. et al. (2012). Kindlin-3 mediates integrin αLβ2 outside-in signaling, and it interacts with scaffold protein receptor for activated-C kinase 1 (RACK1). *J. Biol. Chem.* **287**, 10714-10726. doi:10.1074/jbc.M111.299594

García-Alvarez, B., de Pereda, J. M., Calderwood, D. A., Ulmer, T. S., Critchley, D. R., Campbell, I. D., Ginsberg, M. H. and Liddington, R. C. (2003). Structural determinants of integrin recognition by talin. *Mol. Cell* **11**, 49-58. doi:10.1016/S1097-2765(02)00823-7

Gingras, A. R., Bate, N., Goult, B. T., Hazelwood, L., Canestrelli, I., Grossmann, J. G., Liu, H. J., Putz, N. S. M., Roberts, G. C. K., Volkmann, N. et al. (2008). The structure of the C-terminal actin-binding domain of talin. *EMBO J.* **27**, 458-469. doi:10.1038/sj.emboj.7601965

Gingras, A. R., Lagarrigue, F., Cuevas, M. N., Valadez, A. J., Zorovich, M., McLaughlin, W., Lopez-Ramirez, M. A., Seban, N., Ley, K., Kiosses, W. B. et al. (2019). Rap1 binding and a lipid-dependent helix in talin F1 domain promote integrin activation in tandem. *J. Cell Biol.* **218**, 1799-1809. doi:10.1083/jcb.201810061

Goksoy, E., Ma, Y.-Q., Wang, X., Kong, X., Perera, D., Plow, E. F. and Qin, J. (2008). Structural basis for the autoinhibition of talin in regulating integrin activation. *Mol. Cell* **31**, 124-133. doi:10.1016/j.molcel.2008.06.011

Goult, B. T., Bouaouina, M., Elliott, P. R., Bate, N., Patel, B., Gingras, A. R., Grossmann, J. G., Roberts, G. C. K., Calderwood, D. A., Critchley, D. R. et al. (2010). Structure of a double ubiquitin-like domain in the talin head: a role in integrin activation. *EMBO J.* **29**, 1069-1080. doi:10.1038/emboj.2010.4

Goult, B. T., Xu, X.-P., Gingras, A. R., Swift, M., Patel, B., Bate, N., Kopp, P. M., Barsukov, I. L., Critchley, D. R., Volkmann, N. et al. (2013). Structural studies on full-length talin1 reveal a compact auto-inhibited dimer: implications for talin activation. *Hybrid Methods Macromol. Struct.* **184**, 21-32. doi:10.1016/j.jsb.2013.05.014

Haining, A. W. M., Lieberthal, T. J. and del Río Hernández, A. (2016). Talin: a mechanosensitive molecule in health and disease. *FASEB J.* **30**, 2073-2085. doi:10.1096/fj.201500080R

Harburger, D. S., Bouaouina, M. and Calderwood, D. A. (2009). Kindlin-1 and −2 directly bind the C-terminal region of β integrin cytoplasmic tails and exert integrin-specific activation effects. *J. Biol. Chem.* **284**, 11485-11497. doi:10.1074/jbc.M809233200

Hemmings, L., Rees, D. J. G., Ohanian, V., Bolton, S. J., Gilmore, A. P., Patel, B., Priddle, H., Trevithick, J. E., Hynes, R. O. and Critchley, D. R. (1996). Talin contains three actin-binding sites each of which is adjacent to a vinculin-binding site. *J. Cell Sci.* **109**, 2715-2726.

Hughes, P. E., Diaz-Gonzalez, F., Leong, L., Wu, C., McDonald, J. A., Shattil, S. J. and Ginsberg, M. H. (1996). Breaking the Integrin Hinge: A defined structural constraint regulates integrin signaling. *J. Biol. Chem.* **271**, 6571-6574. doi:10.1074/jbc.271.12.6571

Hynes, R. O. (2002). Integrins: bidirectional, allosteric signaling machines. *Cell* **110**, 673-687. doi:10.1016/S0092-8674(02)00971-6

Jorgensen, W. L., Maxwell, D. S. and Tirado-Rives, J. (1996). Development and testing of the OPLS all-atom force field on conformational energetics and properties of organic liquids. *J. Am. Chem. Soc.* **118**, 11225-11236. doi:10.1021/ja9621760

Kalli, A. C., Campbell, I. D. and Sansom, M. S. P. (2013). Conformational changes in talin on binding to anionic phospholipid membranes facilitate signaling by integrin transmembrane helices. *PLoS Comput. Biol.* **9**, e1003316. doi:10.1371/journal.pcbi.1003316

Kang, B. S., Cooper, D. R., Devedjiev, Y., Derewenda, U. and Derewenda, Z. S. (2002). The structure of the FERM domain of merlin, the neurofibromatosis type 2 gene product. *Acta Crystallogr. Sect. D.* **58**, 381-391. doi:10.1107/S0907444901021175

Katzemich, A., Long, J. Y., Panneton, V., Fisher, L. A. B., Hipfner, D. and Schöck, F. (2019). Slik phosphorylation of Talin T152 is crucial for proper Talin recruitment and maintenance of muscle attachment in Drosophila. *Development* **146**, dev176339. doi:10.1242/dev.176339

Kumar, S., Stecher, G. and Tamura, K. (2016). MEGA7: molecular evolutionary genetics analysis version 7.0 for bigger datasets. *Mol. Biol. Evol.* **33**, 1870-1874. doi:10.1093/molbev/msw054

Lagarrigue, F., Gingras, A. R., Paul, D. S., Valadez, A. J., Cuevas, M. N., Sun, H., Lopez-Ramirez, M. A., Goult, B. T., Shattil, S. J., Bergmeier, W. et al. (2018). Rap1 binding to the talin 1 F0 domain makes a minimal contribution to murine platelet GPIIb-IIIa activation. *Blood Adv.* **2**, 2358-2368. doi:10.1182/bloodadvances.2018020487

Lenter, M., Uhlig, H., Hamann, A., Jenö, P., Imhof, B. and Vestweber, D. (1993). A monoclonal antibody against an activation epitope on mouse integrin chain beta 1 blocks adhesion of lymphocytes to the endothelial integrin alpha 6 beta 1. *Proc. Natl. Acad. Sci. USA* **90**, 9051-9055. doi:10.1073/pnas.90.19.9051

Li, H., Deng, Y., Sun, K., Yang, H., Liu, J., Wang, M., Zhang, Z., Lin, J., Wu, C., Wei, Z. et al. (2017). Structural basis of kindlin-mediated integrin recognition and activation. *Proc. Natl. Acad. Sci. USA* **114**, 9349-9354. doi:10.1073/pnas.1703064114

Lu, S., Fan, S.-B., Yang, B., Li, Y.-X., Meng, J.-M., Wu, L., Li, P., Zhang, K., Zhang, M.-J., Fu, Y. et al. (2015). Mapping native disulfide bonds at a proteome scale. *Nat. Methods.* **12**, 329-331. doi:10.1038/nmeth.3283

Ma, Y.-Q., Qin, J., Wu, C. and Plow, E. F. (2008). Kindlin-2 (Mig-2): a co-activator of β3 integrins. *J. Cell Biol.* **181**, 439-446. doi:10.1083/jcb.200710196

Monkley, S. J., Zhou, X.-H., Kinston, S. J., Giblett, S. M., Hemmings, L., Priddle, H., Brown, J. E., Pritchard, C. A., Critchley, D. R. and Fässler, R. (2000). Disruption of the talin gene arrests mouse development at the gastrulation stage. *Dev. Dyn.* **219**, 560-574. doi:10.1002/1097-0177(2000)9999:9999<::AID-DVDY1079>3.0.CO;2-Y

Monkley, S. J., Kostourou, V., Spence, L., Petrich, B., Coleman, S., Ginsberg, M. H., Pritchard, C. A. and Critchley, D. R. (2011). Endothelial cell talin1 is essential for embryonic angiogenesis. *Dev. Biol.* **349**, 494-502. doi:10.1016/j.ydbio.2010.11.010

Montanez, E., Ussar, S., Schifferer, M., Bösl, M., Zent, R., Moser, M. and Fässler, R. (2008). Kindlin-2 controls bidirectional signaling of integrins. *Genes Dev..* **22**, 1325-1330. doi:10.1101/gad.469408

Moore, D. T., Nygren, P., Jo, H., Boesze-Battaglia, K., Bennett, J. S. and DeGrado, W. F. (2012). Affinity of talin-1 for the β3-integrin cytosolic domain is modulated by its phospholipid bilayer environment. *Proc. Natl. Acad. Sci. USA* **109**, 793-798. doi:10.1073/pnas.1117220108

Moser, M., Nieswandt, B., Ussar, S., Pozgajova, M. and Fässler, R. (2008). Kindlin-3 is essential for integrin activation and platelet aggregation. *Nat. Med.* **14**, 325-330. doi:10.1038/nm1722

Moser, M., Bauer, M., Schmid, S., Ruppert, R., Schmidt, S., Sixt, M., Wang, H.-V., Sperandio, M. and Fässler, R. (2009). Kindlin-3 is required for β2 integrin-mediated leukocyte adhesion to endothelial cells. *Nat. Med.* **15**, 300-305. doi:10.1038/nm.1921

Mould, A. P., Akiyama, S. K. and Humphries, M. J. (1995). Regulation of integrin α5β1-fibronectin interactions by divalent cations: evidence for distinct classes of binding sites Mn2+, Mg2+, and Ca2+. *J. Biol. Chem.* **270**, 26270-26277. doi:10.1074/jbc.270.44.26270

O'Connell, K. L. and Stults, J. T. (1997). Identification of mouse liver proteins on two-dimensional electrophoresis gels by matrix-assisted laser desorption/ionization mass spectrometry of in situ enzymatic digests. *Electrophoresis.* **18**, 349-359. doi:10.1002/elps.1150180309

Orłowski, A., Kukkurainen, S., Pöyry, A., Rissanen, S., Vattulainen, I., Hytönen, V. P. and Róg, T. (2015). PIP2 and Talin Join Forces to Activate Integrin. *J. Phys. Chem. B.* **119**, 12381-12389. doi:10.1021/acs.jpcb.5b06457

Pinon, P., Pärssinen, J., Vazquez, P., Bachmann, M., Rahikainen, R., Jacquier, M.-C., Azizi, L., Määttä, J. A., Bastmeyer, M., Hytönen, V. P. et al. (2014). Talin-bound NPLY motif recruits integrin-signaling adapters to regulate cell spreading and mechanosensing. *J. Cell Biol.* **205**, 265-281. doi:10.1083/jcb.201308136

Qu, H., Tu, Y., Shi, X., Larjava, H., Saleem, M. A., Shattil, S. J., Fukuda, K., Qin, J., Kretzler, M. and Wu, C. (2011). Kindlin-2 regulates podocyte adhesion and fibronectin matrix deposition through interactions with phosphoinositides and integrins. *J. Cell Sci.* **124**, 879-891. doi:10.1242/jcs.076976

Rangarajan, E. S., Primi M. C., Colgan, L. A., Chinthalapudi, K., Yasuda, R. and Izard, T. (2020). A distinct talin2 structure directs isoform specificity in cell adhesion. *J. Biol. Chem.* **295**, 12885-12899. doi:10.1074/jbc.RA119.010789

Rees, D. J. G., Ades, S. E., Singer, S. J. and Hynes, R. O. (1990). Sequence and domain structure of talin. *Nature* **347**, 685-689. doi:10.1038/347685a0

Roberts, G. C. K. and Critchley, D. R. (2009). Structural and biophysical properties of the integrin-associated cytoskeletal protein talin. *Biophys. Rev.* **1**, 61-69. doi:10.1007/s12551-009-0009-4

Rognoni, E., Ruppert, R. and Fässler, R. (2016). The kindlin family: functions, signaling properties and implications for human disease. *J. Cell Sci.* **129**, 17-27. doi:10.1242/jcs.161190

Šali, A. and Blundell, T. L. (1993). Comparative protein modelling by satisfaction of spatial restraints. *J. Mol. Biol.* **234**, 779-815. doi:10.1006/jmbi.1993.1626

Saltel, F., Mortier, E., Hytönen, V. P., Jacquier, M.-C., Zimmermann, P., Vogel, V., Liu, W. and Wehrle-Haller, B. (2009). New PI(4,5)P2- and membrane proximal integrin–binding motifs in the talin head control β3-integrin clustering. *J. Cell Biol.* **187**, 715-731. doi:10.1083/jcb.200908134

Schmidt, S., Nakchbandi, I., Ruppert, R., Kawelke, N., Hess, M. W., Pfaller, K., Jurdic, P., Fässler, R. and Moser, M. (2011). Kindlin-3-mediated signaling from multiple integrin classes is required for osteoclast-mediated bone resorption. *J. Cell Biol.* **192**, 883-897. doi:10.1083/jcb.201007141

Senetar, M. A. and McCann, R. O. (2005). Gene duplication and functional divergence during evolution of the cytoskeletal linker protein talin. *Gene.* **362**, 141-152. doi:10.1016/j.gene.2005.08.012

Senetar, M. A., Moncman, C. L. and McCann, R. O. (2007). Talin2 is induced during striated muscle differentiation and is targeted to stable adhesion complexes in mature muscle. *Cell Motil. Cytoskelet.* **64**, 157-173. doi:10.1002/cm.20173

Song, X., Yang, J., Hirbawi, J., Ye, S., Perera, H. D., Goksoy, E., Dwivedi, P., Plow, E. F., Zhang, R. and Qin, J. (2012). A novel membrane-dependent on/off switch mechanism of talin FERM domain at sites of cell adhesion. *Cell Res.* **22**, 1533-1545. doi:10.1038/cr.2012.97

Soto-Ribeiro, M., Kastberger, B., Bachmann, M., Azizi, L., Fouad, K., Jacquier, M.-C., Boettiger, D., Bouvard, D., Bastmeyer, M., Hytönen, V. P. et al. (2019). β1D integrin splice variant stabilizes integrin dynamics and reduces integrin signaling by limiting paxillin recruitment. *J. Cell Sci.* **132**, jcs224493. doi:10.1242/jcs.224493

Sun, Z., Guo, S. S. and Fässler, R. (2016). Integrin-mediated mechanotransduction. *J. Cell Biol.* **215**, 445-456. doi:10.1083/jcb.201609037

Tadokoro, S., Shattil, S. J., Eto, K., Tai, V., Liddington, R. C., de Pereda, J. M., Ginsberg, M. H. and Calderwood, D. A. (2003). Talin binding to integrin beta tails: a final common step in integrin activation. *Science* **302**, 103-106. doi:10.1126/science.1086652

Theodosiou, M., Widmaier, M., Böttcher, R. T., Rognoni, E., Veelders, M., Bharadwaj, M., Lambacher, A., Austen, K., Müller, D. J., Zent, R. et al. (2016). Kindlin-2 cooperates with talin to activate integrins and induces cell spreading by directly binding paxillin. *eLife* **5**, e10130. doi:10.7554/eLife.10130

Tria, G., Mertens, H. D. T., Kachala, M. and Svergun, D. I. (2015). Advanced ensemble modelling of flexible macromolecules using X-ray solution scattering. *IUCrJ* **2**, 207-217. doi:10.1107/S205225251500202X

Van Der Spoel, D., Lindahl, E., Hess, B., Groenhof, G., Mark, A. E. and Berendsen, H. J. C. (2005). GROMACS: Fast, flexible, and free. *J. Comput. Chem.* **26**, 1701-1718. doi:10.1002/jcc.20291

Waterhouse, A. M., Procter, J. B., Martin, D. M. A., Clamp, M. and Barton, G. J. (2009). Jalview Version 2–a multiple sequence alignment editor and analysis workbench. *Bioinformatics* **25**, 1189-1191. doi:10.1093/bioinformatics/btp033

Wegener, K. L., Partridge, A. W., Han, J., Pickford, A. R., Liddington, R. C., Ginsberg, M. H. and Campbell, I. D. (2007). Structural basis of integrin activation by Talin. *Cell.* **128**, 171-182. doi:10.1016/j.cell.2006.10.048

Wiedle, G., Johnson-Léger, C. and Imhof, B. A. (1999). A chimeric cell adhesion molecule mediates homing of lymphocytes to vascularized tumors. *Cancer Res.* **59**, 5255-5263.

Xing, B., Thuppal, S., Jedsadayanmata, A., Du, X. and Lam, S. C.-T. (2006). TA205, an anti-talin monoclonal antibody, inhibits integrin–talin interaction. *FEBS Lett.* **580**, 2027-2032. doi:10.1016/j.febslet.2006.02.077

Ye, F., Petrich, B. G., Anekal, P., Lefort, C. T., Kasirer-Friede, A., Shattil, S. J., Ruppert, R., Moser, M., Fässler, R. and Ginsberg, M. H. (2013). The mechanism of kindlin-mediated activation of integrin αIIbβ3. *Curr. Biol.* **23**, 2288-2295. doi:10.1016/j.cub.2013.09.050

Ye, X., McLean, M. A. and Sligar, S. G. (2016). Phosphatidylinositol 4,5-bisphosphate modulates the affinity of talin-1 for phospholipid bilayers and activates its autoinhibited form. *Biochemistry* **55**, 5038-5048. doi:10.1021/acs.biochem.6b00497

Zhang, H., Chang, Y.-C., Huang, Q., Brennan, M. L. and Wu, J. (2016). Structural and functional analysis of a talin triple-domain module suggests an alternative talin autoinhibitory configuration. *Structure* **24**, 721-729. doi:10.1016/j.str.2016.02.020

Zhu, L., Yang, J., Bromberger, T., Holly, A., Lu, F., Liu, H., Sun, K., Klapproth, S., Hirbawi, J., Byzova, T. V. et al. (2017). Structure of Rap1b bound to talin reveals a pathway for triggering integrin activation. *Nat. Commun.* **8**, 1744. doi:10.1038/s41467-017-01822-8

PUBLICATION
II

Crystal structure of the FERM-folded talin head reveals the determinants for integrin binding

Zhang, P., Azizi, L., Kukkurainen, S., Gao, T., Baikoghli, M., Jacquier, M. C., Sun, Y., Määttä, J. A. E., Cheng, R. H., Wehrle-Haller, B., Hytönen, V.P., Wu, J.

Proc. Natl. Acad. Sci. 2020 Dec 22;117(51):32402-32412
doi: 10.1073/pnas.2014583117

Crystal structure of the FERM-folded talin head reveals the determinants for integrin binding

Pingfeng Zhang[a,1], Latifeh Azizi[b,c], Sampo Kukkurainen[b,c,2], Tong Gao[a,2], Mo Baikoghli[d,2], Marie-Claude Jacquier[e,2], Yijuan Sun[a], Juha A. E. Määttä[b,c], R. Holland Cheng[d], Bernhard Wehrle-Haller[e,3], Vesa P. Hytönen[b,c,3], and Jinhua Wu[a,3]

[a]Molecular Therapeutics Program, Fox Chase Cancer Center, Philadelphia, PA 19111; [b]Faculty of Medicine and Health Technology, Tampere University, FI-33520 Tampere, Finland; [c]Department of Clinical Chemistry, Fimlab Laboratories, FI-33520 Tampere, Finland; [d]Department of Molecular and Cellular Biology, University of California, Davis, CA 95616; and [e]Department of Cell Physiology and Metabolism, Centre Médical Universitaire, University of Geneva, 1211 Geneva 4, Switzerland

Edited by Janet L. Smith, University of Michigan–Ann Arbor, Ann Arbor, MI, and approved October 28, 2020 (received for review July 10, 2020)

Binding of the intracellular adapter proteins talin and its cofactor, kindlin, to the integrin receptors induces integrin activation and clustering. These processes are essential for cell adhesion, migration, and organ development. Although the talin head, the integrin-binding segment in talin, possesses a typical FERM-domain sequence, a truncated form has been crystallized in an unexpected, elongated form. This form, however, lacks a C-terminal fragment and possesses reduced β3-integrin binding. Here, we present a crystal structure of a full-length talin head in complex with the β3-integrin tail. The structure reveals a compact FERM-like conformation and a tightly associated N-P-L-Y motif of β3-integrin. A critical C-terminal poly-lysine motif mediates FERM interdomain contacts and assures the tight association with the β3-integrin cytoplasmic segment. Removal of the poly-lysine motif or disrupting the FERM-folded configuration of the talin head significantly impairs integrin activation and clustering. Therefore, structural characterization of the FERM-folded active talin head provides fundamental understanding of the regulatory mechanism of integrin function.

talin | integrin | FERM domain | cell adhesion | NPxY motif

Integrins are heterodimeric adhesion receptors that mediate cell adhesion and migration (1, 2). Abnormal expression and hyperactivity of integrins lead to severe pathological phenotypes, including cardiovascular diseases (CVDs), impaired inflammatory responses, T cell proliferation defects, and enhanced tumor metastasis (3, 4). Activation of integrins is driven by the intracellular association of the activator talin and its coactivator kindlin through a so-called inside-out integrin activation pathway. This pathway is induced by the activation and talin head interaction of RAP1 GTPase and, in lymphocytes, requires RAP1 effector molecule RAP1-interacting adaptor molecule (RIAM) to mediate the translocation of talin to the plasma membrane (5–7).

Talin is a multidomain, homo-dimeric protein. This 270-kDa molecule can be divided in a four-subdomain head segment and a rod region containing 13 domains consisting of four or five helical bundles with a C-terminal dimerization helix (8–11) (Fig. 1*A*). The talin N-terminal head domain (residues 1 to 433, defined by calpain II cleavage) contains two ubiquitin-like subdomains (F0 and F1), an acyl-CoA–binding protein-like subdomain (F2), and a phosphotyrosine binding-like, integrin-binding subdomain (F3), followed by a linker that is cleaved by calpain II processing (10).

Sequence analysis indicates that the talin head possesses a FERM domain (residues 84 to 405). FERM domain proteins are often found in proteins that link different functionalities to the plasma membrane, such as the binding to the actin cytoskeleton (myosin-VII and -X, moesin, ezrin...), or kinases (FAK), and bind to transmembrane receptors as adaptor molecules (ICAM, CD44, etc.) (12, 13). FERM domain proteins share a conserved and compact cloverleaf-like fold of three subdomains (F1, F2, and F3) that have been shown by X-ray crystallography for several members of the family, including kindlin-2, a coactivator of integrin and most homologous to talin (14). Interestingly, unlike a typical FERM domain, a functionally impaired 1 to 400 talin fragment, missing the loop in the F1 subdomain (del139–168), as well as the C-terminal poly-lysine motif in the F3 domain, has been crystallized in an elongated conformation (15, 16). However, small-angle X-ray scattering experiments with this truncated construct have indicated that the talin head exists in an equilibrium of open and partially closed conformations in solution (15), proposing a flexible head domain. Moreover, recent electron microscopy (EM)-based studies of full-length talin-1 have revealed either a compact, autoinhibited talin-dimer (17) or, alternatively, a more open conformation of the talin monomer, in which however the F0-F1 head domains could not be localized or identified (18). Therefore, the structure of the biologically active talin head domain is still not known.

In addition to talin, knockout studies of kindlin-1, -2, and -3, as well as patients with kindlin-3 deficiencies, have shown that kindlins are also required for integrin activation and clustering

Significance

Although efforts have been made to determine the structure of talin and the way it interacts with integrins through the "head" domain, our work shows now that many of the previous mechanistic models based on the talin adapter are likely to be misleading as they are constructed on a crystal structure representing an improperly folded talin head domain. In this work, we identified the problem with the current talin head model and proposed a FERM-folded talin head. By analyzing these structural features of the FERM-folded talin head in a cellular context, involving also the kindlin adapter, we are making a critical and unprecedented contribution to the understanding and regulation of cell-matrix adhesions.

Author contributions: B.W.-H., V.P.H., and J.W. designed research; P.Z., L.A., S.K., T.G., M.B., M.-C.J., Y.S., J.A.E.M., R.H.C., B.W.-H., V.P.H., and J.W. performed research; J.W. contributed new reagents/analytic tools; P.Z., L.A., S.K., T.G., M.B., M.-C.J., J.A.E.M., R.H.C., B.W.-H., V.P.H., and J.W. analyzed data; and P.Z., S.K., T.G., J.A.E.M., R.H.C., B.W.-H., V.P.H., and J.W. wrote the paper.

The authors declare no competing interest.

This article is a PNAS Direct Submission.

[1] Present address: Cancer Center at Renmin Hospital of Wuhan University, Wuhan 430062, China.

[2] S.K., T.G., M.B., and M.-C.J. contributed equally to this work.

[3] To whom correspondence may be addressed. Email: Bernhard.Wehrle-Haller@unige.ch, vesa.hytonen@tuni.fi, or Jinhua.wu@fccc.edu.

This article contains supporting information online at https://www.pnas.org/lookup/suppl/doi:10.1073/pnas.2014583117/-/DCSupplemental.

First published December 7, 2020.

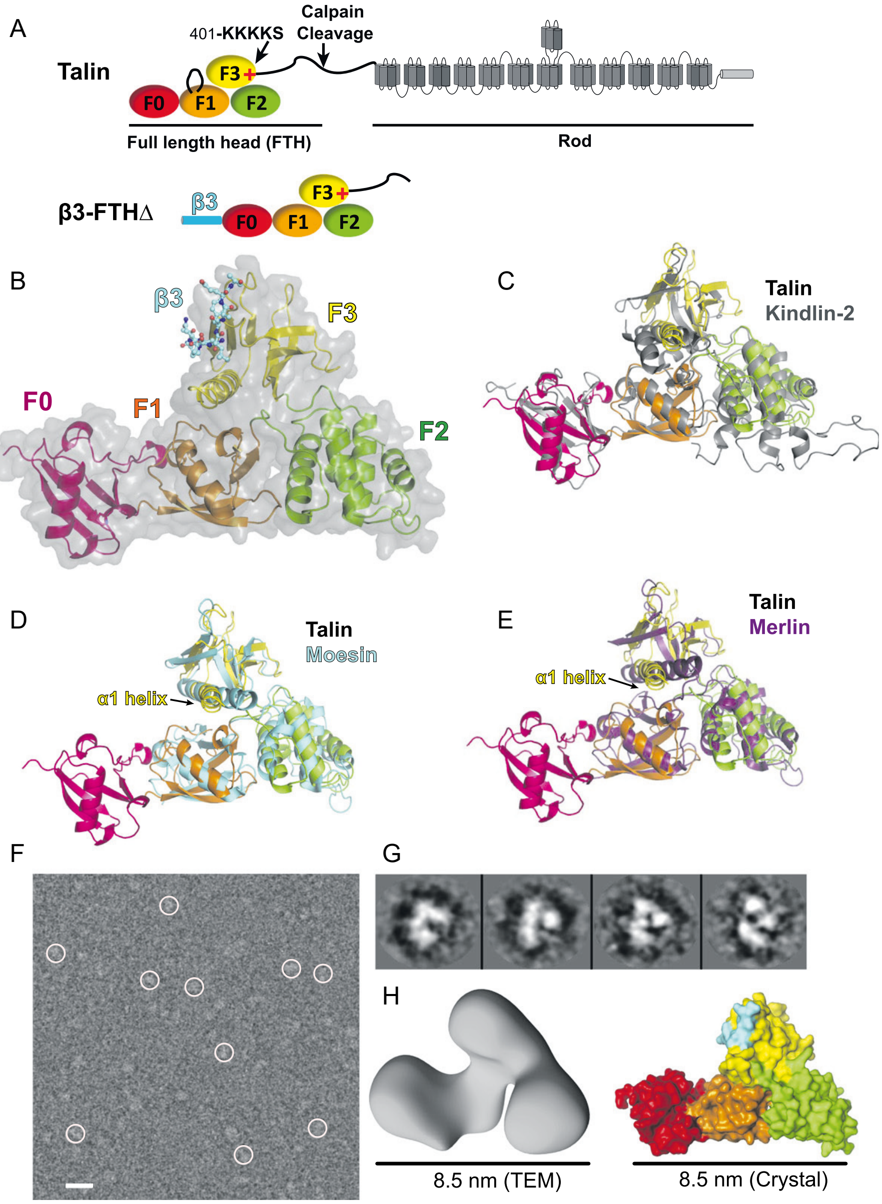

Fig. 1. Crystal structure of talin head in a FERM-folded configuration. (*A*, *Upper*) Schematic domain structure of talin. The poly-lysine motif at the end of the F3 subdomain is indicated by a red "+" mark. (*A*, *Lower*) Schematic structure of the β3-FTHΔ fusion protein. (*B*) Overall structure of β3-FTHΔ. The talin head is shown in schematic and surface. The F0 domain is red. The F1, F2, and F3 subdomains of the FERM domain are in orange, green, and yellow, respectively. Bound β3 is shown in stick representation. (*C*–*E*) Superposition of the talin head, in the same color scheme as in B, and various FERM proteins. (*C*) The talin head with kindlin-2 (gray). (*D*) The talin head with moesin (cyan). (*E*) The talin head with merlin (purple). (*F*) Field view of negatively stained talin head t1-405 captured by TEM. (Scale bar: 10 nm.) (*G*) Shown are 2D class average images. (*H*, *Left*) A 3D TEM volume of t1-405. Resolution, 15.2 Å. (*H*, *Right*) Surface representation of the talin head in the crystal structure.

(19–21). However, in most experimental settings, a sufficient amount of endogenous kindlin is present in cells, and, hence, integrins have been shown to be activated by talin head overexpression (22). In addition to integrin activation, the expression of the talin head induces integrin clustering (23), which required the membrane proximal interactions of a hydrophobic (24) and acidic (D723/E726) motif in β3-integrins to interact with basic residues (K316/K324) in the talin F3 subdomain (25). In addition, other basic residues of the F2 and F3 subdomains interact with acidic membrane lipids, such as phosphatidylinositol 4,5-bisphosphate (PIP2), to stabilize the integrin/talin complex at the plasma membrane (25, 26). Hence, due to their integrin and lipid interactions, the talin head subdomains F2-F3 are sufficient for activation of αIIbβ3 integrin, when recorded with the PAC-1 antibody in detached cells (22). Interestingly, however, the F2-F3 segment of the talin head failed to activate α5β1 integrin, when probed with a soluble fibronectin fragment (27), proposing that, at least in the latter case, soluble ligand binding requires the entire talin head domain, potentially involving an additional lipid-binding domain in the F1 subdomain (28). In addition, RAP1 binding to the F0 and/or F1 subdomains of the talin head has been proposed to recruit talin to the plasma membrane, contributing to integrin activation and Rap1-mediated cell-matrix adhesion (25, 26, 29). Thus, talin, RAP1, and kindlin play important roles in the integrin activation step while kindlin also induces clustering of activated integrins (30–33).

Talin is so far the only FERM family protein that has not been shown to fold into a conserved cloverleaf-like shape. Here, we present a crystal structure of the full-length talin head with an F1-loop deletion in complex with the β3-integrin cytoplasmic tail. The structure reveals that the F1-F2-F3 subdomains of the talin head indeed adopt a canonical FERM-like fold. The complete C-terminal helix in F3, including the poly-lysine motif, stabilizes the compact FERM conformation by interaction with the F1 subdomain and simultaneously contributing to a hydrophobic cavity suitable to accommodate the Leu746 of the N-P-L-Y motif of the β3-integrin. Removal of the C-terminal poly-lysine motif of the F3 subdomain leads to reduced affinity with β3-integrin, decreased thermal stability of the talin head, and impaired integrin activation and clustering. The FERM fold of the entire talin head is further confirmed by transmission electron microscopy (TEM) and charge-complementation mutagenesis at the interface between the F1 and F2 subdomains. Together, our results reveal a physiologically functional and structurally stable talin head in a FERM-folded configuration, which ensures a tight association with integrin β tail for integrin activation and clustering.

Results

Crystal Structure of a FERM-Folded Talin Head in Complex with the β3-Integrin Tail. In order to better understand the physiological roles of the F0-F1 domains and C-terminal basic residues for talin-mediated integrin activation and clustering, we initiated a structural approach to determine the crystal structure of the talin segment representing the full-length talin head (FTH), when generated by natural cleavage of talin by calpain (residues 1 to 433) (34). To facilitate crystallization, we removed the calpain binding site (residues 431 to 433) and the F1-loop (residues 139 to 168, subsequently indicated as del30). The resulting talin head construct, FTHΔ, which failed to yield crystals, was then fused with a peptide derived from the cytoplasmic segment of integrin β3, known to contain the membrane proximal talin-binding N-P-L-Y^{747} motif (residues 720 to 750) (Fig. 1*A*). The resulting β3-FTHΔ fusion protein was expected to induce *trans* interaction of the β3 fusion peptide and the talin head to facilitate crystal packing, as well as to ensure an equal stoichiometry of the two segments. Crystals of the fusion protein were obtained by the hanging drop vapor diffusion method. The crystals belong to the space group of $P2_12_12_1$ with one β3-FTHΔ molecule in each asymmetric unit. The structure of β3-FTHΔ was determined by molecular replacement to 2.8-Å resolution (Table 1). The N-terminal (residues 720 to 740 of β3) and C-terminal segments (residues 407 of 430 of talin) of the fusion polypeptide were disordered in the crystal. As expected, the F3 subdomain of one β3-FTHΔ molecule binds to the β3 segment from the neighboring molecule.

The structures of the four individual subdomains, F0, F1, F2, and F3, are similar to the previously reported structures (15, 28). Nevertheless, unlike the elongated domain organization observed in the structure of the talin head construct TH′ (residues 1 to 400 del139-168/del30), the F1-F2-F3 domains of the β3-FTHΔ construct adopt a canonical FERM-folded configuration (Fig. 1*B*). The interface of the F0 and the F1 subdomains in the β3-FTHΔ structure is virtually identical to that observed in the TH′ structure. The FERM-folded conformation of F1-F2-F3 is mainly attributed to the conformational rearrangement of the F1-F2 linker, resulting in a three-leaf clover architecture, with the F3 subdomain residing on the top of the F1 and F2 subdomains. The overall domain organization of β3-FTHΔ is highly homologous to that of monomeric kindlin-2 (PDB ID code 5XPY) (Fig. 1*C*) (14). Compared to kindlin-2, however, which shows a short helical extension at the C terminus, amino acids beyond the α1-helix in F3 of the talin head (406 to 430), although predicted to be partially α-helical, were disordered in the structure. The FERM domain of β3-FTHΔ is also similar to the classic FERM proteins merlin and moesin. Interestingly, the α1-helix at the C terminus of the talin F3 subdomain undergoes a significant rotation with respect to merlin (PDB ID code 4ZRJ) and moesin (PDB ID code 1EF1), resulting in a much wider cleft for integrin binding to the F3 subdomain, and a different connectivity with the F1 domain or F1-F2 linker (Fig. 1 *D* and *E*). Overall, the structure of β3-FTHΔ reveals a full-length talin head, with an F1-loop deletion, in a canonical FERM-folded

Table 1. Crystallographic data collection and refinement statistics

Data collection	
Light Source	NSLS-II AMX
Wavelength, Å	0.92010
Space group	$P2_12_12_1$
Cell dimensions	
a, *b*, *c*, Å	66.07, 66.82, 114.47
α, β, γ, °	90, 90, 90
Resolution, Å	29.62∼2.78 (2.85–2.78)
R_{merge}, %	8.2 (65.5)
I/σ	12.1 (1.9)
CC(1/2), %	99.8 (69.9)
Completeness, %	92.4 (92.5)
No. of reflections	58,557 (4,244)
Multiplicity	2.4 (2.7)
Refinement	
Resolution, Å	29.62∼2.78
$R_{\mathrm{work}}/R_{\mathrm{free}}$, %	21.2/26.5
No. of atoms	3,070
Protein	3,056
Water	14
Wilson B factor, Å^2	63.9
RMSD	
Bond lengths, Å	0.003
Bond angles, °	0.60
Ramachandran plot, %	
Favored	95
Allowed	100

Parentheses denote highest resolution bin 2.85 to 2.78 Å.

conformation, in complex with the cytoplasmic segment of the β3-integrin.

Nevertheless, to further confirm that the intact talin head possesses the FERM fold, we purified talin t1-405 with the intact F1 loop and analyzed its structure in solution by negative-stain TEM. Monodispersed talin proteins were selected through a semiautomated particle selection approach. Reference-free two-dimensional (2D) classification was carried out with a total of 65 classes. The 2D classes clearly showing the four domains of talin were selected for figure preparation. The three-dimensional (3D) map was calculated using the top 50 classes in an iterative manner. The iterative approach to the single-particle reconstruction is aimed to progressively reduce heterogeneity in the data. The 3D map shown in Fig. 1*H* is a representation of the most stable conformation of the talin head (Fig. 1*F*). None of the initial models and preliminary structures showed an elongated structure for t1-405, suggesting that t1-405 does not exist in the elongated conformation as shown in the t1-400(del30) crystal structure (15) (Fig. 1*G*). A 3D reconstruction of t1-405 reveals a TEM volume with an average length of 8.5 nm, which is consistent with the FERM-folded talin head observed in the crystal structure (Fig. 1*H*). Together these data confirm that the full-length talin head adopts a FERM fold for its function in inducing integrin activation and clustering.

The C-Terminal Poly-Lysine Motif in the Talin F3 Subdomain Is Required for Integrin Activation and Clustering. The FERM configuration of the talin head is stabilized by an extensive intersubdomain interaction network (Fig. 2*A*). In particular, the C-terminal Lys401 and Lys402 of the F3 subdomain form salt bridges with two negatively charged residues, Asp125 and Glu126 of the F1 subdomain, respectively. The F1:F2 interface is fortified by an Arg194:Asp222 salt bridge and an Arg195:Gln218 hydrogen bond. In addition, the F1 subdomain residue Arg195 also forms salt bridges with Glu126 of F1 and Asp201 in the F1-F2 linker. This network of salt bridges and hydrogen bonds connected all three subdomains (F1, F2, and F3) and is likely to be relevant for the structure and function of the talin head. A structure-based alignment of the α1-helix in F3 (residues 394 to 405 in talin) revealed conserved basic residues in kindlin-2, SNX17, and the ERM-family proteins (ezrin, radixin, moesin, and merlin) (Fig. 2*B*). Despite the homology analysis that indicates Lys401 and Lys402 to be part of the F3 subdomain, previous crystallographic studies of the talin-1 head used a truncated F3 subdomain (up to residue 400) (15, 35), which was based on a stable talin head fragment obtained from limited proteolysis analyses (35). Although the truncated F3 subdomain retains the phosphotyrosine-binding (PTB) domain fold, the resulting talin head molecule appeared to be highly flexible in solution and was crystallized in an elongated configuration. This change in structural stability is likely due to the lack of K401:D125 and K402:E126 salt bridges that hold the F1 and F3 subdomains together. Similar intersubdomain interactions were also seen in kindlin and other classic FERM proteins, such as moesin (PDB ID code 1EF1), to maintain their FERM domain stability (Fig. 2*C*). In particular, Arg294 and Arg295 of moesin form salt bridges with Glu92 and Glu87 in the F1-F2 linker, respectively; Arg659 of kindlin-2 (PDB ID code 5XPY) interacts with Glu137 in the F1 subdomain. That these interactions contribute to the overall stability of the compact FERM fold was further supported by differential scanning calorimetry (DSC) of different forms of the talin head, reflecting a consistent downward shift in melting temperature (T_m) upon deletion of the poly-lysine motif (Table 2). Differential scanning fluorimetry cross-validated this finding (*SI Appendix*, Fig. S1). Thus, our structure of the full-size talin head in complex with integrin β3 suggests that the poly-lysine motif at the C terminus of the F3 subdomain is essential for the stability of the FERM-folded conformation of the talin head.

Transfection of the full-length talin head (1 to 435) can induce integrin activation and integrin clustering in various cell types (22, 23, 28). However, talin F2-F3 is reportedly not sufficient to induce α5β1-integrin activation, when measured by soluble fibronectin binding (27), whereas it activates integrin αIIbβ3 when probed with the multivalent PAC-1 IgM antibody (22, 27, 36). To identify also potentially relevant amino acids in the C-terminal part of the talin head, especially those linked to the salt bridges and hydrogen bonds formed between F1, F2, and F3 subdomains, we transfected melanoma B16F1 cells with talin head constructs and examined the αvβ3-integrin activity (Fig. 2*D*). While the sequences between residues 406 and 435 could be removed without affecting integrin activation, the further removal of the poly-lysine motif of residues 401 to 405 caused a loss of integrin activation (Fig. 2*E*). Furthermore, mutation of the conserved Q218, hydrogen bonded to R195, and part of the extensive interdomain interaction network, resulted in a loss of integrin activation (Fig. 2*E*). To assess the kindlin-1–assisted integrin clustering, we developed a more physiological integrin-clustering assay that takes into account the equally critical role of kindlin for integrin activation and clustering (37–39). We analyzed the clustering of GFP-tagged β3-integrin in the presence of the cotransfected talin head and kindlin-1 in B16F1 melanoma cells that were spread on serum-coated glass coverslips (25). The degree of clustering of integrin receptors was calculated from total internal reflection fluorescence (TIRF) microscopy images, by determining the percentage of the cell area covered with integrin clusters (Fig. 2*F*) (25). Similar to the reduced integrin activation by the mutation of Q218 as part of the H-bond network (Q218A), the introduction of a large hydrophilic Gln residue at an F3:F1-F2 interface residue Ser311, which is conserved with kindlins (Ser in kindlin-3, Thr in kindlin-1, -2) and pointing to the core of the FERM domain (*SI Appendix*, Fig. S2), as well as the removal of the poly-lysine motif, led to a loss of integrin clustering, despite the presence of kindlin (Fig. 2*G*). Moreover, removal of the C-terminal end beyond residue 400, particularly the poly-lysine motif (residues 401 to 405), of the full-length talin head significantly diminished the association of the talin head with the cytoplasmic tail of integrin β3 (Fig. 2 *H* and *I*) and caused a significant drop ($\Delta\Delta G_{app}$ 4.8 kJ/mol) in integrin peptide binding measured using biosensor (Table 2). In contrast, the presence of the following linker region to the rod domains (residues 406 to 435) reduced the binding affinity of the talin head and integrin β3 (Fig. 2 *H* and *I*). This observation is consistent with the binding analysis by the Octet optical biosensor (Table 2). Interestingly, the C-terminal poly-lysine motif (residues 401 to 405) was removed from the previously described elongated crystal structures of the talin head (15, 16) and was absent from the crystallized chimeric β3–F2–F3 talin complex (35), suggesting that these structures may not represent physiologically relevant conformations of talin, nor its associated integrin, respectively.

Binding Specificity of the β3-Integrin Tail and the FERM-Folded Talin Head. The structure of β3-FTHΔ fusion protein reveals a *trans* F3:β3 interaction in a typical NPxY:PTB domain binding mode. Interestingly, this interaction is distinctly different from the F3:β3 interaction observed in the structure of the β3-F2-F3 chimeras obtained with a truncated C-terminal helix in F3 (PDB ID code 1MK7) (35) (Fig. 3*A*). Due to the abovementioned rotation and contraction of F2 and F3 domains in the truncated F2-F3 structure and the respective movement of the α1-helix on the surface of the F3 subdomain, the F3 subdomain in the β3-FTHΔ structure possesses a much more extended cleft between the β5 strand and α1-helix than that of the β3-F2-F3 chimera (Fig. 3*B*). The interaction between the C-terminal Lys401/Lys402 and the F1 subdomain residues leads to the α1-helix movement toward the F1 subdomain, resulting in a more “open” β5-α1 cleft (Fig. 3*B*). Moreover, we identified an important interface that involves

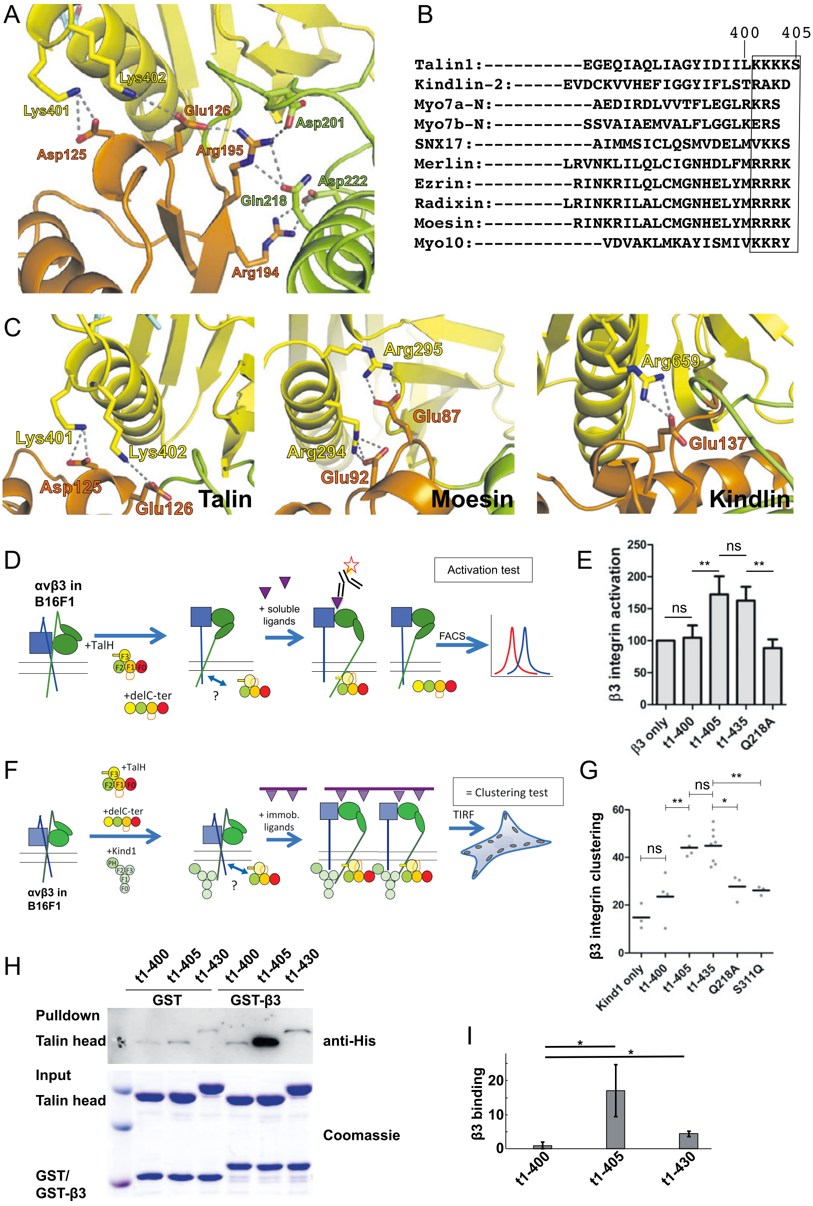

Fig. 2. FERM-folded talin head is required for integrin functions. (*A*) Intersubdomain interaction network in the talin FERM domain. Hydrogen bond interactions are shown by dotted lines. (*B*) Structure-based alignments of the α1-helix of the F3 domain, indicating a conserved patch of basic amino acids (boxed) that are missing in the nonfunctional (1-400) talin head construct. (*C*) Salt bridge interaction mediated by the C-terminal positively charged residues in the F3 subdomain and negatively charged residues in the F1 subdomain (*Left*, talin; *Right*, kindlin) or the F1-F2 linker (*Middle*, moesin). Dashed lines represent hydrogen bonds. (*D*) Integrin αvβ3 activation in B16F1 melanoma cells by the talin head is shown in a schematic representation. Red star represents the fluorescent antibody. Purple triangles indicate integrin ligands, in either soluble (triangle) or substrate-bound (triangle on bars, in *F*) forms. Question mark at bidirectional arrow indicates integrin/adapter interaction sites to be studied. (*E*) Activity indices of integrin αvβ3 in B16F1 cells transfected with full-length talin head (t1-435, residues 1 to 435, $n = 8$), C-terminally truncated talin head (t1-400, $n = 4$; t1-405, $n = 9$), or the FERM-interface mutations (Q218A, residues 1 to 435, $n = 4$). (*F*) Integrin αvβ3 clustering in B16F1 melanoma cells by the talin head and kindlin-1 is shown in a schematic representation. (*G*) Clustering indices of integrin αvβ3 in B16F1 cells transfected with t1-400, t1-405, t1-435, Q218A, and S311Q. (*H*) GST-tagged integrin β3 cytoplasmic tail was used as a bait to pull down purified His6-tagged talin head proteins t1-400, t1-405, and t1-430. (*I*) The blots from *H* were quantified and normalized to the control. Data shown are mean ± SD, $n = 4$ ($^{*}P < 0.02$; $^{**}P < 0.01$; $^{***}P < 0.001$). ns: not significant.

extensive interactions between multiple talin residues and β3 residues Asn744 and Leu746 (*SI Appendix*, Table S1). In the β3-F2-F3 chimera structure, only a weak interaction of F3 residues with Asn744 and Leu746 of the N-P-L-Y motif was observed. However, in our structure, the N-P-L-Y motif of the bound β3 fragment contacts the F3 subdomain extensively through the residues surrounding the cleft. Asn744 makes direct side-chain interactions with Trp359 and Ile396, and Pro745 contacts with Leu400. In addition, Leu746 is buried in a hydrophobic pocket comprising Leu353, Ile396, Ile399, and Leu400 (Fig. 3*C*). Indeed, the L746A mutation in integrin β3 has been shown to significantly reduce talin association and diminish integrin activity (22, 40), and the N744A mutation also led to a loss of β3-mediated cell adhesion (41). Our structure thus provides a molecular basis for the essential role of the N-P-L-Y motif in talin:β3 association and confirms its role in integrin activation and clustering. Furthermore, we found that t1-405, a talin head construct including the C-terminal lysines, exhibits higher affinity with integrin β3 than t1-400, which lacks the C-terminal polylysine motif (Table 2). Our results thus indicate that the C-terminal poly-lysine motif in the talin FERM domain is required for the proper folding of the FERM domain and proper β3-integrin binding.

An F2-F3 segment of talin-2 in complex with integrin β1D (PDB ID code 3G9W) was reported previously by Anthis et al. (26). The bound β1D fragment reveals both the N-P-I-Y motif and the juxtamembrane helix. Both the N-P-I-Y motif of β1D and the N-P-L-Y motif seen in the β3-FTHΔ structure adopt the same canonical PTB-domain–binding configuration, and the side chain conformations for the cleft-surrounding residues in their F3 subdomains are also highly conserved (Fig. 3 *C*, *Left*). In contrast to the β3-F2-F3 structure, in which the F3 subdomain ends at residue 400, the talin-2 F2-F3 construct includes the C-terminal lysines. The talin-2 F3 subdomain adopts an "open" configuration as well, allowing the N-P-I-Y motif of integrin β1D to embed into the β5-α1 cleft. Nonetheless, the openness of the β5-α1 cleft in the talin-2 structure is slightly less compared with that of the FERM-folded talin-1, likely due to the lack of interaction with the F1 subdomain (Fig. 3 *C*, *Right*). Interestingly, in the structures of the X11 PTB domain in complex with the amyloid peptide (X11:APP, PDB ID code 1AQC) and IRS-1 PTB domain in complex with an insulin receptor peptide (IRS-1:IR, PDB ID code 5U1M) (42, 43), both PTB domains adopt a nearly "closed" configuration, similar to the talin F3 structures without the C-terminal lysines (Fig. 3*D*). It appears that the rather bulky and rigid Leu746 in integrin β3 (Ile in β1) is unable to fit in the "closed" cleft of F3 but requires an open cleft for a classic PTB:NPxY interaction. Evidently, this conjecture is supported by the structures of the FERM domain of sorting nexin 17 (SNX17) bound to two different N-P-x-Y fragments. The structure of SNX17 bound to an N-A-A-Y fragment of P-selectin (PDB ID code 4GXB), with an alanine residue at the "x" position, reveals an F3 subdomain in a closed configuration (44). In contrast, the F3 subdomain in the structure SNX17 bound to an N-P-L-F fragment of Krit-1 (PDB ID code 4TKN), with a leucine residue at the "x" position, exhibits a rather open configuration (Fig. 3*E*) (45). In the case of talin, however, substitution of Leu746 by an alanine residue in integrin β3 results in significant loss of talin binding (40), suggesting that the talin F3 subdomain is unable to switch between the open and closed configurations.

The F1-F2 Interface in the FERM-Folded Configuration Is Crucial for Talin Head Function. We compared the structures of the FERM-folded talin head and the elongated talin head (PDB ID code 3IVF). The four subdomains are essentially identical, with root-mean-square deviation (RMSD) of 0.41 Å for the F0 subdomains (residues 1 to 83), 0.70 Å for the F1 subdomains (residues 85 to 196), 0.34 Å for the F2 subdomains (residues 206 to 305), and 0.61 Å for the F3 subdomains (residues 311 to 405) (*SI Appendix*, Fig. S3*A*). Moreover, the F0-F1 and F2-F3 interfaces are also similar, with the exception of the E269/K345 salt bridge that is only seen in the elongated talin head structure (PDB ID code 3IVF) (*SI Appendix*, Fig. S3*B*). The RMSD of the F0-F1 double domains in the two structures is 0.65 Å, and 2.1 Å for that of the F2-F3 double domains. In contrast, superposition of the F2 subdomains reveals that the F1-F2 interface in the FERM-folded structure is drastically different from that of the elongated structure (PDB ID code 3IVF), resulting in a completely rearranged quaternary structure (Fig. 4*A*). The F1-F2 interface in the FERM-folded structure is stabilized by a salt bridge formed by a basic residue Arg194 in the F1 subdomain and an acidic residue Asp222 in the F2 subdomain. The two residues are highly conserved among the FERM-containing proteins (Fig. 4*B*). Nevertheless, the two residues are far apart in the elongated crystal structure of the talin head (Fig. 4*A*). In moesin (PDB ID code 1EF1), the corresponding R81:E108 salt bridge also contributes to the F1-F2 interface (Fig. 4*C*). This conserved interaction is potentially critical in other FERM domain proteins, such as SNX31, where the equivalent of Arg194 was identified as a melanoma driver mutation (46). In the case of the talin head, the charge inversion of Arg194 to Glu (R194E) completely abrogated the talin head (1-435)-induced clustering in the presence of cotransfected kindlin-1 (Fig. 4*D*), and this loss of integrin clustering was rescued by a complementary mutation D222K. The double R194E/D222K mutant of the talin head was capable of inducing integrin clustering comparable to that of wild type (WT) likely by reestablishing the salt bridge in the F1-F2 interface (Fig. 4*D*). In addition, Gln218 in the F2 subdomain that contributes to the F1-F2 interface is also conserved among FERM proteins (Fig. 4*B*). In the case of moesin, the Gln218-equivalent

Table 2. Characterization of talin head

							Integrin binding			
	HPLC				DSC		WT- β3		VE- β3	
Talin	$\mathrm{MW}_{\mathrm{theor.}}$	V_r	$\mathrm{MW}_{\mathrm{SLS}}$	R(h) in DLS	T_m	ΔT_m	ΔG_{app}	$\Delta\Delta G_{\mathrm{app}}$	ΔG_{app}	$\Delta\Delta G_{\mathrm{app}}$
t1-405	51.4	1.80	66.9	4.62 ± 0.35	54.2 ± 0.1	0	−27.1	0.0	−37.1	0.0
t1-400	50.8	1.81	64.3	4.57 ± 0.32	52.3 ± 0.3	−2.0	−22.3	+4.8	−35.0	+2.1
t1-435	54.5	1.77	72.4	4.77 ± 0.37	53.9 ± 0.1	−0.4	−24.3	+2.8	−36.6	+0.5

Characterization of various talin head forms by SEC equipped with in-line SLS and DLS, and analysis of T_m in DSC. Theoretical molecular weight ($\mathrm{MW}_{\mathrm{theor.}}$) and molecular weight determined by SEC-SLS ($\mathrm{MW}_{\mathrm{SLS}}$) are given in kDa. Retention volume (V_r) is given in mL. Hydrodynamic radius R(h) is given in nm. T_m and the difference from T_m (t1-405) (ΔT_m) are given in °C. Binding of wild-type (WT-β3) and high-affinity (VE-β3) β3-integrin was analyzed using the Fortebio Octet RED384 optical biosensor. The approximated Gibbs free energy of binding (ΔG_{app}) and the difference in ΔG_{app} compared to t1-405 ($\Delta\Delta G_{\mathrm{app}}$), are shown in $\mathrm{kJ{\cdot}mol^{-1}}$. HPLC, high-pressure liquid chromatography.

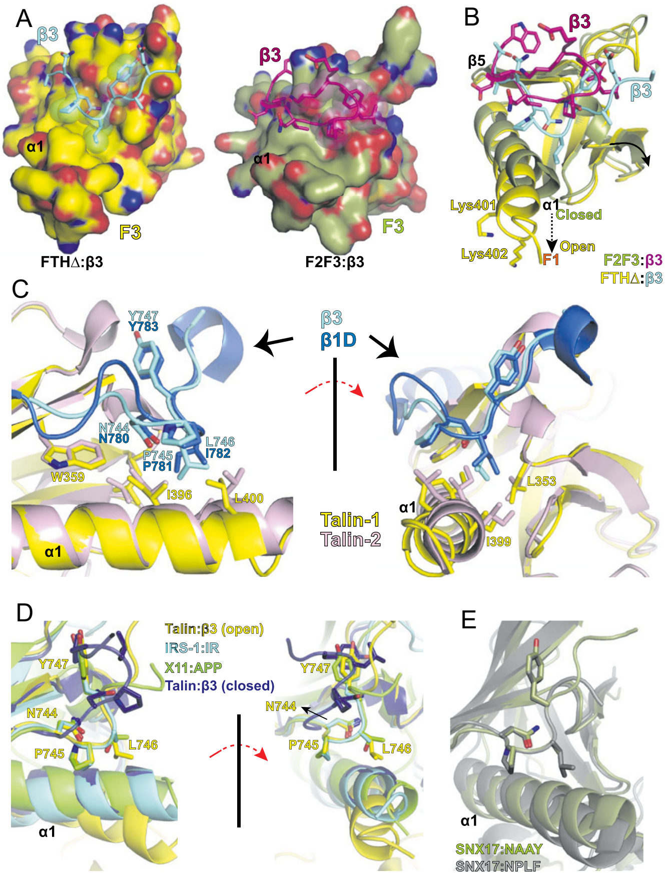

Fig. 3. Interaction of the N-P-L-Y motif with the F3 subdomain of the talin head. (*A*) Comparison of the β3:F3 interactions in β3-FTHΔ (*Left*) and in β3-F2-F3 (*Right*). β3 fragments are shown in stick with the N-P-L-Y motif highlighted in spheres. F3 subdomains are shown in surface representation. β3 and the F3 subdomain (residues 306 to 406) from β3-FTHΔ are colored in cyan and yellow, respectively. β3 and the F3 subdomain (residues 306 to 400) from β3-F2-F3 are colored in purple and olive, respectively. (*B*) Superposition of the N-P-L-Y motifs and their binding sites from the β3-FTHΔ and β3-F2-F3 structures. All fragments adopt the same color scheme as in A. Interactions of Lys401/Lys402 and the F1 subdomain lead to the rotation of the α1-helix in the F3 subdomain and an open β5-α1 cleft. (*C*) Superposition of the β3:F3(talin-1) from β3-FTHΔ and β1D:F3(talin-2) structures. β3:F3(talin-1) adopts the same color scheme as A. β1D and F3 of talin-2 are colored in sapphire and light pink, respectively. Side chains of the NPxY motifs and their contacting residues in the F3 subdomains are shown in stick representation. (*D*) Superposition of the β3:F3(talin-1) in the open (yellow) and closed (purple) configurations and other NPxY:PTB domain complexes. The PTB domain of IRS-1 in complex with the insulin receptor peptide is colored in cyan, and the PTB domain of X11 in complex with the amyloid peptide is colored in green. (*E*) Superposition of SNX17 in complex with an N-A-A-Y peptide (olive) and SNX17 in complex with an N-P-L-F peptide (gray).

Gln105 interacts with the F1-F2 linker residue Tyr85 and Ala82 of the F1 subdomain (Fig. 4*C*). As shown above, substitution of Gln218 by a nonpolar alanine in the talin head significantly diminished integrin activation and clustering (Fig. 2 *E* and *G*). These results suggest that the compact FERM fold and biological activity are preserved via this F1-F2 interface in cells.

Discussion

Talin plays a key role in integrin-mediated cell-matrix interactions, contributing to integrin activation and physical linking of integrins to the cytoskeleton. We determined the structure of the talin head domain containing the C-terminal poly-lysine motif, which stabilizes the FERM-like cloverleaf conformation (Fig. 2). The cloverleaf conformation is common to all FERM-like proteins determined so far, except for the previous talin structures based on C-terminally truncated versions (15, 16). Another key factor enabling the crystallization of talin was the terminal fusion of the β3-integrin sequence, which bound an adjacent talin monomer *in trans*. Importantly, the talin-integrin interface revealed that C-terminal residues of the talin F3 α1-helix interact with the F1 subdomain, thus opening the binding groove to accommodate the N-P-L-Y motif of the integrin β3 peptide (Fig. 3). Analysis of SNX17, another FERM-like protein in complex with different ligands, showed that the N-P-x-Y binding site opening and helix movement correlated with the size of the residue at the x-position. Whether α1-helix movements in the F3 domain are relevant for talin/integrin regulation in vivo is not clear. However, in contrast to a FERM folded talin head, where the position of the F3 α1-helix is

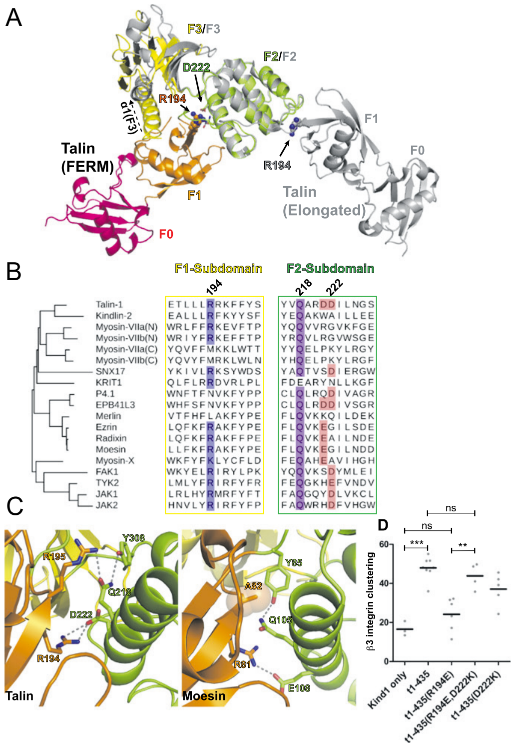

Fig. 4. Full-length talin head has FERM-like subdomain interfaces. (*A*) Superposition of the F2 subdomains from the FERM-fold talin head and elongated talin head conformation. Side chains of R194 and D222 in the FERM-folded talin head are shown in sphere representation (solid arrows). Note the change in orientation of the F0 and F1 subdomains and the position of R194 (sphere, solid arrow) in the elongated talin head structure, as well as the upward rotation of the α1-F3 helix (dashed arrow) in the absence of a centrally positioned F1 domain. (*B*) Structure-based alignments of F1 and F2 domain sequence motifs involved in intersubdomain recognition. The equivalents of R194 and D222 are found in several known FERM domains, and Q218 is highly conserved and interacts with F1 subdomain backbone and residues. (*C*) Conserved F1-F2 interface in talin (*Left*) and moesin (*Right*). In moesin, the side chain of the Q218-equivalent Q105 forms hydrogen bonds with A82 backbone carbonyl and amide groups. (*D*) While R194E had a severe negative effect on **β**3-GFP-integrin clustering, it can be rescued by a complementary mutation (R194E,D222K). $^{***}P < 0.001$; $^{**}P < 0.01$.

stabilized by contacts with the F1 subdomain, the position of the F3 α1-helix appears to switch in F2-F3 or F3-only constructs. This would potentially affect the ligand binding pocket and thus the affinity to the integrin cytoplasmic tail. On the other hand, a consistent reduction in integrin tail binding affinity was noted in the presence of the linker region to the rod domains (residues 406 to 435), suggesting that the linker partially obstructs the integrin binding site in the talin head. Interestingly, the corresponding linker region in kindlin-2 forms another short α-helix (α2), which makes direct contact with the F3-α1-helix and the bound integrin-β (14). Whether the α2-helix in kindlin F3 negatively impacts kindlin:integrin-β interaction remains to be investigated. In the case of talin, phosphorylation of the linker activates integrin and leads to extensive focal adhesion turnover and inhibited cell migration by preventing ubiquitylation and subsequent degradation (47, 48). One can speculate that phosphorylation enables the linker to interact with the lysine residues that are otherwise ubiquitylated, thus stabilizing the linker and resulting in enhanced integrin activity.

While we were preparing this manuscript, a structure of the talin2 head domain was published (49). This structure (PDB ID code 6U4K) reveals an unusual semicloverleaf arrangement of F0-F1-F2 subdomains, as compared with a canonical F1-F2-F3 FERM-like cloverleaf fold. This head domain of talin2 (residues 1 to 403) was constructed based on the linear-form of talin1 head domain structure with residues 1 to 400, therefore missing the critical C-terminal residues that are crucial for the FERM-like cloverleaf fold. The F0-F1 tandem domains in the FERM-like talin1 head domain structure are virtually identical to that of the talin2 head domain structure, and the F2-F3 tandem domains are slightly twisted in the talin2 structure (*SI Appendix*, Fig. S4 *A* and *B*). The major difference is in the F1-F2 interface. In the FTHΔ structure, this F1-F2 interface is stabilized by Arg195-Asp201 and Arg194-Asp222/Asn225 interactions. Although these residues are conserved in talin2 (Arg197-Asp203, Arg196-Asp224/Asn227), the orientation of the F2 subdomain in regard to other subdomains is completely different and these salt bridges are disrupted as a result. Our data indicate that disruption of the Arg194-Asp222 salt bridge led to loss of integrin clustering, suggesting that the semicloverleaf configuration of the talin2 head is also functionally impaired. Interestingly, despite the flexibility of the F1-loop resolved in the talin2 head domain structure, the structural configuration of the remaining F1-loop residues in the FTHΔ structure (residues 130 to 133, 172 to 176) are highly consistent with that of the talin2 F1 domain structure, however projecting the F1 loop toward the membrane proximal integrin binding site in the F3 domain (50) (*SI Appendix*, Fig. S4*C*). Thus, the resolved F1-loop is also compatible with our FERM-folded structure, including the bound β3 peptide. Therefore, the crystal structure of the talin head, even lacking the F1-loop, is consistent with the compact talin head that includes the F1-loop as revealed by the EM structure. The configuration of the F1-loop is also consistent with our analyses of F1-loop function in regulating integrin activity (50). Shape analyses of the talin head domain by EM revealed that the majority of the full-length talin head adopts the FERM-folded configuration, and no linear configuration is observed. Therefore, it is unlikely that talin may transition between the extended linear and FERM folds, with the semicloverleaf fold as an intermediary. Our FERM-folded talin head structure is also compatible with the recently published full-length talin cryo-EM structure (18). Although the F0-F1 segment of the talin head is missing in the cryo-EM model (PDB ID code 6R9T), the F2-F3 segment of our structure superimposes with the corresponding region in the cryo-EM model perfectly. The superposition also reveals that the F0-F1 segment can be well accommodated in the cryo-EM model without any structural conflict (*SI Appendix*, Fig. S4*D*). We also evaluated how FERM-folded talin head would interact with membrane lipids. The previously identified clusters of PIP2 binding residues are spread out in three subdomains (*SI Appendix*, Fig. S4*E*). The PIP2-binding clusters, organized into a triangular pattern, orient talin on the cell membrane such that it can bind integrin in a stable manner.

As an additional consequence of the extensive interaction network formed between the C-terminal basic domain of the F3 subdomain with the F1 and F2 subdomain is the widening of the gap between the F2 and F3 domains on the opposite side of the F1-F3 interface, in respect to the elongated talin head (PDB ID code 3IVF), or the F2-F3 talin-head fragments (PDB ID code 1MK7) (35). In fact, the formation of a salt bridge between K345 and E269 in the elongated and F2-F3 structures causes a contraction of the F2-F3 spacing, resulting in the respective opening of the F2-F3 distance at the site of the F1-F2 linker insertion, potentially preventing the proper spacing required for the wedging of F2-F3 by the F1 domain, normally seen in all FERM folds.

Because the talin head adopts the FERM fold, its F3 subdomain sits on the F1-F2 linker insertion, the K401-D125/K402-E126 salt bridges and the K345-E269 salt bridge may compete for contact like two sides of a seesaw (*SI Appendix*, Fig. S5). Formation of the K401-D125/K402-E126 salt bridges tilts the seesaw, thus disrupting the K345-E269 side and stabilizing the FERM configuration. In the elongated structure, the K345-E269 salt bridge causes an upward movement of the F3-helix, thereby potentially preventing the correct positioning of the F0-F1 module on top of the F2-F3 module. The K345-E269 salt bridge is lost in the presence of the poly-lysine motif in the F3 subdomain, and the FERM-folded configuration is stabilized as a result.

Folding of talin into a canonical FERM configuration provides a scaffold in which talin binds to β-integrins, while stabilizing their activated state in a kindlin-dependent manner, in order to control inside-out and outside-in signaling of integrins. It is noteworthy that the talin-binding site and the kindlin-binding site in integrin β3 are only eight residues apart. The tight association between the full-length talin head and the N-P-L-Y motif in integrin β3 restricts the flexibility of the proceeding kindlin-binding motif. Thus, when integrin binds to talin and kindlin simultaneously, extensive contacts between talin and kindlin seem inevitable. It may therefore be more relevant to probe the formation of the integrin-β:talin:kindlin trimeric complex rather than that of the dimeric integrin-adaptor complexes separately when assessing changes in signaling upon modification to these proteins. In particular, posttranslational modification on either integrin β or talin/kindlin may impact integrin signaling by affecting the formation of the trimeric complex. Moreover, we demonstrated that conserved FERM domain motifs at the F1-F2 interface (R194-D222, Q218) and C-terminal poly-lysine motif in the F3 subdomain are important for the efficient activation and clustering of integrins. These contact interfaces might be promising targets for drug development. Overall, our results reveal the importance of FERM-like conformation of the talin head for the coactivation and clustering of integrins in collaboration with kindlin.

Materials and Methods

Protein Crystallography. A human integrin β3 fragment including residues 720 to 750 was fused to the amino terminus of the talin head domain containing residues 1 to 430, with the loop in the F1 subdomain (residues 139 to 168) deleted. The fusion polypeptide was cloned into a modified pET-28 vector with a tobacco etch virus (TEV) cleavable histidine tag at the N terminus. The plasmid was transformed into *Escherichia coli* BL21(DE3) for protein production. Cells were lysed in 50 mM Tris, pH 7.5, 500 mM NaCl. Protein was extracted from the supernatant with a HisTrap HP column (GE Healthcare) and eluted with an imidazole gradient. The His-tag was removed by TEV protease. Untagged protein was further purified using a Resource S column. The fusion protein was concentrated to 8 mg/mL, in 20 mM 4-(2-hydroxyethyl)-1-piperazineethanesulfonic acid, pH 7.0, 2 mM dithiothreitol (DTT), and 200 mM NaCl. Crystallization was performed by the hanging-drop vapor diffusion method. Crystals were observed with a well solution containing 100 mM 2-(*N*-morpholino)ethanesulfonic acid (MES), pH 6.5, 100 mM NaCl, and 10% polyethylene glycol (PEG) 4000 at room temperature for approximately 3 to 5 d. X-ray diffraction data were collected at the NSLS-II AMX beamline. Data were indexed, integrated, and scaled with FastDP. Data collection and refinement statistics are listed in Table 1. The crystal structure was determined by molecular replacement by Phaser. The atomic coordinates and structure factors have been deposited in the Protein Data Bank with accession number 6VGU. A stereoview of a representative electron density map is shown in *SI Appendix*, Fig. S6.

Protein Production. Talin head domain proteins (Table 2) used for size-exclusion chromatography (SEC), static light scattering (SLS), dynamic light scattering (DLS), and analysis of T_m in DSC were expressed using the pTrcHis C vector (Thermo Fisher Scientific) with an N-terminal His_6-tag MGGSHHHHHHGMASMTGGQQMGRDLYDDDDKDRWIRPRA. The sequence-confirmed plasmids were introduced into *E. coli* BL21-Star cells (Thermo Fisher Scientific). Bacteria were cultured in Luria broth (LB) medium containing 100 μg/mL ampicillin at 37 °C. Isopropyl β-D-1-thiogalactopyranoside (IPTG) (1 mM) was used to induce protein expression at an optical density of 0.4 and were harvested after 5 h of incubation. *E. coli* extracts were prepared by homogenization (Emulsiflex C3) in 20 mM NaPO4, 1 M NaCl, and 20 mM imidazole, pH 7.4. Clarified lysates were applied on a HisTrap FF 5-mL affinity column (GE healthcare) using ÄKTA Purifier (GE Healthcare). Talin head domains were eluted from columns using 20 mM sodium phosphate buffer (1 M NaCl, pH 7.4) with gradually increasing imidazole concentration (20–700 mM). Eluted fractions were analyzed by sodium dodecyl sulfate polyacrylamide gel electrophoresis (SDS/PAGE) and Coomassie staining and pooled when appropriate. Furthermore, talin head domains were purified with a HiTrap SP FF 1-mL column (GE Healthcare) after dilution (1:10) to 20 mM NaPO4, pH 7.4 buffer. Elution was performed by preparing the linear NaCl gradient with 20 mM NaPO4, 1 M NaCl, pH 7.4 buffer.

GST-integrin tail fusion constructs (WT-β3, GST-GSKLLITIHDRKEFAKFEEERARAKWDTANNPLYKEATSTFTNITYRGT; VE-β3, GST-GSKLLITIHDRKEFAKFEEERARAKWVENPLYKEATSTFTNITYRGT) were expressed with a similar approach in *E. coli* BL21-Star (51). Cells were lysed by homogenization (Emulsiflex C3) in phosphate-buffered saline (PBS), pH 7.4 buffer, and proteins were purified with Glutathione SepharoseTM (GE Healthcare 4 Fast Flow) using 50 mM Tris·HCl, 20 mM reduced glutathione, pH 8 buffer as eluent. Eluted fractions were analyzed with SDS/PAGE, Coomassie staining, and Western blot using mouse anti-GST B-14 (Santa Cruz) and goat anti-mouse antibodies. Fractions containing desired proteins were dialyzed into 50 mM sodium phosphate buffer (150 mM NaCl, pH 7.2) and stored at −20 °C.

The homogeneity of the purified proteins was evaluated using DLS (Zetasizer nano ZS). The purified talin proteins were also subjected to high-resolution mass spectrometric analysis. The mass spectra indicated that the protein samples were pure and homogeneous and the determined accurate masses were in a full agreement to those calculated from the sequences.

GST Pulldown Assay. Purified GST-tagged β3 or GST (final concentration at 15 μM) was incubated with purified His-tagged talin head proteins (t1-400/t1-405/t1-430, final concentration at 10 μM) in the binding buffer (50 mM Tris, pH 7.5, 100 mM NaCl, 2 mM DTT) to a final volume of 200 μL on ice for 5 min. Protein mixtures were then incubated with glutathione agarose beads on a rotator for 1 h at 4 °C. After washing with binding buffer three times, bound proteins were eluted with 50 μL of elution buffer (50 mM Tris, pH 7.5, 100 mM NaCl, 2 mM DTT, 20 mM reduced glutathione). Eluted samples were applied to SDS/PAGE and Western blotting for further analysis. Data were collected from four independent experiments. Western blots were developed using a FluorChem E System (Proteinsimple) with a charge-coupled device (CCD) camera. The CCD detector possesses a dynamic range of 65,536 gray scales and automatically records the 16-bit gray scale within the maximal dynamic range to ensure best linearity. After Western blotting, band density was acquired by software FIJI (Image J), subtracted by the GST negative control, and normalized to the band density level of t1-400 and GST-β3. Significance was calculated between t1-400 and t1-405/t1-430 (*t* test) ($^*P < 0.02$).

Analytical Light Scattering. Proteins were analyzed using a liquid chromatography instrument (CBM-20A; Shimadzu Corporation, Kyoto, Japan) equipped with an autosampler (SIL-20A), ultraviolet-visible (UV-VIS) (SPD-20A), and a fluorescence detector (RF-20Axs). Molecular weight was determined using SEC with a Malvern Zetasizer μV instrument (Malvern Instruments Ltd.) measuring inline SLS and DLS. Data were processed using Lab Solution Version 5.51 (Shimadzu Corporation) and OmniSec 4.7 (Malvern Instruments Ltd.) software. Samples (50 μg) were injected into the column (Superdex 200 Increase 5/150; GE Healthcare, Uppsala, Sweden) using the autosampler. The column was equilibrated with 50 mM Na_3PO_4, 150 mM NaCl, pH 7.2 running buffer. The measurements were run with a flow rate of 0.1 mL/min at 20 °C. The monomeric peak of bovine serum albumin (BSA) was used for calibrating the system to calculate molecular weight from the measured SLS intensity.

DSC. Talin samples were analyzed using the VP-DSC instrument (MicroCal; Malvern Instruments Ltd.) with protein concentrations of ~0.2 mg/mL in 50 mM NaH_2PO_4, 150 mM NaCl, pH 7.2 containing 1 mM ethylenediaminetetraacetic acid (EDTA) and 1 mM DTT. Concentrations were measured before the analysis by NanoDrop using the theoretical molar extinction coefficient calculated using ProtParam software. Samples were stored at +4 °C prior to analysis. Solutions were degassed prior to measurements. Samples were heated from 20 °C to 130 °C at a scanning rate of 2 °C/min. Feedback mode was set to low, and filter period was 5 s. T_m and calorimetric heat change (ΔH) were obtained by subtracting the baseline and using the Levenberg–Marquardt nonlinear least-squares method to the data using MicroCal Origin 7.0 software (MicroCal; Malvern Instrument Ltd.).

Differential Scanning Fluorimetry. For talin t1-400 and t1-405 differential scanning fluorimetry analysis, protein quality was checked using batch DLS (Zetasizer nano ZS) prior to analysis. Protein samples (2 μM) were prepared in a clear 96-well plate (Multiplate PCR plates, MLL9601; Bio-Rad) in phosphate-buffer containing 150 mM NaCl, pH 7.2. The thermal scanning was conducted on a Bio-Rad CFX96 real-time PCR instrument. To monitor thermal-induced unfolding, SYPRO Orange protein gel stain (ex470/em570 nm; Thermo Fisher Scientific) was used by preparing first a 1:100 dilution in dH_2O, and then 3 μL was added per well containing 22 μL of protein solution (6x Sypro Orange final concentration). As a control, a buffer sample without protein was prepared. The plate was covered with a qPCR sealing sheet (Biotop) to prevent evaporation and gently centrifuged to remove air bubbles. The thermal screening experiment was performed from 25 °C to 85 °C with temperature increase 2 °C/min. Data were normalized in Excel, and the T_m values were calculated by fitting the Boltzmann sigmoidal function using the GraphPad Prism nonlinear regression method.

Biosensor Analysis of Talin-Integrin Interaction. Biosensor analysis was carried out on a ForteBio Octet RED384 instrument (Pall Life Sciences) using nickel-nitrilotriacetic acid (Ni-NTA) sensors following a strategy similar to the one described in ref. 51. Samples or buffers were prepared into 96- or 384-well plates at a volume of 200 μL or 80 μL per well, respectively. Sensors were prewetted with buffer (50 mM Na_3PO_4, 150 mM NaCl, pH 7.2) in order to get baseline measurements prior to protein immobilization. An operating temperature of 27 °C and a stirring speed of 1,000 rpm were used throughout the experiment. Sensors were chemically activated by immersion in 0.05 M 1-ethyl-3-(3-dimethylaminopropyl)carbodiimide (EDC) and 0.1 M *N*-hydroxysuccinimide (NHS) in water for 100 s. Different talin head mutant samples (50 μg/mL) were immobilized on the sensor's surface for 300 s. The excess sulfo-NHS esters were quenched by 1 M ethanolamine, pH 8.5 for 100 s. Serially diluted GST-β3-integrin-tail fusion proteins were applied on the talin-coated sensors in concentrations of 20, 80, 320, 1,250, and 5,000 nM to obtain the relative affinity of talin to GST-β3. Each concentration of GST-β3 binding to the sensor was measured for 300 s before moving to a higher concentration.

Talin-WT-β3 and talin-VE-β3 binding data from the Octet biosensor (20, 80, 320, 1,250, and 5,000 nM) were treated as follows: Background (GST control) was subtracted, and all of the data were normalized to t1-405 at concentration 1,250 nM to allow comparison between experiments. The normalized data were analyzed with linear regression analysis in GraphPad Prism 5.02 (GraphPad Software, La Jolla, CA) assuming one-site specific binding. Bmax was set to 8.6 for WT β3-integrin binding data, and to 1.265 for VE-β3.

Cell Lines. Mouse melanoma B16F1 cells were cultured in Dulbecco's modified Eagle's medium (DMEM), 10% fetal calf serum (FCS), and antibiotics and passaged by trypsin treatment as described (25). Expression levels of the transiently transfected proteins and representative cell images for integrin clustering assays are shown in *SI Appendix*, Fig. S7 *A* and *B*, respectively.

DNA Constructs. WT and mutant human talin1-head domain constructs used for mammalian cell transfection were cloned in pcDNA3 as N-terminal cyan fluorescent protein-fusion proteins, according to standard molecular biology protocols, and confirmed by automated DNA sequencing (25). His-tagged human talin1 head domain constructs were cloned into the pTrcHis C vector. N-terminal TagRFP-labeled human kindlin-1 (kindly provided by Hongquan Zhang and Staffan Strömblad, Karolinska Institutet, Stockholm, Sweden) was cloned into pcDNA3. The GST-β3-cytoplasmic tail integrin construct has been described earlier (51). C-terminal GFP-tagged mouse β3-integrin constructs were cloned in pcDNA3, and the linker region was modified by two additional amino acids (DG) as described in ref. 50.

Transfections and Western Blotting. B16F1 cells were transfected in 6-well culture dishes with the JET PEi transfection reagent (polyplus-transfection) according to the manufacturer's recommendation. For coexpression of multiple proteins, different DNA plasmids were mixed at equimolar concentrations. The transfection mixture was removed and replaced with fresh medium after 6 h. For Western blot analysis of cyan fluorescent protein-talin-head transfected cells, 48 h after transfection, cells were lysed in 300 μL of Tris-buffered saline containing 2% Triton X-100, 0.1% Nonidet P-40, 5 mM *N*-ethylmaleimide, 1 mM phenylmethylsulfonyl fluoride (PMSF), and protease inhibitors at 1 μg/mL (chymotrypsin, leupeptine, aprotinin, and pepstatin; Sigma) for 10 min at 4 °C. Then, 40 μL of the lysate was subsequently run under reducing conditions on an SDS/PAGE (10%), transferred to nitrocellulose, and revealed with a mouse monoclonal anti-GFP antibody (clone B34, MMS-118P; Covance) according to standard protocols.

Integrin Clustering Analysis. After 6 h in transfection mixture, melanoma B16F1 cells were detached with trypsin/EDTA and plated on ethanol sterilized glass-bottom dishes in FCS-containing culture medium. After 48 h on the FCS-coated glass surface, cells were fixed with 4% PFA (paraformaldehyde in PBS) for 10 min. Cells were subsequently immerged in PBS for total internal fluorescence microscopy. Integrin clustering analysis was then performed from total internal reflection fluorescence (TIRF) images according to ref. 25; in brief, after background removal, an arbitrary threshold that allowed one to distinguish clustered from membrane-inserted integrins was used to quantify the amount of area exhibiting integrin clusters in respect to the total cell surface.

Integrin Activation Assay. Forty-eight hours after transfection, mouse melanoma B16F1 were detached with nonenzymatic cell-dissociation solution (C5788; Sigma), washed twice in PBS containing 0.5 mg/mL BSA, and split into two equal populations. Antibody staining or soluble ligand incubation was performed in PBS containing 0.5 mg/mL BSA on ice. For one cell population, the total amount of cell-surface integrin was revealed by staining with a hamster anti–β3-integrin (anti-mouse CD61; Pharmingen, BD). The other cell population was incubated with an arginylglycylaspartic acid-containing fusion protein of the snake venom disintegrin (Kistrin) and the first Ig-domain of CD31 (SKI-7), followed by the incubation with a rat anti-CD31 monoclonal antibody (GC51) as described (25). Subsequent detection of the anti–β3-integrin and the bound β3-integrin ligand (SKI-7)/GC51 complex was achieved with phycoerythrin-labeled affinity purified anti-hamster (127.115.161; The Jackson Laboratory) or $F(ab')_2$ fragments of goat anti-rat antibodies, respectively, and analyzed in an Accuri flow cytometer. Integrin activation was determined by the ratio of the signal between the activation-specific and total integrin-binding antibodies as described in ref. 25.

TEM and Single Particle Reconstruction. TEM was utilized to image monodispersed talin t1-405 proteins. The sample at optimized concentration was incubated for 30 s on continuous carbon grids, washed with distilled H_2O, and stained with 5% ammonium molybdate and 0.1% trehalose. The grids were dried at room temperature for 2 h and imaged with a 2130f JEOL electron microscope. A total of 15 CCD images were captured by 2130f JEOL TEM and processed for single particle analysis. The particles were low-pass filtered to 10 Å and high-pass filtered to 300 Å to reduce background noise interference. A total of 1,300 particles were selected via semiautomated particle selection. Reference-free 2D classification was carried out with a total of 65 classes. The 3D map was calculated using the top 50 classes in an iterative manner. The iterative approach to the single-particle reconstruction is aimed to progressively reduce heterogeneity in the data. The reference-free averages were then used to generate a low-resolution initial model (low-pass filtered to 20 Å). Parameter centering and Euler orientation determination were refined over 10 cycles of refinement. The final map was rendered via UCSF Chimera (52), with a final resolution of 15.2 Å by 0.143 Fourier shell correlation criteria.

Statistics. Statistical analyses were carried out in GraphPad Prism 5.02 for Windows (GraphPad Software, La Jolla, CA). All clustering and activation data were analyzed with one-way ANOVA and a Tukey's multiple comparison test for differences between the groups.

Data Availibility. The atomic coordinates and structure factors have been deposited in the Protein Data Bank with accession number 6VGU. All other study data are included in the article and *SI Appendix*.

ACKNOWLEDGMENTS. Ulla Kiiskinen, Niklas Kähkönen, and Monica Julio Barreto are acknowledged for excellent technical help. Hongquan Zhang and Staffan Strömblad kindly provided the kindlin-1 construct. We acknowledge Prof. Janne Jänis (University of Eastern Finland) for the determination of total mass of the purified talin head proteins. M.B. and R.H.C. were supported by the NIH (grants TR002866, EB021230, CA225266, and CA198880) (R.H.C.) and National Institute of Food and Agriculture (CAD-MCB7399H) (R.H.C.). We acknowledge Academy of Finland (Grant 290506) for research funding (to V.P.H.). Biocenter Finland is acknowledged for infrastructure support. S.K. was supported by the Tampere Graduate Program in Biomedicine and Biotechnology. B.W.-H. and M.-C.J. were supported by Swiss National Science Foundation Grants 31003A_166384 and 310030_185261. P.Z., T.G., Y.S., and J.W. were supported by NIH Grant GM119560 (to J.W.) and American Cancer Society Grant RSG-15-167-01-DMC (to J.W.).

1. M. H. Ginsberg, A. Partridge, S. J. Shattil, Integrin regulation. *Curr. Opin. Cell Biol.* **17**, 509–516 (2005).
2. M. Bachmann, S. Kukkurainen, V. P. Hytönen, B. Wehrle-Haller, Cell adhesion by integrins. *Physiol. Rev.* **99**, 1655–1699 (2019).
3. S. Huveneers, H. Truong, H. J. Danen, Integrins: Signaling, disease, and therapy. *Int. J. Radiat. Biol.* **83**, 743–751 (2007).
4. J. S. Desgrosellier, D. A. Cheresh, Integrins in cancer: Biological implications and therapeutic opportunities. *Nat. Rev. Cancer* **10**, 9–22 (2010).
5. H. S. Lee, C. J. Lim, W. Puzon-McLaughlin, S. J. Shattil, M. H. Ginsberg, RIAM activates integrins by linking talin to ras GTPase membrane-targeting sequences. *J. Biol. Chem.* **284**, 5119–5127 (2009).
6. J. P. Wynne *et al*., Rap1-interacting adapter molecule (RIAM) associates with the plasma membrane via a proximity detector. *J. Cell Biol.* **199**, 317–330 (2012).
7. Y. C. Chang *et al*., Structural and mechanistic insights into the recruitment of talin by RIAM in integrin signaling. *Structure* **22**, 1810–1820 (2014).
8. D. A. Calderwood, I. D. Campbell, D. R. Critchley, Talins and kindlins: Partners in integrin-mediated adhesion. *Nat. Rev. Mol. Cell Biol.* **14**, 503–517 (2013).
9. A. R. Gingras *et al*., The structure of the C-terminal actin-binding domain of talin. *EMBO J.* **27**, 458–469 (2008).
10. G. C. Roberts, D. R. Critchley, Structural and biophysical properties of the integrin-associated cytoskeletal protein talin. *Biophys. Rev.* **1**, 61–69 (2009).
11. H. Zhang, Y. C. Chang, Q. Huang, M. L. Brennan, J. Wu, Structural and functional analysis of a talin triple-domain module suggests an alternative talin autoinhibitory configuration. *Structure* **24**, 721–729 (2016).
12. M. C. Frame, H. Patel, B. Serrels, D. Lietha, M. J. Eck, The FERM domain: Organizing the structure and function of FAK. *Nat. Rev. Mol. Cell Biol.* **11**, 802–814 (2010).
13. D. C. Bosanquet, L. Ye, K. G. Harding, W. G. Jiang, FERM family proteins and their importance in cellular movements and wound healing (review). *Int. J. Mol. Med.* **34**, 3–12 (2014).
14. H. Li *et al*., Structural basis of kindlin-mediated integrin recognition and activation. *Proc. Natl. Acad. Sci. U.S.A.* **114**, 9349–9354 (2017).
15. P. R. Elliott *et al*., The Structure of the talin head reveals a novel extended conformation of the FERM domain. *Structure* **18**, 1289–1299 (2010).
16. K. Chinthalapudi, E. S. Rangarajan, T. Izard, The interaction of talin with the cell membrane is essential for integrin activation and focal adhesion formation. *Proc. Natl. Acad. Sci. U.S.A.* **115**, 10339–10344 (2018).
17. B. T. Goult *et al*., Structural studies on full-length talin1 reveal a compact auto-inhibited dimer: Implications for talin activation. *J. Struct. Biol.* **184**, 21–32 (2013).
18. D. Dedden *et al*., The architecture of Talin1 reveals an autoinhibition mechanism. *Cell* **179**, 120–131.e13 (2019).
19. E. Montanez *et al*., Kindlin-2 controls bidirectional signaling of integrins. *Genes Dev.* **22**, 1325–1330 (2008).
20. H. Qu *et al*., Kindlin-2 regulates podocyte adhesion and fibronectin matrix deposition through interactions with phosphoinositides and integrins. *J. Cell Sci.* **124**, 879–891 (2011).
21. M. Theodosiou *et al*., Kindlin-2 cooperates with talin to activate integrins and induces cell spreading by directly binding paxillin. *eLife* **5**, e10130 (2016).
22. S. Tadokoro *et al*., Talin binding to integrin beta tails: A final common step in integrin activation. *Science* **302**, 103–106 (2003).
23. C. Cluzel *et al*., The mechanisms and dynamics of (alpha)v(beta)3 integrin clustering in living cells. *J. Cell Biol.* **171**, 383–392 (2005).
24. K. L. Wegener *et al*., Structural basis of integrin activation by talin. *Cell* **128**, 171–182 (2007).
25. F. Saltel *et al*., New PI(4,5)P2- and membrane proximal integrin-binding motifs in the talin head control beta3-integrin clustering. *J. Cell Biol.* **187**, 715–731 (2009).
26. N. J. Anthis *et al*., The structure of an integrin/talin complex reveals the basis of inside-out signal transduction. *EMBO J.* **28**, 3623–3632 (2009).
27. M. Bouaouina, Y. Lad, D. A. Calderwood, The N-terminal domains of talin cooperate with the phosphotyrosine binding-like domain to activate beta1 and beta3 integrins. *J. Biol. Chem.* **283**, 6118–6125 (2008).
28. B. T. Goult *et al*., Structure of a double ubiquitin-like domain in the talin head: A role in integrin activation. *EMBO J.* **29**, 1069–1080 (2010).
29. D. Camp *et al*., Direct binding of Talin to Rap1 is required for cell-ECM adhesion in *Drosophila*. *J. Cell Sci.* **131**, jcs225144 (2018).
30. S. W. Feigelson *et al*., Kindlin-3 is required for the stabilization of TCR-stimulated LFA-1:ICAM-1 bonds critical for lymphocyte arrest and spreading on dendritic cells. *Blood* **117**, 7042–7052 (2011).
31. C. Feng *et al*., Kindlin-3 mediates integrin αLβ2 outside-in signaling, and it interacts with scaffold protein receptor for activated-C kinase 1 (RACK1). *J. Biol. Chem.* **287**, 10714–10726 (2012).
32. S. Schmidt *et al*., Kindlin-3-mediated signaling from multiple integrin classes is required for osteoclast-mediated bone resorption. *J. Cell Biol.* **192**, 883–897 (2011).
33. F. Ye *et al*., The mechanism of kindlin-mediated activation of integrin αIIbβ3. *Curr. Biol.* **23**, 2288–2295 (2013).
34. D. J. Rees, S. E. Ades, S. J. Singer, R. O. Hynes, Sequence and domain structure of talin. *Nature* **347**, 685–689 (1990).
35. B. García-Alvarez *et al*., Structural determinants of integrin recognition by talin. *Mol. Cell* **11**, 49–58 (2003).
36. D. A. Calderwood *et al*., The phosphotyrosine binding-like domain of talin activates integrins. *J. Biol. Chem.* **277**, 21749–21758 (2002).
37. D. S. Harburger, M. Bouaouina, D. A. Calderwood, Kindlin-1 and -2 directly bind the C-terminal region of beta integrin cytoplasmic tails and exert integrin-specific activation effects. *J. Biol. Chem.* **284**, 11485–11497 (2009).
38. Y. Q. Ma, J. Qin, C. Wu, E. F. Plow, Kindlin-2 (Mig-2): A co-activator of beta3 integrins. *J. Cell Biol.* **181**, 439–446 (2008).
39. M. Moser *et al*., Kindlin-3 is required for beta2 integrin-mediated leukocyte adhesion to endothelial cells. *Nat. Med.* **15**, 300–305 (2009).
40. B. G. Petrich *et al*., The antithrombotic potential of selective blockade of talin-dependent integrin alpha IIb beta 3 (platelet GPIIb-IIIa) activation. *J. Clin. Invest.* **117**, 2250–2259 (2007).
41. E. J. Filardo, P. C. Brooks, S. L. Deming, C. Damsky, D. A. Cheresh, Requirement of the NPXY motif in the integrin beta 3 subunit cytoplasmic tail for melanoma cell migration in vitro and in vivo. *J. Cell Biol.* **130**, 441–450 (1995).
42. Z. Zhang *et al*., Sequence-specific recognition of the internalization motif of the Alzheimer's amyloid precursor protein by the X11 PTB domain. *EMBO J.* **16**, 6141–6150 (1997).
43. W. Cai *et al*., Domain-dependent effects of insulin and IGF-1 receptors on signalling and gene expression. *Nat. Commun.* **8**, 14892 (2017).
44. R. Ghai *et al*., Structural basis for endosomal trafficking of diverse transmembrane cargos by PX-FERM proteins. *Proc. Natl. Acad. Sci. U.S.A.* **110**, E643–E652 (2013).
45. A. L. Stiegler, R. Zhang, W. Liu, T. J. Boggon, Structural determinants for binding of sorting nexin 17 (SNX17) to the cytoplasmic adaptor protein Krev interaction trapped 1 (KRIT1). *J. Biol. Chem.* **289**, 25362–25373 (2014).
46. E. Hodis *et al*., A landscape of driver mutations in melanoma. *Cell* **150**, 251–263 (2012).
47. C. Huang *et al*., Talin phosphorylation by Cdk5 regulates Smurf1-mediated talin head ubiquitylation and cell migration. *Nat. Cell Biol.* **11**, 624–630 (2009).
48. J. K. Jin *et al*., Talin1 phosphorylation activates β1 integrins: A novel mechanism to promote prostate cancer bone metastasis. *Oncogene* **34**, 1811–1821 (2015).
49. E. S. Rangarajan *et al*., A distinct talin2 structure directs isoform specificity in cell adhesion. *J. Biol. Chem.* **295**, 12885–12899 (2020).
50. S. Kukkurainen *et al*., The F1 loop of the talin head domain acts as a gatekeeper in integrin activation and clustering. *J. Cell Sci.* **133**, jcs239202 (2020).
51. P. Pinon *et al*., Talin-bound NPLY motif recruits integrin-signaling adapters to regulate cell spreading and mechanosensing. *J. Cell Biol.* **205**, 265–281 (2014).
52. E. F. Pettersen *et al*., UCSF Chimera–A visualization system for exploratory research and analysis. *J. Comput. Chem.* **25**, 1605–1612 (2004).

PUBLICATION
III

Cancer-associated talin point mutations disorganise cell adhesion and migration

Azizi, L., Cowell, A. R., Mykuliak, V. V., Goult, B. T., Turkki, P. and Hytönen, V. P.

Scientific Reports 2021 Jan 11;11(1):347
doi: 10.1038/s41598-020-77911-4

www.nature.com/scientificreports

scientific reports

OPEN

Cancer associated talin point mutations disorganise cell adhesion and migration

Latifeh Azizi[1], Alana R. Cowell[2], Vasyl V. Mykuliak[1], Benjamin T. Goult[2]✉, Paula Turkki[1,3]✉ & Vesa P. Hytönen[1,3]✉

Talin-1 is a key component of the multiprotein adhesion complexes which mediate cell migration, adhesion and integrin signalling and has been linked to cancer in several studies. We analysed talin-1 mutations reported in the Catalogue of Somatic Mutations in Cancer database and developed a bioinformatics pipeline to predict the severity of each mutation. These predictions were then assessed using biochemistry and cell biology experiments. With this approach we were able to identify several talin-1 mutations affecting integrin activity, actin recruitment and Deleted in Liver Cancer 1 localization. We explored potential changes in talin-1 signalling responses by assessing impact on migration, invasion and proliferation. Altogether, this study describes a pipeline approach of experiments for crude characterization of talin-1 mutants in order to evaluate their functional effects and potential pathogenicity. Our findings suggest that cancer related point mutations in talin-1 can affect cell behaviour and so may contribute to cancer progression.

For cells to maintain homeostasis and co-operate within tissues, they need to dynamically interact with the extracellular matrix (ECM). In recent years the role of the microenvironment has become increasingly recognised[1] and disturbances between cell–ECM interactions, intracellular signalling events, and signals derived from the ECM have been shown to contribute to cancer progression. Talin is a major component of focal adhesions (FAs), responsible for mediating the link between the ECM via integrins and the actin cytoskeleton (Fig. 1a). Talin is a large ~ 250 kDa mechanosensitive protein consisting of an N-terminal FERM head domain (F0, F1, F2, F3; residues 1–405) followed by a linker (~ 80aa) and ~ 2000aa rod region comprised of 13 domains (R1 to R13) ending in a C-terminal dimerisation domain (DD)[2] (Fig. 1b). The FERM domain interacts with the membrane-proximal NPxY motif of beta integrin tail and the negatively charged plasma membrane[3,4]. The rod domain contains two F-actin binding sites (ABS2 and ABS3)[5–7], 11 vinculin binding sites (VBS)[8] and binding sites for regulatory proteins such as RIAM, KANK[9,10] and the tumour suppressor DLC-1[11,12] (Fig. 1b). Studies have shown that ABS3 is essential for FA assembly[13], whereas ABS1 and ABS2 have a reinforcing role[14,15].

Talin is the main scaffold protein in focal adhesions which form at the leading edge of a polarised cell. Talin links the intracellular tails of integrins to the actin cytoskeleton and mechanical forces exerted on talin can disrupt and reveal binding sites leading to formation of mature multiprotein FA complexes[16–18]. These are dynamic processes regulated by a complex signalling network, gathering information from intracellular and extracellular events. The mechanical properties of the ECM are reflected by intracellular changes via the FAs and actomyosin network, having a direct effect on cell behaviour, such as cell shape, migration and proliferation[19,20] (Fig. 1a).

Talin-1 overexpression has been shown to correlate with increased invasion and decreased survival with oral squamous cell carcinoma[21] as well as migration, invasion and anoikis resistance in prostate cancer cells[22]. Loss of talin-1 leads to diminished in vivo metastasis of prostate cancer cells via FAK–Src complexes and AKT kinase signalling[22]. Talin-1 knockdown was also shown to significantly reduce the proliferation, migration and invasion of colorectal cancer cell line. This was associated with downregulation of several factors which are involved in the epithelial-to-mesenchymal transition, such as STAT3 and vimentin[23]. Conversely, downregulation of talin-1 has also been shown to promote hepatocellular carcinoma progression[24].

The COSMIC (Catalogue Of Somatic Mutations In Cancer) database[25] contains exon sequencing data of human cancers and provides a vast resource of somatic mutation information. In light of talins integral role in regulating cell behaviour, integrin adhesion signalling and its connection to cancer progression, we sought to explore how cancer-associated talin mutations may alter talin function and the behaviour of cells.

[1]BioMediTech, Faculty of Medicine and Health Technology, Tampere University, Tampere, Finland. [2]School of Biosciences, University of Kent, Canterbury CT2 7NJ, Kent, UK. [3]Fimlab Laboratories, Tampere, Finland. ✉email: B.T.Goult@kent.ac.uk; paula.turkki@tuni.fi; vesa.hytonen@tuni.fi

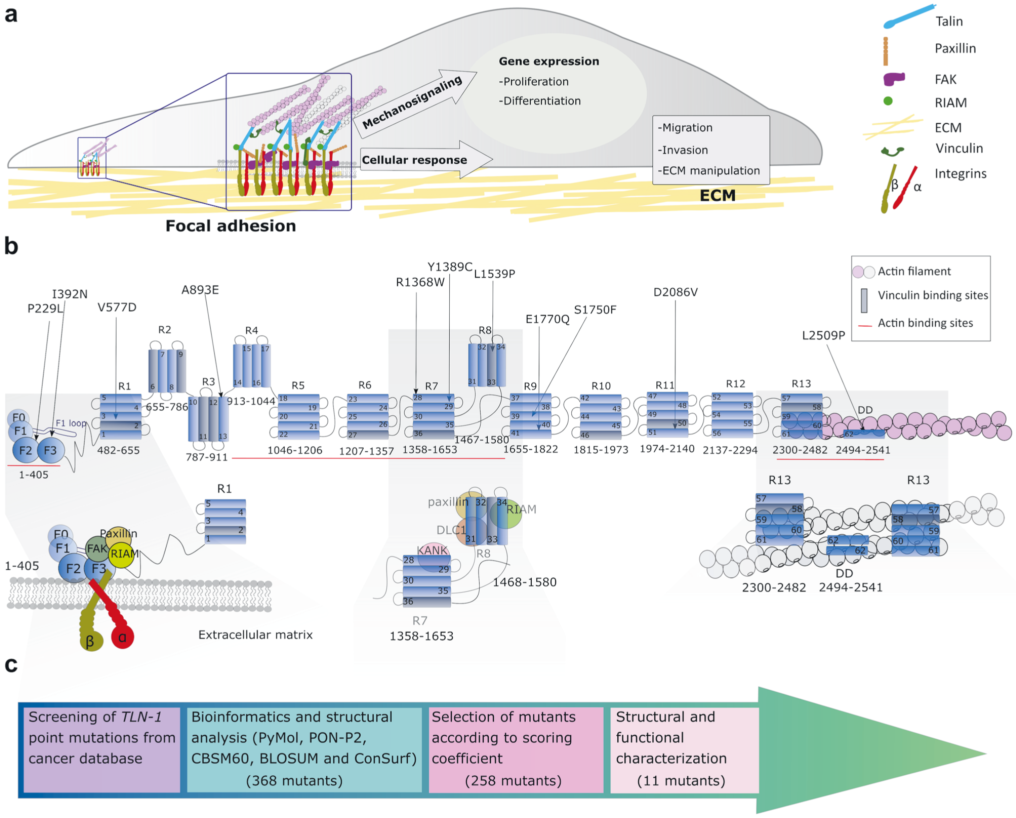

Figure 1. Analysis of talin-1 mutations found in the COSMIC database. (**a**) Schematic representation of focal adhesion role on cell function. (**b**) Schematic representation of talin-1 and the positions of the selected missense mutations. Bottom: cartoon of the talin head complexes that form with integrin, FAK, paxillin and RIAM (left), talin R7–R8 complexes with KANK, DLC-1, RIAM and paxillin (middle) and the R13–DD actin cytoskeletal linkage (right). (**c**) Flowchart showing the study pipeline to investigate TLN–1 mutations from COSMIC database.

Here we provide a pipeline approach in order to evaluate the effect of talin-1 mutations. First, we applied a set of bioinformatic prediction tools in order to rank each mutation based on its location and predicted effects on protein structure. We used the scoring function to select mutations with the potential to disrupt talin function and/or affect its interactions with known binding partners for further characterisation. Next, we assessed the mutations effects via computational methods, and biochemical and cell biological analysis was performed to determine the mutations effects on known interactions. Lastly, we studied the effects of mutations on essential cellular behaviours, such as cell migration, invasion and proliferation. This pipeline would be amenable to other proteins and so provides a way to convert the COSMIC information into biological insights.

Results

Screening of *TLN-1* mutations from COSMIC database.

To investigate functional consequences of talin-1 point mutations, 368 talin-1 mutations in COSMIC database (accessed January 2017) were evaluated, and 258 missense mutations were further screened using bioinformatic tools (Fig. 1c). We investigated each of the 258 point mutations individually and determined the position of the mutation within the talin structure (Fig. 1b; Supplementary Fig.S1). The pathogenicity of the amino acid substitutions were predicted using the PON-P2-algorithm[26]. We used a BLOSUM62 substitution matrix[27] and CBSM60 matrix[28] to obtain a numeric penalty for each amino acid deviation and to predict the protein structure/function, respectively. Next we investigated if the mutations cause changes in amino acid polarity as the stability of talin domains are strongly dependent on hydrophobic effect[29,30]. The degree of evolutionary conservation of the amino acids in the talin sequence was investigated using ConSurf[31]. Finally, we evaluated if the mutation is close to known ligand-binding sites. All

Talin-1 mutant	Recurrence	Primary tissue	Histology	Domain	Location	PON–P2 probability of pathogenicity	Normalised BLOSUM 62–matrix score	Normalised CBSM60 matrix score	Normalised ConSurf score	Final score
P229L	2	Skin	Carcinoma	F2	BH/buried	0.94	1	1	1	8.20
I392N	1	Pancreas	Carcinoma	F3	Buried	0.86	1	0.83	1	8.95
V577D	1	Liver	Carcinoma	R1	Buried	0.94	1	1	0.60	8.39
A893E	3	Central nervous system/pituitary	Glioma/Craniopharyngioma	R3	BH/buried	0.95	0.75	0.33	0.60	7.63
R1368W	2	Hematopoietic and lymphoid tissue /large intestine	Lymphoid neoplasm / carcinoma	R7	Surface	0.98	1	1	1	7.75
Y1389C	2	Liver	Carcinoma	R7	Buried	0.90	0.87	0.67	1	8.58
L1539P	1	Liver	Carcinoma	R8	Buried	0.98	1	1	0.60	8.45
S1750F	1	Skin	Malignant melanoma	R9	Buried	0.89	0.87	0.5	0.60	7.55
E1770Q	1	Breast	Carcinoma	R9	Surface	0.81	0.37	− 0.33	1	6.01
D2086V	1	Breast	Carcinoma	R11	Surface	0.96	1	1	1	7.71
L2509P	1	Large intestine	Carcinoma	DD	DD /Surface	0.96	1	1	0.64	7.46

Table 1. The list of talin-1 point mutations selected from the COSMIC database. In each column a normalised value close to 1 predicts defects in protein function. *BH* mutation located between helices, *DD* dimerisation domain, *CBSM60* conformation–specific amino acid substitution matrix, *BLOSUM62* BLOcks SUbstitution Matrix. The recurrence value has been updated September 13th, 2020.

these factors were used to build a scoring coefficient and the weight for each variable was obtained using the manual iteration process described in the Supplementary material.

Based on this analysis, eleven mutations were selected for further investigation with the E1770Q mutation also included despite a lower score due to its location in the previously defined talin autoinhibition site[32,33] (Table 1 and Fig. 1b).

We next evaluated the selected COSMIC mutations against the 1000 Genomes Project database, which is a large database of human genetic variant data[34]. The R1368W mutation from our selection was the only one additionally found in the 1000 Genomes database (accessed September 8th, 2020), indicating that this mutation has also been found in apparently healthy individuals.

Molecular dynamics simulations suggest that the majority of mutations destabilise the talin-1 subdomains.

To investigate how mutations affect talin-1 subdomain stability, we employed Molecular Dynamics (MD) simulations. Non-equilibrium alchemical MD simulations were conducted to predict the free energy changes in subdomain stability upon mutation (Supplementary Fig. S2a). All mutations were analysed except those that involve proline (P229L, L1539P and L2509P), which is not supported for the analysis. The majority of the mutations showed destabilisation of the corresponding subdomains, where the strongest destabilisation effect was for mutations V577D in R1 (52.15 ± 13.71 kJ/mol) and I392N in F3 (38.28 ± 1.27 kJ/mol). Strong destabilisation was also showed for Y1389C in R7 (20.60 ± 4.09 kJ/mol). Weaker, but still significant destabilisation was observed for mutations D2086V in R11 (12.96 ± 0.82 kJ/mol), R1368W in R7 (12.63 ± 0.27 kJ/mol), and A893E in R3 (10.5 ± 1.91 kJ/mol). Mutation E1770Q in R9 (−4.17 ± 0.35 kJ/mol) showed mild stabilisation effect, and S1750F also in R9 (2.28 ± 2.33 kJ/mol) did not cause any significant change in the subdomain's stability.

For more detailed characterisation, we next selected mutations closest to sites with known interaction partners and employed equilibrium MD simulations. In particular, we selected: P229L and I392N due to their proximity to the integrin binding site in F3; R1368W, Y1389C, and L1539P within the R7–R8 fragment which is known to interact with paxillin, RIAM, KANK and DLC-1; and L2509P which is situated within the DD and the C-terminal actin binding site, ABS3[7] (Fig. 1c).

The P229L mutant is located at the interface between F2–F3. Analysis of F2–F3 inter-subdomain binding energy for F2–F3 WT and P229L mutant suggested that the mutation did not alter the F2–F3 interactions significantly (Supplementary Fig. S2b). Mutation of Isoleucine 392, which is located inside the hydrophobic core of the F3 subdomain, to Asparagine (I392N) leads to replacement of the hydrophobic isoleucine side chain with a hydrophilic side chain. This strongly destabilises the F3, and equilibrium MD suggests that water molecules can penetrate the destabilised F3 fold (Fig. 2a).

MD simulations carried out for R7–R8 WT and associated mutants (R1368W, Y1389C, and L1539P) gave the unexpected finding that the R7 and R8 subdomains interact over the course of 100 ns MD (Supplementary Fig. S2c). Whilst this interaction was detected for all four variants, the analysis of the R7–R8 inter-domain binding energy for WT and R1368W mutant suggested that the R1368W mutation enhances this transient interaction between R7 and R8 (Fig. 2b, Supplementary Fig. S2b). The Y1389C mutation is positioned close to a cysteine residue C1392, raising the possibility of a potential intradomain disulphide bond forming. To explore this, two forms of the Y1389C mutation were analysed in equilibrium MD, one where C1389 forms a disulphide bond with C1392, and one where it remains reduced (Fig. 2c). Although the mutation strongly destabilises R7

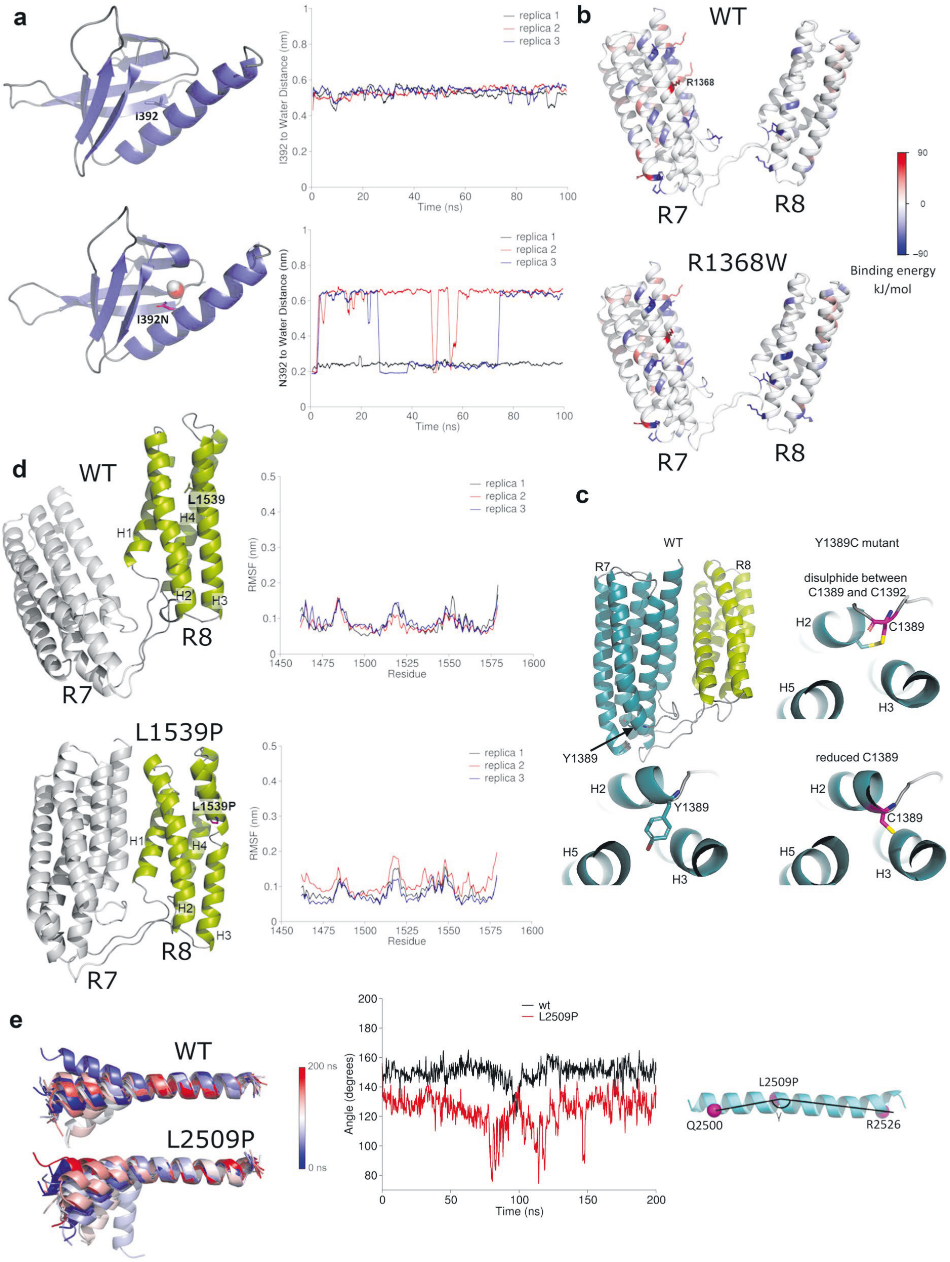
a
I392
I392 to Water Distance (nm)
replica 1
replica 2
replica 3
Time (ns)
I392N
N392 to Water Distance (nm)
b
WT
R1368
R7
R8
R1368W
90
0
−90
Binding energy
kJ/mol
d
WT
L1539
H1
H4
H2
H3
R7
R8
RMSF (nm)
Residue
L1539P
c
WT
Y1389C mutant
disulphide between
C1389 and C1392
H2
C1389
H5
H3
Y1389
reduced C1389
e
WT
L2509P
200 ns
0 ns
Angle (degrees)
wt
Time (ns)
Q2500
R2526

◂**Figure 2.** MD simulation analysis of the effects of cancer–associated mutations on talin domains. (**a**) Structure snapshots of the F3 subdomain for WT and I392N mutant. Residue 392 and a water molecule inside the F3 domain in the I392N mutant simulation are shown. The plots show the distance between the residue 392 side chain and the closest water molecule as function of the MD simulation time in WT (top) and I392N mutant (bottom). Three 100 ns replicas are shown. The distance of ~ 0.6 nm in the WT indicates that the closest water molecule is located at the F3 surface, while in the I392N mutant the distance ~ 0.2 nm indicates that the nearest water molecule has penetrated the F3 fold. (**b**) R7–R8 inter-domain binding energy distribution for WT and R1368W predicted using MM-PBSA. Residue R1368W and others that have contribution to the inter–domain binding energy lower than −50 kJ/mol and higher than 50 kJ/mol are shown as sticks. (**c**) Visualisation of Y1389C mutation in R7–R8 structure. (**d**) R7–R8 structure snapshots captured at 100 ns of MD for WT and L1539P (in R8); the R7–R8 was used in the simulations, but the Root Mean Square Fluctuation (RMSF) analysis was performed for R8 only. Proline breaks the secondary structure and increases the flexibility of the domain, reflected in the RMSF. R7 is shown in grey and R8 in green. (**e**) MD simulations for DD helix showing increased flexibility of the helix caused by L2509P compared to the WT. Superposition was performed using C-alpha atoms of residues 2510 to 2529. The angle (γ) in L2509P mutant and WT in a single helix measured as a function of time.

by 20.60 ± 4.09 kJ/mol, equilibrium simulations did not show significant structural changes in R7 in either of these scenarios. MD simulations revealed that the L1539P mutation effectively breaks the structure of helix three (H3) in the R8 subdomain (Fig. 2d), and secondary structure analysis indicated clear disruption of H3 in the L1539P-mutated R8 when compared to WT (Supplementary Fig.S2d). Finally, the L2509P mutation in the DD helix breaks its helical structure and causes higher flexibility of the DD (Fig. 2e).

Biochemical characterisation indicates that Y1389C decreases R7–R8 domain stability and L2509P leads to loss of dimerisation. We selected mutations located in the previously identified binding sites for known talin interactors and which showed strong destabilization of the domain in free energy calculations (I392N, R1368W, Y1389C, L1539P and L2509P) for further biochemical characterisation. For this purpose, we recombinantly expressed talin head fragment 1–405 with mutation I392N, the R7–R8 fragment 1355–1652 versions containing mutations R1368W, Y1389C, L1539P and the R13–DD fragment 2300–2541 with mutation L2509P in *E. coli*. In addition, we expressed the corresponding wildtype protein fragments. We found that the talin head fragment containing I392N mutation purified as two separate fragments and the fragment sizes suggested that cleavage had occurred within the vicinity of the mutated site. A similar cleavage was observed previously with a recombinantly expressed, G340E (equivalent to G331E in mouse talin-1) mutant in fly talin F3 domain[35] suggesting that destabilisation of F3 leads to exposure of proteolytically sensitive regions that are degraded by *E. coli* proteases. Adding a cocktail of proteolysis inhibitors during the lysis and purification did not help sufficiently to enable production of intact mutant for biochemical analysis. Additionally, R7–R8 containing the mutation L1539P in R8 expressed poorly with evidence of heavy aggregation, making it impossible to obtain protein concentrations high enough for further biochemical analyses. Therefore, we did not pursue further with the biochemical characterization of mutants I392N and L1539P. Wildtype R7–R8, R7–R8 R1368W and R7–R8 Y1389C expressed well and had clear monomeric peaks on size exclusion chromatography (SEC) (Fig. 3a). We used Nuclear Magnetic Resonance (NMR) and Circular Dichroism (CD) to provide biophysical insight into the structural effects of these mutations. Comparison of the ^{15}N-HSQC spectra of the R7–R8 WT and R7–R8 R1368W mutant revealed similar peak dispersion in both spectra, with only minor shifts in peak positions that occur as a result of the altered sidechain suggesting that R7–R8 R1368W does not significantly affect talin R7–R8 structure (Supplementary Fig.S4a). In support of this, CD analysis of the R7–R8 WT and R7–R8 R1368W proteins yielded similar spectra confirming similar secondary structure, and no change in thermal stability (Fig. 3b,c).

In contrast, the R7–R8 Y1389C mutation caused a striking 6.5 °C reduction in the thermostability of R7–R8 (45.5 °C compared with 52 °C for the wildtype) assessed using CD (Fig. 3c). Mutation to cysteine introduces the possibility of a potential to form a disulphide bond with the adjacent cysteine C1392. To test whether the thermal destabilization was due to intramolecular disulphide bond, we performed this analysis in the presence and absence of dithiothreitol and saw no difference between the melting point (data not shown). Unfortunately, NMR analysis of this mutant was not possible, potentially linked to reduced solubility of the mutated protein making concentrating the sample difficult.

Finally, L2509P, located in the talin dimerisation domain, was predicted to disrupt talins ability to dimerise and thus alter actin binding as shown in previous research[7]. Size exclusion chromatography with Multi-Angle Light Scattering (SEC–MALS) showed that R13–DD WT (residues 2300–2541) is a constitutive dimer, consistent with our previous study[7]. In contrast the R13–DD L2509P mutant runs as a monomer, confirming that the proline is disrupting talin dimerisation (Fig. 3d).

Most of the talin mutations have only minor effects on cell morphology, except for the L2509P mutation. We transiently transfected talin double knock-out (TLN1$^{-/-}$TLN2$^{-/-}$) mouse kidney fibroblasts (MKF)[36] with full length talin-1 constructs containing the mutations shown in Table 1 using equal quantities of plasmid. Western blot analysis ensured translation of full-length proteins (Supplementary Fig. S3a,e). Whereas, in the biochemical section above, the I392N and L1539P were hard to work with due to difficulties in generating sufficient pure, intact mutant domains, this issue was not evident in the full length mammalian expression, with all the twelve constructs expressing full length talin protein. However, we observed decreased protein expression level for I392N and slightly increased expression for S1750F and D2086V, but otherwise the expression levels

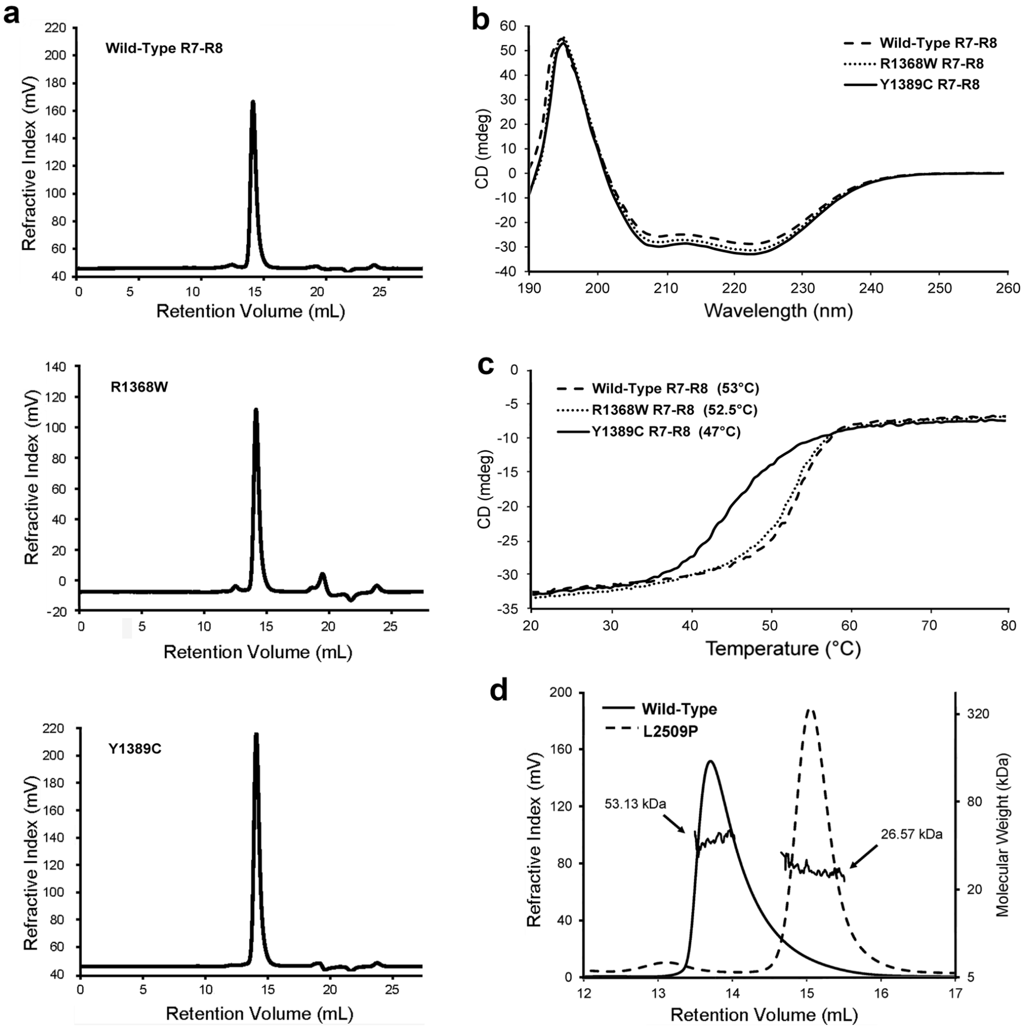

Figure 3. Influence of point mutations on biophysical properties of talin. (**a**) Full SEC profile of R7–R8 WT, R7–R8 R1368W and R7–R8 Y1389C showing the monomeric state. (**b**,**c**) CD analysis of R7–R8 WT, R7–R8 R1368W and R7–R8 Y1389C. (**b**) CD spectra of each mutant. (**c**) Melting temperature curves; the melting temperature of each protein is shown. (**d**) SEC–MALS analysis of R13–DD WT and R13–DD L2509P showing that the R13–DD L2509P is monomeric. The molecular weight obtained from MALS is shown for each peak.

were constant (Supplementary Fig. S3a,e). The adhesion size and abundance were analysed from the cell periphery and did not reveal significant changes in either the adhesion area or adhesion number with the various talin mutations (Supplementary Fig. S4b,c).

To evaluate the effect the mutations have on cell morphology, we visualised talin and vinculin in transfected fibroblast cells devoid of talins (Fig. 4a) and quantified the effect of the mutations on cell area and circularity (Supplementary Fig.S4d,e). The mutations caused little variance on cell morphology when compared to WT, except for cells carrying the dimerisation domain (DD) mutation L2509P, which were significantly smaller than the WT expressing cells and showed a more circular cell phenotype (Supplementary Fig. S4d,e), indicating a loss in cell polarisation.

We next assessed the levels of vinculin, and paxillin within the talin-1 rich adhesion sites with the aid of immunofluorescence labelling and confocal imaging (Fig. 4b,c), and assessed the total level of phosphorylated FAK in cells via western blotting (Fig. 4d; Supplementary Fig.S3f). FAK phosphorylated at tyrosine 397

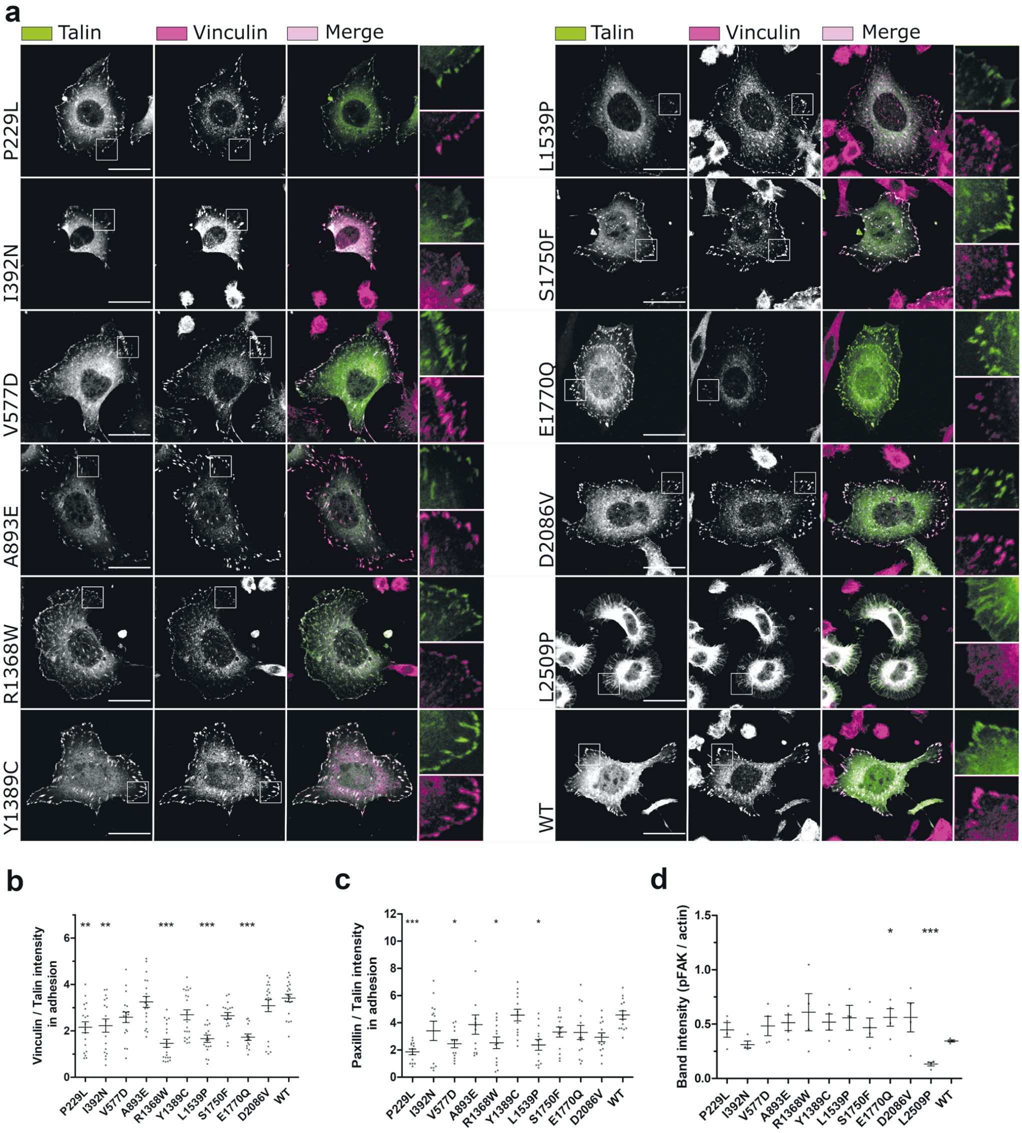

Figure 4. Talin mutations influence the colocalization with vinculin, paxillin and pFAK. (**a**) SUM projections of z–stacks of TLN1$^{-/-}$TLN2$^{-/-}$ mouse kidney fibroblast cells expressing GFP–tagged talin-1 forms and immunolabeled for vinculin. Scale bars are 25 µm, zoom–in square size is 12.5 µm × 12.5 µm. (**b**,**c**) Analysis of vinculin (**b**) and paxillin (**d**) colocalisation with talin in adhesions; $n \sim 20$ cells per mutation from two separate experiments. (**d**) FAKpTyr397 expression levels quantified from four western blots. The statistical significance in (**b**,**c**) was analysed by one-way ANOVA and Bonferroni test: $^{*}P < 0.05$, $^{**}P < 0.01$, $^{***}P < 0.001$. The statistical analysis in (**d**) was calculated by unpaired t–test.

(FAKpTyr397) is a marker for adhesion maturation and corresponds with mechanical activation of talin. Very little FAKpTyr397 is present in non-transfected talin double knock-out MKF cells[37], which enabled us to monitor the relative levels of FAK phosphorylation with western blotting. Interestingly, several mutants showed decreased

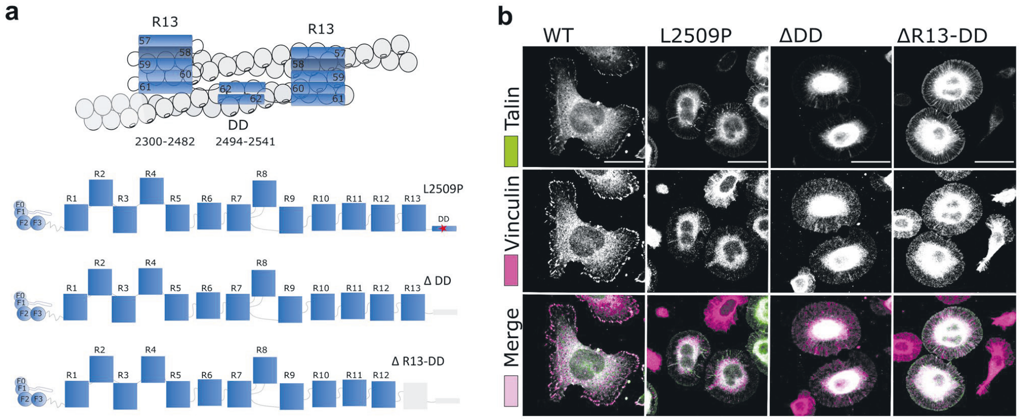

Figure 5. The point mutation L2509P has the same effect on cell morphology as the deletion of the whole dimerisation domain. (**a**) Cartoon of the R13–DD bound to actin (top) and schematic representations of the point mutation L2509P in full-length talin and the truncations; ΔDD and ΔR13-DD. (**b**) SUM projections of z–stacks of TLN1$^{-/-}$TLN2$^{-/-}$ mouse kidney fibroblast cells expressing WT, L2509P, ΔDD, ΔR13–DD talin and immunolabeled against vinculin. No clear localisation of vinculin was evident with any of the mutants. Scale bars are 25 µm.

levels of vinculin and paxillin within the adhesion sites compared to cells expressing WT talin-1, with the mutants R1368W, L1539P and E1770Q showing significantly less recruitment (Fig. 4b,c). We noticed that total vinculin expression level was not majorly influenced by the expression of the talin-1 mutants (Fig. 4a; Supplementary Fig.S3c). In contrast, expression of the talin mutants, P229L, V577D, A893E, L1539P and D2086V led to lower levels of the total paxillin expression when compared to WT-talin expressing cells (Supplementary Fig. S3d). FAKpTyr397 levels were constant with all mutants except a small increase seen with E1770Q and drastic decrease with L2509P when compared to WT talin expressing cells. With L2509P there was also a decrease seen in total FAK levels (Supplementary Fig. S3b,g) suggesting that the lack of adhesion maturation and cell polarisation can affect FAK levels in general.

In order to study the L2509P mutation in more detail, we engineered a series of truncated talin-1 constructs with deletions in the c-terminus as follows: WT (residues 1–2541), ΔDD (residues 1–2493) and ΔR13-DD (residues 1–2299) (Fig. 5a). Immunofluorescence analysis of the cells transfected with L2509P, ΔDD and ΔR13-DD all showed the same cell morphology (Supplementary Fig. S4f,g) accompanied with the loss of; i) adhesion maturation, ii) localisation of the FA components paxillin and vinculin, and iii) filamentous actin within he adhesion sites, indicating that the L2509P point mutation disrupts dimerisation and interaction with actin to the same extent as deletion of the entire domain (Fig. 5b; Supplementary Fig.S4h).

Predicting the effect of mutations on talin interactions with other adhesion proteins through cellular and biochemical analysis. The recombinant R7–R8 WT and mutant (R1368W and Y1389C) proteins were used to assess interactions with ligands using biochemical assays. Two of the vinculin binding sites of talin are located in the R7–R8 region, and their exposure is regulated by stability of the α-helical bundles in response to mechanical load[38–40]. To determine whether vinculin Vd1 domain (residues 1–258) binding to talin was affected by the R7–R8 R1368W and R7–R8 Y1389C mutations, we used a size exclusion chromatography (SEC) assay as described previously[38]. Our previous study showed that despite containing two VBS, only one of them is accessible to vinculin[38], and here we found that R7–R8 WT and R7–R8 R1368W both only bind one vinculin Vd1 molecule (Fig. 6a,b). In contrast, the R7–R8 Y1389C mutation, which is in the core of the R7 domain, can bind two Vd1 molecules (Fig. 6c), indicating that this mutation enhances the accessibility of the R7 vinculin binding site and alters the stoichiometry of the R7–R8-vinculin interaction. On its own the R7–R8 Y1389C mutation runs as a monomer (Figs. 3a, 6c), eluting at the same position as the R7–R8 WT. So, the 2:1 vinculin stoichiometry is due to the R7 domain being destabilised making the VBS more accessible rather than the protein being denatured.

Both R7 and R8 contain binding sites for proteins that contain LD-motifs and so a Fluorescence Polarisation (FP) assay was used to determine the impact of these mutations on binding of the LD-motifs of KANK1 and RIAM to R7 and R8 respectively. Neither KANK1 binding to R7 nor RIAM binding to R8 had significant differences in binding affinity with the R7–R8 R1368W and R7–R8 Y1389C mutants as compared to R7–R8 WT confirming that these mutations do not perturb the LD-motif binding surfaces (Fig. 6d). The talin–KANK1 interaction is important for coordinating the targeting of microtubules to adhesion sites[9] and consistent with the negligible impact on the talin–KANK1 interaction, no apparent changes in tubulin organisation between WT, R1368W, Y1389C, and L1539P were observed in cell experiment (Fig. 6f; Supplementary Fig. S5a).

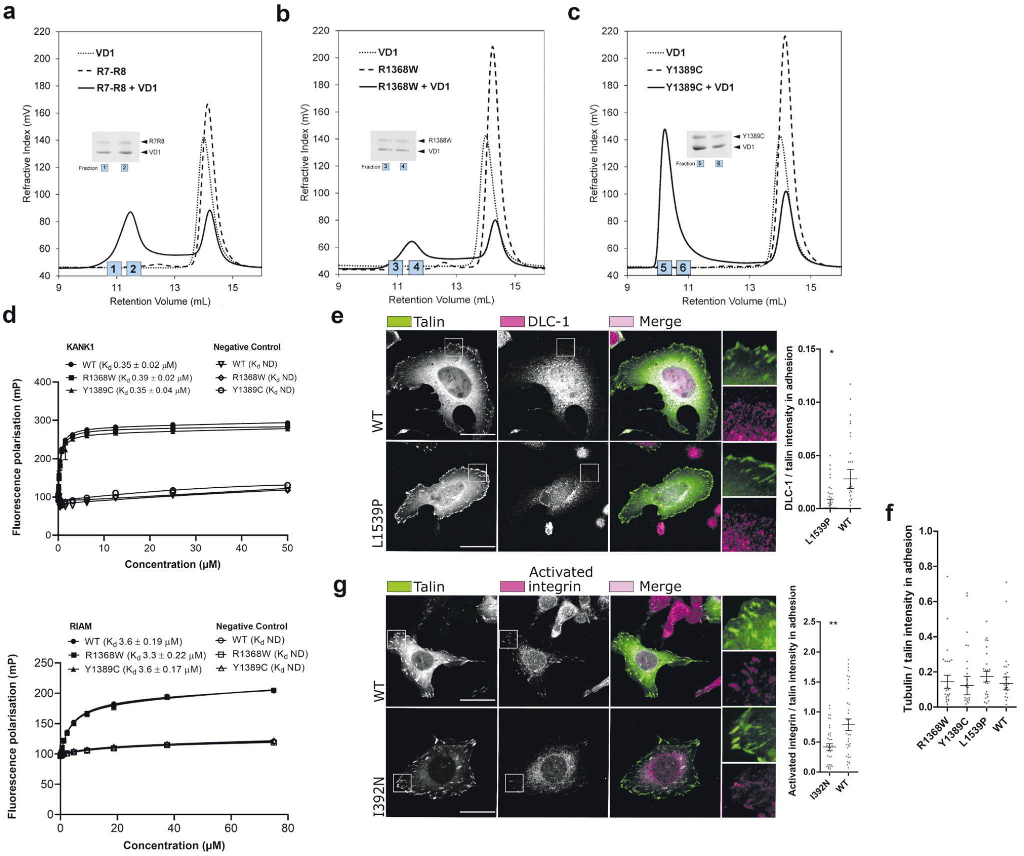

Figure 6. Mutations alter the interaction and colocalisation of talin with vinculin, DLC-1 and activated β1–integrin. (**a**–**c**) Vinculin Vd1 binding analysed by size exclusion chromatography for R7–R8 WT (**a**), R7–R8 R1368W (**b**) and R7–R8 Y1389C (**c**) purified as recombinant proteins in *E. coli*. The SDS-PAGE gel of the elution fractions is shown. (**d**) Fluorescence Polarisation (FP) assay for purified R7–R8 WT/mutant binding to KANK (top) and RIAM (bottom) peptides. R7–R8 R1368W and R7–R8 Y1389C showed no significant changes in the interaction with KANK and RIAM compared with R7–R8 WT. Fluorescence polarisation assays were performed using protein serially diluted from a starting concentration of 60 µM with target KANK1 (30–68) peptide at 1 µM and 75 µM with target RIAM (4–30) peptide concentration at 1 µM. Measurements were taken using a CLARIOstar plate reader (BMGLabTech) at 20 °C. GraphPad Prism 7 software was used for data analysis with one-site total binding equation used to generate a K$_d$. (**e**) Representative confocal immunofluorescence images of the co-localisation of DLC-1 in the TLN1$^{-/-}$TLN2$^{-/-}$ mouse kidney fibroblast cells transfected with full length talin WT and L1539P. (**f**) Data obtained from the colocalisation of tubulin in adhesion sites. (**g**) Representative confocal immunofluorescence images of the co-localisation of activated integrin CD29 organisation in the cells transfected with full length talin WT and I392N. SUM projections of z-stacks of cells expressing GFP-tagged talin-1 (WT and/or point mutated) and immunolabeled against integrin CD29 or DLC-1, and ~ 30 cells per label have been analysed. The statistical significance of all results was analysed by one-way ANOVA and Bonferroni test: $*P < 0.05$, $**P < 0.01$, $***P < 0.001$. Scale bars are 25 µm, zoom-in square size is 12.5 µm × 12.5 µm.

Since L1539P is located near to the DLC-1 binding site we also assessed the mutations effect on DLC-1 recruitment to the adhesions in mouse fibroblasts. For this we quantified the amount of DLC-1 within the adhesions and found that L1539P leads to ~ 42% decrease in DLC-1 amount within the adhesion as compared to the WT (Fig. 6e). As I392N is in close proximity to the integrin binding site in F3, (PDB:2H7D)[41], we assessed whether the mutation can affect the talin-mediated integrin activation. For this, we quantified the amount of activated integrins within adhesions. Expression of I392N lead to ~ 53% decrease in the amount of activated integrin when compared to WT talin (Fig. 6g).

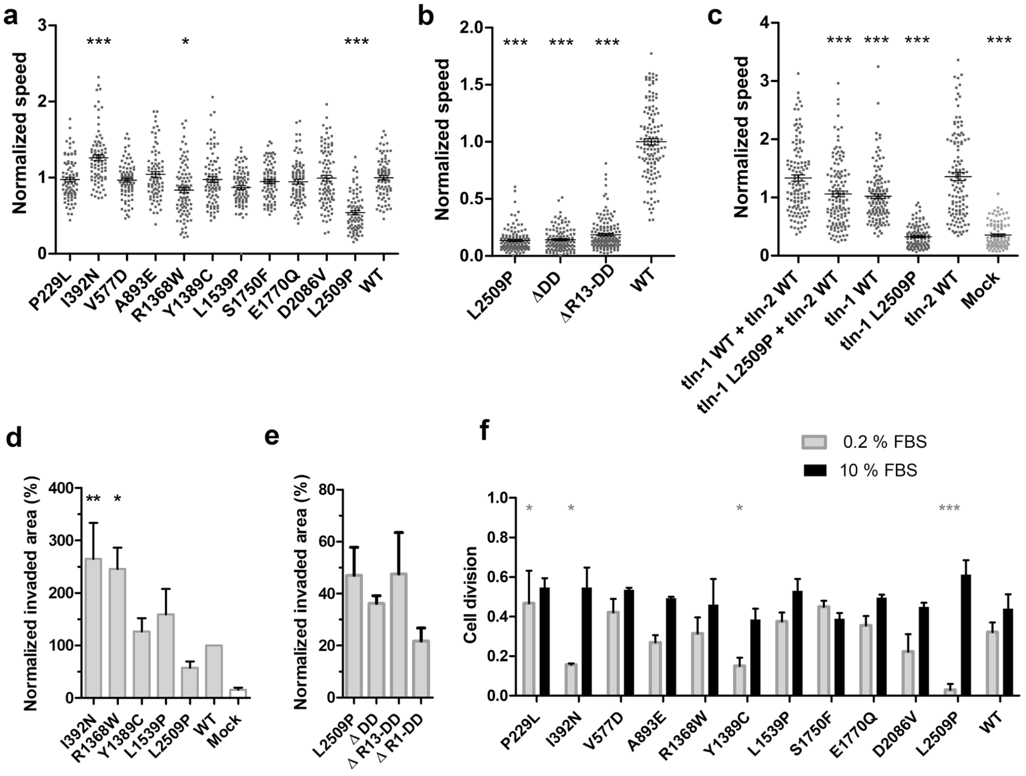

Figure 7. Talin mutations affect cell migration and proliferation. (**a**) Random migration speed (μm/min) determined from time-lapse images of talin expressing cells. (**b**) Migration speed on 2D surface showing reduced migration speed in all mutated/truncated constructs in comparison to WT. (**c**) Migration assay on 2D surface showing reduced migration speed in cells co-transfected with talin-1 L2509P and full-length WT talin-2. The statistical significance of all results analysed in comparison to talin-1 WT + talin-2 WT by one-way ANOVA and Bonferroni test: *P < 0.05, **P < 0.01, ***P < 0.001. The results are normalised with talin-1 WT. (**d**) Invasion assay through Matrigel matrix towards 10% FBS containing medium. Control cells were mock-transfected with GFP-expressing plasmid. The values are normalised to WT and statistical significance measured in comparison to WT. Data are mean + /−SEM. The statistical significance was analysed by one-way ANOVA and Bonferroni test: *P < 0.05, **P < 0.01, ***P < 0.001. (**e**) Cell invasion through Matrigel in 3D environment showing the invasiveness potential of the L2509P and truncated talin constructs. Invasion assay was repeated at least three times in triplicate chamber for each construct on separate days. (**f**) Cell proliferation analysis in the presence of 10% FBS and 0.2% FBS, showing the number of times the cells divide in 12 h; n ~ 80 cells per mutation from four separate experiments. The statistical analysis was calculated by t-test, non-parametric test of Mann–Whitney: *P < 0.05, **P < 0.01, ***P < 0.001 compared to WT for each condition.

Cancer-derived talin-1 point mutations affect cell migration, invasion and proliferation. To study the functional characteristics of the talin mutants, we measured random cell migration speed on cells cultured on fibronectin-coated coverslips (Fig. 7a,b). WT-transfected cells had an average migration speed of 0.65 μm/min. I392N was the only mutant that caused increased migration speed (0.82 μm/min). In contrast, R1368W caused a slight decrease and L2509P caused a marked decrease in cell migration with average speeds of 0.54 and 0.37 μm/min respectively, with the migration speed of L2509P close to that of non-transfected cells (0.35 μm/min) (Supplementary Fig. S5b).

Since many cell types express both, talin-1 and talin-2, we were curious to see whether the L2509P mutation in talin-1 would show a phenotype when expressed together with talin-2. Indeed, we found that the mutation caused significant decrease in migration speed in cells co-transfected with talin-2 when compared to cells expressing both WT talins (Fig. 7c).

Based on the migration assay, we selected I392N, R1368W, Y1389C, L1539P and L2509P for further analysis. We characterised how these five mutants affected the ability of cells to invade through a 3D Matrigel matrix

Mutation	MD simulations		Cell morphology	Interactions (protein–protein* or within adhesions)	Proliferation 0.2% FBS	Proliferation 10% FBS	Migration speed (µm/min)	Invasion	Bioinformatic score	Biochemical analysis
	Free energy change ΔΔG, kJ/mol (comment)	Equilibrium MD								
P229L	–*	↔	↔	vinculin↓ paxillin↓ pFAK↔	↑	↔	0.64±0.19	–	8.20	–
I392N	38.28±1.27 (severe destabilisation)	water molecules penetrate F3	↔	vinculin↓ paxillin↔ pFAK↔ β1 active↓	↓	↔	0.82±0.24	↑	8.95	Prone to proteolysis
V577D	52.15±13.71 (severe destabilisation)	–	↔	vinculin↔ paxillin↓ pFAK↔	↔	↔	0.63±0.16	–	8.39	–
A893E	10.5±1.91 (significant destabilisation)	–	↔	vinculin↔ paxillin↔ pFAK↔	↔	↔	0.68±0.22	–	7.63	–
R1368W	12.63±0.27 (significant destabilisation)	enhances R7–R8 interaction	↔	vinculin↓ paxillin↓ pFAK↔ Vd1↔ KANK1↔ RIAM↔ tubulin↔	↔	↔	0.54±0.23	↑	7.75	NMR ↔ CD ↔
Y1389C	20.6±4.09 (strong destabilisation)	↔	↔	vinculin↓ paxillin↓ pFAK↔ Vd1↑ KANK1↔ RIAM↔ tubulin↔	↓	↔	0.64±0.21	↔	8.58	– CD↓
L1539P	–*	breaks H3 in R8	↔	vinculin↔ paxillin↔ pFAK↔ Vd1↔ DLC–1↓ tubulin↔	↔	↔	0.57±0.15	↔	8.45	Poorly expressed
S1750F	2.28±2.33 (n.s.)	–	↔	vinculin↔ paxillin↔ pFAK↔	↔	↔	0.62±0.16	–	7.55	–
E1770Q	–4.17±0.35 (mild stabilisation)	–	↔	vinculin↓ paxillin↔ pFAK↑	↔	↔	0.61±0.19	–	6.01	–
D2086V	12.96±0.82 (significant destabilisation)	–	↔	vinculin↔ paxillin↔ pFAK↔	‘↔	↔	0.64±0.24	–	7.71	–
L2509P	–*	breaks the DD helix	non–polarised	vinculin↔ paxillin↔ pFAK↓	↓	↔	0.37±0.20	↔	7.46	SEC (monomer)

↔ indicating no change when compared to WT talin–1
↑ indicating an increase when compared to WT talin–1
↓ indicating a decrease when compared to WT talin–1
– indicating not tested
–* indicating not tested, because proline is not supported for the analysis
* Vinculin Vd1, KANK1, RIAM were assessed via protein–protein interaction.
▨▨▨▨▨
low high

Table 2. Summary table of the analysis of talin-1 mutations. Migration speed for the WT-talin was 0.65 ± 0.18 µm/min.

(Fig. 7d). I392N and R1368W showed the highest invasion rates, whereas Y1389C and L1539P did not significantly differ from WT. Further, the mutant L2509P, which showed a poorly polarised cell phenotype (Fig. 5b) and significantly reduced migration speed on 2D culture (Fig. 7a,b), was only able to promote limited cell invasion in 3D (Fig. 7d). The impact on cell migration and invasion, was the same for the L2509P and the truncated mutants whether we removed the entire rod, R13-DD, DD or applied the point mutation L2509P (Fig. 7b,e).

In full-serum conditions the mutants and the mock-transfected cells (Supplementary Fig.S5c) showed equally efficient cell proliferation rate when compared to WT talin-1 expressing cells (Fig. 7f). However, during serum depletion, I392N, Y1389C, L2509P and mock-transfected cells showed significant decrease (~ 53%, ~ 53%, ~ 91% and ~ 45%, respectively) and the P229L showed ~ 30% increase in cell division as compared to the cells transfected with WT talin-1 (Fig. 7f; Supplementary Fig.S5c), suggesting that talin-1 mediated changes can affect cell proliferation.

Discussion

Loss of anchorage-dependent growth, changes in ECM remodelling, and cytoskeletal changes are necessary for cancer progression[42]. Talins are central regulators of these processes, providing mechanical linkages between ECM and the actin cytoskeleton, In this study we explored whether mutations in talin identified in large scaled cancer exome sequencing might contribute to cancer progression.

There are two isoforms of talin, talin-1 and talin-2, which show different expression patterns[43,44]. While talin-1 is expressed in all tissues, talin-2 has more variability and generally lower expression levels. Overall expression levels, derived from GEPIA (gene expression profiling interactive analysis) server[45], indicate that talin-1 expression levels are more variable between different cancers and their counterpart healthy tissues than those of talin-2 (Supplementary Fig. S6) with several cancer types showing significant changes in talin-1 expression level. The highest overexpression is associated with Glioblastomas (GBM; > 300%), Brain Gliomas (LGG; > 300%) and Pancreatic adenocarcinomas (PAAD; > 300%). In contrast, the most drastic talin-1 downregulation is seen in uveal melanoma (UCS; – 25%) and endometrial carcinoma of the uterine (UCEC; –25%).

These datasets are large and expansive, and so we prioritised bioinformatic analysis as the first stage in our pipeline approach enabling us to explore the large quantity of talin-1 mutations and predict the impact of the mutations on the stability of protein structure. With the aid of bioinformatic classification, molecular modelling, biochemical analyses and functional cell biology assays, we found that mutations in talin-1 affect cellular processes linked with cancer progression, such as migration, invasion and proliferation (Table 2). By this approach, we identified mutations located in the previously identified binding sites showing strong destabilization of the domain in free energy calculations (I392N, R1368W, Y1389C, L1539P and L2509P) for further investigation. Several of the studied mutations were difficult to produce for the biochemical assays, suggesting that these indeed destabilised the corresponding talin domain. However, all of the mutations could be efficiently produced within cells as full-length proteins that were localised to the adhesions. Mutation within the dimerization domain, L2509P, was the only mutation leading to disruption of the adhesion complexes, due to lack of dimerization and actin binding. In contrast the other mutations showed more subtle changes in migration and invasion or in amount or activity of the binding partners within adhesions. Mutations I392N, Y1389C and L1539P had the highest initial bioinformatics scores and this correlated well with the data gained from cell experiments. We showed increased migration and invasion and changes within integrin activation status for cells expressing I392N. For Y1389C and L1539P we observed changes in vinculin binding and DLC-1 recruitment to the adhesions, respectively. Mutation R1368W led to changes in migration, invasion and in recruitment of binding partners although it received an intermediate score in the bioinformatics analysis. Finally, while L2509P received only moderately high score in bioinformatic evaluation, it was found to be highly pathogenic, causing abolishment of talin dimerization.

Out of the eleven mutants studied here, I392N, originally found from pancreatic carcinoma, had the most pronounced effect in terms of driving migration and invasion. A previous study by Isenberg et al. proposed the amino acids 385–406 of F3 helix as a potential membrane–anchoring domain with I392 as one of the residues that inserts into the lipid bilayer[30] and mediates integrin activation[46]. Our results showed a clear decrease in the amount of active integrin in talin–rich adhesions, when compared to WT (Fig. 6g).The mutated helix in F3 experiences mechanical tension applied on talin[47] and this might result in increased dissociation of the destabilised mutated helix from the rest of the F3 under applied load, influencing integrin association and thereby contributing to the adhesion turnover/dynamics. Biochemical experiments with this mutant were hampered by proteolytic truncation of the mutated talin head during recombinant protein expression, indicating folding defect in the C-terminal part of the protein.

The R7–R8 domains have cooperative function, with R8 sitting outside the force transduction pathway, and protected from mechanical stress by R7[40]. In addition, there are binding sites for multiple molecules such as KANK1, DLC-1, RIAM, paxillin and vinculin in both domains. One surprising result from this study was the observation that in every MD simulation carried out for R7–R8 (WT, R1368W, Y1389C, and L1539P), the R7 and R8 subdomains were found to transiently interact over the course of the 100 ns MD. Furthermore, the MD simulations suggested that the R1368W mutant in R7 might enhance these interactions between R7 and R8 domains (Fig. 2b; Supplementary Fig. S2a,b). All the crystal structures of talin R7–R8 reported to date have shown an open conformation where there are limited contacts between the R7 and R8 subdomains[11,38,48] and such an interaction was not readily apparent in the NMR analysis (Supplementary Fig. S4a). However, the recent crystal structure of TLNRD1 (talin rod domain containing protein 1 (PDB:6XZ4[49]), a protein structurally homologous to talin R7–R8, revealed a similar close association of the two subdomains, supporting the notion that the two talin subdomains might also interact. One possibility is that the interaction between the two domains might reduce accessibility to ligand binding sites on the domains, and perturb the localisation of the FA markers within adhesions (Fig. 4b,c), affecting cell behaviour. However, binding affinity of the R1368W mutant for KANK1 and protein stability remained consistent with WT, suggesting that the cellular effects we observed are not due to alterations in known functions of R7. It is possible that this mutation is altering the dynamics of the R7 and R8 domains causing the altered cellular behaviour we observe. Therefore, the role of such an interaction is not fully clear and warrants further investigation.

The VBS in R7 is one of the hardest to expose[38] but can be stretch activated[40], interestingly, the R7–R8 Y1389C mutation significantly enhanced the VBS accessibility. Gel filtration analysis of vinculin Vd1 binding to R7–R8 Y1389C revealed that while R7–R8 WT and the R7–R8 R1368W mutant only bind a single Vd1 molecule, the R7–R8 Y1389C was able to bind two Vd1 (Fig. 6a–c). This suggests that introduction of the mutation destabilises the R7 helical bundle, allowing vinculin binding more readily in the absence of force. Furthermore, reduced R7 stability will likely have a knock-on effect on R8 stability which may indirectly lead to signalling defects by perturbing R8[12]. The additional actin recruitment via vinculin could have a direct effect on FA dynamics by facilitating formation of talin-vinculin pre-complexes, necessary to enable efficient adhesion maturation[50]. This could also affect actomyosin contractility and Rho/ROCK signalling, which have been shown to regulate cell proliferation[51].

DLC-1 is a tumour suppressor[52] and contains an LD-like motif, which is required for the full tumour suppressor activity of DLC-1 via interaction with talin[46]. DLC-1 residue D470 makes direct contact with the positively charged side chain of K1530 and K1544 in R8[11]. In cells transfected with L1539P mutant, the colocalisation between talin and DLC-1 was significantly decreased (Fig. 6e), indicating that this mutation interferes with DLC-1 binding.

In previous studies, talin depletion caused a halt in cell cycle of epithelial cells that could be rescued with expression of C-terminal talin fragment that was able to cause FAK phosphorylation[53]. The linkage between the C-terminal actin-binding site, ABS3 and actin is required for polarisation of cells[37] and this linkage depends on talin dimerisation. Mutation in the dimerization domain, L2509P, resulted in an unpolarised and non-migratory cell phenotype lacking mature FAs and actin contacts on the cell surface. This mutation sits in the talin dimerisation domain, a single helix which forms an antiparallel dimer[7,54]. The same phenotype was observed with complete removal of the dimerisation domain helix (ΔDD) as with L2509P point mutation. Our biochemical results showed that the R13-DD L2509P mutant resulted in complete loss of dimerisation compared to the R13-DD WT which is a constitutive dimer in solution (Fig. 3d).

In this study, we systematically explored hundreds of talin-associated mutations and the bioinformatics pipeline described here enabled us to rapidly and robustly screen this huge number and narrow it down to an experimentally tractable subset for detailed analysis. Using this approach, we selected 11 mutants for thorough analysis and found that the bioinformatic scores reflected the corresponding cell phenotype well in most cases, however, the pathogenicity of the mutations in tissue and cell context is difficult to assess. Here the cell phenotype of cancer-associated talin mutations was observed without the effect of the other mutations commonly found in cancer cells. As the mutations within the common oncogenes will heavily affect the cell signalling, it is difficult to predict exactly what would be the contribution of these studied talin-1 mutations for the cancer progression in their original context. It is however noteworthy that several talin point mutations influenced cell migration, invasion and cell polarisation even when expressed without the other cancer-associated factors.

Investigation of the contribution of talin to cancer progression is timely. During this study ~ 670 more cancer–associated talin-1 point mutations have been added to the COSMIC database (Supplementary Fig.S1) and there are recent studies discussing the connection between talin and cancer[23,55–58]. The work we present here demonstrates an efficient and fast pipeline approach using bioinformatics tools to characterise future talin mutations identified in cancer and other diseases.

Materials and methods

Cell lines and talin constructs. Theodosiou et al.[36] previously described the TLN1$^{-/-}$TLN2$^{-/-}$ mouse kidney fibroblast (MKF) cell line. Cells were maintained in a humidified 37 °C, 5% CO_2 incubator. High glucose Dulbecco´s modified Eagle medium (DMEM) supplemented with 10% fetal bovine serum (FBS) was used in all experiments except in the starvation conditions where 0.2% serum was used. The cell line was regularly tested for mycoplasma contamination. Talin variants were subcloned into a modified pEGFP-C1 vector backbone (Clontech). Cells were transfected with 6 µg plasmid DNA per 10^6 cells using Neon transfection system (Thermo Fisher Scientific) using parameters 1400 V, 30 ms, one pulse. The expression constructs for cell culture experiments with the c-terminal EGFP-tag are as follows: wildtype talin-1 (1–2541); ΔR13–DD (1–2299); ΔDD (1–2493); ΔR1–DD (1–481) and the point mutants in the full-length talin-1 P229L, I392N, V557D, A893E, R1368W, Y1389C, L1539P, S1750F, E1770Q, D2086V, L2509P.

Migration and matrigel invasion analysis. Transfected cells were incubated for 24 h, trypsinised and plated on well-plates coated with 10 µg/ml fibronectin. Cells were allowed to attach for 90 min, after which the media was changed. The time-lapse images captured with EVOS FL auto microscope (Thermo Fisher Scientific) were analysed manually using ImageJ (Fiji) and MTrackJ plugin[59,60].

Corning BioCoat Matrigel Invasion Chamber containing an 8-micron pore size PET membrane with a thin layer of Matrigel basement membrane matrix were used for the invasion assay. Transfected TLN1$^{-/-}$TLN2$^{-/-}$ MKF cells were cultured overnight, followed by cultivation in starvation medium containing 0.2% FBS for 40–45 h. Number of transfected cells was measured by Luna-FL dual Fluorescence Cell Counter (BioCat GmbH) Chambers prepared according to the manufacturer. DMEM medium containing 10% FBS was used as chemoattractant in the lower level of chamber. The chamber plate was incubated at humidified 37 °C and 5% CO_2 incubator for 24 h, after which the cells were fixed with 100% methanol. Cells were stained with 0.2% crystal blue for 10 min following by rinsing the excess stain. The non-invaded cells were removed from the upper membrane surface using cotton tipped swab. The inserts were allowed to air dry overnight. The membrane was removed using scalpel and placed bottom side down on a microscope objective slide on which a small drop of immersion oil. The membranes were scanned using PRIOR OpenStand microscope using 20 × objective and Jilab SlideStrider software (1.2.0). The invaded cell area was calculated using ImageJ (Fiji). Invasion assay was repeated at least three times in triplicate chamber for each selected construct.

Immunostaining and confocal imaging. After 24 h transfection, cells were trypsinised and plated on coverslips coated with 10 µg/ml fibronectin and incubated for 24 h. Cells were fixed with 4% paraformaldehyde, permeabilised and immunostained using standard protocol. Antibodies are listed in Supplementary Table S1.

Immunostained samples were imaged with Zeiss Cell ObserverZ1 inverted microscope and LSM 780 confocal unit (Zeiss, Oberkochen, Germany) using 63×/1.4, WD 0.19 mm oil immersion objective. Images were taken using Zeiss Zen Black software and analysed by ImageJ as described previously[37]. Within each experiment, the imaging parameters were kept constant to allow quantitative image analysis. Detailed image analysis is described in Supplementary material.

Western blotting. Transfected cells were grown for 24 h, lysed with RIPA buffer supplemented with protease inhibitor cocktail (Sigma–Aldrich lot#126M4016V). After centrifugation, cell lysates were applied on an SDS–PAGE to separate protein. A wet blot system was used to transfer the separated protein from gel onto a polyvinylidene fluoride (PVDF) membrane. Blots were quantified using ImageJ. Antibodies are listed in Supplementary Table S1.

Constructs for protein expression in *E. coli*. The talin-1 fragments (head, residues 1–405; R7–R8, residues 1355–1652; R13–DD, residues 2300–2541), generated using full-length mouse talin-1 as a template, were introduced into a modified pHis vector to create N-terminal His6-tagged constructs. The His6-tag is separated from the talin fragment by an eleven-residue linker: SSSGPSASGTG. Mutagenesis was performed using QuikChange II Site-Directed Mutagenesis kit. Talin constructs were expressed in BL21 (DE3) *E. coli* cells and induced with 0.1 mM IPTG at 18 °C overnight. Clarified lysates were loaded onto an affinity column (HisTrap HP 5 ml; GE Healthcare). Eluted protein was further purified using an anion exchange column (HiTrap Q HP 5 ml; GE Healthcare) before buffer exchange into PBS and storage at − 20 °C.

NMR spectroscopy and fluorescence polarisation assay. For NMR analysis, talin constructs were grown in 2M9 minimal media with ^{15}N-labelled NH_4Cl. Protein was purified as above and buffer exchanged into 20 mM Na–phosphate pH 6.5, 50 mM NaCl, 2 mM DTT, 5% (v/v) D_2O. NMR spectra were obtained at 298 K on a Bruker AVANCE III 600 MHz spectrometer equipped with CryoProbe. All R7–R8 ^{1}H, ^{15}N-HSQC spectra were obtained at a concentration of 160 µM. For fluorescence polarisation (FP) experiments, mouse KANK1 and RIAM peptides were synthesised by GLBiochem (China) and coupled with either BODIPY or Fluorescein dye via a C-terminal cysteine residue:

KANK1 (30–68) – PYFVETPYGFQLDLDFVKYVDDIQKGNTIKKLNIQKRRK–C.
RIAM (4–30) – SEDIDQMFSTLLGEMDLLTQSLGVDT–C.

Size exclusion chromatography with multi-angle light scattering. Talin R13–DD wildtype and R13-DD L2509P were analysed by SEC–MALS at a concentration of 100 µM at room temperature with a Superdex 75 column (GE Healthcare Life Sciences). Eluted proteins were analysed with Viscotek SEC–MALS 9 and Viscotek RI detector VE3580 (Malvern Panalytical). Molecular mass was determined using OmniSEC software. For analysis of Vd1 binding to talin, proteins were incubated at a 2:1 ratio at a concentration of 100 µM and analysed at room temperature.

MD simulations. RCSB PDB structures were used as starting conformations for MD: 3IVF for F2–F3 (residues 208–398)[61], 2H7E for F3 (residues 309–405)[41], 1SJ8 for R1 (residues 487–656)[62], 2L7A for R3 (residues 796–909)[63], 2X0C for R7–R8 and R7 (residues 1352–1457, 1585–1659)[38], 2KBB for R9 (residues 1655–1822)[33], 3DYJ for R11 (residues 1975–2140)[64] and 2QDQ for DD domain (residues 2494–2541)[7]. The F2–F3 and R7–R8 inter–subdomain binding energy was calculated using MM–PBSA[65]. Structural analysis was performed using PyMOL. The secondary structure analysis was based on the Dictionary of Secondary Structure of Proteins (DSSP) algorithm[66].

Equilibrium MD simulations were performed using Gromacs[67] at the Sisu supercomputer, CSC, Finland. The CHARMM27 force field[68] and explicit TIP3P water model[69] in 0.15 M KCl solution were used. The energy minimisation of the system was performed in 10,000 steps. The system was equilibrated in three phases using harmonic position restraints on all heavy atoms of the protein, as described in our previous study[70]. Integration time step of 2 fs was used in all the simulations. The temperature and pressure of the system was maintained at 310 K using the V-rescale algorithm[71], and 1 bar using Berendsen algorithm[72]. At least three 100 ns replicas were generated for each system.

Alchemical free energy calculations were prepared using PMX[73] and performed with Gromacs at Puhti supercomputer, CSC, Finland. The Amber99SB*–ILDN force field[74] and TIP3P water model in 0.15 M NaCl solution were used. Each system was energy minimised for 10,000 steps and then equilibrated for 1 ns using harmonic position restraints on all heavy atom of the protein. The temperature and pressure of the system was maintained at 298 K and 1 bar using Berendsen algorithm for the system equilibration, while V-rescale and Parrinello-Rahman[75] algorithms were used for equilibrium MD and non-equilibrium morphing simulations. Integration time step of 2 fs was used in all the simulations. Each state of the system was run for 100 ns equilibrium MD. 100 non-equilibrium morphing simulations were prepared for each physical state of the system, using snapshots captured from the equilibrium trajectories, linearly spaced from 10.9 to 100 ns. Fast non–equilibrium simulations were morphing the system from one state to another in 100 ps for change conserving mutations, and in 200 ps for charge changing mutations. A soft-core potential[76] was used for the non–equilibrium simulations. The whole calculation, including system preparation, was repeated three times and average free energy value was obtained. Approximately 5.6 µs MD simulations in total were performed for the analysis. Proline involving mutations were not analysed as proline is not supported for the analysis.

Received: 24 July 2020; Accepted: 17 November 2020

References

1. Lu, P., Weaver, V. M. & Werb, Z. The extracellular matrix: A dynamic niche in cancer progression. *J. Cell. Biol.* **196**, 395–406 (2012).
2. Goult, B. T. *et al.* Structural studies on full-length talin1 reveal a compact auto-inhibited dimer: Implications for talin activation. *J. Struct. Biol.* **184**, 21–32 (2013).
3. Anthis, N. J. *et al.* The structure of an integrin/talin complex reveals the basis of inside-out signal transduction. *EMBO J.* **28**, 3623–3632 (2009).
4. Tanentzapf, G. & Brown, N. H. An interaction between integrin and the talin FERM domain mediates integrin activation but not linkage to the cytoskeleton. *Nat. Cell Biol.* **8**, 601–606 (2006).
5. Hemmings, L. *et al.* Talin contains three actin-binding sites each of which is adjacent to a vinculin-binding site. *J. Cell. Sci.* **109**(Pt 11), 2715–2726 (1996).
6. Atherton, P. *et al.* Vinculin controls talin engagement with the actomyosin machinery. *Nat. Commun.* **6**, 10038 (2015).
7. Gingras, A. R. *et al.* The structure of the C-terminal actin-binding domain of talin. *EMBO J.* **27**, 458–469 (2008).
8. Gingras, A. R. *et al.* Mapping and consensus sequence identification for multiple vinculin binding sites within the talin rod. *J. Biol. Chem.* **280**, 37217–37224 (2005).
9. Bouchet, B. P. *et al.* Talin-KANK1 interaction controls the recruitment of cortical microtubule stabilizing complexes to focal adhesions. *eLife* **5**, 2 (2016).
10. Sun, Z. *et al.* Kank2 activates talin, reduces force transduction across integrins and induces central adhesion formation. *Nat. Cell Biol.* **18**, 941–953 (2016).
11. Zacharchenko, T. *et al.* LD motif recognition by talin: Structure of the talin–DLC1 Complex. *Structure* **24**, 1130–1141 (2016).
12. Haining, A. W. M. *et al.* Mechanotransduction in talin through the interaction of the R8 domain with DLC1. *PLoS Biol.* **16**, e2005599 (2018).
13. Kopp, P. M. *et al.* Studies on the morphology and spreading of human endothelial cells define key inter- and intramolecular interactions for talin1. *Eur. J. Cell Biol.* **89**, 661–673 (2010).
14. Kumar, A. *et al.* Talin tension sensor reveals novel features of focal adhesion force transmission and mechanosensitivity. *J. Cell Biol.* **213**, 371–383 (2016).
15. Sun, Z., Guo, S. S. & Fassler, R. Integrin-mediated mechanotransduction. *J. Cell Biol.* **215**, 445 (2016).

16. Goult, B. T., Yan, J. & Schwartz, M. A. Talin as a mechanosensitive signaling hub. *J. Cell Biol.* **217**, 3776–3784 (2018).
17. del Rio, A. *et al.* Stretching single talin rod molecules activates vinculin binding. *Science* **323**, 638–641 (2009).
18. Vigouroux, C., Henriot, V. & Le Clainche, C. Talin dissociates from RIAM and associates to vinculin sequentially in response to the actomyosin force. *Nat. Commun.* **11**, 3116–3121 (2020).
19. Nagano, M., Hoshino, D., Koshikawa, N., Akizawa, T. & Seiki, M. Turnover of focal adhesions and cancer cell migration. *Int. J. Cell Biol.* **2012**, 310616–310710 (2012).
20. Murrell, M., Oakes, P. W., Lenz, M. & Gardel, M. L. Forcing cells into shape: The mechanics of actomyosin contractility. *Nat. Rev. Mol. Cell Biol.* **16**, 486–498 (2015).
21. Lai, M. T. *et al.* Talin-1 overexpression defines high risk for aggressive oral squamous cell carcinoma and promotes cancer metastasis. *J. Pathol.* **224**, 367–376 (2011).
22. Sakamoto, S., McCann, R. O., Dhir, R. & Kyprianou, N. Talin1 promotes tumor invasion and metastasis via focal adhesion signaling and anoikis resistance. *Cancer Res.* **70**, 1885–1895 (2010).
23. Ji, L., Jiang, F., Cui, X. & Qin, C. Talin1 knockdown prohibits the proliferation and migration of colorectal cancer cells via the EMT signaling pathway. *Oncol. Lett.* **18**, 5408–5416 (2019).
24. Chen, P. *et al.* Downregulation of Talin1 promotes hepatocellular carcinoma progression through activation of the ERK1/2 pathway. *Cancer Sci.* **108**, 1157–1168 (2017).
25. Tate, J. G. *et al.* COSMIC: The catalogue of somatic mutations in cancer. *Nucleic Acids Res.* **47**, D941–D947 (2019).
26. Niroula, A., Urolagin, S. & Vihinen, M. PON-P2: Prediction method for fast and reliable identification of harmful variants. *PLoS ONE* **10**, e0117380 (2015).
27. Henikoff, S. & Henikoff, J. G. Amino acid substitution matrices from protein blocks. *Proc. Natl. Acad. Sci. U.S.A.* **89**, 10915–10919 (1992).
28. Liu, X. & Zheng, W. M. An amino acid substitution matrix for protein conformation identification. *J. Bioinform. Comput. Biol.* **4**, 769–782 (2006).
29. Fillingham, I. *et al.* A vinculin binding domain from the talin rod unfolds to form a complex with the vinculin head. *Structure* **13**, 65–74 (2005).
30. Isenberg, G., Doerhoefer, S., Hoekstra, D. & Goldmann, W. H. Membrane fusion induced by the major lipid-binding domain of the cytoskeletal protein talin. *Biochem. Biophys. Res. Commun.* **295**, 636–643 (2002).
31. Ashkenazy, H. *et al.* ConSurf 2016: an improved methodology to estimate and visualize evolutionary conservation in macromolecules. *Nucleic Acids Res.* **44**, 344 (2016).
32. Haage, A. *et al.* Talin autoinhibition regulates cell-ECM adhesion dynamics and wound healing in vivo. *Cell Rep.* **25**, 2401-2416.e5 (2018).
33. Goult, B. T. *et al.* The structure of an interdomain complex that regulates talin activity. *J. Biol. Chem.* **284**, 15097–15106 (2009).
34. Clarke, L. *et al.* The 1000 genomes project: Data management and community access. *Nat. Methods* **9**, 459–462 (2012).
35. Ellis, S. J. *et al.* The talin head domain reinforces integrin-mediated adhesion by promoting adhesion complex stability and clustering. *PLoS Genet.* **10**, e1004756 (2014).
36. Theodosiou, M. *et al.* Kindlin-2 cooperates with talin to activate integrins and induces cell spreading by directly binding paxillin. *Elife* **5**, e10130 (2016).
37. Rahikainen, R., Ohman, T., Turkki, P., Varjosalo, M. & Hytonen, V. P. Talin-mediated force transmission and talin rod domain unfolding independently regulate adhesion signaling. *J. Cell. Sci.* **132**, jcs226514 (2019).
38. Gingras, A. R. *et al.* Central region of talin has a unique fold that binds vinculin and actin. *J. Biol. Chem.* **285**, 29577–29587 (2010).
39. Hytonen, V. P. & Vogel, V. How force might activate talin's vinculin binding sites: SMD reveals a structural mechanism. *PLoS Comput. Biol.* **4**, e24 (2008).
40. Yao, M. *et al.* The mechanical response of talin. *Nat. Commun.* **7**, 11966 (2016).
41. Wegener, K. L. *et al.* Structural basis of integrin activation by talin. *Cell* **128**, 171–182 (2007).
42. Jaalouk, D. E. & Lammerding, J. Mechanotransduction gone awry. *Nat. Rev. Mol. Cell Biol.* **10**, 63–73 (2009).
43. Debrand, E. *et al.* Talin 2 is a large and complex gene encoding multiple transcripts and protein isoforms. *FEBS J.* **276**, 1610–1628 (2009).
44. Gough, R. E. & Goult, B. T. The tale of two talins—two isoforms to fine-tune integrin signalling. *FEBS Lett.* **592**, 2108–2125 (2018).
45. Tang, Z. *et al.* GEPIA: A web server for cancer and normal gene expression profiling and interactive analyses. *Nucleic Acids Res.* **45**, W98–W102 (2017).
46. Li, A., Guo, Q., Wei, A., Zhou, Y. & Hu, W. Role of the helix in talin F3 domain (F3 Helix) in talin-mediated integrin activation. *Cell Biochem. Biophys.* **75**, 79–86 (2017).
47. Austen, K. *et al.* Extracellular rigidity sensing by talin isoform-specific mechanical linkages. *Nat. Cell Biol.* **17**, 1597–1606 (2015).
48. Chang, Y. C. *et al.* Structural and mechanistic insights into the recruitment of talin by RIAM in integrin signaling. *Structure* **22**, 1810–1820 (2014).
49. Cowell, A. R. *et al.* Talin Rod Domain Containing Protein 1 (TLNRD1) is a novel actin-bundling protein which promotes filopodia formation. *bioRxiv* https://doi.org/10.1101/2020.05.19.103606. (2020).
50. Han, S. J. *et al.* Formation of talin-vinculin pre-complexes dictates maturation of nascent adhesions by accelerated force transmission and vinculin recruitment. *bioRxiv* https://doi.org/10.1101/735183 (2019).
51. Kumper, S. *et al.* Rho-associated kinase (ROCK) function is essential for cell cycle progression, senescence and tumorigenesis. *Elife* **5**, e12994 (2016).
52. Durkin, M. E. *et al.* DLC-1: A Rho GTPase-activating protein and tumour suppressor. *J. Cell. Mol. Med.* **11**, 1185–1207 (2007).
53. Wang, P., Ballestrem, C. & Streuli, C. H. The C terminus of talin links integrins to cell cycle progression. *J. Cell Biol.* **195**, 499–513 (2011).
54. Smith, S. J. & McCann, R. O. A C-terminal dimerization motif is required for focal adhesion targeting of Talin1 and the interaction of the Talin1 I/LWEQ module with F-actin. *Biochemistry* **46**, 10886–10898 (2007).
55. Huang, H. K. *et al.* Chemoresistant ovarian cancer enhances its migration abilities by increasing store-operated Ca(2+) entry-mediated turnover of focal adhesions. *J. Biomed. Sci.* **27**, 36–45 (2020).
56. Mohamed, A. A. *et al.* Talin-1 gene expression as a tumor marker in hepatocellular carcinoma patients: A pilot study. *Open Biomark. J.* **10**, 15–22 (2020).
57. Song, Y. *et al.* Inward tension of talin and integrin-related osmotic pressure are involved synergetically in the invasion and metastasis of non-small cell lung cancer. *J. Cancer.* **11**, 5032–5041 (2020).
58. Malla, R. R. & Vempati, R. K. Talin: A potential drug target for cancer therapy. *Curr. Drug Metab.* **21**, 25–32 (2020).
59. Schneider, C. A., Rasband, W. S. & Eliceiri, K. W. NIH image to ImageJ: 25 years of image analysis. *Nat. Methods* **9**, 671–675 (2012).
60. Meijering, E., Dzyubachyk, O. & Smal, I. Methods for cell and particle tracking. *Methods Enzymol.* **504**, 183–200 (2012).
61. Elliott, P. R. *et al.* The Structure of the talin head reveals a novel extended conformation of the FERM domain. *Structure* **18**, 1289–1299 (2010).
62. Papagrigoriou, E. *et al.* Activation of a vinculin-binding site in the talin rod involves rearrangement of a five-helix bundle. *EMBO J.* **23**, 2942–2951 (2004).
63. Goult, B. T. *et al.* RIAM and vinculin binding to talin are mutually exclusive and regulate adhesion assembly and turnover. *J. Biol. Chem.* **288**, 8238–8249 (2013).

64. Gingras, A. R. *et al.* Structural determinants of integrin binding to the talin rod. *J. Biol. Chem.* **284**, 8866–8876 (2009).
65. Kumari, R., Kumar, R. & Lynn, A. g_mmpbsa—A GROMACS tool for high-throughput MM-PBSA calculations. *J. Chem. Inf. Model.* **54**, 1951–1962 (2014).
66. Touw, W. G. *et al.* A series of PDB-related databanks for everyday needs. *Nucleic Acids Res.* **43**, 364 (2015).
67. Abraham, M. J. *et al.* GROMACS: High performance molecular simulations through multi-level parallelism from laptops to supercomputers. *SoftwareX* **1–2**, 19–25 (2015).
68. MacKerell, A. D. *et al.* All-atom empirical potential for molecular modeling and dynamics studies of proteins. *J. Phys. Chem. B* **102**, 3586–3616 (1998).
69. Jorgensen, W. L. & Madura, J. D. Quantum and statistical mechanical studies of liquids. 25. Solvation and conformation of methanol in water. *J. Am. Chem. Soc.* **105**, 1407–1413 (1983).
70. Mykuliak, V. V., Haining, A. W. M., von Essen, M., Del Rio Hernandez, A. & Hytonen, V. P. Mechanical unfolding reveals stable 3-helix intermediates in talin and alpha-catenin. *PLoS Comput. Biol.* **14**, e1006126 (2018).
71. Bussi, G., Parrinello, M. & Donadio, D. Canonical sampling through velocity rescaling. *J. Chem. Phys.* **126**, 014101–014107 (2007).
72. Berendsen, H., Postma, J., Vangunsteren, W. F., Dinola, A. & Haak, J. R. Molecular-dynamics with couplingto an external bath. *J. Chem. Phys.* **81**, 3684–3690 (1984).
73. Gapsys, V., Michielssens, S., Seeliger, D. & de Groot, B. L. pmx: Automated protein structure and topology generation for alchemical perturbations. *J. Comput. Chem.* **36**, 348–354 (2015).
74. Lindorff-Larsen, K. *et al.* Improved side-chain torsion potentials for the Amber ff99SB protein force field. *Proteins* **78**, 1950–1958 (2010).
75. Parrinello, M. & Rahman, A. Polymorphic transitions in single crystals: A new molecular dynamics method. *J. Appl. Phys.* **52**, 7182–7190 (1981).
76. Gapsys, V., Seeliger, D. & de Groot, B. L. New soft-core potential function for molecular dynamics based alchemical free energy calculations. *J. Chem. Theory Comput.* **8**, 2373–2382 (2012).

Acknowledgements

This research was supported by the Academy of Finland (Grant 290506 to V.P.H. and grant 323021 to V.V.M.), a Biotechnology and Biological Sciences Research Council Grant BB/N007336/1 (B.T.G.) and a Human Frontier Science Program grant RGP00001/2016 (B.T.G.). L.A. received support from the graduate school of Tampere University and the Anu Kirra´s grant foundation. We acknowledge CSC for supercomputing resources and Biocenter Finland for infrastructure support. The authors acknowledge the Biocenter Finland (BF) and Tampere Imaging Facility (TIF) for the services. We thank Prof. Reinhard Fässler and Dr Carsten Grashoff (Max Planck Institute of Biochemistry) for help with TLN$^{1-/-}$TLN$^{2-/-}$ cells; Prof. Michael Sheetz (National University of Singapore) for providing the mouse wildtype talin expression construct. We thank Rolle Rahikainen, Anssi Nurminen and Sampo Kukkurainen (Tampere University) for their support and insights. Ulla Kiiskinen and Niklas Kähkönen (Tampere University) are acknowledged for technical support.

Author contributions

L.A. performed cell biology experiments supervised by P.T. and V.P.H. A.C. performed biophysical analyses under supervision of B.T.G. V.V.M. performed computational analyses under supervision of V.P.H. L.A. drafted the manuscript and all the authors contributed to manuscript revision. All authors accepted the final version of the manuscript.

Competing interests

The authors declare no competing interests.

Additional information

Supplementary information is available for this paper at https://doi.org/10.1038/s41598-020-77911-4.

Correspondence and requests for materials should be addressed to B.T.G., P.T. or V.P.H.

Reprints and permissions information is available at www.nature.com/reprints.

PUBLICATION
IV

Talin variant P229S compromises integrin activation and associates with multifaceted clinical symptoms

Azizi, L., Varela, L., Turkki, P., Mykuliak, V. V., Korpela, S., Ihalainen, T. O., Church, J., Hytönen, V. P. and Goult, B. T.

Hum Mol Genet. 2022 Dec 16;31(24):4159-4172
doi: 10.1093/hmg/ddac163

Human Molecular Genetics, 2022, Vol. 31, 24, 4159–4172
https://doi.org/10.1093/hmg/ddac163
Advance access publication date 21 July 2022
Original Article

Talin variant P229S compromises integrin activation and associates with multifaceted clinical symptoms

Latifeh Azizi[1,†], Lorena Varela[2,†], Paula Turkki[1,3,†], Vasyl V. Mykuliak[1], Sanna Korpela[1], Teemu O. Ihalainen[1], Joseph Church[4,*], Vesa P. Hytönen[1,3,*] and Benjamin T. Goult[2,*]

[1]Faculty of Medicine and Health Technology, Tampere University, Tampere, Finland
[2]School of Biosciences, University of Kent, Canterbury CT2 7NJ, UK
[3]Fimlab Laboratories, Tampere, Finland
[4]Clinical Immunology and Allergy, Children's Hospital Los Angeles, Los Angeles, CA, USA
*To whom correspondence should be addressed. Email: B.T.Goult@kent.ac.uk (Benjamin T. Goult), vesa.hytonen@tuni.fi (Vesa P. Hytönen), JChurch@chla.usc.edu (Joe Church)

†These authors contributed equally to this work.

Abstract

Adhesion of cells to the extracellular matrix (ECM) must be exquisitely coordinated to enable development and tissue homeostasis. Cell–ECM interactions are regulated by multiple signalling pathways that coordinate the activation state of the integrin family of ECM receptors. The protein talin is pivotal in this process, and talin's simultaneous interactions with the cytoplasmic tails of the integrins and the plasma membrane are essential to enable robust, dynamic control of integrin activation and cell–ECM adhesion. Here, we report the identification of a *de novo* heterozygous c.685C>T (p.Pro229Ser) variant in the *TLN1* gene from a patient with a complex phenotype. The mutation is located in the talin head region at the interface between the F2 and F3 domains. The characterization of this novel p.P229S talin variant reveals the disruption of adhesion dynamics that result from disturbance of the F2–F3 domain interface in the talin head. Using biophysical, computational and cell biological techniques, we find that the variant perturbs the synergy between the integrin-binding F3 and the membrane-binding F2 domains, compromising integrin activation, adhesion and cell migration. Whilst this remains a variant of uncertain significance, it is probable that the dysregulation of adhesion dynamics we observe in cells contributes to the multifaceted clinical symptoms of the patient and may provide insight into the multitude of cellular processes dependent on talin-mediated adhesion dynamics.

Introduction

Adhesion of cells to the extracellular matrix (ECM) is a critical part of the development of multicellular organisms and is tightly regulated by multiple signalling pathways. Integrins are the primary ECM receptors and in response to the correct signals support the adhesion of cells to the ECM, maintaining tissue integrity. Integrins are $\alpha\beta$-heterodimers and comprise a large extracellular domain that engages the ECM. Each subunit contains a single transmembrane helix and a short cytoplasmic tail that couples the integrin-ECM complexes to the cytoskeleton and signalling machinery. Integrins can exist in low or high affinity states for the ECM, and integrin activation is needed for the maturation of adhesion complexes. The process is exquisitely regulated to ensure correct functioning and to allow the modulation of adhesion strength, critical for processes that require dynamic assembly and disassembly of these attachments (1,2). Tight regulation of integrin activation is important in the regulation of cell cycle, cell migration and survival affecting vital processes such as differentiation, development and immunity.

Talin is a core component of ECM-adhesion complexes and is essential for the activation and regulation of integrin activity (3,4). It is a large ∼250 kDa protein consisting of a head domain that is responsible for integrin binding, an unstructured neck region, a large rod region comprised of 13 helical bundles, R1-R13, and a C-terminal dimerization domain (DD) (Fig. 1A) (5). The R13 and the dimerization domain mediate the primary actin binding and allow the tensile force-dependent stretching of talin (6). The talin rod domains R1-R13 serve as mechanical binary switches that interact with numerous proteins dictated by force-mediated conformational changes in the alpha-helical bundles exposing or disrupting different binding sites such as vinculin (7–9), DLC1 (10,11), CDK1 (12), RIAM (10) and KANK proteins (13,14), reviewed in (15).

The need for tightly regulated integrin adhesion is illustrated by the complex signalling that controls this process, both from inside the cell (inside-out signalling) or from outside (outside-in) (reviewed in 1). Integrin activation and clustering require tightly coordinated interactions between the talin head subdomains, the

Received: May 8, 2022. **Revised:** June 13, 2022. **Accepted:** July 12, 2022

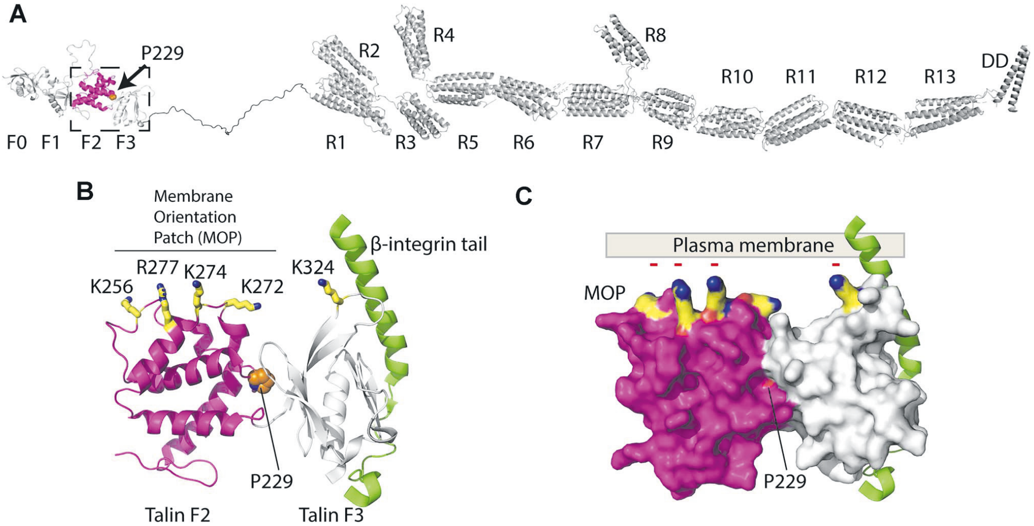

Figure 1. Talin–integrin interaction in the vicinity of the plasma membrane. (**A**) Structural model of talin1. Talin has 2541 amino acids organized into 18 domains. The location of proline 229 is highlighted between the F2 (magenta) and F3 (white) domains of the talin head. (**B**) Cartoon of the F2F3 domains bound to the β-integrin cytoplasmic domain (green). The location of proline 229 (orange) in the interface between F2 and F3 is shown. The basic residues in the membrane orientation patch (MOP) on F2 (yellow) are highlighted. (**C**) Surface representation of (B) showing the P229 is buried in the F2-F3 interface. The negatively charged plasma membrane is shown to illustrate the tripartite interaction between talin F2F3, the β-integrin and the plasma membrane that needs to occur to get robust integrin activation.

integrin tails and the plasma membrane, and the protein kindlin (16,17). Disruption of the interaction between talin and integrin and/or the plasma membrane prevents controlled integrin signalling and thereby cell adhesion. Therefore, while mutations in individual integrins may generate rather specific phenotypes centred on that specific integrins function (reviewed in 18), a mutation in talin that heavily influences talin-mediated integrin activation would be predicted to be lethal, unless leading to very subtle changes in integrin regulation (19). However, such a talin variant would impact on the function of all integrins that are regulated by talin.

The talin head domain comprises four subdomains, F0, F1, F2 and F3, which are all required for robust integrin activation (20). While F3 contains the phosphotyrosine-binding (PTB) domain that directly binds to the NPxY motif of most β-integrin cytosolic domains, the F0-F2 domains bind with anionic lipids such as phosphatidylinositol 4,5-bisphosphate (PIP2) in the vicinity of the integrin (21). Mutations in the F0 and F1 domains that disrupt the interaction with Rap1 perturb the integrin activation process (22–24). Similarly, the extended loop within the F1 subdomain of talin head also contributes to integrin activation via direct interactions with integrin (25,26) and the membrane (27). In all the talin head structures resolved to date the F0F1 and F2F3 domains are fixed double domain modules where the orientation between the domains is mediated by extensive interactions. The fixed arrangement of the F2F3 domains has been reported to be important for activation as the F2 domain contains a basic surface, the membrane orientation patch (MOP), that binds tightly to the plasma membrane (4). Upon binding to the integrin tail via the F3 domain, the F2F3 module rotates to engage the MOP with the plasma membrane and this rotation applies torque on the integrin tail to stabilize the active conformation (Fig. 1). Mutations in the MOP region prevent integrin activation (4).

We previously studied the effects of cancer-associated point mutations within talin as reported in the COSMIC database and found talin variants that affect cell morphology, cell migration and cell proliferation (28). Despite the large size of talin and the presence of numerous interaction partners, a single point mutation targeting a critical position can have drastic and even crippling effects on talin functionality and cell adhesion. An example of this is seen with point mutations in the dimerization domain that disrupt dimerization and lead to a loss of cell spreading (28). Similarly, a genetic screen in Drosophila identified a mutant G334E (equivalent to G331E in human talin1) that causes severe morphogenetic defects (29). G334E is located at the interface between the F2 and F3 talin head domains, located on the F3 face. Similarly, loss of talin autoinhibition in flies with a single point mutant, E1777A (30) leads to lethal morphogenetic defects.

These findings suggest that whilst mutations appearing somatically that dysregulate adhesion dynamics might be advantageous for cancer cells, germline mutations that disrupt talin function are likely embryonic lethal (talin1 deficiency is lethal in mice (31)). This is supported by the fact that until recently talin has not had any gene-disease associations, although reports of disease-causing mutation in the *TLN1* gene have emerged, which challenge this picture, including a number of cardiovascular disease-associated mutations in the *TLN1* gene; spontaneous coronary artery dissection (SCAD) (32) and thoracic aortic aneurysm (33). Further, a heterozygous *TLN2* mutation, S339L in F3, was also reported as the cause of nonsyndromic Camptodactyly, which also presented with mild cardiac symptoms, including sinus arrhythmia and sinus bradycardia (34).

We recently identified a patient with a very rare and unusual, complex phenotype. Having excluded all established disease-causing genes involvement in the probands complex checklist of symptoms, the *de novo* TLN1 variant presented in this work was then characterized. Here, we report this novel p.P229S variant and link the human genetics to the biophysical and cell biological consequences to demonstrate the disruption of adhesion dynamics that result from disturbance of the F2-F3 domain interface in the talin head.

Results

Case summary—identification of a *de novo* heterozygous variant in the *TLN1* gene

A 20-year-old man of Mexican ancestry was first evaluated at six years of age for thrombocytopenia, T lymphopenia, and low IgG levels. He was born at 35 weeks gestational age and a birth weight of 2100 g. He spent his first month in neonatal intensive care for respiratory distress and persistent thrombocytopenia. Although his platelet count remained approximately 20 000/mcL throughout his course, he never had a serious bleeding episode. At approximately 10 years of age to the present, he continued to experience intermittent sinusitis, otitis media and bronchitis. Treatment with oral antibiotics for each of these multiple episodes resulted in clearance of each clinical infection. He never experienced infections characteristic of T-cell or neutrophil dysfunction.

At 18 years of age, he developed intermittent pain that shifted focus regularly. He had abdominal pain at times diagnosed as small intestinal bacterial overgrowth, headaches often treated as migraines, and joint pain with limited signs of active arthritis. Multiple imaging and laboratory studies failed to identify a cause of these complaints, and an empiric trial of hydroxychloroquine for a possible autoimmune process did not alter his symptoms.

At 19 years of age, he complained of keloid-like skin changes at the sites of very mild linear skin abrasions. The family history was notable for hidradenitis suppurativa in his father and sister who were shown to share a pathogenic variant in *NCSTN* with the patient. Additional problems have included bilateral congenital cataracts, intermittent eczema and intermittent haematuria, the latter judged by Haematology consultation as not related to his chronic thrombocytopenia.

Upon multiple physical examinations, the patient typically appeared alert, cooperative and well-oriented, but generally complaining of moderate to severe headache, abdominal or joint pain. His vital signs were unremarkable. There was rarely evidence of active respiratory tract infection. There was no hepatosplenomegaly or lymphadenopathy. His skin examination revealed mild eczema and multiple linear, narrows, keloid-like scars on his arms and feet.

Abnormal laboratory findings (performed at the Children's Hospital Los Angeles Clinical Laboratory) over the patient's history have revealed the following:

1. Thrombocytopenia: generally <20 000/mcL but without significant bleeding
2. Lymphopenia: absolute lymphocyte counts <1000/mcL and low absolute T-cells
3. Recent B-cell subset analysis revealed 96% naïve and 4% switched memory B-cells
4. Initial serum immunoglobulin levels at six years of age included: IgG 273, IgA 130, IgM 36.

Because of poor antibody responses to pneumococcal vaccine, he was started on immunoglobulin replacement therapy, which he has continued to the present.

We acknowledge that the case study presented here may appear somewhat confusing, but this is because we have intentionally provided all the symptoms besides the primarily haematological/immunological presentation. We also describe the lines of investigation we have undertaken during our long-standing oversight of the patients' treatment in our efforts to determine the basis of this disease of unknown cause. The lack of a simple narrative in this section partially reflects the diverse ailments of the patient, and that we have not yet identified a satisfactory explanation to describe the cause of this complex condition or the diverse presentation.

When he was 16 years of age whole exome sequencing was performed at the Children's Hospital of Los Angeles Centre for Personalized Medicine Clinical Genomics Laboratory, which is certified under the Clinical Laboratory Improvement Amendments as qualified to perform high complexity clinical laboratory testing. It did not reveal a likely genetic aetiology for his immunologic changes. Most recently, re-analysis of his exome revealed a *de novo*, heterozygous variant in *TLN1* (c.685C > T, p.229Pro > Ser) that was not seen in the parents' exomes thus confirming the *de novo* nature of the variant and leading to *in vitro* assessment of the variant's function.

Biophysical characterization of the P229S and P229L mutations on the structure of F2F3

P229 is located within the F2 domain of the talin head at the interface between F2 and F3 (Fig. 1). The F2F3 domains mediate the interaction with the membrane proximal region of the β-integrin cytoplasmic tail and with the plasma membrane (3,4). Our earlier analysis of the COSMIC database (28) identified a P229L mutation at this site that has the potential to be deleterious. To understand the consequences of these mutations, we set out to compare the biochemical characteristics of wild-type, P229S and P229L talin and their biological function in cells.

To characterize the effect of the P229S and P229L mutations, we generated the following F2 and F2F3 constructs; F2-WT, F2-P229S and F2-P229L, and F2F3-WT, F2F3-P229S and F2F3-P229L. All these recombinant proteins expressed and purified well without signs of proteolysis suggesting that the mutations do not perturb the folding of the domains. This was in stark contrast to the G331E mutation located near to residue 229 where the F2F3-G331E protein was far more proteolytically sensitive (29). We next performed circular dichroism (CD) to determine the secondary structure composition and thermal stability of each protein. Far-UV spectra were collected at 20°C and showed similar alpha helical composition for F2-WT, F2-P229S and F2-P229L (Fig. 2E). Similarly, the F2F3-WT, F2F3-P229S and F2F3-P229L all showed similar secondary structure composition of beta strand and alpha helix (Fig. 2G). These results show that neither the P- > S nor the P- > L mutation cause significant change to the overall secondary structure of the domains. We next measured the thermal stability of each F2 (Fig. 2F) and F2F3 (Fig. 2H) variant by recording the ellipticity at 222 nm from 20 to 80°C. The unfolding profile of all the constructs was similar showing cooperative unfolding, although a small but significant decrease in the melting temperature (Tm) of the mutated proteins was observed, which was more pronounced in the case of the F2F3 domain (P229S, $\Delta Tm = -4.4°C$) than in the F2 domain (P229S, $\Delta Tm = -3.0°C$). This suggests that the P229 mutations cause a subtle but significant effect on the overall protein stability.

To gain insights into the perturbations caused by each mutation on the tertiary structure of the F2 and F2F3 domains, we carried out NMR collecting ^{15}N SOFAST-HMQC spectra of F2-WT, F2-P229S and F2-P229L (Fig. 2A) and F2F3-WT, F2F3-P229S and F2F3-P229L (Fig. 2C). The overall protein folding is very similar in all variants confirming that the folding of both the F2 and the F3 domains is maintained. However, significant shifts in a number of peaks are observed indicative of a local alteration in structure. Using chemical shift mapping, the peaks shifted by the mutation were mapped onto the structures of the F2 and F2F3 domains (taken from pdb 3IVF (35)). Only residues in close proximity to the mutation showed significant chemical shift changes (Fig. 2B, D). In the case of the F2F3 double domain, the mutations in F2 caused significant changes in the proximal residues on both sides of the F2 and F3 interface. This biophysical analysis confirms that both P229S and P229L mutations cause a subtle but specific effect on the structure of the F2F3 double domain affecting residues on either side of the F2F3 interface, and this perturbation leads to a decrease in the thermal stability of F2F3.

Molecular dynamics simulations suggest that P229S reduces F2F3 interaction affinity

To investigate how mutations affect the F2F3 domain interface, we employed non-equilibrium alchemical MD simulations. The method allows to quantitatively estimate free energy changes in protein thermostability or protein–protein binding upon mutation, using extensive atomistic simulations. The calculations involve relaxation of both WT and mutant forms of a protein, followed by numerous alchemical (non-physical) simulations for morphing of the system from WT to mutant forms and opposite, to sufficiently sample multiple conformational states for reliable free energy estimation (36). The whole procedure was performed for both F2 and F2F3 double domains to predict the change in F2–F3 interaction energy. We did not observe major changes in protein conformation or obvious disturbances in F2–F3 interface. However, mutation P229S reduced the F2F3 interaction energy by 5.6 ± 2.2 kJ/mol, suggesting a modest but consistent destabilization of the interface. Such effect was not detectable in the case of P229L (0.1 ± 1.2 kJ/mol).

Truncated versions of talin can be used to study adhesion maturation in a simplified setting

To understand the phenotypic effects of the talin1 variants at the cellular level, we used talin1 and talin2 knockout cells (16). Talin knockout cells are unable to adhere on substrate, show low levels of FAK phosphorylation and are unable to activate integrins (16), but these defects can be rescued by transfection with full-length WT talin. In order to study different aspects of talin function in these cells, we also used three previously characterized versions of talin: full-length talin, talin head and mini-talin (Fig. 3A) (37). To learn about talin-integrin interface, we used the talin head construct, which contains the integrin-binding site in F3, but due to lack of the C-terminal rod region, it cannot form the link to the actin cytoskeleton (Fig. 3A and B). To get information about the early talin-mediated integrin activation events, we used mini-talin (Head-R13-DD), which contains the integrin-binding site in F3 connected to the actin binding region R13-DD. Therefore, mini-talin can facilitate force transmission between the cell cytoskeleton and the integrin-ECM complexes, leading to integrin activation. However, mini-talin lacks the talin rod domains R1-R12 and the diverse signalling molecules that they recruit as a function of mechanical load, leading to a simplified model for studying talin head–integrin interaction in detail.

Talin knockout cells re-transfected with full-length WT talin polarize and spread to an average area of 1250 μm^2 (Fig. 3C). Full-length expressing cells also showed high auto-phosphorylation of FAK and clustering of activated integrin within the talin-rich adhesions (Fig. 3D and E). Mini-talin expressing cells showed isotropic spreading with average area of 750 μm^2 (Fig. 3C), decreased FAK phosphorylation and integrin

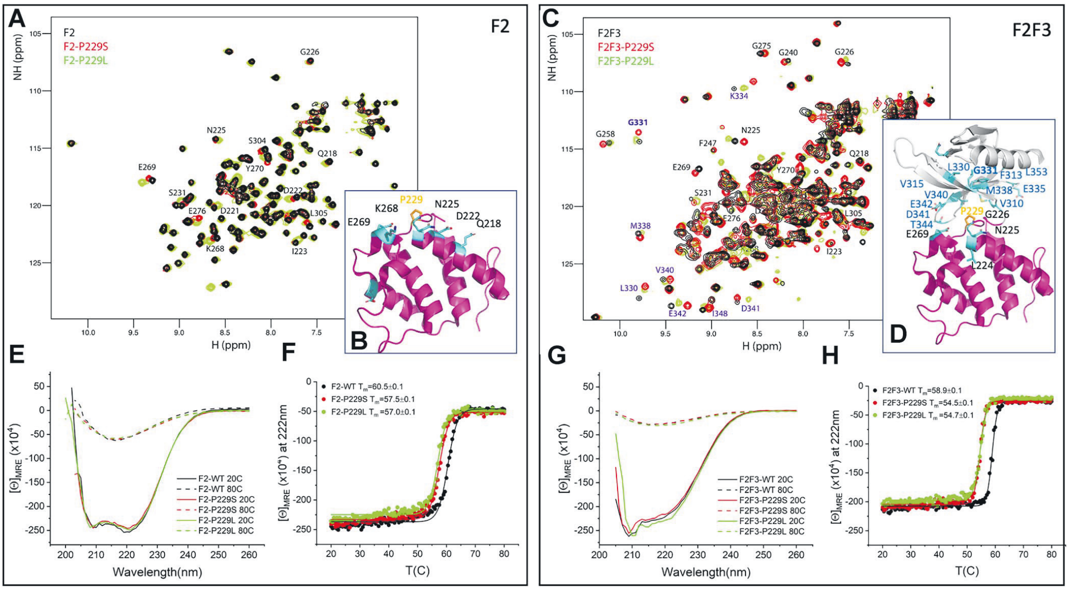

Figure 2. Biochemical characterization of the talin1 F2 and F2F3 domains (black) and the P229S (red) and P229L (green) variants. (**A**, **C**) 2D ^{15}N-SOFAST HMQC spectra recorded at 25°C of F2 (A) and the F2F3 double domain (C) showing part of the backbone assignment of the WT. (**B**, **D**) Chemical shift mapping of residues perturbed by the mutations (cyan) on the crystal structure of the F2 domain (B) (magenta) and the F2F3 domains (D) (magenta and grey, respectively). Residue P229 is highlighted in orange. (**E**, **G**) CD far UV spectra at 20 and 80°C of the F2 domain (E) and the F2F3 domain (G) showing no effect of the mutations in the overall secondary structure. (**F**, **H**) Melting curves recorded monitoring the CD signal at 222 nm of the F2 (F) and F2F3 (H) proteins. The calculated melting temperatures (°C) for each protein are shown in the legend. The CD signal is represented as molar ellipticity, [Θ] in deg·dmol^{-1}.cm^2.

activation (Fig. 3D and E), as expected when the rod bundles and their interactions that allow the full maturation of focal complexes are omitted. The talin head alone lacked the C-terminal actin binding site and therefore lacks the force-transmission ability of talin, and as a result, the cell area decreased to an average of 500 μm^2 and FAK signalling and integrin activity were almost lost (Fig. 3D and E).

P229S variant causes significant defects in cell migration

Having characterized the three talin constructs, we next introduced the P229S and P229L point mutations into each of them. Western blot analysis confirmed that the cells produced similar amount of each of these proteins at the correct molecular weights (Supplementary Material, Fig. S1A).

Talin-knockout cells transfected with full-length P229S have a slightly larger surface contact area (*P*-value 0.045) and have higher circularity (*P*-value 0.019) in comparison with cells transfected with full-length WT (Fig. 4A–C). P229L caused less severe changes to these characteristics (Fig. 4A–C). Next, the influence of P229S on the cells ability to polarize and accommodate a restricted footprint was quantified using a single-cell approach, where cells are grown on micro-engineered cell adhesive islands with an 'ice-cream' shape of 400 μm^2 surface area (Supplementary Material, Fig. S2A). This analysis did not show statistically significant differences between WT and P229S, but a slight decrease in cells ability to cover the pattern was noticed with P229S-bearing cells (Supplementary Material, Fig. S2A).

Analysis of the random migration of individual cells on either fibronectin (Fig. 4D) or vitronectin (Fig. 4E) revealed that cells expressing the P229S variant showed a significant decrease in migration rate compared to WT in full serum media. In addition, the cell migration speed of both P229S and P229L transfected cells on vitronectin in serum-free medium was decreased in comparison with WT (Supplementary Material, Fig. S2B). Interestingly, P229L did not significantly affect the cell migration rate on fibronectin when compared to WT (Fig. 4D). Next, to understand the effect on collected cell migration, we studied the cells with a wound closure assay. The delay in the closure of the scratch with both mutants was already evident within 12 h. With P229S, the effect was more pronounced as, after 12 h, the cells had travelled only three-quarters of the distance compared to the WT (Fig. 4F and G). After 20 h, WT and P229S transfected cells, had filled ∼96 and ∼61%, respectively, of the scratch length. Altogether, these results showed that the P229S variant has a clear negative effect on the cell migratory capacity.

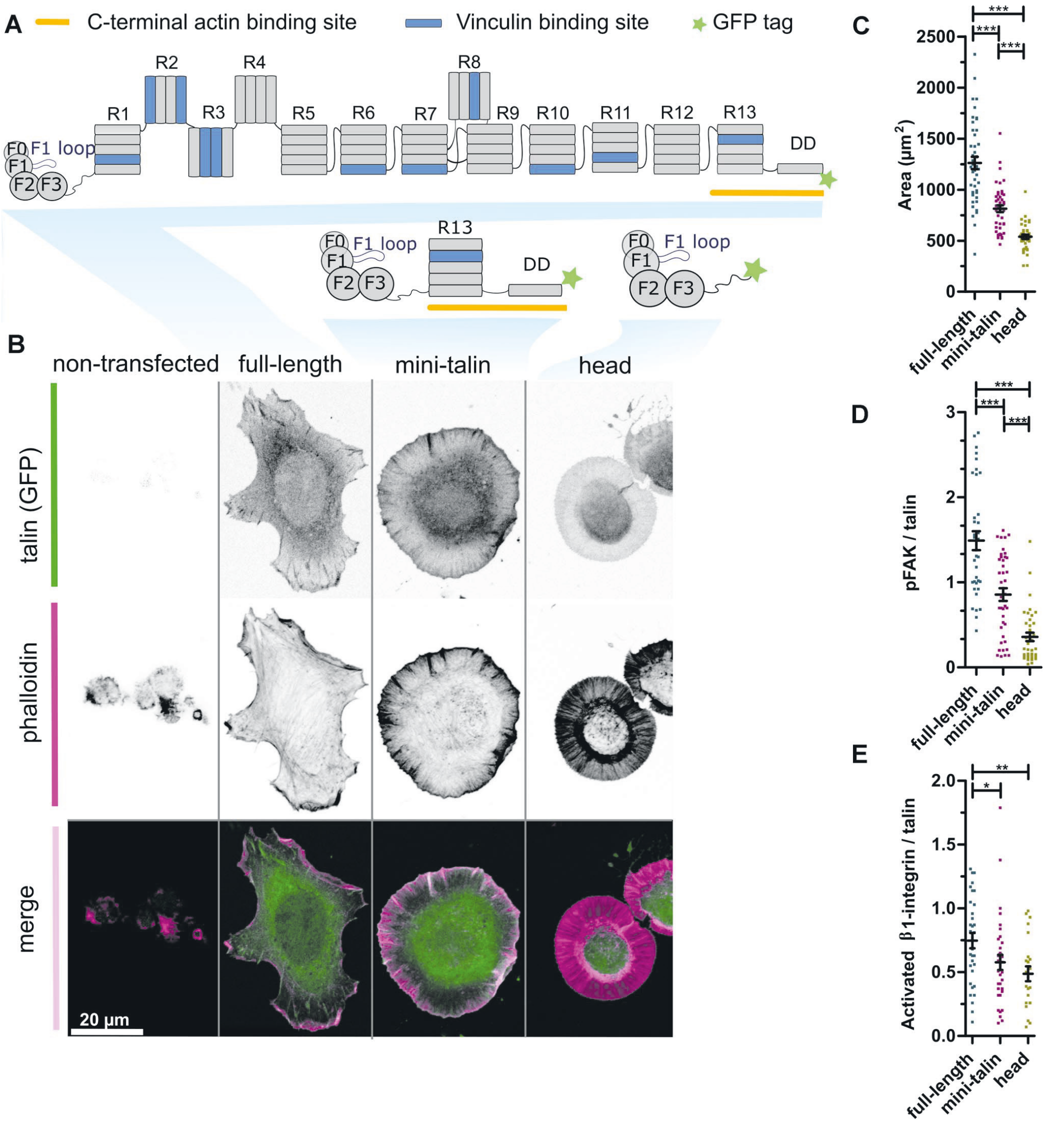

Figure 3. Mini-talin enables cell spreading and integrin-mediated cell signalling. (**A**) Schematic illustration of the full-length talin and the truncated talin proteins, mini-talin and talin head. (**B**) Representative images of TLN1$^{-/-}$TLN2$^{-/-}$ cells expressing full-length talin, mini-talin and talin head. Phalloidin staining is used to visualize the actin cytoskeleton. Non-transfected cell is shown as control. (**C**) Analysis of the cell area for the cells expressing various talin versions, $n \sim 40$ cells pooled from three independent experiments. (**D**, **E**) Fluorescence intensity analysis for adhesion localized pTyr397 FAK (D) and activated $\beta1$ integrin relative to talin intensity (E). $n \sim 35$ cells pooled from three independent experiments. The statistical analysis in (C), (D) and (E) was done by *t*-test Mann–Whitney test; $^{*}P < 0.05$, $^{**}P < 0.01$, $^{***}P < 0.001$. Data represent the mean values with SEM.

P229S leads to disrupted adhesion signalling

Integrin-mediated adhesions start as nascent adhesions at the cell leading edge, where several crucial signalling molecules, including FAK and paxillin, are recruited to the adhesions and subsequently phosphorylated (38). Some nascent adhesions are short-lived (39) but with correct signals some grow and mature into larger focal complexes. As the adhesion mature, and more paxillin and FAK get recruited and phosphorylated, monitoring phosphorylation of paxillin and FAK allows for quantifying adhesion maturation. Similarly, the maturation and turnover rate of the adhesions lead to changes in cell size,

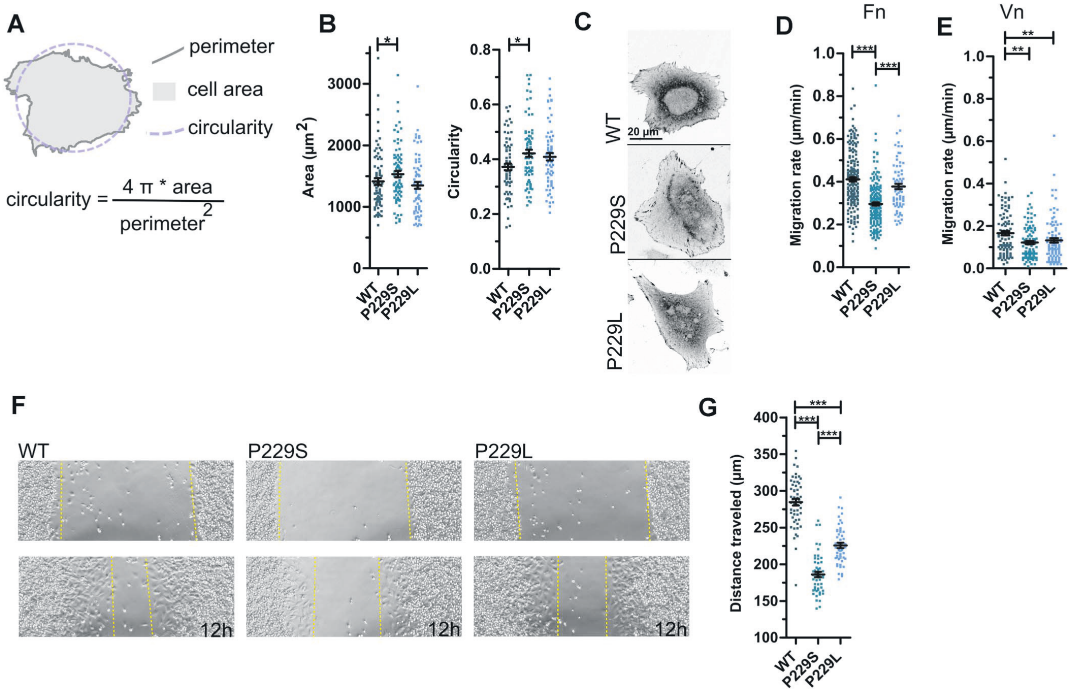

Figure 4. Talin variants P229S and P229L compromise cell spreading, migration and wound closure. (**A**) Schematic illustration of the morphological parameters of a cell; the area covered by the cell is known as cell 'area'; the distance around the cell is called 'perimeter' and the normalized ratio of cell area and the perimeter is called 'circularity'. (**B**) Cell area and circularity measured for the cells expressing full-length versions of talin WT, P229S and P229L. *n* ∼ 70 cells pooled from three independent experiments for each set of analysis. (**C**) Representative images of cells expressing full-length talin proteins (WT, P229S, P229L). (**D**) Random migration analysis of the cells transfected with full-length talin WT, P229S and P229L on fibronectin (10 μg/ml) (Fn) coated surface. *n* ∼ 95 cells pooled from three independent experiments. Experiment performed in 10% FBS medium. (**E**) Random migration analysis of the cells transfected with full-length talin WT, P229S and P229L on vitronectin (10 μg/ml) (Vn) coated surface. *n* ∼ 90 cells pooled from three independent experiments. Experiment performed in 10% FBS medium. (**F**) Representative images of the wound closure assay for the cells transfected with full-length talin WT, P229S and P229L in 0 h (upper) and after 12 h (lower). (**G**) The distance travelled (μm) by the cells to close the wound, was calculated by analyzing the scratched area from 0 h and after 12 h. *n* ∼ 25 scratches from three independent experiments. The statistical analysis in (B), (D), (E) and (G) was done using *t*-test Mann–Whitney test; $^{*}P < 0.05$, $^{**}P < 0.01$, $^{***}P < 0.001$. Data represent the mean values with SEM.

polarization and migration ability that can also be measured as read-outs of these signalling events. Therefore, to understand the defects in cell migration and adhesion signalling caused by the variant P229S, we next assessed the maturation of the adhesion complex by measuring; (i) the auto-phosphorylation status of FAK, (ii) the degree of integrin activation within the adhesions, (iii) paxillin localization to adhesions (iv) phosphorylation status of paxillin at tyrosine 31 (pY31) and (v) the average size of adhesion complexes at the cell boundary, all established readouts of adhesion signalling.

In full-length versions of talin WT and P229S variant, we could not see any differences in either pFAK or β1-integrin status within the adhesions (Fig. 5A and D; Supplementary Material, Fig. S1C). Furthermore, no significant difference in the level of vinculin within the adhesion sites was observed between the full-length talin WT and P229S (Supplementary Material, Fig. S1D). However, the mini-talin P229S variant led to a decrease in both pFAK and activated β1-integrin levels within adhesions (Fig. 5B; Supplementary Material, Fig. S1C), suggesting that the complexity of the rod-mediated interactions and signalling might mask the effects of the mutation in the full-length version in cultured cells. With the cells expressing talin head constructs, we could not observe any effects of the mutations, most likely because the overall integrin activation level was already extremely low due to the lack of force-transmitting connection to the actin cytoskeleton via R13-DD (Fig. 5C and D). We next assessed the localization and phosphorylation status of paxillin at tyrosine 31 (pY31) in adhesion sites. We did not see any effect on the total levels of paxillin or phosphorylated paxillin in cells transfected with the full-length constructs (Supplementary Material, Fig. S1E) but in the case of mini-talin, we saw a significant decrease in both paxillin and phospho-paxillin levels when comparing cells expressing P229S to WT (Fig. 5E and F). Together, these results highlight the subtle but consistent disturbance on adhesion signalling as a result of the P229S mutation.

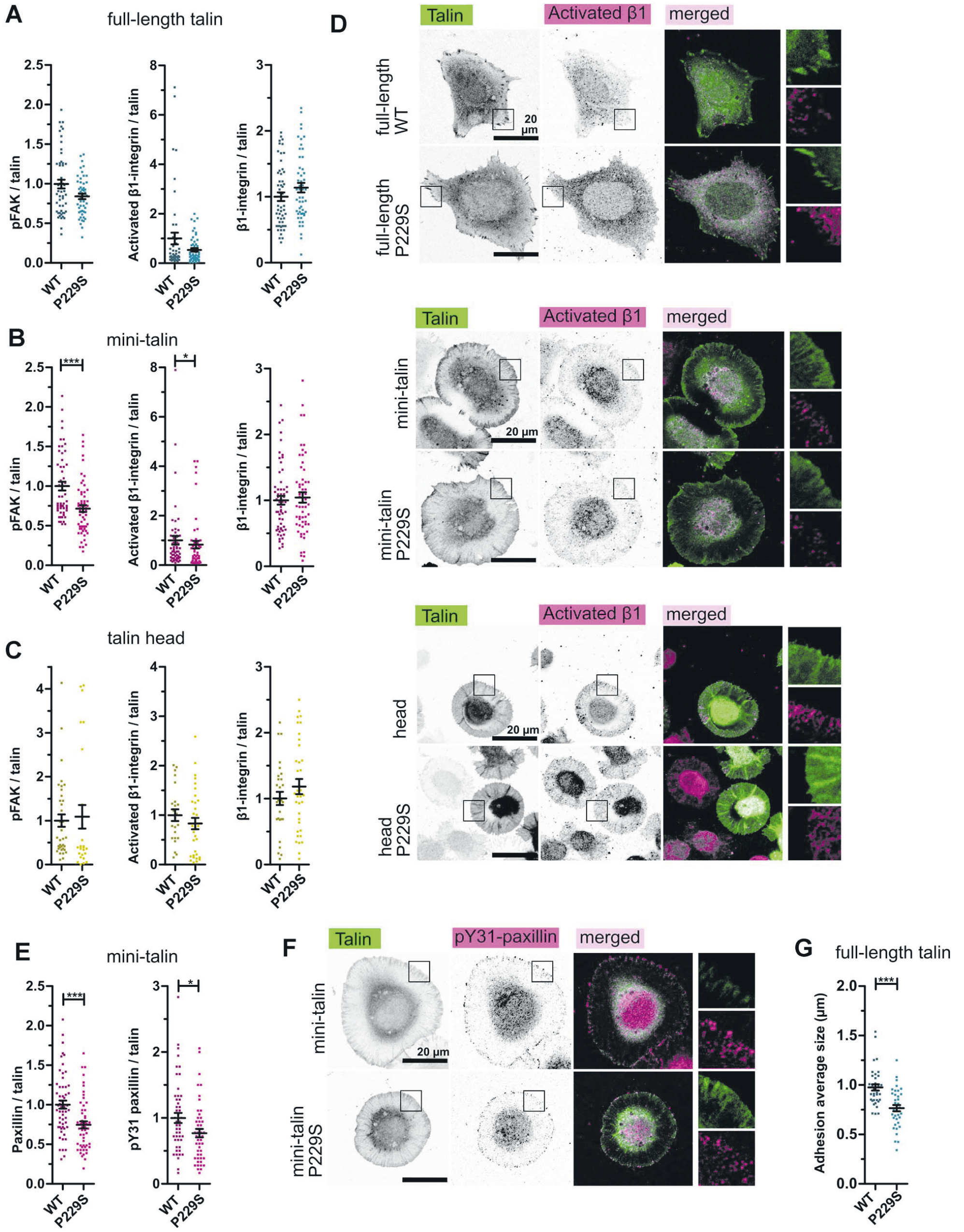

Figure 5. P229S influences integrin activation and adhesion signalling. (**A**) pTyr397 FAK/talin, activated β1-integrin/talin and total β1-integrin/talin intensity ratios for the cells transfected with full-length talin WT and P229S. $n \sim 50$ cells pooled from three independent experiments. (**B**) pTyr397 FAK/talin, activated β1-integrin/talin and total β1-integrin/talin intensities ratios for the cells transfected with mini-talin, WT and P229S. $n \sim 50$ cells pooled from three independent experiments. (**C**) pTyr397 FAK/talin, activated β1-integrin/talin and total β1-integrin/talin intensities ratios for the cells transfected with talin head, WT and P229S. $n \sim 30$ cells pooled from three independent experiments. (**D**) Representative images of cells expressing full-length/truncated talin proteins. Activated β1-integrin is shown in the staining. (**E**) Paxillin/talin and pY31 paxillin/talin intensities of mini-talin data. $n \sim 50$ cells pooled from three independent experiments. (**F**) Representative images of pY31 paxillin/talin intensity of cells expressing mini-talin. (**G**) Adhesion average size quantification (μm) from the periphery area of the cells transfected with full-length talin WT and P229S. The data in (A), (B), (C), (E) and (G) are normalized to the WT in each set. The statistical analysis in (A), (B), (C), (E) and (G) was done by t-test Mann–Whitney test; $^{*}P < 0.05$, $^{**}P < 0.01$, $^{***}P < 0.001$. Data represent the mean values with SEM.

Adhesion signalling further regulates the adhesion maturation process that goes hand in hand with the growth of the adhesion complex (38). To define the influence of mutations on adhesion maturation, we quantified the adhesion number and size around the cell periphery using the paxillin staining from cells expressing the full-length talin constructs. There was a significant decrease in the average size of adhesions in cells expressing P229S variant (P229S: 0.77 μm, WT: 0.98 μm; $P < 0.0001$; Fig. 5G) while the total number of adhesions per cell was slightly higher in the P229S transfected cells in comparison with the WT transfected cells (P229S: 76, WT: 64; $P = 0.13$; Supplementary Material, Fig. S2C). The total adhesion area remained the same for both constructs (Supplementary Material, Fig. S2C) suggesting that although the P229S-expressing cells' adhesions might be more numerous, they do not reach the size observed in the WT-transfected cells. These results show that the disrupted signalling leads to decrease in adhesion size possibly indicating interference in the adhesion maturation process.

Discussion

Integrin activation and its connection to actin cytoskeleton is vital for cell-ECM-dependent physiological functions during development, tissue morphogenesis, tissue repair, cancer and immune response (40,41). To initiate the communication between cell interior and ECM, talin is recruited to the plasma membrane, and the head region of talin engaging the integrin leads to integrin activation. Specifically, this interaction is due to the F3 domain binding to the β-integrin cytoplasmic domain, and positively charged residues in F2 and F3 domains, which engage the plasma membrane and directly contribute to integrin activation (4,35,42,43). Here, we report the characterization of a novel talin variant, P229S, which was identified in the tri-exome sequencing of a patient with a complex medical condition. We showed that proline 229 is critical to the intimate juxtaposition of F2F3, and modification to serine (or leucine) disrupts this interface severing the tight linkage between the two domains, resulting in a subtle but specific decrease in protein stability, which manifests as defects in cell movement, integrin activation and adhesion signalling.

Coordination of talin-integrin-membrane interactions is critical for robust adhesion signalling

The F3 engages the integrin cytoplasmic tail (44), but the F3 domain alone is unable to sustain integrin activation and the entire talin head region, spanning F0-F3, is required for maximal activation (20,26). However, the F2F3 domains alone can partially activate integrins, and the role of a cluster of residues on the F2 domain, comprising K256, K272, K274 and R277, dubbed the membrane orientation patch (MOP) are required to bind to the plasma membrane to sustain robust integrin activation (Fig. 6).

Analysis of the crystal structure of talin bound to integrin revealed that to optimally engage the integrin tail and the plasma membrane simultaneously, a 20° rotation of the F2F3-integrin complex was required (4) leading to a model of integrin activation mediated by the membrane-based reorientation of the integrin tail as a result of F2F3 binding (Fig. 6B). This model (4,45) implicates the role of plasma membrane in the activation process and proposes that the torque generated on the beta tail as the talin head rotates to fully engage the membrane helps to activate the integrin, but also to stabilize the active conformation. This model requires F2F3 to function as a single module such that the rotation of F2 leads to rotation of F3. We hypothesize that P229S mutation reported here perturbs the coupling between F2 and F3 domains, with the consequence that the rotation of F2 to engage the membrane no longer applies enough torque on the F3-integrin to facilitate activation (Fig. 6C). It is the decoupling of membrane binding and integrin binding that we believe is the basis for why the P229S variant disrupts the regulation of integrin activation.

Mini-talin: a potential tool to detect minor changes in talin head functions

The talin head by itself can bind to and partially activate integrins but talin knockout cells rescued with the talin head alone do not spread well and it is not possible to visualize the adhesive structures that form (Fig. 3A). Measuring integrin activation metrics alone here would not provide the sensitivity required to detect nuanced changes in this process. On the other hand, full-length talin is rich in interactions and contributes to numerous cellular signalling pathways, and therefore modest effects on adhesion dynamics or integrin activation status can be difficult to detect in the context of such complex protein assemblies. This is exemplified in the current study, where, despite the full-length talin P229S construct showing a clear decrease in adhesion size indicative of defects in adhesion maturation and cell migration capacity, it was challenging to pin-point the exact signalling events that were affected. In contrast, the mini-talin P229S construct displayed stalled adhesion dynamics when compared to the wild type, enabling us to visualize the impact of P229S on the adhesion maturation process. We therefore propose that mini-talin represents a suitable molecular tool for the purpose of studying talin variants that impact integrin activation and the dynamic nascent adhesion maturation process. This engineered talin protein couples the talin head to the C-terminal actin binding and dimerization domain in R13-DD (Fig. 3A) and therefore connects the integrin-talin head complexes to the actin cytoskeleton. This construct omits the 12 talin rod domains, R1-R12, whose switch-like behaviours, contribute to the regulation of adhesion strength and signalling (15). In contrast with the head alone, which enables some cell attachment

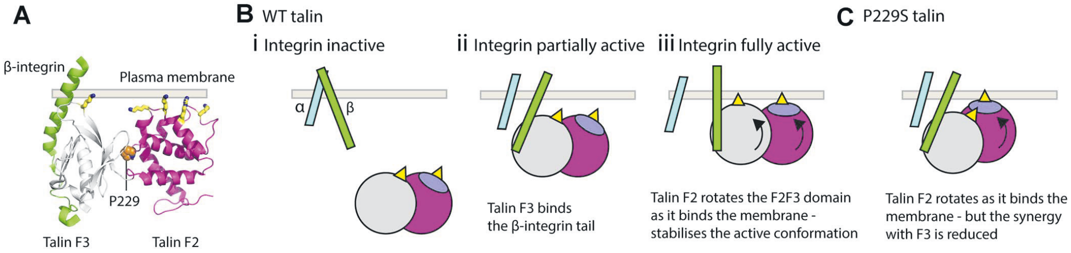

Figure 6. Proposed model for P229 function in the synergistic coordination of the talin-integrin-plasma membrane interactions. (**A**) Cartoon representation of the F2 (magenta) and F3 (grey) bound to the β-integrin tail (green). Proline 229 is shown in orange at the interface between the two domains. The talin F2 and F3 domains work together to induce integrin activation by binding to the β-integrin tail and the plasma membrane simultaneously, the interaction with the membrane orientation patch (MOP; yellow) on F2 is essential for robust integrin activation. (**B**) Model of the integrin activation process mediated via the F2F3 domains (based on the model proposed by (4)). (i) Integrins exist in an inactive state in the absence of talin binding. (ii, iii) The F2F3 double domain module inextricably links integrin binding to membrane binding. To simultaneously optimize the interactions of both F3-integrin and F2-membrane, the F2F3 module needs to undergo a 20° rotation and this torque (iii) is thought to help lock integrin in the active conformation. (**C**) The P229S mutation disrupts the tight apposition of F2 and F3 and uncouples the tight interplay between integrin and membrane binding. With the two domains able to move independently, the optimization of the F2-membrane interface no longer exerts torque onto the F3–integrin interaction perturbing the tight regulation of the talin-mediated integrin dynamics.

without proper integrin activation, mini-talin enables extensive isotropic cell spreading and leads to integrin activation and nascent adhesion formation, albeit to a lesser extent compared to full-length talin. Therefore, this construct supports the mechanocoupling to actomyosin and enables adhesive structures to be observed meaning that the talin head functions can be explored with a greater precision than using the head alone. This construct (submitted to Addgene) will facilitate the study of talin head interactions in a simplified system in a more quantitative manner than currently available integrin activation assays. It should also enable a more detailed examination of the integrin activation process than the current approaches, and with less multifactorial contributions from the mechanical signalling of the talin rod.

A subtle talin disruption would manifest in a wide spectrum of conditions

There are many pathogenic integrin variants known to cause specific conditions in processes dependent on the affected integrin. For instance, leukocyte adhesion deficiency (LAD) is caused by a range of mutations in the $\beta2$ integrin, and Glanzmann's thrombasthenia, is caused by numerous mutations in αIIb or $\beta3$ integrin (18). However, because talin is an activator and adapter protein for multiple integrins (46), it is expected that a talin variant causing a defect in integrin activation would impact all integrins and so, likely be embryonically lethal. However, the loss of synergy between the F2F3 domains as a result of the P229S mutation is subtle, resulting in a small shift in the biophysical properties of the protein, which manifest as a minor disruption of cellular processes. However, at the organismal level, because the P229S variant maintains the basic talin functions, but subtly influences the fine-tuned balance of integrin activation, we anticipate it will impact on all integrin processes that are talin-dependent. Our data show that the P229S mutation impacts on both $\beta1$ and $\beta3$ integrin-dependent processes, which suggests that other integrins will be affected as well. Many of the symptoms experienced by the proband involve processes that require talin-dependent integrins. For example, thrombocytopenia has been found to be associated with integrin $\beta3$ mutations (47,48) and $\beta3$ integrins play a critical role in platelet aggregation (49). Furthermore, integrins are essential to maintain normal myeloid and B lymphoid differentiation (50) and $\beta2$-integrins are essential for leukocyte trafficking, immune suppression and immune deficiency disease (51), which could explain the multiple immune system-related defects. Further work would be needed to establish a causal link between the variant identified here and the phenotype of the patient.

It is important to stress that our biophysical, biochemical and cell biology experiments show that the P229S variant affects the function of the talin protein in cells, but we do not have evidence yet that the P229S talin variant is the cause of the multitude of delocalized symptoms affecting the patient. Therefore, we would like to emphasize that this talin variant P229S should be considered a variant of uncertain significance (VUS) until additional cases with similar variants and phenotypes are identified.

In conclusion, we show that talin variant P229S results in subtle perturbation of the talin head structure, that influences the fine control of integrin dynamics leading to disturbance in adhesion maturation and compromised cell migration. As talin coordinates many integrin subtypes, we propose that this modest dysregulation would likely impact many cellular processes leading to numerous symptoms. This study emphasizes the central role of talin as integrin activator and as a link between cytoskeleton and extracellular environment.

Materials and Methods

Protein expression and purification

Talin1 F2 and F2F3 constructs in their WT version and with sequence variations P229S and P229L were synthesized into a pET151 plasmid (GeneArt). All constructs were expressed in BL21(DE3) *E. coli* cells and grown at 37°C in LB media or 2 M9 minimal media supplemented with ^{15}N-labelled ammonium chloride for NMR. Expression was induced with 1 mM IPTG when OD_{600} reached 0.7 and cells were then incubated at 20°C overnight. Following harvesting, the cell pellets were resuspended in 50 mM imidazole, 500 mM NaCl, and 20 mM Tris–HCl, pH 8 and lyzed using sonication. The proteins were purified by nickel affinity chromatography using a HisTrap HP column (Cytiva) and the his-tag cleaved using TEV protease. The cleaved His-tag and TEV protease were removed using a HiTrap SP HP cation exchange column (Cytiva) (52). All bacterial expression constructs have been deposited in Addgene at http://www.addgene.org/ben_goult.

CD experiments

Protein samples at a concentration of 50 μM were placed in a quartz cuvette and far-UV spectra were collected between 260 and 200 nm wavelengths using a JASCO J-715 spectropolarimeter. Protein thermal unfolding was monitored by following the change in CD signal at 222 nm between 20 and 80°C.

NMR characterization

^{15}N-labelled protein samples at 0.1–0.3 mM were placed in a Shigemi NMR tube containing 10% D_2O and 2D ^{1}H-^{15}N SOFAST-HMQC spectra were collected at 298 K with 256 increments on a Bruker Avance3 spectrometer operating at a ^{1}H frequency of 600 MHz equipped with a TCI-P CryoProbe. All spectra were processed using NMRPipe (53) and Bruker Topspin and analysis of the amide backbone chemical shifts and chemical shift mapping was carried out using CcpNmr Analysis (54) and NMRView (55). For the chemical shift mapping, the previously determined backbone assignments (BMRB accession numbers 16 932 (F2F3) and 16 930 (F2) (56)) were used to identify the shifted peaks, which were mapped onto the F2 and F2F3 crystal structures (taken from PDB ID 3IVF (35)) using PyMOL (Schrödinger LLC).

MD simulations

Alchemical free energy calculations were prepared using PMX software (57) and performed with Gromacs (58) at Mahti supercomputer, CSC, Finland. The Amber99SB*–ILDN force field (59) and TIP3P water model in 0.15 M NaCl solution were used. Each system was energy minimized for 10 000 steps and then equilibrated for 1 ns using harmonic position restraints on all heavy atoms of the protein. The temperature and pressure of the system was maintained at 298 K and 1 bar using Berendsen algorithm (60) for the system equilibration, while V-rescale (61) and Parrinello–Rahman (62) algorithms were used for equilibrium MD and non-equilibrium morphing simulations. Integration time step of 2 fs was used in all the simulations. Each state of the system was run for 200 ns equilibrium MD. 186 non-equilibrium morphing simulations were prepared for each physical state of the system, using snapshots captured from the equilibrium trajectories, linearly spaced from 15 to 200 ns. Fast non–equilibrium simulations were morphing the system from one state to another in 100 ps. A soft-core potential (63) was used. The whole calculation, including system preparation, was repeated three times and average free energy value was obtained. The calculated free energy changes upon mutation P229S: F2 (-4.4 ± 0.9 kJ/mol), F2F3 (-4.3 ± 1.2 kJ/mol); P229L: F2 (-2.3 ± 0.6 kJ/mol) F2F3 (3.3 ± 2.2 kJ/mol) were used to calculate the influence of the mutation into the F2F3 interface. 3IVF PDB structure (35) was used for MD.

Cell line, transfection and talin expression constructs

The TLN1$^{-/-}$ TLN2$^{-/-}$ mouse kidney fibroblast (MKF) cell line used were described previously (16). Cells were maintained in a humidified 37°C, 5% CO_2 incubator. High glucose Dulbecco's modified Eagle medium (DMEM) supplemented with 10% fetal bovine serum (FBS) was used in all experiments. The cell line was regularly tested for mycoplasma contamination. Talin variants were subcloned into a modified pEGFP-C1 vector backbone (Clontech). Cells were transfected with 6 μg plasmid DNA per 10^6 cells using Neon transfection system (Thermo Fisher Scientific) using parameters 1400 V, 30 ms, one pulse. The expression constructs for cell culture experiments with the C-terminal EGFP-tag are as follows: full-length wild-type talin1 (1–2541); mini-talin (1–490 + 2296–2541; head-R13-DD domains); head (1–490) and the P229S variant for each construct. These expression constructs are available with maps and sequences in Addgene (https://www.addgene.org/Vesa_Hytonen/).

Migration rate analysis and western blotting

Transfected cells were incubated overnight in the cell culture incubator, trypsinized and plated on the well-plates coated with 10 μg/ml fibronectin. Cells were allowed to attach for 90 min, after which the medium was changed. The time-lapse images captured with EVOS FL auto microscope (Thermo Fisher Scientific) were analyzed manually (12 h) using ImageJ (Fiji) and MTrackJ plugin (64,65). Cells analyzed from either fibronectin (10 μg/ml) and vitronectin (10 μg/ml) coated surfaces, were cultured in 10% FBS containing medium. In addition, cells were analyzed in 0% FBS medium on surface coated with vitronectin (10 μg/ml).

For western blot, cells were cultured in the same time range as for migration speed analysis (48 h post transfection), after which they were collected, boiled at 100°C for 10 min and run on the gel for wet blotting. Band intensities were analyzed using ImageJ (Fiji).

Wound closure assay

Transfected cells were incubated in high confluency (90%) in a 24-well plate for 48 h in the cell culture incubator. The wound (approximately 800 μm) was created using a 100 μl pipette tip. After wounding, the wells were washed with the media to remove dead and detached cells. The wound closure was observed using EVOS FL auto microscope. The images were analyzed manually using ImageJ (Fiji) by using a freehand line tool measuring the distance that cells travelled in 12 h from the starting point.

Immunostaining and confocal imaging

Transfected cells were incubated overnight in the cell culture incubator, trypsinized and plated on coverslips coated with 10 μg/ml human fibronectin and incubated overnight again. Cells were fixed with 4% paraformaldehyde, permeabilized and immunostained using standard protocol. Antibodies are listed in Supplementary Material, Table S1.

Image analysis: protein expression level quantification from confocal images

Immunostained samples were imaged with Zeiss LSM800 laser scanning confocal microscope, mounted on inverted Zeiss Axio Observer.Z1 (Zeiss, Oberkochen, Germany) using Plan-Apochromat 63×/1.40, WD 0.19 mm oil immersion objective. For the quantification of adhesion-localized protein intensity, 5–10 adhesion sites per cell were selected based on the EGFP-talin channel and each selection was copied to the red fluorescence channel, followed by measurement of intensities from both channels using ImageJ. Background was assessed from the EGFP channel, from areas devoid of fluorescence signal and these areas were again copied to the red fluorescence channel, followed by measurement of the intensities. The background intensities were subtracted from the measured adhesion protein intensities for each channel.

Image analysis: quantification of adhesion number and size

For the quantification of adhesion number and size (Supplementary Material, Table S1), samples immunostained against paxillin were used. Paxillin is one of the well-accepted markers of focal adhesions. We used the paxillin single channel image with raw data without any pre-processing. All quantification processes were carried out using ImageJ. Quantification was done with ImageJ as previously shown (66). Shortly, we created an 8-bit image and converted it to greyscale binary image. The peripheral area of the cell was selected using free-hand tool in ImageJ. to analyze particles command with the pre-defined parameters (size = 0.2–5 μm^2, circularity = 0–1) was then executed, which scans the thresholded (binary) image detecting the adhesion sites. It measures the number and size of each adhesion and provides the total area of the adhesion sites.

Photoresist lift-off assisted patterning of ECM proteins (LOP)

To analyze the behaviour of a single cells transfected with full length WT and P229S and to see the effect of the mutation on a single cell in detail, we used the method of photoresist lift-off assisted patterning of ECM proteins (LOP). Previously, Moeller *et al*. described the detailed protocol for this method (67). Shortly, the coverslips (18 × 18 mm Paul Marienfeld GmbH & Co. KG Lauda-Königshofen Germany) were cleaned using acetone, isopropanol and MQH_2O, dried and treated with oxygen plasma for 2 min (Vision 320 RIE, Advanced Vacuum). The photoresist S1818 (Microchem, Westborough, Massachusetts, USA) was spin-coated on the coverslips using the standard contact photolithography and 2 μm thick resist layer was photopatterned (5.6–7.5 mW/cm^2 at 365 nm, OAI instruments). The ice-cream patterns were designed using a chrome mask. The S1818 structure on the coverslip was treated with oxygen plasma for 15 s at 80 W (PICO plasma cleaner; diener) followed by incubating the S1818 structure with 0.1 mg/ml PLL-g-PEG in PBS solution for 30 min at room temperature. The coverslip was then rinsed with MQ and placed in a previously cleaned beaker for the lift-off procedure, protein coating and cell culturing. The lift-off and cell culturing procedures are described in the Supplementary Material.

Supplementary Material

Supplementary Material is available at *HMG* online.

Acknowledgements

We acknowledge Academy of Finland (projects 331946, 323021), Sigrid Juselius Foundation and Cancer Foundation Finland for financial support. We acknowledge CSC for supercomputing resources and Biocenter Finland for infrastructure support. L.A. received support from the graduate school of Tampere University and the Anu Kirra's grant foundation. Ulla Kiiskinen and Niklas Kähkönen (Tampere University) are acknowledged for technical support.

Conflict of Interest statement. The authors declare no competing interests.

Funding

Academy of Finland (331946 to V.P.H., 323021 to V.V.M.); Biotechnology and Biological Sciences Research Council (BB/S007245/1 to B.T.G.).

References

1. Bachmann, M., Kukkurainen, S., Hytönen, V.P. and Wehrle-Haller, B. (2019) Cell adhesion by integrins. *Physiol. Rev.*, **99**, 1655–1699.

2. Barczyk, M., Carracedo, S. and Gullberg, D. (2010) Integrins. *Cell Tissue Res.*, **339**, 269–280.
3. Tanentzapf, G. and Brown, N.H. (2006) An interaction between integrin and the talin FERM domain mediates integrin activation but not linkage to the cytoskeleton. *Nat. Cell Biol.*, **86**, 601–606.
4. Anthis, N.J., Wegener, K.L., Ye, F., Kim, C., Goult, B.T., Lowe, E.D., Vakonakis, I., Bate, N., Critchley, D.R., Ginsberg, M.H. and Campbell, I.D. (2009) The structure of an integrin/talin complex reveals the basis of inside-out signal transduction. *EMBO J.*, **28**, 3623–3632.
5. Goult, B.T., Xu, X.-P., Gingras, A.R., Swift, M., Patel, B., Bate, N., Kopp, P.M., Barsukov, I.L., Critchley, D.R., Volkmann, N. and Hanein, D. (2013) Structural studies on full-length talin1 reveal a compact auto-inhibited dimer: Implications for talin activation. *J. Struct. Biol.*, **184**, 21–32.
6. Gingras, A.R., Bate, N., Goult, B.T., Hazelwood, L., Canestrelli, I., Grossmann, J.G., Liu, H., Putz, N.S.M., Roberts, G.C.K., Volkmann, N., *et al.* (2008) The structure of the C-terminal actin-binding domain of talin. *EMBO J.*, **27**, 458–469.
7. Gingras, A.R., Ziegler, W.H., Frank, R., Barsukov, I.L., Roberts, G.C.K.K., Critchley, D.R. and Emsley, J. (2005) Mapping and consensus sequence identification for multiple vinculin binding sites within the talin rod. *J. Biol. Chem.*, **280**, 37217–37224.
8. del Rio, A., Perez-Jimenez, R., Liu, R., Roca-Cusachs, P., Fernandez, J.M. and Sheetz, M.P. (2009) Stretching single talin rod molecules activates vinculin binding. *Science*, **323**, 638–641.
9. Hytönen, V.P. and Vogel, V. (2008) How force might activate talin's vinculin binding sites: SMD reveals a structural mechanism. *PLoS Comput. Biol.*, **4**, e24.
10. Zacharchenko, T., Qian, X., Goult, B.T.T., Jethwa, D., Almeida, T.B.B., Ballestrem, C., Critchley, D.R.R., Lowy, D.R.R. and Barsukov, I.L.L. (2016) LD motif recognition by talin: structure of the talin-DLC1 complex. *Structure*, **24**, 1130–1141.
11. Haining, A.W.M., Rahikainen, R., Cortes, E., Lachowski, D., Rice, A., von Essen, M., Hytönen, V.P. and del Río Hernández, A. (2018) Mechanotransduction in talin through the interaction of the R8 domain with DLC1. *PLoS Biol.*, **16**, e2005599.
12. Gough, R.E., Jones, M.C., Zacharchenko, T., Le, S., Yu, M., Jacquemet, G., Muench, S.P., Yan, J., Humphries, J.D., Jørgensen, C., *et al.* (2021) Talin mechanosensitivity is modulated by a direct interaction with cyclin-dependent kinase-1. *J. Biol. Chem.*, **297**, 100837.
13. Bouchet, B.P., Gough, R.E., Ammon, Y.C., van de Willige, D., Post, H., Jacquemet, G., F., M.A., Heck, A.J.R., Goult, B.T. and Akhmanova, A. (2016) Talin-KANK1 interaction controls the recruitment of cortical microtubule stabilizing complexes to focal adhesions. *Elife*, **5**, e18124.
14. Sun, Z., Tseng, H.-Y., Tan, S., Senger, F., Kurzawa, L., Dedden, D., Mizuno, N., Wasik, A.A., Thery, M., Dunn, A.R. and Fässler, R. (2016) Kank2 activates talin, reduces force transduction across integrins and induces central adhesion formation. *Nat. Cell Biol.*, **18**, 941–953.
15. Goult, B.T., Brown, N.H. and Schwartz, M.A. (2021) Talin in mechanotransduction and mechanomemory at a glance. *J. Cell Sci.*, **134**, jcs258749.
16. Theodosiou, M., Widmaier, M., Böttcher, R.T., Rognoni, E., Veelders, M., Bharadwaj, M., Lambacher, A., Austen, K., Müller, D.J., Zent, R. and Fässler, R. (2016) Kindlin-2 cooperates with talin to activate integrins and induces cell spreading by directly binding paxillin. *Elife*, **5**, e10130.
17. Ye, F., Snider, A.K. and Ginsberg, M.H. (2014) Talin and kindlin: the one-two punch in integrin activation. *Front. Med.*, **8**, 6–16.
18. Wickström, S.A., Radovanac, K. and Fässler, R. (2011) Genetic analyses of integrin signaling. Genetic analyses of integrin signaling. *Cold Spring Harb. Perspect. Biol.*, **3**, 1–22.
19. Stefanini, L., Ye, F., Snider, A.K., Sarabakhsh, K., Piatt, R., Paul, D.S., Bergmeier, W. and Petrich, B.G. (2014) A talin mutant that impairs talin-integrin binding in platelets decelerates ??IIb??3 activation without pathological bleeding. *Blood*, **123**, 2722–2731.
20. Bouaouina, M., Lad, Y. and Calderwood, D.A. (2008) The N-terminal domains of talin cooperate with the phosphotyrosine binding-like domain to activate beta1 and beta3 integrins. *J. Biol. Chem.*, **283**, 6118–6125.
21. Moore, D.T., Nygren, P., Jo, H., Boesze-Battaglia, K., Bennett, J.S. and DeGrado, W.F. (2012) Affinity of talin-1 for the β3-integrin cytosolic domain is modulated by its phospholipid bilayer environment. *Proc. Natl. Acad. Sci. U. S. A.*, **109**, 793–798.
22. Gingras, A.R., Lagarrigue, F., Cuevas, M.N., Valadez, A.J., Zorovich, M., Mclaughlin, W., Lopez-ramirez, M.A., Seban, N., Ley, K., Kiosses, W.B., *et al.* (2019) Rap1 binding and a lipid-dependent helix in talin F1 domain promote integrin activation in tandem. **218**, 1799–1809.
23. Lagarrigue, F., Gingras, A.R., Paul, D.S., Valadez, A.J., Cuevas, M.N., Sun, H., Lopez-Ramirez, M.A., Goult, B.T., Shattil, S.J., Bergmeier, W. and Ginsberg, M.H. (2018) Rap1 binding to the talin 1 F0 domain makes a minimal contribution to murine platelet GPIIb-IIIa activation. *Blood Adv.*, **2**, 2358–2368.
24. Camp, D., Haage, A., Solianova, V., Castle, W.M., Xu, Q.A., Lostchuck, E., Goult, B.T. and Tanentzapf, G. (2018) Direct binding of talin to Rap1 is required for cell–ECM adhesion in Drosophila. *J. Cell Sci.*, **131**, jcs225144.
25. Petrich, B.G., Marchese, P., Ruggeri, Z.M., Spiess, S., Weichert, R.A.M., Ye, F., Tiedt, R., Skoda, R.C., Monkley, S.J., Critchley, D.R. and Ginsberg, M.H. (2007) Talin is required for integrin-mediated platelet function in hemostasis and thrombosis. *J. Exp. Med.*, **204**, 3103–3111.
26. Kukkurainen, S., Azizi, L., Zhang, P., Jacquier, M.-C.C., Baikoghli, M., von Essen, M., Tuukkanen, A., Laitaoja, M., Liu, X., Rahikainen, R., *et al.* (2021) The F1 loop of the talin head domain acts as a gatekeeper in integrin activation and clustering. *J. Cell Sci.*, **133**, 1–15.
27. Goult, B.T., Bouaouina, M., Elliott, P.R., Bate, N., Patel, B., Gingras, A.R., Grossmann, J.G., Roberts, G.C.K., Calderwood, D.A., Critchley, D.R. and Barsukov, I.L. (2010) Structure of a double ubiquitin-like domain in the talin head: a role in integrin activation. *EMBO J.*, **29**, 1069–1080.
28. Azizi, L., Cowell, A.R., Mykuliak, V.V., Goult, B.T., Turkki, P. and Hytönen, V.P. (2021) Cancer associated talin point mutations disorganise cell adhesion and migration. *Sci. Rep.*, **11**, 347.
29. Ellis, S.J., Lostchuck, E., Goult, B.T., Bouaouina, M., Fairchild, M.J., López-Ceballos, P., Calderwood, D.A. and Tanentzapf, G. (2014) The talin head domain reinforces integrin-mediated adhesion by promoting adhesion complex stability and clustering. *PLoS Genet.*, **10**, e1004756.
30. Ellis, S.J., Goult, B.T., Fairchild, M.J., Harris, N.J., Long, J., Lobo, P., Czerniecki, S., Van Petegem, F., Schöck, F., Peifer, M., *et al.* (2013) Talin autoinhibition is required for morphogenesis. *Curr. Biol.*, **23**, 1825–1833.
31. Monkley, S.J., Zhou, X.H., Kinston, S.J., Giblett, S.M., Hemmings, L., Priddle, H., Brown, J.E., Pritchard, C.A., Critchley, D.R. and Fässler, R. (2000) Disruption of the talin gene arrests mouse development at the gastrulation stage. *Dev. Dyn.*, **219**, 560–574.
32. Turley, T.N., Theis, J.L., Sundsbak, R.S., Evans, J.M., O'Byrne, M.M., Gulati, R., Tweet, M.S., Hayes, S.N. and Olson, T.M. (2019) Rare Missense variants in TLN1 are associated with familial and

sporadic spontaneous coronary artery dissection. *Circ. Genomic Precis. Med.*, **12**, e002437.

33. Li, Y., Gao, S., Han, Y., Song, L., Kong, Y., Jiao, Y., Huang, S., Du, J. and Li, Y. (2021) Variants of focal adhesion scaffold genes cause thoracic aortic aneurysm. *Circ. Res.*, **128**, 8–23.
34. Deng, H., Deng, S., Xu, H., Deng, H.X., Chen, Y., Yuan, L., Deng, X., Yang, S., Guan, L., Zhang, J., Yuan, H. and Guo, Y. (2016) Exome sequencing of a pedigree reveals S339L mutation in the TLN2 gene as a cause of fifth finger camptodactyly. *PLoS One*, **11**, e0155180.
35. Elliott, P.R., Goult, B.T., Kopp, P.M., Bate, N., Grossmann, J.G., Roberts, G.C.K., Critchley, D.R., Barsukov, I.L. and Gu, J. (1993) The structure of the talin head reveals a novel extended conformation of the FERM domain. *Struct. London Engl.*, **18**, 1289–1299.
36. Gapsys, V., Michielssens, S., Seeliger, D. and de Groot, B.L. (2016) Accurate and rigorous prediction of the changes in protein free energies in a large-scale mutation scan. *Angew. Chemie. Int. Ed.*, **55**, 7364–7368.
37. Rahikainen, R., Ohman, T., Turkki, P., Varjosalo, M. and Hytonen, V.P. (2019) Talin-mediated force transmission and talin rod domain unfolding independently regulate adhesion signaling. *J. Cell Sci.*, **132**, jcs226514.
38. Vicente-Manzanares, M. and Horwitz, A.R. (2011) Adhesion dynamics at a glance. *J. Cell Sci.*, **124**, 3923–3927.
39. Han, S.J., Azarova, E.V., Whitewood, A.J., Bachir, A., Guttierrez, E., Groisman, A., Horwitz, A.R., Goult, B.T., Dean, K.M. and Danuser, G. (2021) Pre-complexation of talin and vinculin without tension is required for efficient nascent adhesion maturation. *Elife*, **10**, e66151.
40. Hynes, R.O. (2002) Integrins: bidirectional, allosteric signaling machines. *Cell*, **110**, 673–687.
41. Luo, B.H., Carman, C.V. and Springer, T.A. (2007, 2007) Structural basis of integrin regulation and signaling. Structural basis of integrin regulation and signaling. *Annu. Rev. Immunol.*, **25**, 619–647.
42. Saltel, F., Mortier, E., Hytönen, V.P., Jacquier, M.C., Zimmermann, P., Vogel, V., Liu, W. and Wehrle-Haller, B. (2009) New PI(4,5)P2- and membrane proximal integrin-binding motifs in the talin head control β3-integrin clustering. *J. Cell Biol.*, **187**, 715–731.
43. Wegener, K.L., Partridge, A.W., Han, J., Pickford, A.R., Liddington, R.C., Ginsberg, M.H. and Campbell, I.D. (2007) Structural basis of integrin activation by talin. *Cell*, **128**, 171–182.
44. Calderwood, D.A., Yan, B., de Pereda, J.M., Alvarez, B.G., Fujioka, Y., Liddington, R.C. and Ginsberg, M.H. (2002) The phosphotyrosine binding-like domain of talin activates integrins. *J. Biol. Chem.*, **277**, 21749–21758.
45. Anthis, N.J. and Campbell, I.D. (2011) The tail of integrin activation. The tail of integrin activation. *Trends Biochem. Sci.*, **36**, 191–198.
46. Das, M., Ithychanda, S., Qin, J. and Plow, E.F. (2014) Mechanisms of talin-dependent integrin signaling and crosstalk. *Biochim. Biophys. Acta*, **1838**, 579–588.
47. Ghevaert, C., Salsmann, A., Watkins, N.A., Schaffner-Reckinger, E., Rankin, A., Garner, S.F., Stephens, J., Smith, G.A., Debili, N., Vainchenker, W., *et al.* (2008) A nonsynonymous SNP in the ITGB3 gene disrupts the conserved membrane-proximal cytoplasmic salt bridge in the αIIbβ3 integrin and cosegregates dominantly with abnormal proplatelet formation and macrothrombocytopenia. *Blood*, **111**, 3407–3414.
48. Gresele, P., Falcinelli, E., Giannini, S., D'Adamo, P., D'Eustacchio, A., Corazzi, T., Mezzasoma, A.M., Di Bari, F., Guglielmini, G., Cecchetti, L., *et al.* (2009) Dominant inheritance of a novel integrin β3 mutation associated with a hereditary macrothrombocytopenia and platelet dysfunction in two Italian families. *Haematologica*, **94**, 663–669.
49. Ma, Y.Q., Qin, J. and Plow, E.F. (2007) Platelet integrin αIIbβ3: activation mechanisms. *J. Thromb. Haemost.*, **5**, 1345–1352.
50. Arroyo, A.G., Yang, J.T., Rayburn, H. and Hynes, R.O. (1999) α4 Integrins regulate the proliferation/differentiation balance of multilineage hematopoietic progenitors in vivo. *Immunity*, **11**, 555–566.
51. Fagerholm, S.C., Guenther, C., Asens, M.L., Savinko, T. and Uotila, L.M. (2019) Beta2-Integins and interacting proteins in leukocyte trafficking, immune supression, and immunodeficiency disease. *Front. Immunol.*, **10**, 254.
52. Khan, R.B., Varela, L., Cowell, A.R. and Goult, B.T. (2021) Biochemical characterization of the integrin interactome. *Methods Mol. Biol.*, **2217**, 115–147.
53. Delaglio, F., Grzesiek, S., Vuister, G., Zhu, G., Pfeifer, J. and Bax, A. (1995) NMRPipe: a multidimensional spectral processing system based on UNIX pipes. *J. Biomol. NMR*, **6**, 277–293.
54. Skinner, S.P., Goult, B.T., Fogh, R.H., Boucher, W., Stevens, T.J., Laue, E.D. and Vuister, G.W. (2015) Structure calculation, refinement and validation using CcpNmr analysis. *Acta Crystallogr. Sect. D Biol. Crystallogr.*, **71**, 154–161.
55. Johnson, B.A. and Blevins, R.A. (1994) NMR view: a computer program for the visualization and analysis of NMR data. *J. Biomol. NMR*, **4**, 603–614.
56. Kalli, A.C., Wegener, K.L., Goult, B.T., Anthis, N.J., Campbell, I.D. and Sansom, M.S.P. (2010) The structure of the talin/integrin complex at a lipid bilayer: an NMR and MD simulation study. *Structure*, **18**, 1280–1288.
57. Gapsys, V., Michielssens, S., Seeliger, D. and De Groot, B.L. (2015) pmx: automated protein structure and topology generation for alchemical perturbations. *J. Comput. Chem.*, **36**, 348–354.
58. Abraham, M.J., Murtola, T., Schulz, R., Páll, S., Smith, J.C., Hess, B. and Lindah, E. (2015) Gromacs: high performance molecular simulations through multi-level parallelism from laptops to supercomputers. *SoftwareX*, **1-2**, 19–25.
59. Lindorff-Larsen, K., Piana, S., Palmo, K., Maragakis, P., Klepeis, J.L., Dror, R.O. and Shaw, D.E. (2010) Improved side-chain torsion potentials for the Amber ff99SB protein force field. *Proteins Struct. Funct. Bioinforma.*, **78**, 1950–1958.
60. Berendsen, H.J.C., Postma, J.P.M., Van Gunsteren, W.F., Dinola, A. and Haak, J.R. (1984) Molecular dynamics with coupling to an external bath. *J. Chem. Phys.*, **81**, 3684–3690.
61. Bussi, G., Donadio, D. and Parrinello, M. (2007) Canonical sampling through velocity rescaling. *J. Chem. Phys.*, **126**, 014101.
62. Parrinello, M. and Rahman, A. (1981) Polymorphic transitions in single crystals: a new molecular dynamics method. *J. Appl. Phys.*, **52**, 7182–7190.
63. Gapsys, V., Seeliger, D. and De Groot, B.L. (2012) New soft-core potential function for molecular dynamics based alchemical free energy calculations. *J. Chem. Theory Comput.*, **8**, 2373–2382.
64. Schneider, C.A., Rasband, W.S. and Eliceiri, K.W. (2012) NIH image to ImageJ: 25 years of image analysis. NIH Image to ImageJ: 25 years of image analysis. *Nat. Methods*, **9**, 671–675.
65. Meijering, E., Dzyubachyk, O. and Smal, I. (2012) Methods for cell and particle tracking. *Methods Enzymol.*, **504**, 183–200.
66. Horzum, U., Ozdil, B. and Pesen-Okvur, D. (2014) Step-by-step quantitative analysis of focal adhesions. *MethodsX*, **1**, 56–59.
67. Moeller, J., Denisin, A.K., Sim, J.Y., Wilson, R.E., Ribeiro, A.J.S. and Pruitt, B.L. (2018) Controlling cell shape on hydrogels using lift-off protein patterning. *PLoS One*, **13**, e0189901.